

University of Nottingham
UK | CHINA | MALAYSIA

Additive Manufacture with Copper and Silver Nanoparticles

by David Pervan, MEng

PhD Thesis

Submitted to the University of Nottingham
for the degree of Doctor of Philosophy,
January 2020

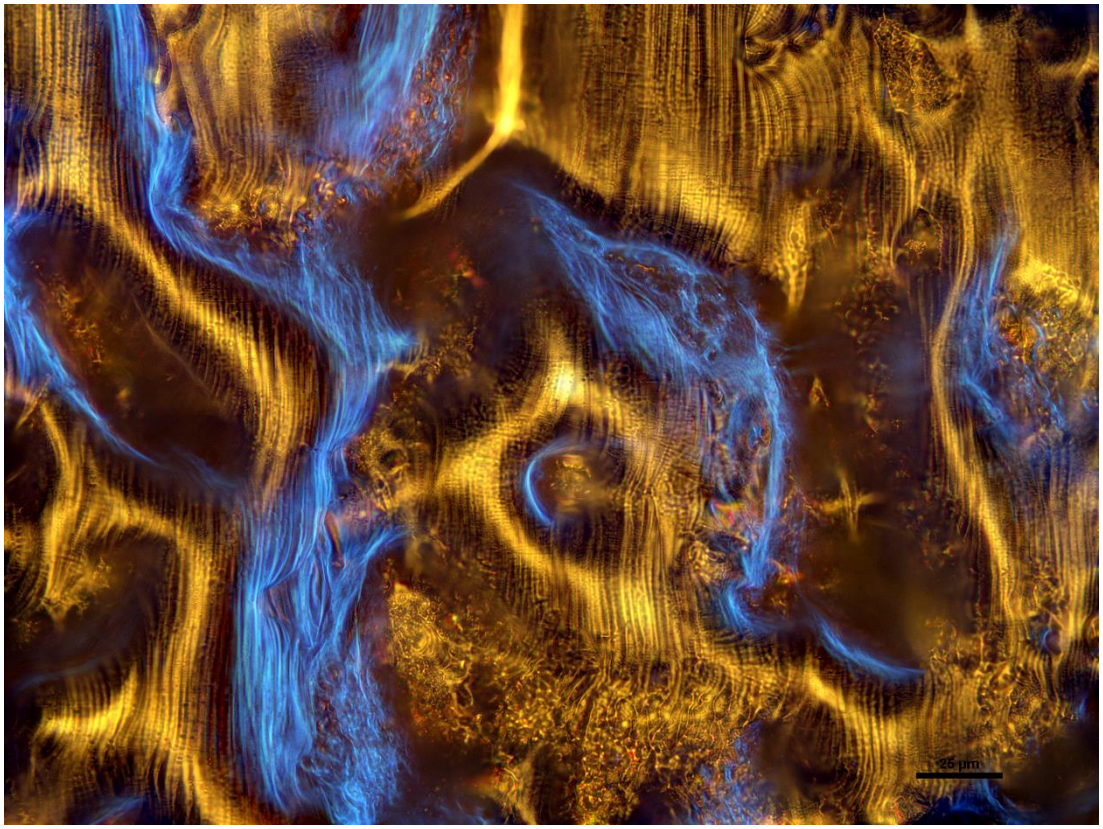


Figure 1. Optical microscopy image of an additively manufactured and laser processed copper surface by the author. This image won several awards.

Abstract

Additive Manufacturing (AM) of electrically conductive copper (Cu) parts is of significant research interested. Cu's high thermal and electrical conductivity combined with its relative abundance and low price makes it an ideal material for thermal and electrical devices. Unlike conventional subtractive manufacturing processes, AM is capable of producing highly geometrically complex parts which is beneficial for many thermal and electrical devices applications. To date there are only capital and energy intensive AM processes which can produce macro-scale Cu parts exist. There is no low-energy process capable of additively manufacturing electrically conductive copper (Cu) microparts. Additively manufactured Cu microparts have potential applications such as microchips, electronic microdevices, medical devices, microfluidic devices, and micro-optical systems. This thesis aims to lay the groundwork for a novel low-power AM process, capable of producing electrically conductive Cu microparts from nanoparticle feedstock in an air environment.

Sequential ink deposition through bar coating and inkjet printing followed by low-power laser sintering in an air environment was used to manufacture multi-layered Cu microparts. The microparts were mechanically and electrically characterised. The use of nanoparticles (NPs) reduced the energy demand for inducing particle sintering. Because of the low laser power of merely 2.5 W and fast heating and cooling rates characteristic for laser irradiation the Cu microparts were unoxidised. The Cu microparts were of low density and highly porous. This had a significant negative effect on the mechanical part properties which were far off from bulk Cu properties. An additional heat treatment to densify the manufactured microparts was suggested in order to improve these mechanical properties. The electrical resistivities of the Cu microparts were close to bulk Cu resistivity.

For two-dimensional (2D) printed electronics applications, silver (Ag) has been the most common conductive material used. Despite its similar electrical conductivity and lower price, copper (Cu) is being used significantly less, mainly because of Cu's tendency to rapidly oxidise which is detrimental to its electrical conductivity. Ultra-fast photonic sintering is capable of "outrunning" the Cu oxidation, yet, the overall

processing cost of Cu remains higher than for Ag. In the first comprehensive study the impact of additions of small amounts of Ag to Cu NPs on ultra-fast and slow sintering processes is investigated. With both ultra-fast sintering techniques, namely IPL and laser sintering, the addition of Ag to Cu NPs does not significantly impact electrical conductivity because the Cu NPs do not oxidise during the ultra-fast sintering. For slow thermal particle sintering the addition of Ag was found to be beneficial. In an air environment the Cu oxidised and hence became dielectric but at a Ag content of 3, 8 and 25 wt%, there was a significant reduction in electrical resistance, which was hypothesised to be due to the Ag content migrating forming a connected grid capable of conducting electricity. During thermal sintering in an inert environment, the Ag content accumulates primarily around the necks of adjacent Cu particles. This was reasoned to be the results of surface tension differences between the Ag-gas and the Ag-Cu interface acting on the mobile Ag. This phenomenon was further investigated in a theoretical simulation, calculating the theoretical reduction in Cu-Cu inter-particle resistance due to Ag accumulation in the necking region.

The most widely reported application of AM with metal NPs is printed electronics. The ability to print and sinter electrically conductive tracks onto heat-sensitive flexible materials enables the manufacture of flexible electronics, such as wearable sensors. To assess whether Cu NPs can be considered a viable replacement for Ag NPs for flexible electronics, the impact of cyclic bending on the electrical resistance and microstructure was investigated. Cu and Ag tracks were inkjet printed and laser sintered at various layers and widths and exposed to cycling bending. Ag NP tracks were significantly more resilient to cyclic bending than Cu NP tracks. Crack growth was the major driver for the observed increase in resistance of the Cu NP tracks which was not found to be the case with the Ag NP tracks. It was hypothesised that the greater width of the Cu particle size distribution compared to Ag likely contributed to the Cu tracks being less resilient to cyclic bending.

Acknowledgements

There have been many people who have helped me through the course of my PhD research, and I am grateful to every one of them.

First and foremost, I'd like to express my sincere gratitude to my supervisors Prof Ricky Wildman, Prof Ed Lester, Prof Chris Tuck and Prof Richard Hague. I have highly appreciated their support and advice and thoroughly enjoyed working with them.

I would like to thank the technical team of the Centre for Additive Manufacturing (CfAM) Mark Hardy, Mark East and Joe White. Their technical support was crucial. I appreciated their willingness to always seek a solution to any technical challenge that occurred.

My thanks go to the (at the time of my PhD) postdoctoral researchers of the CfAM Dr Jayasheelan Vaithilingam, Dr Ehab Saleh, Dr Yinfeng He, Dr Nesma Aboulkhair, Dr Marco Simonelli, and Dr Elizabeth Clark for the useful discussions I had with them over the years as well as the technical training I received from them.

I would like to thank the administrative staff of the CfAM Mirela Axinte and Romina Davoudi for their extraordinary organisational capacities and consistently swift email responses.

Thank you to the technical staff of the NMRC for the training and support I received by Dr Elizabeth Steer, Dr Michael Fay, Dr Chris Parmeter and in particular Dr Martin Roe for his time and dedication with FEG-SEM and its hot-stage.

My thanks go to the technical staff of the Wolfson Building for the training I received and the support by Dr Hannah Constantin, Jason Greaves, and Dr Nigel Neate.

I would like to thank my friend Gonzalo García Luna for training and support on Metrology equipment.

My thanks go to Prof Miquel Gimeno-Fabra, Benjamin Hanby, Greg Mungall, Jack Profound for their support.

My thanks go to Prof Buddhika Hewakandamby for the useful conversations I had with him over the years.

I would like to thank Promethean Particles and their staff for the help and support I received by Dr Selina Ambrose, Dr Pete Gooden, Dr Sean Butterworth, Dr Callum Crawshaw, Dr Jack Turner, Laury Geldenhuys and Bernard Christaud.

Last but not least I would like to thank my parents Dr Birgit Schneider-Pervan, Dr Stjepan Pervan, and my sisters Dr Mascha Pervan and Solvej Krause for their emotional support in good as in bad times over the years.

List of Publications, Conferences, and Awards

Paper under review:

- Gustavo Trindade, Feiran Wang, Yinfeng He, Jisun Im, Adam Balogh, David Scurr, Ian Gilmore, Mariavitalia Tiddia, **David Pervan**, Lyudmila Turyanska, Christopher Tuck, Ricky Wildman, Richard Hague, Clive Roberts, *"Distribution of residual polymer stabiliser within conductive silver nanoparticles (AgNPs) for inkjet-based 3D printing applications"*

Papers in preparation:

- **David Pervan**, Christopher Tuck, Edward Lester, Richard Hague, Ricky Wildman, "*Additive Manufacture of Multi-layered Copper Microparts from Nanoparticle Feedstock in an Air Environment*"
- **David Pervan**, Edward Lester, Christopher Tuck, Ricky Wildman, Richard Hague, "*Hybrid Copper and Silver Nanoparticle Inks and their Electrical Performance under Laser, IPL and Thermal Sintering*"

Conference presentation:

- **David Pervan**, Christopher Tuck, Edward Lester, Richard Hague, Ricky Wildman, "Additive Manufacture of Metal Parts from Nanoparticle Feedstock" at The Enlighten Conference: Metal Powder-based Additive manufacturing in Coventry, U.K., October 2018

Awards:

- "Elizabeth and JD Masden Award" 2015 based on character, personality, exceptional academic performance, as well as active engagement in university activities and extra-curricular activities
- Recognised as an "Inspirational Student" by the University of Nottingham's Student Union for outstanding academic and extracurricular achievements, 2017

- Winner of the “Engineering and Science Graduate Centre (ESGC) Research Community Photo Competition”, 2018
- Winner of the European-wide “CERIC Science Picture Contest” 2018
- Winner of European-wide “Science in the Street” photo contest, 2019

Table of Contents

Abstract _____ *I*

Acknowledgements _____ *III*

List of Publications, Conferences, and Awards _____ *V*

Papers in preparation: _____ **V**

Conference presentation: _____ **V**

Awards: _____ **V**

Table of Contents _____ *VII*

1 INTRODUCTION _____ *1*

1.1 Context _____ **1**

1.2 Aim and Objectives _____ **3**

1.3 Novelty _____ **3**

1.4 Thesis Structure _____ **4**

2 LITERATURE REVIEW _____ *7*

2.1 Introduction _____ **7**

2.2 Additive Manufacturing (AM) – An Overview and its History _____ **7**

2.3 2D Printed Electronics _____ **12**

2.3.1 Nanoparticle synthesis _____ 13

2.3.2 Conductive inks _____ 15

2.3.3 Post-deposition Annealing of Nanoparticles _____ 16

2.3.4 Cu-Ag synergies _____ 20

2.3.5 Cyclic Bending of Inkjet Printed Copper (Cu) and Silver (Ag) Tracks and its Impact on Electrical Resistance _____ 22

2.4 Additively Manufacturing Electrically Conductive Multi-layered Objects: Competing Technologies _____ **23**

2.4.1 Metal Jetting _____ 23

2.4.2 High Energy Manufacture of Multi-layered Copper Structures _____ 24

2.4.3 Inkjet Printing and Sintering of Multiple Electrically Conductive Layers _____ 31

2.5 **Summary and Gap in the Literature** _____ **32**

3 ADDITIVE MANUFACTURE OF ELECTRICALLY CONDUCTIVE MULTILAYERED COPPER (Cu) MICROPARTS FROM NANOPARTICLE (NP) FEEDSTOCK 34

3.1 Introduction 34

3.2 Materials and Methodology 35

3.2.1 Copper Nanoparticle Synthesis and Formulation 35

3.2.2 Deposition of Copper (Cu) Nanoparticle (NP) Ink through Bar Coating 38

3.2.3 Deposition of Copper (Cu) Nanoparticle (NP) Ink through Inkjet Printing 39

3.2.4 Identifying the Copper (Cu) Nanoparticles (NPs) Sintering Temperature Range 39

3.2.5 Laser Irradiation of Copper (Cu) Nanoparticle (NP) Ink to Induce Particle Sintering 39

3.2.6 Manufacturing Process to Additively Manufacture Multi-layered Cu Microparts Using Sequential Ink Deposition, Bar Coating, and Laser Sintering 42

3.2.7 Determination of the Width of the Sintered Area from a Single One-directional Laser Pass 43

3.2.8 Investigations into Potential Oxidation of the Copper (Cu) Nanoparticle (NP) Ink due to Laser Irradiation using X-ray Diffraction (XRD) 43

3.2.9 Nano-hardness and Creep Behaviour of Multi-layered Copper (Cu) Microparts 44

3.2.10 Quantifying Surface Roughness of Multi-layered Copper (Cu) Microparts 46

3.2.11 Electrical Sheet Resistance and Resistivity Measurements of Multi-layered Copper (Cu) Microparts 47

3.2.12 Particle Size Analysis, Visual Evaluation of Internal Defects and Quantification of Internal Porosity of Multi-layered Copper (Cu) Micropart Cross-sections 48

3.2.13 Heat Treatment of Printed and Sintered Multi-layered Copper (Cu) Microparts to Enhance Densification 49

3.3 Pre-experimental Work to Define the Process to Additively Manufacture Multi-layered Copper (Cu) Microparts from Nanoparticle (NP) Feedstock in an Air Environment 50

3.3.1 The Size of the Metal Particles Used and The Sintering Process 50

3.3.2 Quantification of the Particle Size Distribution 54

3.3.3 Deposition of the Nanoparticle (NP) Ink 55

3.3.4 The Drying Process of the Deposited Copper (Cu) Nanoparticle (NP) Film 56

3.3.5 The Impact of the Deposited Layer Thickness on the Additive Manufacturing (AM) Process of Multi-layered Copper (Cu) Microparts from Nanoparticle (NP) Feedstock 58

3.3.6 Image Analysis of the Impact of Laser Sintering of Copper (Cu) Nanoparticles (NPs) through Field-emission Gun (FEG) Scanning Electron Microscopy (SEM) Imaging 62

3.3.7 Elemental Analysis of Laser Sintering of Copper (Cu) Nanoparticles (NPs) through XRD 63

3.4 Sintering induced by Laser Irradiation of a Single Layer of Copper (Cu) Nanoparticle (NP) Ink 64

3.5 Additive Manufacture (AM) of Multi-layered Copper (Cu) Microparts from Nanoparticle (NP) feedstock – A Comparison Between Bar Coating and Inkjet Printing 72

3.5.1 Scanning Electron Microscopy (SEM) Imaging of Cross-sections of Multi-layered Copper (Cu) Microparts 72

3.5.2 Quantification of the Internal Porosity through Image Analysis of Scanning Electron Microscopy (SEM) images of Cross-sections of Multi-layered Printed Copper (Cu) Microparts 74

3.5.3 An Investigation into Surface Roughness of the Multi-layered Printed Copper (Cu) Microparts through White Light Interferometry (WLI) 75

3.5.4 An Investigation into Mechanical Properties of the Multi-layered Printed Copper (Cu) Microparts using Nanoindentation 77

3.5.5 An Investigation into the Density and a Heat Treatment to Increase Density of the Multi-layered Printed Copper (Cu) Microparts 81

3.5.6 An Investigation of Electrical Properties of the Multi-layered Printed Copper (Cu) Microparts through Sheet Resistance Measurements 84

3.6 Discussion of the Comparison between Inkjet Printing and Bar Coating as a Deposition Methods for Additive Manufacture of Multi-layered Printed Copper (Cu) Parts from Nanoparticle (NP) Feedstock 89

3.7 Summary of Additive Manufacturing (AM) of Multi-layered Printed Copper (Cu) Microparts from Nanoparticle (NP) Feedstock 90

4 2D PRINTING AND SINTERING OF COPPER (Cu) AND SILVER (Ag) NANOPARTICLES 92

4.1 Introduction 92

4.2 Materials and Methodology 92

4.2.1 Copper Nanoparticle and Silver Nanoparticle Synthesis and Ink Formulation and Ink Deposition 92

4.2.2 Particle Sintering of Copper (Cu) – Silver (Ag) Hybrid Inks 93

4.2.3 Thermally Induced Nanoparticle (NP) Sintering in-situ the Electron Microscope 94

4.2.4 Image Analysis of FEG-SEM Images of Nanoparticles (NPs) 95

4.2.5 Laser Diffraction Analysis (LDA) of Copper (Cu) – Silver (Ag) Hybrid Inks 97

4.2.6 Differential Scanning Calorimetry (DSC) of Copper (Cu) – Silver (Ag) Hybrid Inks 98

4.2.7 X-ray Diffraction (XRD) Analysis of Copper (Cu) – Silver (Ag) Hybrid Inks 98
4.2.8 Sheet Resistance Measurements of Sintered Copper (Cu) – Silver (Ag) Hybrid Inks 98
4.3 Characterisation of Copper (Cu) – Silver (Ag) Hybrid Inks 99
4.4 Laser Sintering of Copper (Cu) – Silver (Ag) Hybrid Inks 100
4.5 Intense Pulsed Light (IPL) Sintering of Copper (Cu) – Silver (Ag) Hybrid Inks 101
4.6 Thermal Sintering of Copper (Cu) – Silver (Ag) hybrid inks 102
4.6.1 Air (Oxygen-containing) Environment 102
4.6.2 Oxygen-free Environment 106
4.6.3 Theoretical Simulation of the Neck Formation of Silver (Ag) and Copper (Cu) Nanoparticle (NP) Sintering 119
4.7 Discussion 127
4.7.1 Ultra-fast Nanoparticle (NP) Sintering 127
4.7.2 Slow Nanoparticle (NP) Sintering 129
4.8 Summary 135
5 A CYCLIC BENDING STUDY OF INKJET PRINTED AND LASER SINTERED COPPER (Cu) AND SILVER (Ag) TRACKS ON FLEXIBLE PET SUBSTRATES 137
5.1 Introduction 137
5.2 Materials and Methodology 137
5.2.1 Copper (Cu) and Silver (Ag) Nanoparticle (NP) Inks Used, Ink Deposition and Laser Processing 137
5.2.2 Imaging Copper (Cu) and Silver (Ag) Tracks: Light Microscopy, Scanning Electron Microscopy (SEM), and Energy-dispersive X-ray (EDX) Spectroscopy Analysis 138
5.2.3 Investigations into Potential Oxidation of Copper (Cu) and Silver (Ag) Tracks due to Laser Irradiation using X-ray Diffraction (XRD) 139
5.2.4 Cyclic Bending of Inkjet Printed and Laser Sintered Copper (Cu) and Silver (Ag) Tracks 139
5.2.5 Electrical Characterisation of Inkjet Printed Tracks 141
5.2.6 Experimental Matrix 142
5.2.7 Sample Manufacture 142
5.3 X-ray Diffraction (XRD) Elemental Analysis of Inkjet Printed and Laser Sintered Copper (Cu) and Silver (Ag) Tracks 143
5.4 Particle Size Distribution Analysis of the Copper (Cu) and Silver (Ag) Nanoparticle (NP) inks 145

5.5 The Impact of Cyclic Bending on Electrical Resistance 146

5.6 Scanning Electron Microscopy (SEM) and Energy-dispersive X-ray (EDX) Spectroscopy Analysis of Copper (Cu) and Silver (Ag) Tracks Before and After Cyclic Bending 148

5.7 Discussion 149

5.7.1 Printing and Sintering Characteristics 149

5.7.2 The Impact of Cyclic Bending on Electrical Resistance 151

5.8 Summary 154

6 CONCLUSION & RECOMMENDATIONS FOR FUTURE WORK 156

7 REFERENCES 158

8 APPENDIX 187

8.1 Technical Data Sheet of the Copper (Cu) Inkjet Nanoparticle (NP) Ink 187

8.2 MATLAB Script of Image Analysis of Copper (Cu) Nanoparticle (NP) Sintering In-situ a Field-emission Gun Scanning Electron Microscope (FEG-SEM) 188

8.2.1 Analysis of Sintering Copper (Cu) Nanoparticles 188

8.2.2 Analysis of Sintering Silver (Ag) Nanoparticles 188

8.3 XRD Spectra 190

8.3.1 XRD Spectrum of a Bar Coated Multi-layered Cu Sample After Heat Treatment 190

8.3.2 XRD Spectrum of Copper (Cu) Nanoparticles (NPs) prior and after Intense Pulsed Light (IPL) Sintering 190

8.3.3 XRD Spectra of Thermally Sintered Ag-Cu NPs in an Air Environment 191

8.4 Data Tables of Mean Crystallite Sizes Before and After Sintering 193

8.5 Optical Images of Laser Sintering Experiments 194

8.6 Energy-dispersive X-ray (EDX) Spectroscopy Data from Copper (Cu) – Silver (Ag) Nanoparticle (NP) Ink 197

8.7 Differential Scanning Calorimetry (DSC) Curves of Copper (Cu) - Silver (Ag) NPs 199

8.8 Computational Simulation of Ag Accumulation in Adjacent Copper (Cu) Particle Necks 200

8.8.1 Adjacent Copper (Cu) Particles of Equal Size: MATLAB Code 200

8.8.2 Adjacent Copper (Cu) Particles of Varying Size: MATLAB Code 203

1 INTRODUCTION

1.1 Context

Additive Manufacturing (AM) describes the process of manufacturing a part additively as opposed to subtractively or formatively. The starting point is normally a Computer-aided Design (CAD) drawing of the part to be manufactured, which is digitally sliced into parallel layers. The information on the layers as well as its processing parameters are executed by additively stacking layer upon layer to manufacture the desired part. Sometimes support structures are introduced to ensure structural integrity during the built which are later removed. The American Society for Testing and Materials International (ASTM) classifies AM into seven process categories (ISO/ASTM, 2015):

- **Binder jetting**: *"an AM process in which a liquid bonding agent is selectively deposited to join powder materials".*
- **Directed energy deposition**: *"an AM process in which focused thermal energy is used to fuse materials by melting as they are being deposited".*
- **Material extrusion**: *"an AM process in which material is selectively dispensed through a nozzle or orifice".*
- **Material jetting**: *"an AM process in which droplets of build material are selectively deposited".*
- **Powder bed fusion**: *"an AM process process in which thermal energy selectively fuses regions of a powder bed".*
- **Sheet lamination**: *"an AM process process in which sheets of material are bonded to form a part".*
- **Vat photopolymerisation**: *"an AM process in which liquid photopolymer in a vat is selectively cured by light-activated polymerization".*

Historically, the roots of AM can be traced back to the late 19th century due to the emergence of sculpture and topography (Gao et al., 2015). However, it wasn't until the 1980s that AM was first commercialised when 3D Systems released a stereolithography printer (Gibson et al., 2015). Due to the ability to rapidly

manufacture unique parts at low volume, AM techniques became widely known as rapid prototyping. In the following decades until now, AM has developed significantly, particularly in the areas of materials, processes, software and equipment (Pham and Dimov, 2003). Advantages of AM over traditional manufacturing (Gibson et al., 2015) include the ability to produce complex and lightweight geometries including topology optimisation (Compton and Lewis, 2014; Hague et al., 2004), the ability to produce one-off parts (Conner et al., 2014; Matilainen et al., 2014) as well as functionally graded parts (Gao et al., 2015), and lower material waste. Today AM is being used a wide range of industries, including aerospace (Thomas et al., 1996), automotive (Song et al., 2002), and biomaterials (Giannatsis and Dedoussis, 2009; Sachlos and Czernuszka, 2003). However, challenges with AM remain in areas such as printing speed, printable material portfolio and part accuracy (Gibson et al., 2015).

The miniaturisation of products in various industries such as medical, automotive, optics, electronics, and biotechnology has led to a demand for improvements in micro-fabrication technologies (Alting et al., 2003). Microfabrication processes include laser ablation, plating, photolithography, lithography, electroplating, molding, chemical etching, microextrusion, laser patterning/cutting/drilling, EDM, microinjection molding, microembossing, microstamping, and micromechanical cutting (Qin, 2010). However, most of these techniques are restricted when applied to new microproducts which require different materials and have complicated 3D microstructures with high aspect ratios (Vaezi et al., 2013). Manufacturing technologies for 3D microcomponents are crucial for the development of various functional applications such as biochips, integrated microsensors, medical devices, microelectromechanical systems (MEMS), microfluidic devices, micro-optical systems, and photonic crystals (J. W. Lee et al., 2008; K. Lee et al., 2008). These technologies will advance substantially if more complex 3D microstructures can be manufactured.

1.2 Aim and Objectives

The aim of this PhD has been to additively manufacture electrically conductive 3D Cu microparts and further, to better understand if the addition of silver (Ag) to copper (Cu) nanoparticles (NPs) can facilitate the copper (Cu) nanoparticle (NP) sintering.

The objectives can be summarised as:

- Develop a low power (< 10 W) laser process capable of additively manufacturing Copper (Cu) microparts from Nanoparticle (NP) feedstock in an air environment
- Investigate 2D printing and sintering of Cu and Ag NPs
    - Establish an understanding of the effect of additions of Ag to Cu NPs on both ultra-fast and slow sintering techniques
    - Investigate Ag and Cu mass transport mechanisms in Cu-Ag NP systems and analyse its impact on inter-particle resistance
    - Compare the impact of cyclic bending on electrical resistance of inkjet printed Cu and Ag tracks

1.3 Novelty

This PhD has created novel understanding of AM with metal NPs. Novelty was demonstrated in two specific and complementary areas.

Prior to this PhD no process existed that was capable of additively manufacturing Cu microparts from with a low-power energy source (2.5 W) in an air environment. In this PhD the groundwork was laid to achieve this by sequential recoating or the inkjet printing of Cu NP inks and laser processing. Multi-layered parts were manufactured using both deposition techniques. The multi-layered parts were characterised to give a thorough understanding of their mechanical and electrical properties and their microstructure.

Printing and sintering of copper (Cu) and silver (Ag) nanoparticles (NPs) has been investigated. Though literature exists, novel aspects were investigated in two different results chapters as follows.

Specifically, in a comparative study it was shown for the first time that for ultra-fast sintering techniques during which Cu does not oxidise, Ag addition does not improve processing parameters. Moreover, no prior literature exists on real-time monitoring at regular temperature intervals of Cu and Ag NP sintering *in-situ* an SEM and the quantification of this process. It was shown that during thermal treatment, Ag migrates predominantly to Cu-Cu particle contact points, increasing contact area between adjacent Cu particles. For the first time, the resulting theoretical reduction in inter-particle electrical resistance of this effect was quantified.

The impact of cyclic bending on electrical resistance of inkjet printed Cu and Ag NPs was investigated. Individual studies on both Cu and Ag NP materials exist in the literature, however, they vary significantly in terms of sample manufacturing and testing methodology – making this the first study directly comparing the two materials using the same methodology.

1.4 Thesis Structure

Chapter 2: "Literature Review" provides a thorough review of the relevant literature of this thesis. It covers the background and a brief history of Additive Manufacturing (AM). Thereafter printing of electronics is investigated in terms of the conductive metal inks used as well as the different sintering techniques applied. Mixing Cu with small amounts of Ag and the synergies that can arise are discussed as well as the impact of the cyclic bending on electrical resistance of inkjet printed Cu and Ag tracks. It follows a review of the AM techniques capable of manufacturing multi-layered Cu parts. Finally, the following gaps in the literature are identified. Firstly, no study exists which comparatively investigates the impact of Ag addition to Cu NPs on laser sintering, Intense Pulsed Light (IPL) sintering, and thermal sintering in an air environment as well as in an inert environment; secondly, there is no literature on

the impact of Ag migration during thermal treatment to Cu particle contact points on electrical resistance; thirdly, there is no study comparing the impact of cyclic bending on electrical resistance of identically manufactured inkjet printed Ag NP tracks with Cu NP tracks; and fourthly, there are no records of a low-power AM process to manufacture electrically conductive multi-layered Cu microparts in an air environment.

Chapter 3: "Additive Manufacture of Electrically Conductive Multi-layered Parts from NP Feedstock" first explains the methodology used for part manufacture and characterisation. The results then describe some basic characterisation of the Cu NP ink. It then develops an understanding of the impact of laser sintering of a single layer of Cu NP ink. It follows the characterisation of multi-layered Cu samples as a comparison between the two different ink deposition methods, namely bar coating and inkjet printing. A thorough discussion compares the two deposition methods and compares this AM process to other processes capable of manufacturing multi-layered Cu microparts.

Chapter 4: 2D "2D Printing and Sintering of Copper (Cu) and Silver (Ag) Nanoparticles" investigates the sintering process of Cu and Ag NPs and the impact of the addition of small amounts (≤ 25 wt%) of Ag to Cu NPs. The methodology of the NP ink synthesis, formulation, deposition, sintering and characterisation is explained followed by the results of the Cu and Ag NPs sintering. Firstly, the sintering process of solely Cu NPs and solely Ag NPs separately is analysed. Secondly, the impact of Ag addition to Cu NPs on oxidation stability and electrical resistance during laser, IPL and thermal sintering is investigated. During thermal sintering, the observed phenomenon of Ag accumulating in the necks of Cu particles is computationally modelled. A discussion follows on the sintering behaviour of Cu and Ag NPs and whether additions of Ag to Cu NPs can harness synergistic effects beneficial for the sintering process.

Chapter 5: "A Cyclic Bending Study of Inkjet Printed Copper (Cu) and Silver (Ag) Tracks on Flexible PET Substrates": The most widely reported application of AM with metal NPs is printed electronics. The ability to print and sinter onto flexible materials

enables flexible electronics for which copper (Cu) nanoparticle (NP) ink is considered a cost-effective alternative to silver (Ag) NP ink. This chapter is a comparative study of the impact of cyclic bending on electrical resistance of Cu and Ag inkjet printed tracks to assess whether Cu NPs could replace Ag NPs. It explains the methodology of the metal nanoparticle ink printing and annealing (a.k.a. sintering), the cyclic bending of the tracks and the characterisation carried out before and after cyclic bending. The results are presented as the impact of cyclic bending on electrical resistance as well as characterisation prior and post cyclic bending. A discussion follows investigating the hypothesis for the disparity in the resilience towards cyclic bending of the two materials, Cu and Ag.

Chapter 6: "Conclusion & Recommendations for Future Work" summarises the main findings of the thesis and describes how the aims were fulfilled.

2 LITERATURE REVIEW

2.1 Introduction

The literature review is organised into several sections, namely on AM generally and its history, printed electronics, and additively manufacturing electrically conductive multi-layered objects.

AM is explained, including a description, its historical background and some of its applications are elaborated on. AM applied to electronics through printed electronics is covered in more depth, elaborating on nanoparticle synthesis, the various conductive inks, and NP sintering techniques. Cu-Ag synergies are discussed followed by a review of cyclic bending studies of inkjet printed tracks. Finally, all relevant AM processes capable of fabricating multi-layered Cu parts are reviewed, including metal jetting and inkjet printing, as well as higher energy processes such as SLM, EBM and binder jetting.

2.2 Additive Manufacturing (AM) – An Overview and its History

The ISO/ASTM F42 Technical Committee defines additive manufacturing (AM) as the "process of joining materials to make objects from three-dimensional (3D) model data, usually layer upon layer, as opposed to subtractive manufacturing methodologies" (ISO/ASTM, 2015).

The historical roots of AM can be traced back to photo sculpture and topography which arose in the 1860s and the 1890s respectively (Gao et al., 2015). These two early technologies led to the "photo-glyph recording" technique whereby layers of a transparent photo emulsion are selectively exposed while scanning cross-sections of the object to be replicated; a process that was patented in 1951 (Munz, 1956). Subsequent advances in computing, lasers and photopolymers led to stereolithography (SLA) in 1984 (Hull, 1986; Jacobs, 1992). Further patents, as well as publications, paved the way for modern day AM from the late 1980s and early 1990s including vat photopolymerisation (Deckard et al., 1992), Fused Deposition Modeling (FDM) (Crump, 1992; Marcus et al., 1994) (an example can be seen in

Figure 2), material extrusion, Three Dimensional Printing (3DP) (Sachs et al., 1993), Selective Laser Sintering (SLS) (Beaman et al., 1997), Laminated Objective Manufacturing (LOM) (Feygin and Hsieh, 1991) and Laser Metal Deposition (LMD) (Mazumder et al., 1999). To date, a variety of materials can be used in these processes, including polyamide, photo-curable resin, wax, acrylonitrile-butadiene-styrene (ABS), polycarbonate, metal/ceramic/polymer powders, adhesive coated sheets (Guo and Leu, 2013).

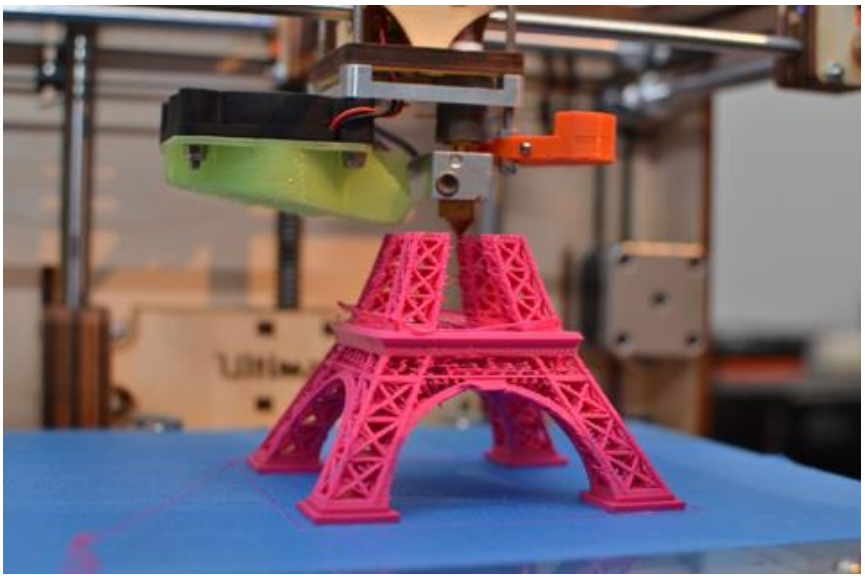


Figure 2: Model Eiffel Tower being additively manufactured layer-by-layer.

In the past decade, AM has gained popularity in the media where it is widely referred to as 3D printing, particularly through platforms such as Do-It-Yourself (DIY) and the Maker Movement (Anderson, 2012). Significant advancements in the past two decades in the areas of materials, processes, software and equipment have led to improved design flexibility, part accuracy and time and cost efficiency which consequentially saw AM being applied in industry beyond solely prototyping in rapid tooling and manufacturing (Pham and Dimov, 2003). A few examples of industrial applications follow.

Many aerospace components such as the engine housing in Figure 3 require complex geometries from advanced materials such as superalloys and ultra-high-temperature materials which are costly and time-consuming to manufacture with conventional subtractive techniques. Moreover the small volume nature of production runs in the

aerospace industry adds to the benefits of the application of AM (Thomas et al., 1996).

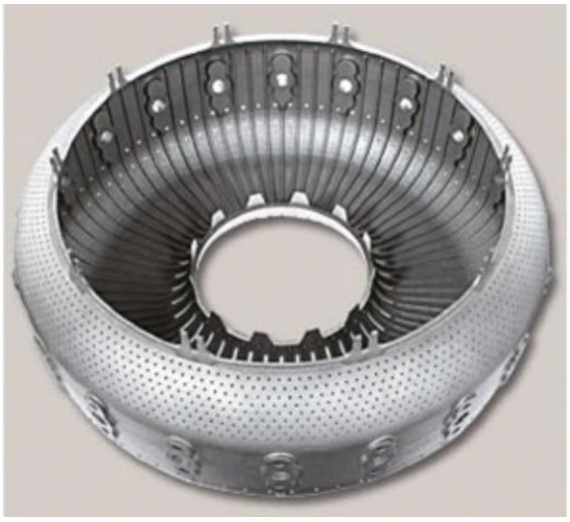


Figure 3: Aerospace engine housing with internal cooling channels additively manufactured through Selective Laser Melting (SLM) technique (Guo and Leu, 2013).

In the automotive industry AM techniques have been utilised for structural and functional parts such as engine exhausts or drive shafts of passenger cars as well as motorsports vehicles because AM is able to shorten product development cycles and reduce manufacturing costs (Song et al., 2002).

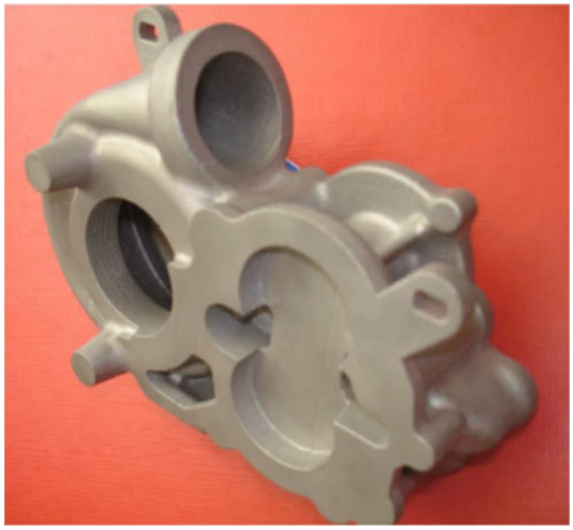


Figure 4: Lightweight cooling water pump for a sports car manufactured through Selective Laser Melting (SLM) technique (Guo and Leu, 2013).

Thanks to recent developments in biomaterials, AM techniques have increasingly been applied in the biomedical realm for applications such as orthopaedic implants

and tissue scaffolding. Printing protein and cells has opened the door to research on additively manufacturing biologic chips, micro-vasculature networks and artificial organs (Giannatsis and Dedoussis, 2009; Sachlos and Czernuszka, 2003).



Figure 5: Hip stems with mesh, hole and solid configurations to tailor mechanic properties that mimic the stiffness of bone to reduce stress shielding; manufactured by Electron Beam Melting (EBM) of Ti6Al4V (Guo and Leu, 2013).

Despite recent progress, challenges remain such as the limited variety of materials available, the lack of fundamental design guidelines or standardisation of best practices (Gao et al., 2015), relatively poor part accuracy due to “stair-stepping” effect (Onuh and Yusuf, 1999) (see Figure 6 for a visualisation) as well as poor repeatability and consistency (Guo and Leu, 2013).

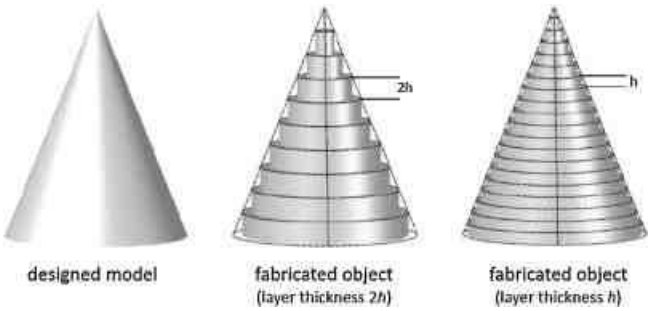


Figure 6: An example of the stair-stepping effect on a cone and the resulting disparity between a designed and fabricated object. With decreasing layer height h this disparity is reduced.

Lately there has been a greater push beyond solely geometric complexity towards added functionality. Multi-material printing for instance enables the creation of parts

with functionally graded materials and their corresponding properties such as hardness, flexibility, adhesive properties, stiffness and colour on a voxel-by-voxel basis (Gao et al., 2015).



Figure 7: Additively manufactured prosthetic arm as an example for a multi-functional product consisting of a linked assembly of multiple materials (The University of Nottingham, n.d.).

Printed assemblies are another example of multi-functionality. It often requires sacrificial support materials which are removed leaving a captive assembled linkage. Thereby physical working models (Alam et al., 1999; Laliberté et al., 1999; Lipson, 2007; Lipson et al., 2005; Mavroidis et al., 2000), compliant mechanisms (Canfield and Frecker, 1999; Goldfarb and Speich, 1999), articulated models (Bächer et al., 2012; Cali et al., 2012), locomotive robots (Felton et al., 2013; Onal et al., 2011) and prosthetics (He et al., 2006; M.-Y. Lee et al., 2008; Rengier et al., 2010; Singare et al., 2007; Wang et al., 2004) have been manufactured. The ability to embed foreign components throughout builds is a fundamental advantage of AM's layer-by-layer fabrication. By embedding functional components, i.e. circuits, motors and sensors, direct fabrication of functional assemblies and mechanisms is possible, thereby making a secondary assembly step redundant. This enables the manufacture of objects such as robotic limbs, smart structures with embedded sensors and energy harvesting devices with embedded piezoelectric materials (Gao et al., 2015). With its capabilities of printing circuits, sensors and batteries, printed electronics has been developing functionality in AM further, which will be described in the following section.

2.3 2D Printed Electronics

Traditionally most conventional electronics can be manufactured subtractively as opposed to additively, such as photolithography, vacuum deposition, and electroless plating. They are all multi-staged, they require expensive equipment and produce a lot of hazardous chemical waste (Kamyshny and Magdassi, 2014). Photolithography, which is the most common manufacturing technique, has been described as the cornerstone of modern day computer chip manufacture. It consists of several process steps as shown in Figure 8 whereby patterns of light are used to chemically modify solubility of coated polymer films (Parekh et al., 2015).

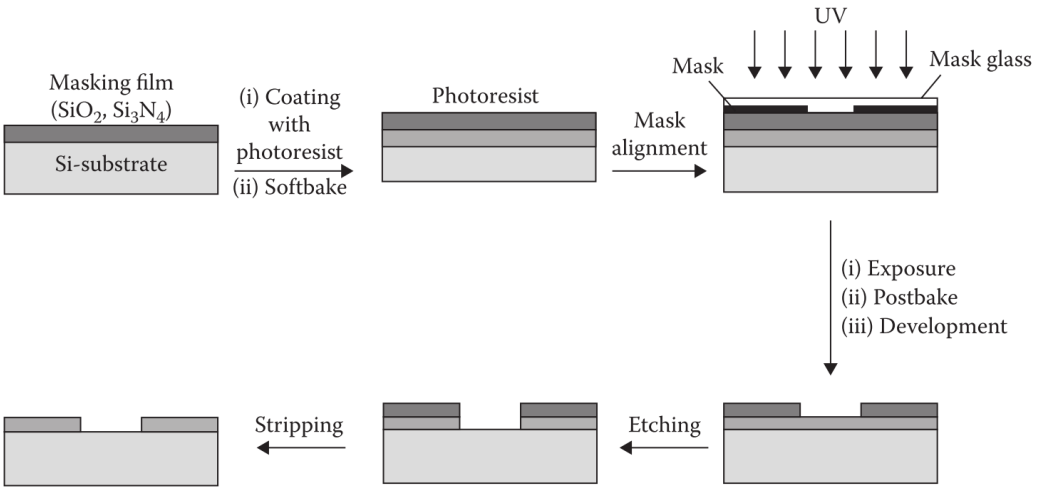


Figure 8.: Schematic overview of the photolithography process. The source is a website in (Parekh et al., 2015)

Photolithography is a subtractive multi-step manufacturing process which uses a host of hazardous chemicals. The great majority of the deposited conductive material is removed through etching and is not recovered from the etched solution – making this a highly resource inefficient process.

In contrast to resource inefficient conventional subtractive manufacturing techniques of electronics, additive manufacture of circuitry is capable of selectively depositing conductive material digitally controlled precisely where it is required, making it highly resource efficient. This is particularly important with precious

conductive metals. The ability to selectively print and anneal conductive materials onto a variety of substrates challenges the status quo of electronics manufacture.

Printed electronics enables manufacture of thin, lightweight and extremely cost-efficient electronics systems. Currently the main applications of printed electronics in industry include organic photovoltaics (Shrotriya, 2009), flexible batteries (Hilder et al., 2009; Ho et al., 2008), electro-optic devices (Argun et al., 2004; Chang et al., 1999; Yoshioka and Jabbour, 2006), field effect transistors (FETs) and thin film transistors (TFTs) (Gamerith *et al.*, 2007; Kim *et al.*, 2007; Ko *et al.*, 2007; Sekitani *et al.*, 2009; Song *et al.*, 2009), sensors (Chang et al., 2006, 2007; Loffredo et al., 2007; Marinov et al., 2007; Möller et al., 2008) and radio frequency identification (RFID) tags (Subramanian et al., 2005). The printed electronics market is predicted to exceed $300 billion over the next 20 years (Lupo et al., 2013).

However, printing electronics comprises various challenges. The conductive material must exist in the form of a well dispersed and stable ink which can be printed. Apart from reactive inks, inorganic inks generally require post-deposition treatment to anneal or sinter the ink. Furthermore, printing of electronics has not been able to produce the similar minimum feature sizes to conventional manufacturing techniques.

2.3.1 Nanoparticle synthesis

The most significant attributes of NPs are size, morphology and surface area. Material synthesis and handling significantly impacts these attributes. NP synthesis can generally be categorised into two categories: top-down and bottom-up.

2.3.1.1 Top-down NP synthesis

Town-down approaches start off with a larger scale of solid material which is broken down to a smaller scale. The most common process is mechanochemical milling

(Chen et al., 2010) and laser ablation (Amendola et al., 2011). Compared to bottom-up synthesis approaches, top-down approaches have several disadvantages. These include very limited control of final average particle size and the particle size distribution tends to be very wide. Moreover, top-down approaches are often very energy and time intensive. The literature on bottom-up NP synthesis is therefore much greater.

2.3.1.2 Bottom-up NP synthesis

Bottom-up synthesis generally involves starting off with a smaller building block than the size of the final particle size. For NPs the starting point are commonly atoms (Rotello, 2004). For synthesis of metal NPs relevant to printed electronics and AM such as Cu and Ag, liquid-phase methods are the most common synthesis routes. Liquid-phase NP synthesis methods include co-precipitation, microemulsion, sol-gel, and hydothermal/solvothermal synthesis (Tang et al., 2014).

Hydrothermal synthesis uses water at high temperature and pressure to crystallise materials (Ballman and Laudise, 1963). Demazeau defined high temperature in the context of hydrothermal processes as above the boiling temperature at which point elevated pressure is involved too (Demazeau, 2011). Hydrothermal synthesis can be classified into whether the water is above (supercritical) or below (sub-critical) its critical point ($T_C = 374\,°C,\ P_C = 22.1 \times 10^6\,Pa$). Above its critical point, the hydrogen bonds in water break down, increasing the H^+ and OH^- concentration at which point water is considered supercritical (Lester et al., 2006). Sub-critical water is polar. Supercritical water, on the other hand, is weakly-polar and can dissolve non-polar molecules. At the same time, however, it only has a low solubility for inorganic ionic salts causing them to precipitate out and form solid-state particles.

Where hydrothermal synthesis uses water, solvothermal synthesis uses non-aqueous solvents such as alcohols. Depending on the solvent its critical point is different to water and so different temperatures and pressures for supercritical solvothermal

synthesis. With solvents generally being more expensive than water, solvothermal synthesis entails higher costs than hydrothermal synthesis. In some cases such as often for metal NPs, however, using solvents rather than water is favourable as no addition of toxic reducing agents is necessary (Choi et al., 2010).

2.3.2 Conductive inks

In 1909 Pawlow predicted a decrease in melting point of metallic nanoparticles (NPs) (Pawlow, 1909). Buffat and Borel demonstrated that this is indeed the case with gold NPs (Buffat and Borel, 1976). Due to the high surface-to-volume ratio and the consequentially high surface energy of NPs, their thermodynamic driving force for sintering is extremely large (Fang and Wang, 2010). The energy required to induce sintering or melting is therefore significantly lower than their respective bulk materials. The possibility to formulate NPs into stable and inkjet printable inks makes NPs attractive for digital additive manufacturing of electrically conductive tracks.

Perelaer et al. defined the ideal metal containing ink to have the following properties: cheap, easy to prepare, store and jet, achieving high values of conductivity after deposition and post-processing (Perelaer et al., 2010). The majority of literature on printing of metal NP inks is on silver, followed by copper and gold and to a lesser extent also aluminium and nickel. Of all the conductive materials for printed electronics available to date, silver has been most widely used despite its relatively expensive nature. This is largely due to the absence of practical issues during use including issues with sintering temperatures, oxidation and agglomeration (Cummins and Desmulliez, 2012; Grouchko et al., 2011; Kamyshny et al., 2011; Kamyshny and Magdassi, 2014; Perelaer et al., 2012, 2006; Rae and Hammer-Fritzinger, 2006; Wolf et al., 2013). The above mentioned materials vary significantly in terms of their raw material price, with prices per ounce of silver, copper, gold, aluminium and nickel respectively at $15.00, $0.20, $1288, $0.06 and $0.53 (Money Metals Exchange, 2019). Prices per ounce do not accurately represent production prices of respective inks, however, they indicate the relative price range of the bulk metals which gives an indication of the disparity of the value of the metal content of

inks. For instance, the high price of gold prohibits gold from becoming an industry standard for printed electronics. They vary slightly in terms of their bulk resistivity (1.59×10^{-8} Ω m, 1.72×10^{-8} Ω m, 2.44×10^{-8} Ω m, 2.82×10^{-8} Ω m, 6.99×10^{-8} Ω m respectively). Literature on the use of nickel and aluminium in printed electronics is limited. In 2009 Li et al. ink jetted nickel tracks. However, resistivities of six hundred times the resistivity of bulk nickel were obtained. Moreover, resistivity significantly increased further over time due to oxidation and the formation of Nickel oxide which occurred at ambient conditions (Li et al., 2009). The only successful results for conductive nickel tracks were obtained in 2014 by Park & Kim. They conducted similar experiments, in contrast though, pulsed flash lamps were used for sintering. Resistivities of approximately eleven times the resistivity of bulk nickel were achieved (Park and Kim, 2014). Almost no literature was found on successful applications of aluminium as a conductive material in printed electronics. According to Kamyshny et al. this is because aluminium undergoes rapid oxidation in air leading to the formation of a dense thin amorphous aluminium oxide layer (Campbell et al., 1999; Foley et al., 2005) which results in a loss of electrical conductivity (Kamyshny et al., 2011).

In recent years, copper nanoparticles have attracted attention as a significantly cheaper alternative due to their potential for replacing silver as a conductive material for printed electronics, as copper has a very similar resistivity but comes at a fraction of the cost compared to silver.

2.3.3 Post-deposition Annealing of Nanoparticles

High electrical conductivity values are a critical factor for the successful application of printed electronics. Post-deposition annealing (also known as sintering) of ink is the decisive process impacting final conductivity and remains the key challenge and focus of research over the past decade (Huang et al., 2003; Lu et al., 2007; Perelaer et al., 2008; Smith et al., 2006). Sintering describes particles bonding together when heated through a combination of several atomic mass transport mechanisms, including diffusion, creep, viscous flow, plastic flow and evaporation (German, 2010).

The resistivity obtained through a sintering process is generally a multiple of the resistivity of the bulk material. This is because processing temperatures during sintering are significantly below the melting point of the material. Increasing temperature towards the melting point increases the degree of densification which in turn reduces resistivity towards the bulk material resistivity. Therefore, elevated temperatures are required to achieve low values of resistivity which generally is desirable with electrically conductive materials.

A major obstacle for Cu to be widely used in printed electronics is its inherent tendency to oxidise making it dielectric in ambient conditions which greatly accelerates at elevated temperatures during sintering. There have been various approaches to overcome this challenge. One of them is coating the copper nanoparticles with a protective layer consisting of an organic polymer, alkene chains, amorphous carbon, graphenes, or even inorganic materials such as silica or an inert metal (Magdassi et al., 2010). However, introducing a less or non-conductive shell on the copper nanoparticles has a negative effect on the electrical conductivity of the printed pattern. Silver shells appear to be the best reported route to avoiding oxidation, since they do not appear to reduce conductivity (Grouchko et al., 2009). However, coating copper in silver significantly raises the material and processing costs. Lee et al. approached the oxidation challenge by printing metal-organics on substrates (Lee et al., 2009). The metal metal-organics then decomposed into highly conductive copper metal when annealed at temperatures above 250°C to form copper metal and nano-sized copper hydroxide.

2.3.3.1 Thermal Sintering

Thermal sintering of Cu NPs commonly requires temperatures of >250 °C and exposure times of >30 minutes. The elevated temperature and time requirements limit the compatibility of heat-sensitive substrates such as common polymer foils such as polyethylene terephthalate (PET) or polycarbonate (PC). In order to avoid the oxidation of Cu, this sintering process has to be carried out in a sealed chamber in an inert environment. Even though literature on thermal sintering of Cu NPs exist (Park

et al., 2007; Yabuki and Arriffin, 2010), these process requirements limit the applicability of thermal sintering to solely research based experiments. The cost savings of using copper rather than silver are thereby significantly reduced. Its application to large scale industrial manufacturing process, such as roll-2-roll manufacturing lines to date seems highly unlikely.

2.3.3.2 Photonic Ultra-fast Sintering

Photonic sintering is capable of inducing sufficiently high heating and cooling rates in order to induce sintering in a period of time so short that it is not sufficient for the Cu to oxidise. Energy is supplied in the form of spatially (and sometimes timely) concentrated photons. This allows a spatially confined volume of deposited particulate material to be heated to the necessary sintering temperatures, which then subsequently cools through energy dissipation, all within milliseconds. As a consequence, the substrate is exposed to significantly less thermal stress, meaning that less thermally stable polymers such as PET and PC can be used.

2.3.3.2.1 Laser Sintering

In the past few years reports have been increasing on the use of laser irradiation for sintering of metal NPs. The first successful report of sintering any metal NPs was published in 2007 by Ko et al., who reported successful laser sintering of gold (Au) NPs (Ko *et al.*, 2007). Joo et al. first reported on laser sintering of a Cu paste in a nitrogen atmosphere using an ultraviolet (UV) laser beam at 355 nm (Joo et al., 2011). A minimum resistivity of eleven times the resistivity of bulk copper was achieved. Various other reports of Cu NP ink laser sintering in inert environments followed Joo et al.. However, as the stated aim of this study is to be carried out in an ambient environment, they are not of interest.

Halonen et al. were the first to publish on successful laser sintering of Cu NP ink under ambient conditions in 2013 (Halonen et al., 2013). Cu NP ink was inkjet printed onto

a polyimide (PI) substrate and laser sintered with a continuous-wave 808 nm diode laser. A minimum sheet resistance of 90 mΩ/□ was achieved.

Zenou et al. a commercial ink (metal load of 25 wt%) was spin-coated onto glass substrates and dried in ambient air on a hot plate at 70 °C (Zenou et al., 2014). The sample was then laser sintered using a continuous wave (CW) Nd: YAG laser. Zenou et al. were able to successfully laser sinter copper resulting in resistivities of less than 3 times bulk copper resistivity (sintered layer thickness 121-450 nm). By reducing the laser spot diameter to 4 µm Zenou et al. were able to reduce conductive linewidths down to 6.7 µm.

In 2015 Niittynen et al. published a comparative study of laser sintering and intense pulsed light sintering of inkjet printed Cu NP inks both in ambient air (Niittynen et al., 2015). Niittynen et al. were not able to successfully laser sinter single layer Cu-NP ink due to the appearance of intensive cracking during laser sintering; they instead laser sintering 2-4 layers of inkjet-printed Cu-NP ink. The result with the highest electrical conductivity through laser sintering was approximately 16 % of bulk copper conductivity. Niittynen et al. are the only publication who printed, though just up to 4, multiple layers. The maximum thickness of the Cu NP film that was laser sintered was approximately 1.9 µm.

Kwon et al. bar coated a Cu NP paste onto glass and polyethylene (PE) substrates (Kwon et al., 2016). An air plasma treatment was performed at 50 W for 1 min before the bar-coating process to enhance adhesion strength between Cu NPs and substrates. A CW diode-pumped ND:YAG laser at 532 nm wavelength was used for laser sintering under ambient conditions (film thickness of as prepared and laser sintered were 11 and 3.2 µm respectively). TG-DTA measurements showed sintering occurs at around 150-240 °C. The minimum sheet-resistivity produced was less than 1 Ω/□. Kwon et al. were able to produce a flexible and transparent conductor grid pattern on PEN film with 20 µm of line width and effectively demonstrating its functionality as a touch panel.

In 2017 Roy et al. published a paper in which computational simulation of laser sintering of Cu NP ink was compared with experimental data (Roy et al., 2017). For the experimental data they spin-coated Cu NP ink onto glass and aluminium substrates to give a layer thickness of 1.2 µm. A femtosecond laser (800 nm wavelength) and a nanosecond laser (532 nm wavelength) were used for laser sintering. The computational simulation of the laser sintering process of Cu NP ink by Roy et al. predicts the energy fluence range at which sintering should occur. The majority of the experimental laser sintering results appear to confirm this prediction, however, this does not apply to all of the laser sintering results. Roy et al. did not quantify sintered Cu by measuring conductivity or resistivity, the sole validation of successful sintering was SEM images to show particle neck growth.

2.3.3.2.2 Intense Pulsed Light (IPL) Sintering

Kim et al. used a xenon flash lamp at room temperature in ambient condition for IPL sintering (Kim et al., 2009). The xenon flash lamp causes flash lamp annealing (FLA), a millisecond sintering process using irradiation of lights over a broad spectrum in the visible range. The resistivity was measured after varying levels of light intensity, with the best result at three times as high as bulk copper. Kim et al. concluded that the short sintering time (approximately 2 ms) avoids copper oxidation. Therefore, this process does not require an inert gas or vacuum chamber as required with thermal sintering. It is worth noting, however, that IPL flash lamps are expensive (in the range of hundreds of thousands of US Dollars) and thereby add significantly to capital cost of a copper annealing process.

2.3.4 Cu-Ag synergies

The most common approach of utilising small amounts of Ag with Cu NPs for AM processes is as core-shell particles where the core is made of Cu which has a Ag shell. The Ag shell is meant to create a physical barrier between Cu and surrounding air and hence prevent Cu oxidation. There are three common synthesis routes for Cu-Ag

core-shell NPs: galvanic displacement (Zhang et al., 2008), seeded growth (Grouchko et al., 2009), and co-reduction (Kim et al., 2011). In the past few years, galvanic displacement has seen the biggest traction. It is a rather simple transmetalation reaction during which surface Cu atoms act as a reducing agent for Ag ions and which causes elemental Ag formation on the Cu particle surface (see Figure 9).

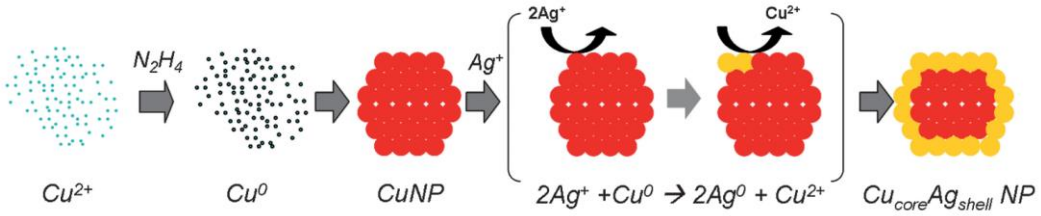


Figure 9. Schematic illustration of a single Cu NP synthesis and the formation of a Ag shell by transmetalation reaction. Thereby the surface Cu atoms serve as reducing agents for the silver ions. (Grouchko et al., 2009).

The Ag shell is able to protect the Cu core from oxidation up to a temperature depending on the publication between 100 °C (Chen et al., 2013) and 400 °C (Njagi et al., 2017; Tsai et al., 2013) with the great majority between 150 and 250 °C (Chee and Lee, 2014, 2017; Kim et al., 2014; J. Li et al., 2017; W. Li et al., 2017; Pajor-Świerzy et al., 2017a, 2017b; Park et al., 2015; Y. S. Park et al., 2016; Tian et al., 2016; Yim et al., 2016; Zhang et al., 2010). At this point the Ag shell starts to dewet the Cu core and the Ag accumulates on the surface, thereby leaving the Cu surface exposed to potential oxidation as shown in Figure 10.

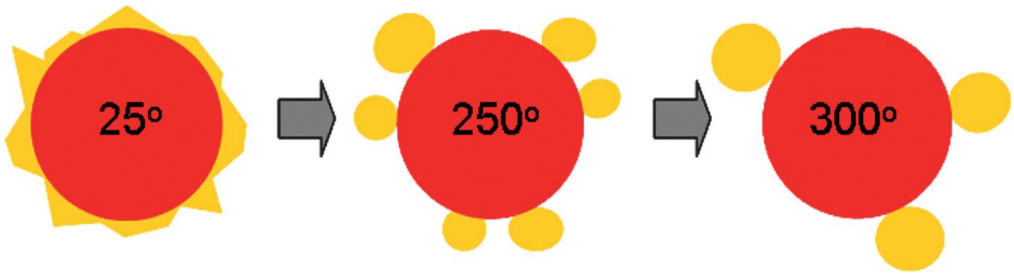


Figure 10. Dewetting and accumulation of Ag on the surface of Cu particles (Grouchko et al., 2009).

The protective Ag shell therefore only functions effectively in obstructing Cu oxidation below the temperature at which the Ag shell dewets the Cu surface. This

limits its use to applications of thermal sintering in an oxygen environment below the temperature of Ag dewetting, mostly between 150 and 250 °C.

There are differing reports in the literature on where the Ag migrates to. Some report Ag migration to the Cu particle necks (Kim et al., 2010; J. Li et al., 2017; Park et al., 2015; Tian et al., 2016; Yu et al., 2017). However, no theoretical or experimental study has been conducted on the impact of Ag accumulation in Cu neck on electric resistance. Tsai et al. on the other hand reported that Ag does not migrate to Cu necks and that Cu particles form necks independent of the Ag (Tsai et al., 2013).

Other than the Cu-Ag core-shell synergistic effects of adding Ag to Cu NPs have been reported by Morisada et al., who showed that the addition of Ag NPs to Cu NPs increases bonding strength (Morisada et al., 2010). Wang et al.'s computational simulation of Cu-Ag core-shell NPs showed that the Cu core enhances the mobility of the Ag shell atoms thus enhancing sinterability and sintering strength (Wang et al., 2016). Li et al. synthesised Cu-Ag core-shell particles with excessive amounts of Ag NPs present in the matrix (Li et al., 2016). They showed that the excessive amount of Ag NPs increases packing density and consequentially reduces electrical resistivity and improves resistance to cyclic bending. This was later confirmed by Lui et al. who also showed that increasing the concentration of small Ag particles increases packing density during sintering and reduces pores (Liu et al., 2019). However, if the addition of excessive amounts of Ag NPs is required to induce a processing benefit, at the same time the material cost increase of using Ag instead of Cu becomes significant and may outweigh processing benefit.

2.3.5 Cyclic Bending of Inkjet Printed Copper (Cu) and Silver (Ag) Tracks and its Impact on Electrical Resistance

The ability of flexible electronics (as opposed to traditional non-flexible electronics) to retain a high degree of electrical conductivity despite being temporarily physically deformed enables their application where flexible circuitry is required, such as for wearable electronics (Huang and Zhu, 2019). An understanding of the impact of cyclic

bending, simulating the use of the device over its lifetime, on the resistance of electronic tracks is crucial for the design of the circuitry. Inkjet printing has been established as a common deposition method for printing of flexible electronics (Calvert, 2001; De Gans et al., 2004; Singh et al., 2010; Yin et al., 2010). Previous studies have been conducted on inkjet printed Cu and Ag NP tracks separately to evaluate the impact of cyclic bending on resistance. For Ag NP printed tracks Lee et al. reported no significant increase in resistance (Jaehwan Lee et al., 2014) and Yang et al. reported a relative increase of $5\ \%$ (Yang et al., 2014) both over 1,000 bending cycles. For Cu NPs tracks also over 1,000 bending cycles relative increases in resistance of $< 5\ \%$ (Kwon et al., 2016) and $30\ \%$ (Min et al., 2016) have been reported. All of these studies use different inkjet printing and laser sintering methodologies. There is no study which compares Ag NP tracks and Cu NP tracks using the same methodology sample manufacturing and cyclic bending methodology.

2.4 Additively Manufacturing Electrically Conductive Multi-layered Objects: Competing Technologies

2.4.1 Metal Jetting

Metal jetting, also known as liquid metal jet printing (LMJP), is an emerging AM process which is analogue to inkjet printing. This additive method dispenses individually controlled micro-droplet of molten metals to precise locations using digitally stored computer-aided design (CAD) data in a highly reproducible manner (Priest et al., 1997). Upon contact with the substrate micro-droplets solidify and form a solid object. Continuous jetting and Drop On Demand (DOD) jetting are the two basic jetting methods (Thirumangalath et al., 2017). In the continuous jetting method, a liquid metal jet is streamed and broken up through a perturbation stimulus into a continuous stream at a measurable distance from the orifice (Priest et al., 1997; Sukhotskiy et al., 2017). In the drop-on-demand method, well-defined droplets are ejected from a nozzle in a discontinued or periodic manner, and are deposited on to a substrate in a precise location (Sukhotskiy et al., 2017; Thirumangalath et al.,

2017). The precision of the DOD jetting process enables a reduction in material waste and makes it more advantageous comparing to continuous jetting.

Metal jetting is able to produce 3D metal parts. Printable material selection has thus far been restricted to aluminium, low temperature Pb-Sn alloys, Ag and Cu (Thirumangalath et al., 2017). In a recent publication, Simonelli et al. reported successful metal jetting of tin (Sn) and Ag structures (Simonelli et al., 2019). The Sn structures had excellent macroscopic geometrical fidelity to the digital models and were printed precisely with no satellites or wrongly-positioned droplets. Moreover, the Sn structures had high densities of above 99.9 % and had electrical resistivities of one or more orders of magnitude lower than reported for inkjet printing of nanoparticle inks. The authors' metal jetted Ag structures were in comparison more fragile with an average "green" density of 92 %. Simonelli et al. publication demonstrates the ability of metal jetting to manufacture high density parts of low- and relative high-melting temperature metals.

Significantly high equipment and processing costs of metal jetting have so far prevented metal jetting from being commercialised. Whether it is possible to reduce the cost will likely be the determining factor for its success outside research institutions.

2.4.2 High Energy Manufacture of Multi-layered Copper Structures

2.4.2.1 Very High Power (VHP) Ultrasonic AM (UAM) of Multi-layered Copper (Cu) Parts

Sriraman et al. report the use of VHP ultrasonic vibrations to merge additional layers of 150 µm-thick copper sheets into previous layers (Sriraman et al., 2010). The vibrations are at amplitudes of up to 52 µm and are applied under static normal force of up to 15 kN. Sriraman et al. report that final parts reveal instabilities at the inter-sheet-areas. Hardness across the part is between 11 to 23 % of the single sheet hardness. Grain size reduces from an average single-sheet grain size of 25 µm to a final part grain size ranging from 0.3 to 10 µm.

This process can be considering to be additive in nature as multiple copper sheets are merged into each other to form one continuous part, a process also known as sheet lamination. However, the lack of subsequent publications in on this process suggests it does not seem likely that this manufacturing process will be able to produce complex multi-layered architectures as competing AM processes discussed here are capable of.

2.4.2.2 Selective Laser Melting (SLM) of Multi-layered Copper (Cu) Parts

Creating a multi-layered part by laser-induced melting and fusing of successive layers of powder material is known as SLM. It is thereby capable of producing near net-shape parts up to 99.9 % relative density (Yap et al., 2016). The most common powder materials used in SLM include steel (Tolosa et al., 2010) and iron-based alloys (Kruth et al., 2004), titanium and its alloys (Leuders et al., 2013) as well as Inconel (Amato et al., 2012) and nickel-based alloys (Clare et al., 2008).

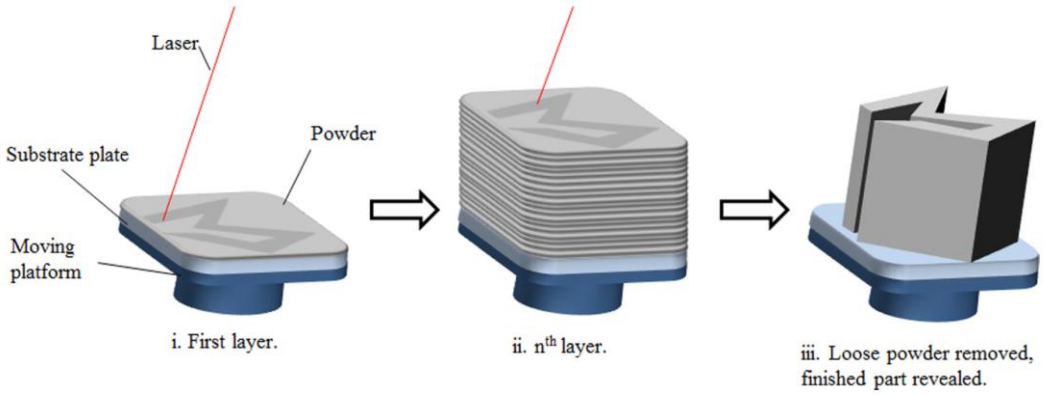


Figure 11.: Schematic of an SLM process. (i) Laser irradiance melts selective areas of the powder bed. (ii) The process is repeated for multiple layers. Interlayer melting/fusion occurs between adjacent layers. (iii) Loose powder is removed and the finished part is revealed. (Adapted from Yap et al., 2016)

The use of Cu in SLM is more challenging than the materials mentioned above. Cu has a high thermal conductivity (385 W m^{-1} K^{-1} at 20 °C). This causes heat to rapidly dissipate away from the melt area into the bulk resulting in low thermal gradients, leading to layer curling, delamination and ultimately build failure (Singer et al., 2017). Its high reflectivity prevents an effective energy coupling into the material (Kaden et al., 2017). Copper particles have the tendency to agglomerate, impeding powder

deposition and reducing overall flowability. Copper's inherent tendency to spontaneously oxidise even at ambient conditions means extra precautions are required in handling and storage before, during and after part manufacture (Singer et al., 2017).

However, literature on successful SLM of copper exists. Tang et al. used a combination of pure copper and copper(I) phosphide in an SLM process with a 200 W CO_2 laser (Tang et al., 2003). They were able to manufacture parts of up to 82 % density. Pogson et al. were the first to report on SLM processing of pure copper, using a 90 W nanosecond-pulsed laser (Pogson et al., 2003). Their part resolution and porosity were insufficient for commercial applications. In 2011 the Fraunhofer Institute for Laser Technology (ILT) reported on using a 1 kW laser with a uniform laser beam energy profile for processing of Havadur K220 (copper-nickel-silicium alloy) in SLM to manufacture parts with 99.9 % relative density (Fraunhofer Institute for Laser Technology (ILT), 2011). To date the most advanced publication in the academic literature in terms of SLM of pure copper parts is by Kaden et al. (Kaden et al., 2017). A femtosecond-pulsed laser at 1030 nm was used for SLM processing of pure (>99 %) copper parts. Thin-wall structures with thicknesses below 100 µm were produced. Even though the density of the fabricated parts was not quantified, they were found to have a highly porous morphology. However, a high density is crucial for most potential commercial applications, such as thermal management and electric applications. The authors explain the high porosity to be a result of the low laser-spot-size-to-particle-size ratio; in their case it was as low as 1 for the largest particles in their size distribution. They conclude that in order to achieve a higher density, one would require a higher laser-spot-size-to-particle-size ratio. This can be achieved by either using a larger laser spot size with at least the same energy density and/or using particle with a smaller particle size distribution. A larger energy spot size with at least the same energy density would require either a higher-powered laser or a higher pulse repetition rate; if at all possible both would significantly increase the cost of the laser equipment. Using a smaller particle size distribution in an SLM process would introduce significant challenges to the powder handling and spreading processes due to reduced pourability through enhanced agglomeration.

The company 3T RPD® claimed in 2014 to have successfully manufacturing the first pure copper part using SLM (3T RPD®, 2014). They report to have tackled the high reflectivity of copper by modifying the SLM machine and by accurately calibrating the parameter set. Moreover, they state that conventional support structures as they are used in SLM of harder metals are not feasible for relatively soft copper, so they used a different approach for their support structures. However, no academic literature or other proof was found to verify these claims.



Figure 12.: 3T RPD® claim this to be their concept heat exchanger made of pure copper through SLM (3T RPD®, 2014)

The aerospace industry has been highly interested and involved in metal AM developments. The manufacture of airplane and rocket engines for instance could benefit significantly from AM technologies, as they composed of various complex parts and materials making them particularly costly for traditional manufacturing. Preston Jones, the US National Aeronautics and Space Administration (NASA) director of the Engineering Directorate at Marshall describes metal AM as a process which “could reduce future rocket engine costs by up to a third and manufacturing time by 50 percent” (NASA, 2017).

In 2015 NASA recognised the significance of the ability to additively manufacture 3D copper parts by reporting on the “milestone” of having successfully additively

manufactured and tested the first full-scale copper alloy rocket part – a combustion chamber liner (see Figure 13). It is a part of the rocket combustion chamber in which super-cold propellants are mixed and heated to extremely high temperatures required to send rockets to space. To prevent melting of the part more than 200 cooling channels are required to circulate a cooling fluid (NASA, 2015). Hence this part must withstand extreme temperatures and pressures and it also requires intricate internal features. Manufacturing this copper lines was the first step of NASA's Low Cost Upper Stage-Class Propulsion Project. They hope these technologies will revolutionise future space endeavours, including NASA's journey to Mars.



Figure 13.: NASA's additively manufactured rocket engine combustion chamber liner made of a copper alloy (GRCo-84). Internal cooling channels are visible at the top and bottom rim (adapted from (NASA, 2015).

The Fraunhofer ILT announced in a press release in 2017 their success in SLM manufacture of pure copper parts. They report to have circumvented the issue of copper having a high reflectivity at 1,064 nm wavelength by using a green laser at 515 nm (400 W) instead (see Figure 14) and are thereby able to use laser powers of

400 W. Fraunhofer presented this technology at the formnext conference in Frankfurt am Main, Germany in November 2017.

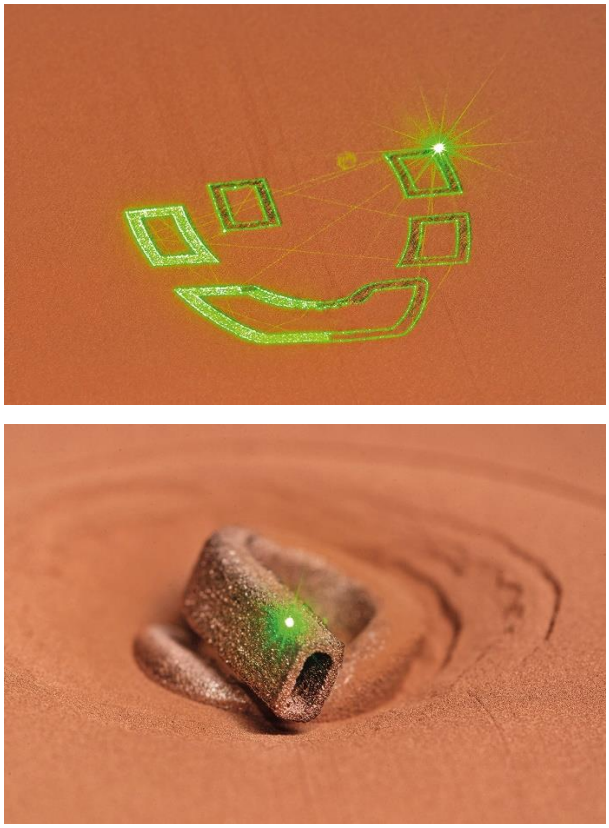


Figure 14.: Two images of SLM process using a green laser to process pure copper (Fraunhofer ILT, 2017)

2.4.2.3 Electron Beam Melting (EBM) of 3D Copper (Cu) Parts

EBM of Cu was successfully reported by Ramirez et al. who additively manufactured open-cellular structures (Ramirez et al., 2011). They used a 99.8 % pure Cu powder with an average diameter of approximately 65 µm. A focused electron beam is used to first pre-heat and eventually melt the deposited Cu powder. By varying the scale of the internal scaffolding they were able to vary the part density between 8.1 and 74.4 % of bulk Cu density. The company RadiaBeam Technologies LLC also successfully reported on the use of EBM for AM of 3D Cu parts (Frigola et al., 2014). Although not many process details are provided, they claim to have produced parts with 98.3 % bulk Cu density. Despite an applied vacuum it is stated that oxidation of

Cu was identified to be the main challenge to be overcome and a higher vacuum might be a promising approach to mitigate this.

Raab et al. used EBM to additively manufacture 99.91 % pure Cu parts with 99.95 % of bulk Cu density. Electrical conductivity of the manufactured parts is reported as up to 96.24 % of bulk Cu conductivity. However, resistivity was in fact not directly measured but rather back calculated through surface conductivity based on the assumption of isotropic properties (Dyos, 2012).

Similar to SLM of Cu, EBM of a highly thermally conductive metal such as Cu requires high energy densities to induce melting. Additionally, electron beams only travel significant distances in a vacuum, requiring the entire process to be carried out in a pressure chamber under vacuum. The equipment and operating costs of EBM are therefore significantly high.

2.4.2.4 Binder Jetting of 3D Copper (Cu) Parts

Bai & Williams have pioneered in the field of binder jetted Cu parts. In their first study publication (Bai and Williams, 2015) they employed the following process: A layer of Cu powder of 91.0 to 96.4 % purity and of median particle size of 15.3 – 75.2 µm was spreaded by a counter-rotating roller; either a polymer binder, a Cu NP binder, or a Cu Metal-Organic-Decomposition (MOD) ink was then inkjetted into the powder bed which selectively binds the powder particles. To reduce porosity and to increase density the part then undergoes heat treatment up to peak temperatures of 1,040 to 1,080 °C in a pure hydrogen atmosphere to induce Cu oxide reduction and prevent Cu oxidation. The impact of powder size, sintering profile and atmospheric control on final part density and shrinkage was investigated. The presence of hydrogen during the final heat treatment was found to increase final part purity by up to 3.9 % and density by up to 25.3 % compared to an air with vacuum environment. Final densities of between 63.2 and 85.5 % of bulk Cu density and Cu purities of 95.0 to 97.3 % were reported. Part were found to have 55.6 % of the theoretical ultimate tensile strength of bulk Cu which was hypothesised to be due to part porosity.

In a later publication (Bai and Williams, 2018) they used a high purity (> 99 %) Cu powder with a 17 µm median particle size. A polymeric and a Cu MOD binder were used. For the polymeric binder, an intermediate heat treatment to facilitate depending at 450 °C for 30 min under pure hydrogen flow was carried out. Heat treatment at between 1,025 to 1,075 °C was carried out for both binders also under pure hydrogen flow. Green part densities of between 42.3 and 50.5 % of bulk Cu density were reported as well as final part densities of between 70.3 and 80.8 % of bulk Cu density. Final part porosity was between 4.4 and 5.7 %. The sum of the final part densities and the porosities not adding up to 100 % has not been addressed by the authors and so the reason for this discrepancy is unknown.

Bai & Williams have made significant advances towards binder jetting highly dense 3D Cu parts. However, one high cost factor of the process is that due to the high temperatures required for the green part heat treatment, an inert environment is required to prevent Cu oxidation.

2.4.3 Inkjet Printing and Sintering of Multiple Electrically Conductive Layers

There are a number of reports in the literature of inkjet printing and sintering of multiple layers of Ag NP ink (Saleh et al., 2017; Vaithilingam et al., 2018, 2017). The reason for increasing the number of layers was to reduce the resistance of the electrically conductive track. These studies are aimed at 2D printed electronics applications. Increasing layers therefore is a trade-off between reducing resistance and increasing process time and material usage (Perelaer et al., 2010).

Vaithilingam et al. were the first to inkjet print multiple layers of Ag NP ink for the purpose of manufacturing 3D structures. In their first publication they reported inkjet printing and infrared (IR) sintering up to 50 layers of AP NP ink to create a conductive structure with a thickness of 37.2 ± 1.3 µm (Vaithilingam et al., 2017). The final object had a resistivity of approximately 8.6 times bulk silver and was found to have a some between 22 and 36 % void fraction. In their later publication Vaithilingam et al. upscaled the same process and reported on up to 1,000 printed and IR sintered silver NP ink layers to create 3D structures up to 3 mm tall (Vaithilingam et al., 2018);

micro-structure, surface, porosity, hardness as well as the impact of two different drop spacings during inkjet printing were investigated. Vaithilingam et al.'s publications comprise the only published and successful attempt at inkjet printing 3D objects from NP feedstock. The company XJet claims to have developed a system to produce metal parts from nanoparticles ("XJET," n.d.), however, no publications are available.

Contrary to Ag, the only evidence that exists in the literature of printing and sintering of multiple layers of Cu NP ink is by Niittyynen et al. who merely went up to 4 layers (Niittynen et al., 2015). Their reasoning for this that with more than 4 layers they were not able to successfully laser sinter a single layer Cu NP ink due to the appearance of intensive cracking during laser sintering and so they used 2 to 4 layers instead, as opposed to using multiple layers in order to build 3D structures. There is no evidence in the literature of printing and sintering of more than 4 layers of Cu NP ink.

2.5 *Summary and Gap in the Literature*

Following a thorough review of the literature it is clear that there is a gap in the literature concerning the low temperature sintering of multi-layered Cu structures beyond 4 layers using a low energy process using nanoparticulate feedstock that does not require to be carried out in an inert environment. Previous work on additively manufacturing multi-layered Cu parts has concentrated on high energy manufacturing processes such as SLM, EBM and Binder Jetting. NPs, however, generally require much lower sintering temperatures than micron-sized powder. Ample literature of NP sintering using ultra-fast photonic treatments has demonstrated that Cu NPs can be sintered in an air environment without oxidation. Inkjet printing and sintering of Ag NP ink of up to 1,000 layers to create multi-layered parts has been successfully demonstrated (Vaithilingam et al., 2018). However, Cu NP ink has to date only been printed and sintered up a maximum layer count of 4 layers (Niittynen et al., 2015).

In the field of 2D printed electronics, Cu NP inks have emerged as a significantly cheaper alternative to Ag NP inks. However, from a processing perspective Cu has two main disadvantages: its inherent tendency to oxidise which turns it into dielectric copper oxide as well as Cu requiring higher sintering temperatures than Ag. Harnessing synergistic effects of combining small amounts of Ag with Cu NPs has been explored in isolated studies on e.g. Cu-Ag core-shell particle systems or the impact of Ag addition on packing density and bonding strength. However, no study exists which comparatively investigates the impact of Ag addition to Cu NPs on laser sintering, IPL sintering, and thermal sintering in an air environment as well as in an inert environment. Moreover, conflicting literature exists on the migration of Ag during thermal sintering of Cu-Ag NP systems. Some suggest that the Ag migrates to the Cu particle contact points. The impact of this phenomenon on electrical resistance has not been investigated.

Flexible electronics have created much interest in the past few years. Crucial for flexible electronics is an understanding of the impact of bending on track resistance. A review of the literature has shown that to date there is no conclusive study which directly compares inkjet printed Ag NP tracks with Cu NP tracks using the same sample manufacturing and testing methodology.

3 ADDITIVE MANUFACTURE OF ELECTRICALLY CONDUCTIVE MULTILAYERED COPPER (Cu) MICROPARTS FROM NANOPARTICLE (NP) FEEDSTOCK

3.1 Introduction

The aim of this chapter is to additively manufacture an electrically conductive multi-layered copper (Cu) microstructure using a low-power (< 10 W) process in an air environment. The main research theory is that an electrically conductive multi-layered copper microstructure can be additively manufactured by sequentially depositing and selective laser sintering of multiple layers of copper (Cu) nanoparticle (NP) ink.

The following specific technical objectives were set:

i. Printing of liquid Cu NP ink to give dry Cu deposition
ii. Sintering of printed Cu to conduct electricity
iii. Depositing multiple Cu layers on top of one another without significant damage to previous copper layers
iv. Laser sintering of deposited copper resulting in interlayer sintering and therefore enabling vertical conductivity

Laser sintering of copper for conductive applications in two dimensions has been reported in the literature multiple times as it is outlined in the *Literature Review* section 2.3.3 "*Post-deposition Annealing of Nanoparticles*". However, additively manufacturing multi-layered electrically conductive objects necessitates novel development.

To the author's knowledge, no evidence has been found of an electrically conductive multi-layered Cu microparts which were additively manufactured in an oxygen environment using a low power (< 10 W) sintering process to date. Printing and sintering of Cu NP ink has so far only been carried out with a single deposited layer or with a very low amount of layers (≤ 4 layers) and thicknesses below 2 µm (Niittynen et al., 2015). All AM processes, which have produced 3D Cu parts are high

energy processes, which need to be carried out in an inert environment. Solely binder jetting stands out as not being a high energy process, which does not need to be carried out in an inert atmosphere, however, it does require high temperature post-printing heat treatment (Bai and Williams, 2015).

3.2 Materials and Methodology

This section lays out the equipment, materials, and methods used in this study. This involves NP ink synthesis and formulation, NP ink printing (bar coating and inkjet printing), laser sintering, as well as the characterisation of the sintered multi-layered Cu microparts, *e.g.* Diffraction Scanning Calorimetry (DSC), optical microscopy, X-Ray Diffraction (XRD), nanoindentation, White Light Interferometry (WLI), Scanning Electron Microscopy (SEM), and electrical sheet resistance measurements.

3.2.1 Copper Nanoparticle Synthesis and Formulation

The bar coating Cu ink was supplied by Promethean Particles Ltd. It was synthesised using a continuous supercritical hydrothermal synthesis (see Figure 15 for a process flow diagram). The up-flow into the reactor (FS stream in Figure 15) consisted of copper nitrate ($Cu(NO_3)_2$). The down-flow into the reactor (FW stream in Figure 15) was made up of sodium hypophosphite ($NaPO_2H_2$) at a concentration of 0.02M in water. The flowrate of the up-flow and down-flow into the reactor was 20 ml min^{-1} and both were pressurised to 172 bar. The up-flow enters the reactor at approximately 18 °C, whereas the down-flow enters the reactor at 250 °C. The up-flow and the down-flow mix in a counter-current nozzle flow-reactor (see Figure 15). During this mixing the chemical reaction listed in Equation 2 take place. By controlling process parameters such as temperature, pressure and residence time it is possible to control particle characteristics such as size, composition and shape (Lester et al., 2006). The use of surfactants (i.e. PVP) in the process can reduce the formation of aggregates (Aksomaityte et al., 2013). Once the particle dispersions were collected from the process, they were centrifuged, the supernatant was poured off and the particle dispersions were redispersed in propan-2-ol (purchased from Sigma-Aldrich).

This washing process was repeated three times in order to remove unreacted copper and hypophosphite ions particle dispersions. On the final washing cycle, the particle dispersions were redispersed to give a pigment concentrate with a metal particle content of approximately 38 wt%.

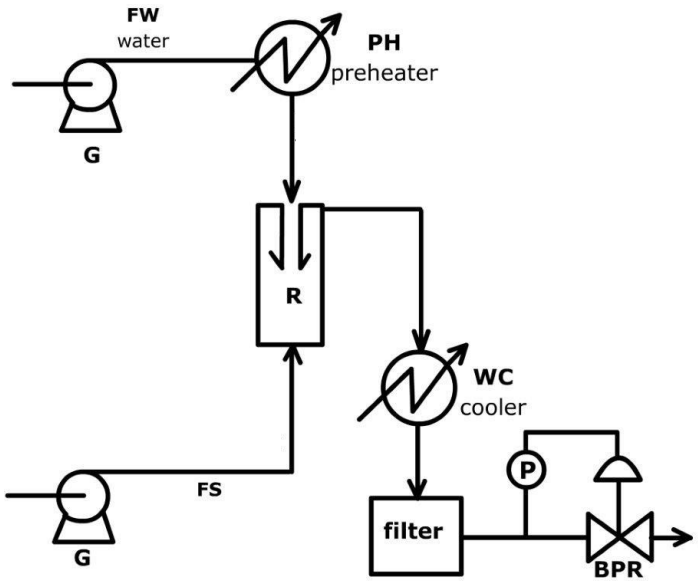


Figure 15. Process diagram of Promethean Particle's continuous hydrothermal nanoparticle manufacturing process (Lester et al., 2006). G are the pumps, FW is the supercritical water stream, FS is the cold metal salt stream, R is the reactor, WC is the cooler, and BPR is the backpressure regulator.

Equation 1. Half reactions of Cu NP synthesis.

$$\mathrm{Cu}^{2+} + 2e^- \rightarrow Cu^0$$

$$H_2PO_2^- + H_2O \rightarrow H_2PO_3^- + 2H^+ + 2e^-$$

Equation 2. Full reaction of Cu NP synthesis.

$$\mathrm{Cu}^{\mathbf{2}+} + H_2PO_2^- + H_2O \rightarrow \mathrm{Cu}^0 + H_2PO_3^- + 2H^+$$

Its metal weight loading was stated as $35 - 37\ \%$ by the manufacturer. The bar coating Cu ink's main solvent is propan-2-ol (C_3H_8O) with the addition of 5 g L^{-1} 2-Hydroxypropanoic acid (also known as lactic acid). The viscosity of the bar coating Cu was not supplied by the manufacturer, it was therefore measured as shown in Figure 16 using a Malvern Kinexus rheometer (see Figure 16). Viscosity decreases with increasing shear rate so theCu NP ink shows shear thinning characteristics which is common for particle suspensions. Shear thinning ink characteristics are desirable for

bar coating. While the ink is spread, high shear forces are applied, which lowers the viscosity of the ink, facilitating an even ink spread. Once the shear force is no longer applied, the viscosity of the ink increases, causing the ink the remain in place.

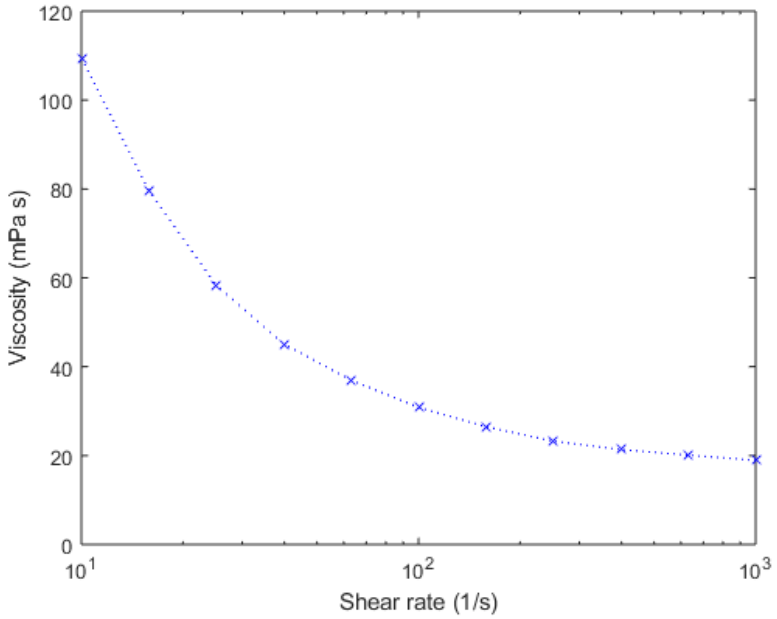


Figure 16. Viscosity against shear of the bar coating Cu ink measured at 25°C.

The inkjet printing Cu ink was supplied by Promethean Particles Ltd.. It was also synthesised using the same process of continuous supercritical hydothermal synthesis. Its metal weight loading was stated as $35 - 37\ \%$ by the manufacturer. The main solvent is 2-(2-ethoxyethoxy) ethanol ($C_6H_{14}O_3$) (also known as diethylene glycol monoethyl ether often abbreviated to DGME). Even though the presence of additional additives is acknowledged, no information on which ones and at what concentrations was provided. The ink has a viscosity of $22\ cPs\ @\ 25\ °C$ and a surface tension of $35.2\ mN\ m^{-1}$ according to its technical data sheet (which can be found in *Appendix* section 8.1).

The particle weight loading of the inks was measured by depositing using a glass pipette a drop of the ink onto a weighing boat. Its weight was measured immediately as well as after 2 hours at which point the ink looked completely dry and its weight did not significantly change anymore. In order to adjust the ink's weight loading, either its main solvent was added or it was placed in a vacuum oven at 30 °C.

Afterwards the particle weight loading was repeated until the desired particle weight loading was achieved.

3.2.2 Deposition of Copper (Cu) Nanoparticle (NP) Ink through Bar Coating

Bar coating was used as one of the two deposition methods for the NP inks in this chapter. It was chosen because it produces consistent films with relatively high layer thicknesses (approximately 1 to 9 µm) compared to other ink deposition techniques (Kwon et al., 2016). The Cu NP ink was kept in a sonication bath. The ink was only removed from the bath for the ink deposition which was carried out using a glass pipette . Bar coating was carried out using metal bars (see Figure 17) purchased from the company "RK Print". A substrate clamp is used to hold the substrate in place. Liquid ink is dispensed onto the substrate. The hand screen printer is then manually pulled across the substrate, thereby spreading the ink across the substrate as it ca been see in Figure 17. After screen printing the deposited ink was left to dry which generally took less than 30 seconds leaving behind a dry film.

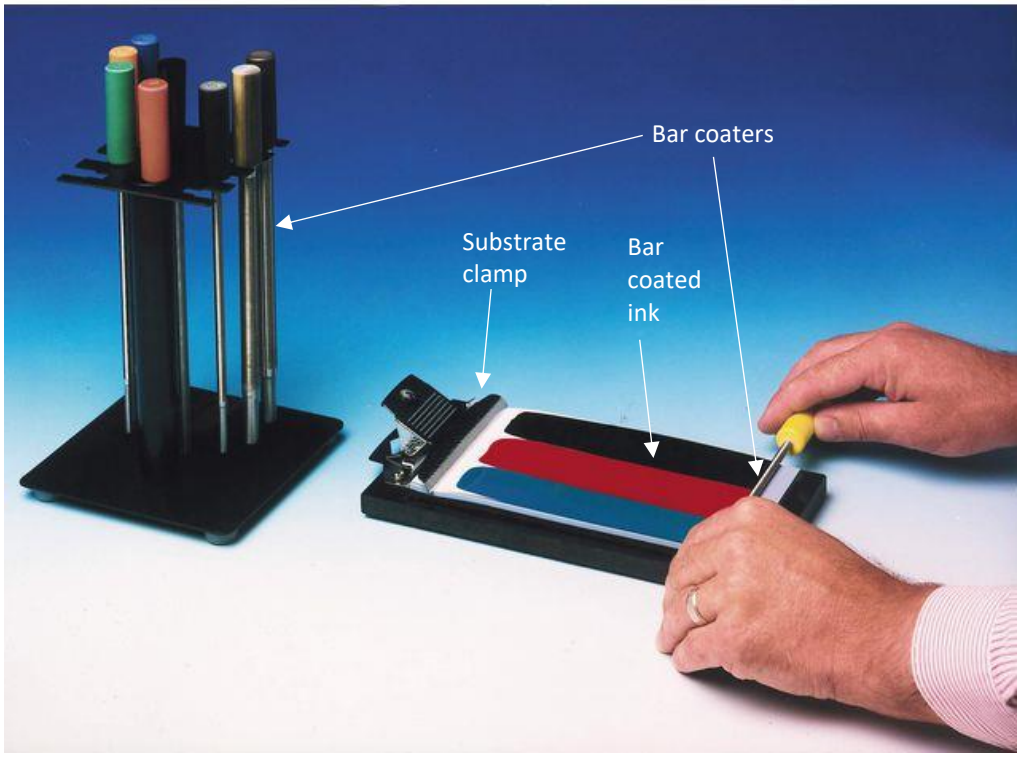


Figure 17: Bar coating of an ink onto a piece of paper (RK Print, n.d.).

3.2.3 Deposition of Copper (Cu) Nanoparticle (NP) Ink through Inkjet Printing

Inkjet printing was used as the second of the two deposition methods for the NP inks in this chapter. It was chosen due to its high degree of automation. 5x1 mm^2 rectangles were printed using an inkjet printer (Fujifilm Dimatix Materials Printer DMP-2900 Series). A standard waveform was used. The drop spacing was set to 40 µm. The substrate was heated to 60 °C throughout the printing process. After each printed layer the ink was left to dry for 90 seconds as inspection using an optical microscope showed that this duration was sufficient for the ink to dry. The printing and drying processes were repeated five times before laser processing.

For multi-layered Cu microparts using inkjet printing as a deposition method, after the inkjet printed layer had dried, the substrate with the printed layer(s) was placed into the laser enclosure and it was laser sintered. Sequential inkjet printing, drying, and laser sintering was repeated until the desired part thickness was reached.

3.2.4 Identifying the Copper (Cu) Nanoparticles (NPs) Sintering Temperature Range

DSC measurements were carried out to measure the temperature range at which the Cu NPs sinter, identifiable through an exothermic sintering peak. This was carried out on a TA Q600 unit. The sample ink was placed into an alumina pan and dried in a vacuum oven at 40 °C prior to the DSC measurement. The temperature profile during the DSC measurement was cyclic, starting at room temperature going up to 1,200 °C, down to 150 °C, and back up to 1,200 °C. This cycle was repeated three times. All heating and cooling temperature ramps were set to 10 degrees min^{-1}. The entire DSC experiment was carried out under constant 100 m l in^{-1} nitrogen flow to prevent oxidation.

3.2.5 Laser Irradiation of Copper (Cu) Nanoparticle (NP) Ink to Induce Particle Sintering

Low power laser sintering was carried out to sinter deposited NPs. The laser system used was custom built by the author with technical support and consists of a fibre

laser (BKtel) with ≤ 10 W at a wavelength of 1,064 nm, a scan head (SCANLAB hurrySCAN), a 164 mm T-theta lens and control software (laserDESK). The laser power used was 2.5 W and the laser scan rate used was 150 mm s^{-1} (unless otherwise stated). The laser was always operated in Continuous Wave (CW) mode. The hatch distance between the parallel laser scan lines was 50 µm.

Laser irradiation of the Cu NPs was always carried out in an air environment. For multiple vertical layer builds, a computer controlled adjustable z-stage was built inside a laser-enclosure, which can be seen in Figure 18.

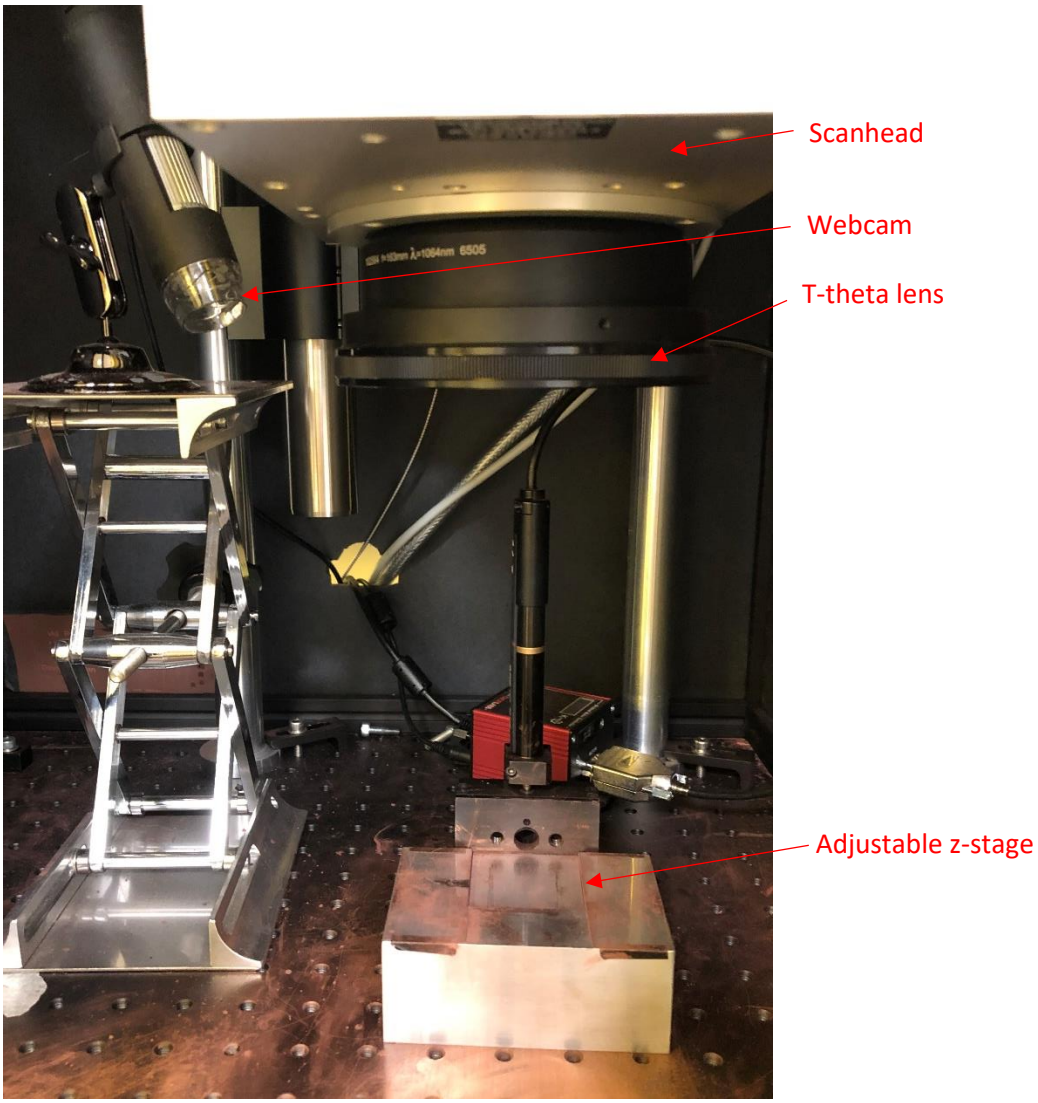


Figure 18. Adjustable z-stage setup.

The laser beam profile was measured using a laser beam profiler which comprises of a camera (SPIRICON SP62OU) with an attached beam splitter (SPIRICON LBS-300-BB).

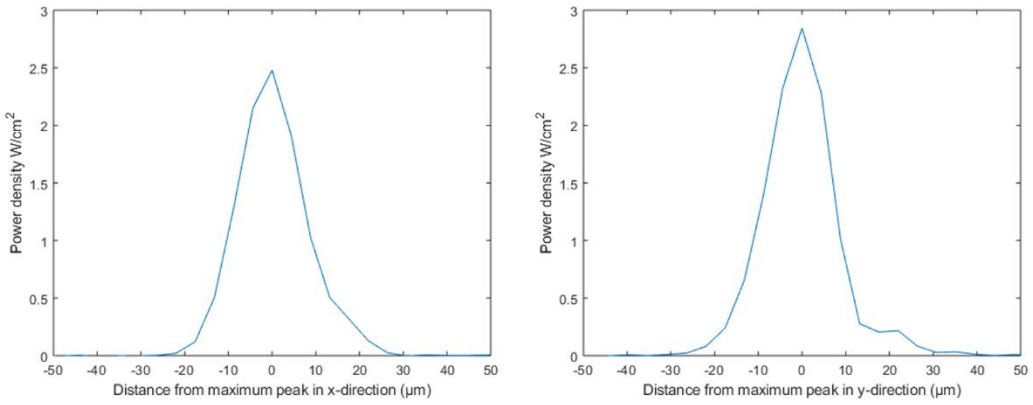


Figure 19. Laser beam power density measurement in x-direction on the left and in y-direction on the right.

The Beam profile measurements in Figure 20 showed a Gaussian laser beam profile. The 90/10 knife edge was found to be 32 µm in x and y-direction.

The laser power output against voltage input was measured using a sensor for low power lasers (LASERPOINT A-40/200-D25-USB).

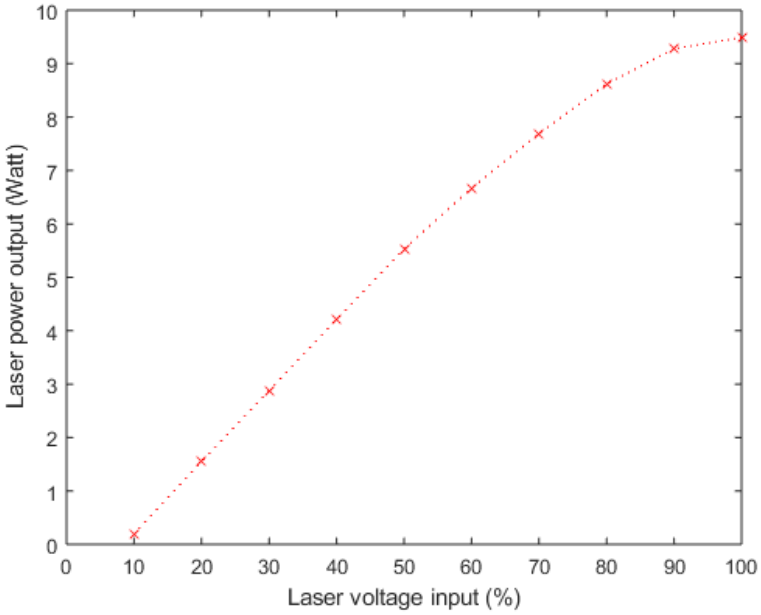


Figure 20. Laser power output against laser voltage input.

The measurements in Figure 20 were used to relate input voltage to power output for the analysis of the data.

3.2.6 Manufacturing Process to Additively Manufacture Multi-layered Cu Microparts Using Sequential Ink Deposition, Bar Coating, and Laser Sintering

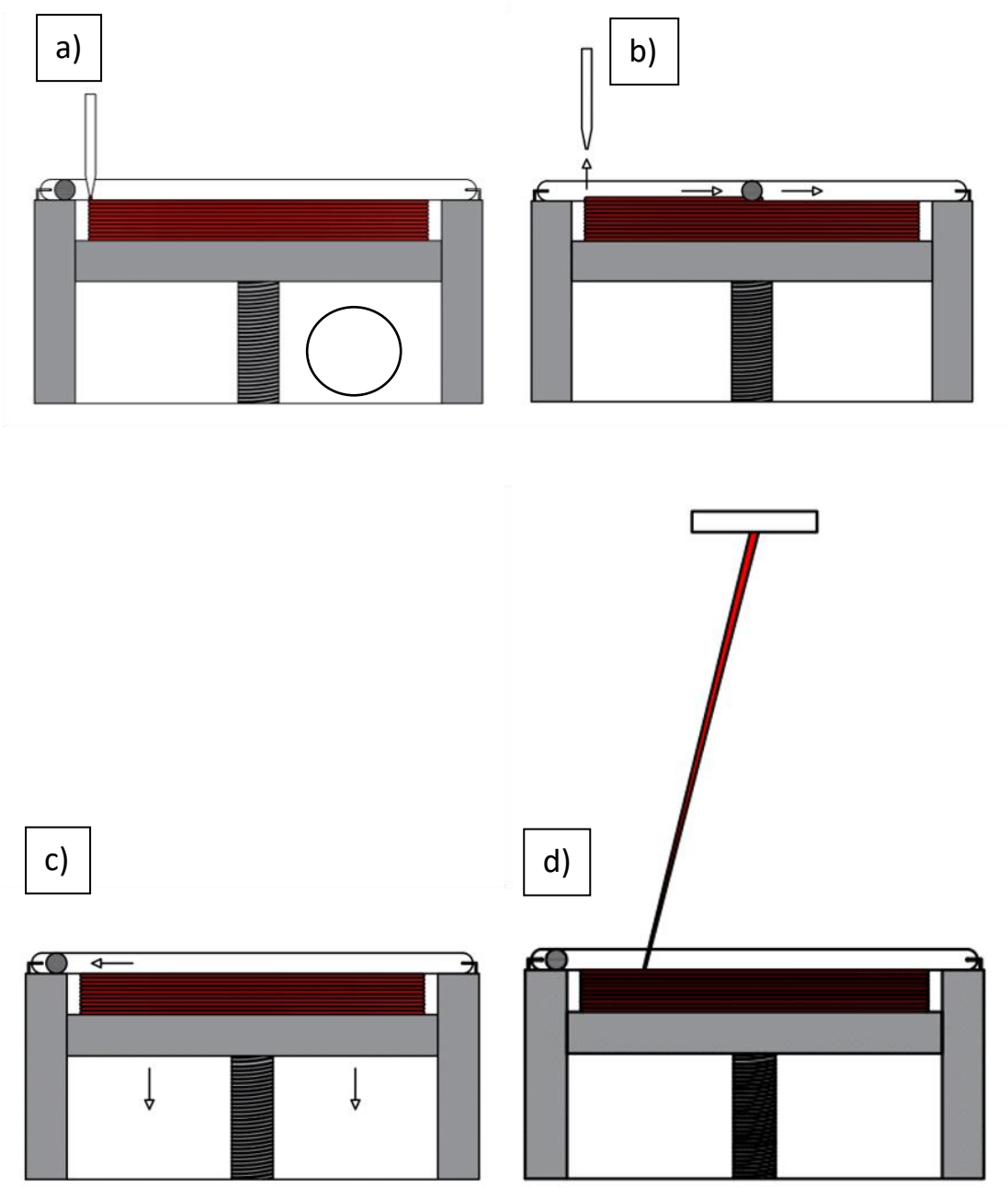


Figure 21. Diagram of the Cu NP ink deposition and laser sintering process. a): The Cu NP ink is deposited through nozzle onto the build platform in the case of the first layer, otherwise onto the previous layer. b) A metal bar with a wire wrapped around it moves across the build platform and spreads the deposited ink to create an even layer. c) the build platform moves down and the metal bar moves back to its original position. Between c) and d) there is a time interval of 30 seconds to allow the ink to dry. d) The laser beam is focussed onto the surface through an f-theta lens moves across the surface to selective sinter the Cu NP layer into the previous layer.

A diagram of the process used to manufacture multi-layered microparts can be seen in Figure 21. Cu NP layers are sequentially deposited and laser sintered up to the desired part thickness. For this work the ink was deposited manually using a glass pipette and the bar coater was moved across the build platform manually. For future work both are recommended to be automated in order to ensure reproducibility of the ink spreading.

3.2.7 Determination of the Width of the Sintered Area from a Single One-directional Laser Pass

Optical microscopy was carried out to measure the width of sintered lines from a single laser pass as well as to visually inspect the top surface of additively manufactured multi-layered Cu microparts. For optical microscopy a Nikon Eclipse LV100ND was used together with the Nikon NIS-Elements microscope imaging software.

3.2.8 Investigations into Potential Oxidation of the Copper (Cu) Nanoparticle (NP) Ink due to Laser Irradiation using X-ray Diffraction (XRD)

XRD analysis was carried out to inspect whether oxidation occurred during the various sintering techniques. It was carried out using a Bruker D8 Advance Da Vinci. The scans were carried out for 2θ values between 10° and 100°. A step size of 0.02° and a counting time of 74.5 s were used.

Mean crystallite size was quantified before and after sintering using the Scherrer Equation:

$$t = \frac{0.9\lambda}{B_{size}\cos\theta_B} \qquad \text{Equation 3}$$

where t is the mean crystallite size, 0.9 is the shape factor, λ is the wavelength, B_{size} is the crystallite size broadening, and θ_B is the Bragg angle (Schwartz and Cohen, 1987).

The peak shapes were assumed to be Gaussian. It follows

$$B_{exp}^2 = B_{size}^2 + B_{strain}^2 + B_{inst}^2 \quad \text{Equation 4}$$

where B_{exp} is the experimentally measured Full Width Half Maximum (FWHM), B_{strain} is the FWHM due to micro strain, and B_{inst} is the FWHM due to the instrument (Cullity and Stock, 2014). All examined samples were nanoparticles and their only processing history were different heat treatments (laser, intense pulsed flashlight and thermal); therefore B_{strain} was assumed to be negligible. In order to subtract the instrument broadening from the experimentally measured FWHM, the instrument broadening was measured using a bulk Cu reference sample. For the reference sample it can be assumed that no peak broadening due to crystallite size (crystallite sizes are sufficiently large) or micro-strains occurred and therefore only the instrument broadening is measured. The instrument broadening for the angles other than the angles of the Cu reference sample peaks were modelled (Caglioti et al., 1958). The $K\alpha_2$ contribution to scans was subtracted prior to all peak width measurements.

3.2.9 Nano-hardness and Creep Behaviour of Multi-layered Copper (Cu) Microparts

Nanoindentation was carried out to test and compare the local mechanical properties of the additively manufactured multi-layered Cu microparts. Due to the small size and fragile nature of the samples, the only experimental technique capable of measuring mechanical properties of the samples was nanoindentation. Nanoindentation testing was conducted on a Micro Materials NanoTest P3 (Micro Materials Limited, Willow House, Yale Business Village, Ellice Way, Wrexham, LL13 7YL, UK). To minimise the impact from environmental pertubation the machine was

located inside a polymethyl methacrylate (PMMA) enclosure. A Berkovich indenter ($\theta = 65.27°$) was used. Prior to the experiment, the sharpness/bluntness of the Berkovich indenter tip was tested using a standardised material. According to the measured sharpness/bluntness an indenter tip shape correction functions was applied. 5 indents on each of 3 barcoated and 3 inkjet printed Cu samples were performed as well as 15 indents on a piece of bulk Cu (for comparison). The load-displacement curve was recorded during loading, dwell, and unloading. The load applied was increased linearly at a rate of 2 mN s^{-1} up to a maximum load of 80 mN. At 10 mN the load was maintained for 5 s dwell time to allow the material to creep. During this dwell time, change in displacement was measured. The load was then decreased also linearly at a rate of 2 mN s^{-1}.

Indentation hardness (H_{IT}) was defined according to Meyer's Law as

$$H_{IT} = \frac{P}{A} \qquad \text{Equation 5}$$

where P is load and A is projected area of contact. With a Berkovich indenter the projected area of the contact is given by

$$A = 3\sqrt{3}\, h_c^2\, tan^2\theta \qquad \text{Equation 6}$$

where h_c is the contact depth of penetration. With $\theta = 65.27°$ this equates to

$$A = 24.494\, h_c^2$$

Substituting this projected area function (Equation 6) into Meyer's Law (Equation 5) results in

$$H_{IT} = \frac{P}{24.494\, h_c^2} \qquad \text{Equation 7}$$

It should be noted that from the unloading curve substantial elastic recovery was observed. The indentation hardness measured is not a true measure of the resistance of the material to plastic deformation but rather measures the resistance of the material to combined elastic and plastic deformations.

The creep value was obtained from a creep test. At maximum load (10 mN) the load was kept constant and displacement was measured for a time duration of 5 seconds. The creep value was calculated from:

$$C_{IT} = \frac{h_2 - h_1}{h_1}$$ Equation 8

where h_1 is the indentation depth once the maximum load was applied at the beginning of the creep test and h_2 is the indentation depth at the end of the creep test after 5 seconds had passed at the maximum load.

3.2.10 Quantifying Surface Roughness of Multi-layered Copper (Cu) Microparts

White Light Interferometry (WLI) measurements were carried out to quantify and compare surface roughness of additively manufactured multi-layered Cu microparts. Measurements were conducted using focus variation on an Alicona Infinite Focus G5 microscope with a 5x objective. Coaxial light was used and manually tuned to achieve the best possible result by visual inspection. For computing the S_a parameter, the topographies were subjected to levelling by least-squares mean plane subtraction, with no additional filtering operation. Arithmetic mean height (S_a) expresses as an absolute value the mean difference in height of each point compared to the arithmetic mean of the surface. It was obtained from an area of 2 mm × 2 mm avoiding the edges.

3.2.11 Electrical Sheet Resistance and Resistivity Measurements of Multi-layered Copper (Cu) Microparts

Sheet resistance measurements were carried out to electrically characterise and compare the multi-layered Cu samples. Sheet resistance measurements using four-point probes has been established as the most common electrical characterisation technique of thin-films in academia as well as industry, as its measurement unit ($\Omega/square$) enables straightforward comparison of thin film resistivity independent of the 2D size of the sample (assuming it is a square).

A four-point probe (NAGY Instruments: Sheet Resistivity Measuring Device Type SD-800, Measuring Probe Type: SDKR-13) was used to measure the sheet resistance of sintered copper. It consists of four probes which are lined up in a row each the same distance apart (see Figure 22). The probes are spring-loaded to ensure they are applied with a repeatable force. All four probes are simultaneously brought into contact with the specimen of interest. A current is supplied on the outer two probes while at the same time voltage is measure on the inner two probes.

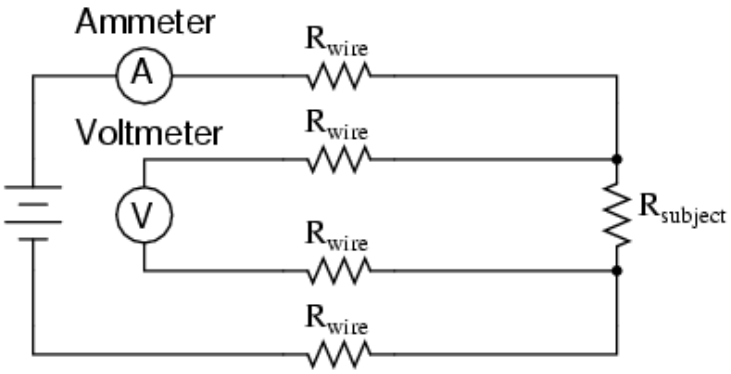


Figure 22. Basic 4-point probe circuitry and equation that is used to calculate resistance.

Sheet resistance relates to resistivity as follows

$$R_S = \frac{\rho}{t}$$

Equation 9

where R_S is sheet resistance ($\Omega/square$), ρ is resistivity (Ωm) and t is thickness (m). This correlation is valid as long as the thickness of the material remains below 40 % of the distance between each adjacent two of the four probes (Topsøe, 1968). The spacing between each of the four probes is 1.3 mm in the case of the four-point probe used for this work. Hence Equation 9 is valid for a material thickness of below 520 µm.

Due to the relationship between sheet resistance and resistivity defined in section Equation 9, in order to determine resistivity from sheet resistance measurements, the sheet resistance measurements were multiplied by the thickness (height in z-direction) of the Cu micropart.

3.2.12 Particle Size Analysis, Visual Evaluation of Internal Defects and Quantification of Internal Porosity of Multi-layered Copper (Cu) Micropart Cross-sections

SEM imaging was carried out to analyse particle size, to inspect multi-layered Cu micropart cross-sections visually as well as through image analysis to obtain part porosity. A Field Emission Gun Scanning Electron Microscopy (FEG-SEM) (JEOL 7100F FE-SEM), which uses an in-lens Schottky field emission source. It is fitted with an integrated Oxford Instruments X-Max silicon drift detector for EDX analysis. The FEG-SEM was operated at 15 keV and a working distance of between 10 and 12.5 mm.

For the imaging of Cu micropart cross-sections, the parts were mounted in cold curing epoxy resin. The epoxy containing the Cu microparts were then grinded and polished to expose the Cu micropart cross-section. A 10 nm carbon coating was applied to each sample using a Quorum Q150 R Plus S carbon coater. This was to ensure conductivity across the entire sample including across the epoxy. Aluminium tape was used to secure the samples to the mount ensuring grounding of the sample to prevent charge build up and ensuring a high-quality image.

Image analysis of SEM images was carried out to quantify the particle size distribution. For the aim of detecting particles, automated edge detection through

image analysis gave inaccurate results. The following manual particle highlighting methodology was chosen because it enabled capture of overlapping particles. SEM images were printed out on paper. An acetate was placed on top of the printout of the SEM image. A thin marker pen was used to highlight edges of particles as well as the scaling bar of the SEM image. The acetates with the highlighted particle edges were then scanned and analysed using MATLAB as follows. The scanned images were converted to a black-and-white binary image using a global threshold. Continuous objects of fewer than 100 pixels were considered image noise and were removed. Particle sizes were obtained using the MATLAB command "regionprops", which measures properties of connected objects in a binary image. The diameter is thereby calculated of a sphere with the same area of the connected objects in the image analysed. The obtained particles diameters were scaled from number of pixels to the equivalent size in nanometres according to the scale bar on the image. An example MATLAB script which was written and used can be seen in *Appendix* section 8.2.

Multi-layered Cu micropart porosity was quantified in order to compare the two different ink deposition methods (bar coating and inkjet printing) in terms of the resulting internal porosities. A quantification of internal porosity gives valuable insight into the degree of densification which impacts the mechanical micropart properties. Image analysis of SEM images of cross sections was carried out using MATLAB. Images were converted to black and white images using a global threshold. Pixel noise smaller than 50 pixels was removed. Black pixels representing pores were counted. The fraction of black pixels to overall pixels was calculated and recorded.

3.2.13 Heat Treatment of Printed and Sintered Multi-layered Copper (Cu) Microparts to Enhance Densification

In order to increase micropart density and decrease porosity, a heat treatment of the deposited multi-layered Cu microparts was attempted based on prior work by Bai and William (Bai and Williams, 2018). Post-printing heat treatments of multi-layered Cu microparts were carried out in a CARBOLITE GERO CTF 12/65/550 tube furnace with a CARBOLITE GERO 3216 controller. The temperature profile consisted of a

heating ramp of 5 °C min^{-1} up to temperatures varying between 1,025 and 1,075 °C where the temperature was held for 2 hours. Cooling through radiation was continued until 40 °C was reached. The entire heat treatment was carried out under constant argon flow.

3.3 Pre-experimental Work to Define the Process to Additively Manufacture Multi-layered Copper (Cu) Microparts from Nanoparticle (NP) Feedstock in an Air Environment

This section describes a number of experiments carried out and conclusions drawn which led to the design of the process used to additively manufacture multi-layered Cu microparts from NP feedstock in an air environment. The experimental work comprises of characterisation of the Cu NP ink used in terms of its particle size distribution through image analysis of FEG-SEM images, sintering temperature range through DSC measurements, and its elemental composition through XRD analysis.

3.3.1 The Size of the Metal Particles Used and The Sintering Process

3.3.1.1 Particle Size and Sintering Temperature

In AM processes, the building block is of a smaller size than the final object. The additively manufactured multi-layered Cu microparts reported on in this chapter were in the sub-millimetre range. Most AM processes capable of manufacturing multi-layered Cu microparts use micron-sized Cu powder as their input material (see section 2.4.2 *"High Energy Manufacture of Multi-layered Copper Structures"*). However, for the work presented here NPs were used because they require significantly lower sintering temperatures. Sintering describes densification through mass transport phenomena, such as diffusion, creep, viscous flow, plastic flow, and evaporation, all of which are dependent on temperature and time (German, 2010). The consumption of surface energy is the predominant driving force for sintering. Surface energy is a measure of the density of broken bonds per unit area (Vitos et al., 1998). The smaller the particles, the higher is the surface area per volume of the material. As increased surface area of a material means an increase in broken bonds,

consequentially the surface area per unit volume increases with decreases particle size. A graphical representation of the reduction in onset temperature of sintering due to particle size can be seen in Figure 23.

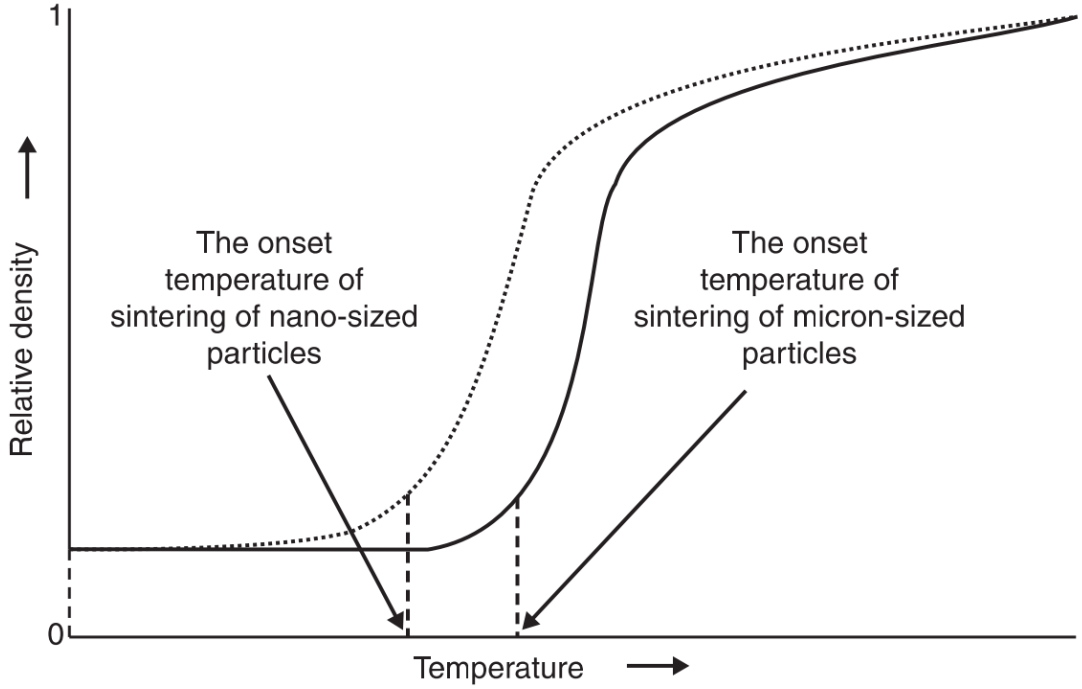


Figure 23. Schematic diagram illustrating different onset temperatures of sintering of nano- and micron-sized particles. (Fang and Wang, 2010)

The temperature required to induce sintering is therefore dependant on particle size which has been widely reported in the literature (Moon et al., 2005). The average particle size of both of the Cu NP inks was 330 nm (as shown in Figure 25) and laser power of between 1 and 5 W was sufficient to induce sintering. In contrast, selective laser melting (SLM) processes commonly use powder with particles sizes in the low micron-range (30 to 80 µm) (Yap et al., 2016) as opposed to NPs which were used in this study. This is partly because powders with a particle size any smaller than 30 µm form aggregates which causes poor powder spreading. SLM of micron-sized Cu powder generally required significantly higher laser powers; for instance, Singer et al. at reported using a laser power of 1,000 W (Singer et al., 2017). It goes without saying that the capital cost of low power fibre laser as it was used in this study is significantly lower than a laser capable of delivering powers of 1,000 W or more.

In order to determine the sintering temperature range, DSC measurements were carried out. Particle sintering is an irreversible exothermic process during which particles give up surface energy to build bonds between particles (German, 2010). Particle sintering is therefore identifiable by the exothermic (positive direction on the y-axis) peak in Figure 24 between approximately 155 and 597 °C. This peak only occurs on the first temperature ramp and does not occur during the second and third temperature ramp, as the sintering is an irreversible one-way process. The reason for the particle sintering peak being so broad is that the particle size distribution is also broad (see Figure 25), ranging from 101 to 1228 nm. Particle sintering temperature is dependant on the particle size; the smaller the particle size, the smaller the sintering temperature (German, 2010).

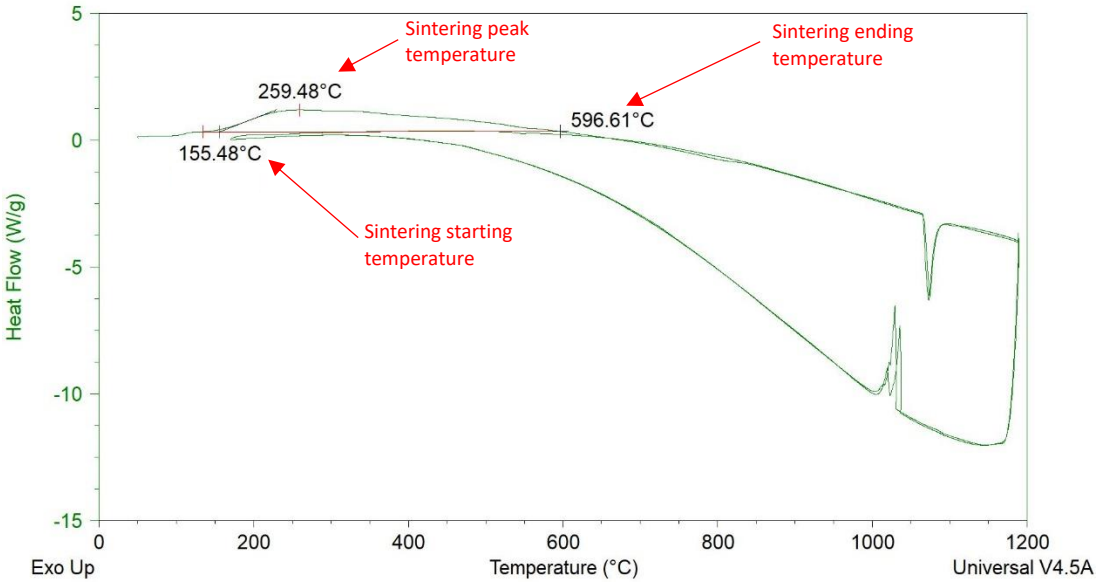


Figure 24. DSC curve of weight corrected heat flow against temperature of Cu NP ink.

3.3.1.2 Sintering Time

Even at room temperatures Cu oxidises. An everyday-life example of Cu oxidation are Cu coins or pipes which start off as shiny become increasingly dark over time. The rate of oxidation increases with increasing temperature (Li et al., 1991). Oxidation can be prevented by reducing the oxygen concentration of the environment in which the sintering takes place by a constant flow of an inert gas (i.e. argon or nitrogen) or through a vacuum. However, this significantly increases process complexity and cost.

Therefore, as Zenou et al. put it nicely, “sintering of copper NP inks in an ambient atmosphere is a race against oxidation” (Zenou et al., 2014).

The DSC measurement in Figure 24 show sintering of the Cu NP starts at 155 °C and ends at 597 °C. Consequentially, in order to induce sintering the temperature must be raised to above approximately 155 °C. Kim et al., who were the first to successfully publish on oxidation-free sintering of Cu NPs in an ambient environment estimated that a sintering time in the millisecond-range is required to “outrun” oxidation (Kim et al., 2009).

The stated aim in the in the INTRODUCTION section 1.2 *“Aim and Objectives”* of developing a system capable of building electrically conductive multi-layered copper microparts in an ambient environment therefore requires heating of the Cu NPs above 155 °C. Within a time period in the millisecond-range the material must have cooled down sufficiently to avoid oxidation. The most widely proven energy sources to be capable of inducing sufficiently high heating and cooling rates are photonic sources, in particular lasers and intense pulsed flashlights (IPL).

As previously mentioned, sintering mass transport phenomena are inherently time-dependant, hence the low sintering time requirement inherently limits the degree of densification obtainable. Sintering time can be prolonged by decreasing laser speeds, however, the sintering time must remain within a millisecond-time period to avoid oxidation. One of the advantages of using a fast sintering speed is that the heating is spatially highly confined. This enables sintering to be carried out on heat-sensitive substrates such as PET (Lopez-Espiricueta et al., 2016; Wei et al., 2015).

All other reports in the literature of additively manufactured electrically conductive multi-layered metal microparts report significantly longer sintering times. The reason for this that they either use different metals with which oxidation is not an issue or the process is carried out in a low-oxygen environment. Vaithilingam et al. for instance in arguably the most comparable study inkjet printed up to 1,000 layers of Ag NP ink and used an IR lamp for sintering (Vaithilingam et al., 2018, 2017).

Vaithilingam et al.'s IR source is non-selective and even though it is not explicitly stated the exposure time can be assumed to be in excess of 1 s. In the case of this study, the photonic sintering source is a laser which has an in-focus spot size of 32 x 32 µm. At a scan rate of 250 mm s^{-1} the average exposure time is therefore approximately 4 orders of magnitude lower. Vaithilingam et al. are able to use significantly longer sintering times, because rather than Cu NP ink they used Ag for which oxidation is not an issue.

3.3.2 Quantification of the Particle Size Distribution

The manufacturer did not supply information on the particle size distribution apart from the claim that the particle size distribution for the two inks was identical as they stem from the same synthesis batch. They were washed into their respective formulations after the synthesis process and the manufacturer does not expect there to be changes of the particle distribution as a consequence of the post-synthesis formulation. The particle size distribution at room temperature was quantified as explained in *Materials and Methodology* section 3.2.12 (see Figure 25). An example of an analysed SEM image can be seen in Figure 27 on the left).

The result was an average particle size of 330 nm with a standard deviation of $\pm$ 186 nm. The difference in the particle size distributions of the two inks were indeed insignificant, as claimed by the manufacturer.

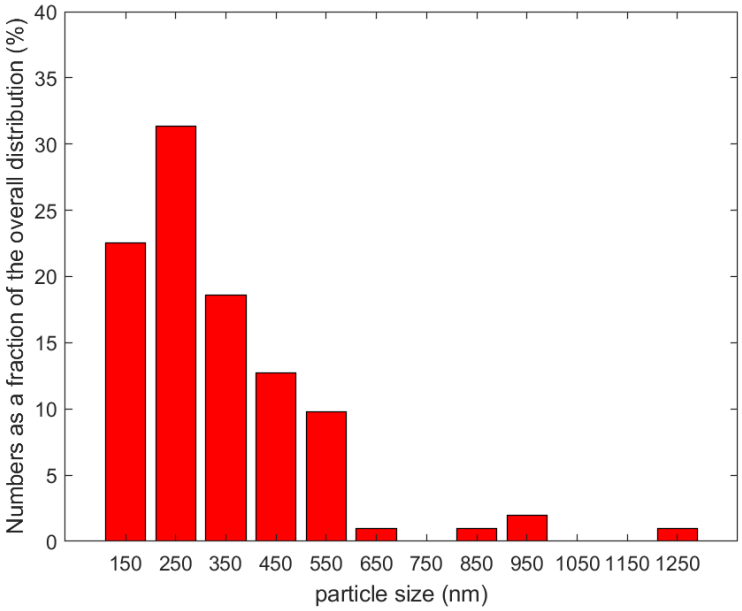


Figure 25. Number of particles as a fraction of the overall particle distribution against particle size to show the Cu particle size distribution.

3.3.3 Deposition of the Nanoparticle (NP) Ink

Literature has shown that NPs are more toxic to humans than microparticles (Chen et al., 2006). Inhaled airborne nanoparticles are significantly more hazardous to humans than NPs in a liquid suspension (Quadros and Marr, 2010). In order to minimise the potential health risk of working with NPs, the experimental strategy was designed to accommodate for all NPs being always handled in a liquid suspension until they were deposited. Spreading NPs in a liquid suspension has the additional advantage over spreading dry NPs in that dry NPs easily agglomerate and negatively affect spreadibility.

In literature the most common ink deposition methods of Cu NP ink are spin coating (Jeonghyeon Lee et al., 2014; J. H. Park et al., 2016), inkjet printing (Soltani et al., 2015; Wang et al., 2017), and bar coating (Kwon et al., 2016). Using spin coating as a deposition method as part of an additive manufacturing process would require sequentially spin coating layers onto previous layers with a selective sintering step in between. This would require a complex stage design. The stage would have to be able to spin at sufficient rounds per minute (rpm) with the ability to abort its spinning

motion always in the same orientation. Additionally, it would have to have the capability to be adjustable in z-direction in order to maintain a constant distance of the top layer to the sintering source (in the case of a laser sintering system the distance of the top layer to the scan head lens would have to be kept at approximately the focal distance of the laser optics). Moreover, an ink deposition system which deposits ink in a very central spot of the stage would have to be retractable to not block sintering photonics during sintering. Due to these highly complex design requirement it does not come as a surprise, that no literature was found which uses spin coating for more than one layer of ink – not even for Ag NP ink for which literature exists on printing multi-layered objects using a nanoparticle ink (Saleh et al., 2017; Vaithilingam et al., 2017).

Inkjet printing is the most common ink deposition method for 2D printed electronics. Up to 4 consecutive layers of Cu NP ink have been successfully inkjet printed and laser sintered by Niittynen et al. (Niittynen et al., 2015). The only examples that exist in the literature of additively manufactured metal parts using a NP feedstock are of Ag and solely use inkjet printing (Vaithilingam et al., 2018, 2017). Therefore, inkjet printing was generally deemed to be a promising ink deposition method.

Even though there is no literature on bar coating of multiple layers of any metal NP ink, it is often used for single layer deposition of metal NP ink. A single layer of bar coated ink tends to be between 1 and 10 µm thick (Kwon et al., 2016) whereas a single inkjet printed layer usually significantly less than 1 µm. For the purpose of building up an additively manufactured object of a significant z-dimension, a thicker layer thickness is of an obvious advantage as to reach a set height less layers are required. Therefore, bar coating was also chosen as a deposition method to additively manufacture multi-layered Cu microparts from NP feedstock.

3.3.4 The Drying Process of the Deposited Copper (Cu) Nanoparticle (NP) Film

Early experiments of laser exposure to varyingly dry Cu NP films showed that laser exposure of a wet film causes an emergence of flashes and smoke, resulting in a

highly inhomogeneous sintering result. It is believed that the high heating rates and thermal gradients cause instantaneous violent solvent evaporation. It was concluded that in order to obtain a homogeneous and repeatable sintering result, the deposited Cu NP film would need to be dried prior to laser exposure.

A more volatile solvent reduces the time a deposited ink layer takes to dry and is therefore from a time-efficiency point-of-view favourable. Bar coated layers generally dried within 15 seconds and the drying process was clearly visible by eye as a distinctive separation between the wet and the dry part of the Cu film emerged. The difference can be described as a darker and more reflective (wet) surface and a lighter and more matt (dry) surface. The line separating the two would usually migrate from one side of the film across to the other side at the expense of the wet surface. The moment at which the Cu film was considered dry was thereby easily identified by eye. In contrast, the drying of inkjet printed layers was not easily identifiable by eye. No distinct differentiating line between wet and dry film emerged. Over a longer period of time, compared to the drying of the bar coated Cu film, a much subtler gradual change in reflectivity was noticeable.

In order to accelerate the drying of the inkjet printed Cu film, the ability of the inkjet printer to heat its printing platform was utilised. It was set to 60 °C which accelerated the described change in reflectivity, however, it still took approximately 90 seconds, significantly longer than the drying process of the bar coated layer which took less than 15 seconds.

In order to accelerate the drying times of the inkjet printed layers, experiments were conducted to evaluate whether it is possible to use the laser scan at a low energy density (low laser power and/or high scanning speed) laser scan to induce and accelerate drying prior to another higher energy density laser scan to induce NP sintering. In practice it was found that the laser exposure of wet ink either caused no drying at all or the previously described violent solvent evaporation and it was impossible to obtain an in-between result where the Cu film dries in a non-

destructive way. Using a UV and IR lamp for drying of the inkjet printed film was also trialled, however, as expected, the Cu NPs oxidised rapidly upon heating.

The layer thickness of the inkjet printed layers was approximately 0.1 to 0.5 µm and hence much lower than the layer thickness which varied between 1 to 10 µm. The inkjet printer and the laser scanning system were not integrated into one system, they were two separate systems. It was found that the vertical spatial extent of the particle sintering went beyond the vertical depth of a single inkjet printed layer. It was therefore concluded that it would be more time-efficient to inkjet print multiple layers prior to each laser sintering scan. As previously discussed the drying of the inkjet printed layers took a significant amount of time. In order to accelerate the entire process, it was attempted to print up to 30 layers at once without intermediate delays to dry the previous layer before applying the following one. Then the entire stack of 30 still wet layers was dried in a vacuum oven at the same temperature as the heated platform of the inkjet printer (60 °C). As expected, the additional vacuum accelerated the drying process. However, a macroscopic deformation of the entire micropart was observed in SEM cross sections (see Figure 36). The deformations were concluded to be caused by the coffee-ring effect (Deegan et al., 1997), whereby particles migrate outwards and accumulate towards the edges of wet areas as a consequence of capillary pressure. Vaithilingam et al. reported a similar macroscopic deformation due to the coffee-ring effect of multiple layers of inkjetted Ag (Vaithilingam et al., 2018). This deformation was considered undesirable for manufacturing consistent multi-layered structures. Therefore, it was concluded that each layer must be dried prior to the addition of the following layer to prevent macroscopic deformation.

3.3.5 The Impact of the Deposited Layer Thickness on the Additive Manufacturing (AM) Process of Multi-layered Copper (Cu) Microparts from Nanoparticle (NP) Feedstock

With inkjet printing, dried layer thickness depends on the metal weight loading of the ink as well as the drop spacing. The weight loading of the ink is not something

that can be freely adjusted as it impacts other ink parameters such as viscosity and surface tension which are required to be within certain previously mentioned narrow ranges.

With bar coating the layer thickness is primarily dependent on the height difference between the vertical plane where the bar coater is dragged across and the top surface of the sample and the metal weight loading of the ink. This height difference is set by a computer-controlled z-stage which according to its manufacturer claims to have a stop size of 20 nm with no mention of accuracy or precision (THOR LABS, 1999). It was found that the lower limit of the metal weight loading of the ink was approximately 5 weight %; any lower resulted in an inconsistent film characterised by patches of no visible Cu film at all. The upper limit was found to be at around 50 weight % metal loading; any higher resulted in the ink not spreading evenly anymore and consequentially the resulting film was found to be inconsistent with patches where there is no Cu.

In terms of build-time minimisation a higher layer thickness is favourable as it reduces the number of layers required in order to reach a certain vertical micropart height. However, for any given particle suspension a critical cracking thickness exists above which cracks form during drying. A Cu layer which contains cracks is catastrophic for multi-layer builds because following layers will be highly uneven due to the cracks. An optical microscope image of an example of a cracked bar coated film can be seen in the *Appendix* in Figure 98.

Cracking in drying colloidal films is a consequence of the balance between capillary pressure and particle network strength. Based on the Griffith's criterion (Griffith, 1921) for crack propagation Singh et al. have derived a relationship to describe the critical film thickness h_{max} as

$$h_{max} = 0.64 \left[\frac{GM\phi_{rep}R^3}{2\gamma}\right]^{\frac{1}{2}} \left[\frac{2\gamma}{(-P_{max})R}\right]^{\frac{3}{2}} \quad \text{Equation 10}$$

where G is the shear modulus of the particles, M is the coordination number, ϕ_{rep} is the particle volume fraction at random close packing, R is the particle radius, γ is the solvent-air interfacial tension, P_{max} is the maximum capillary pressure (Singh and Tirumkudulu, 2007). The maximum capillary pressure was described by White as

$$P_{cap} = \frac{A_{sp}\gamma\phi\cos\theta}{1-\phi} \qquad \text{Equation 11}$$

where A_{sp} is the specific surface area per unit volume of solid, and ϕ is the particle volume fraction (White, 1982). Considering the bar coating ink printing in this study, the particle size distribution was given, however, variables which were adjustable and which impact the critical film thickness are the choice of the ink solvent as well as the ink metal weight loading. The choice of the ink solvent is a balance; increased volatility results in faster drying times but at the same time according to Equation 10 increased evaporation rate increases drying stress and hence in turns reduces the critical film thickness.

In the case of the solvent of choice for the bar coating ink, propan-2-ol, experiments of increasing film thickness until cracks appear during drying showed that the critical cracking height was at approximately 9 µm. Propan-2-ol is a relatively volatile solvent (boiling point of 82.5 °C) and so it has the advantage of speeding up the drying process of the wet Cu film – the drying of the bar coated layers only took less than 15 seconds. A maximum layer thickness of up to the critical cracking height of 9 µm was deemed sufficient as it is already significantly greater than the layer thickness of inkjet printed layers (0.1 to 0.5 µm).

Consistently homogeneous ink spreading was identified as the main challenge for bar coating of multiple layers of Cu NP ink. Uneven layers were characterised by either millimetre-scale holes within the layer or by chunky grains rising well beyond the average height of the layer (an example can be seen in the *Appendix*, Figure 99). It was impossible to remove inconsistent layers once deposited without significant damage to previous layers. If the deposited layer had holes it was also impossible to

fill the holes with a new additional applied layer on top. Therefore, once one bar coated layer turned out significantly inconsistent it practically meant the individual build could not be continued. In order to minimise the chances of poor ink spreading, several factors were identified which impact the homogeneity of the ink spreading. Firstly, it was found that the ink spreading was most consistent at an ink metal weight loading of approximately 45 %. Any higher metal weight loading increased the appearance of chunky grains. Secondly, ultra-sonication of the ink right until the moment it was applied was found to improve homogeneity of the ink. Literature shows that ultra-sonication of colloidal solutions breaks up aggregates (Higashitani et al., 1993) so one can conclude that in this case the ultra-sonication improved spreading of the ink by breaking up Cu aggregates. Thirdly, it was found the ink spreading with a bar coater (made by RK Print) with a wire wrapped around the bar gave a more consistently even result as opposed to ink spreading using a doctor blade. The wire wrapped about the bar coater effectively creates small volumes of gaps along the bar in between consecutive wire wrappings which can be seen in Figure 26. It is believed these volumes act as effective ink reservoirs which by emptying provide ink throughout the bar coating spread. In contrast, a doctor blade is just a straight blade without any volumes which can act as ink reservoirs.

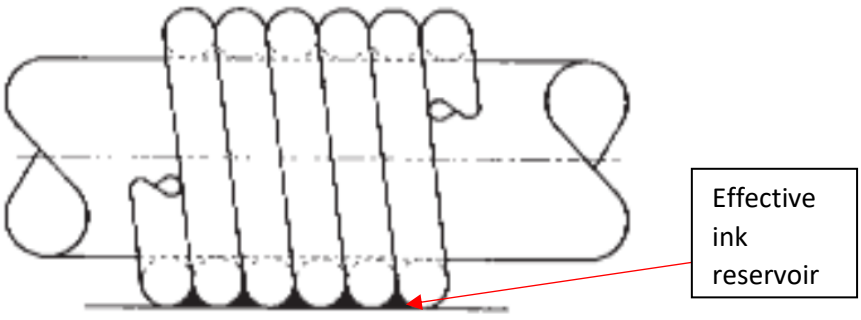


Figure 26. Illustration of wire wrapping around the bar coater used for ink spreading with an indication of the location of an effective ink reservoir. (adapted from RK Print website (RK Print, n.d.)).

Fourthly, it was found that the speed of the bar coated moving across the substrate and spreading the ink impacted the homogeneity of the surface coating; the faster the bar coater moved across the substrate the more even the ink spreading turned out. It was shown in Figure 16 that the Cu NP ink showed shear-thinning

characteristics. It is believed that the increased speed of the bar coater increases the shear forces acting on the ink which in turn reduces its viscosity and causes the ink's spreadability to be enhanced. For the experiments conducted for this study the bar coater was moved across the substrate manually. Despite efforts of maintaining high repeatability in terms of speed and pressure applied, the repeatability of the ink spreading could be improved by integrating a motorised and automated bar coater movement into the experimental setup.

3.3.6 Image Analysis of the Impact of Laser Sintering of Copper (Cu) Nanoparticles (NPs) through Field-emission Gun (FEG) Scanning Electron Microscopy (SEM) Imaging

FEG-SEM images were taken of unsintered and laser sintering Cu NPs and visually inspected to qualitatively assess the impact of laser sintering on particle morphology and size distribution. Figure 27 shows FEG-SEM secondary images of unsintered (left) and laser sintered (right) NPs. Both images were taken at the same magnification of 7,000x. The laser sintering increases particle size and decreases spatial homogeneity.

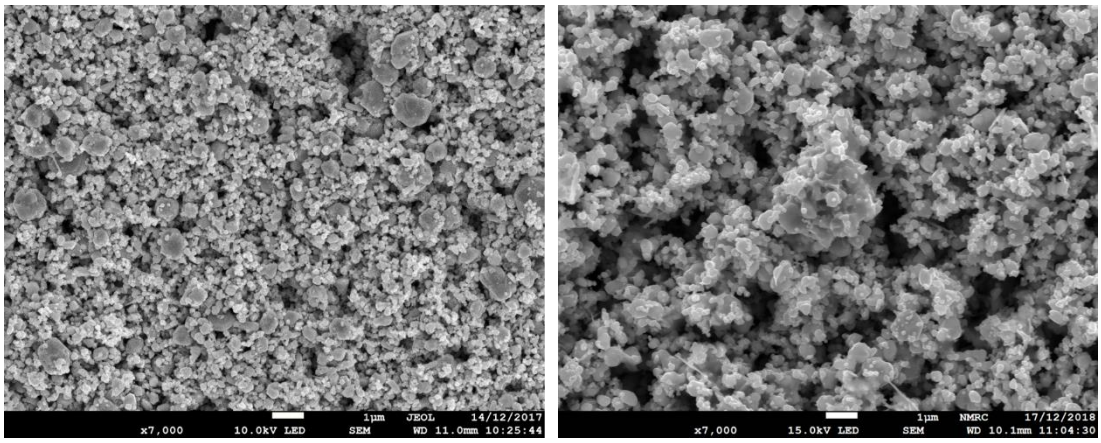


Figure 27. FEG-SEM secondary electron image of **unsintered** Cu particles on the left and **sintered** Cu particles on the right. Note, both images were acquired at the same magnification of 7,000x.

3.3.7 *Elemental Analysis of Laser Sintering of Copper (Cu) Nanoparticles (NPs) through XRD*

No copper oxide peak is evident in the laser sintered XRD spectrum in Figure 28. It was therefore concluded that no copper oxidation occurred during laser sintering.

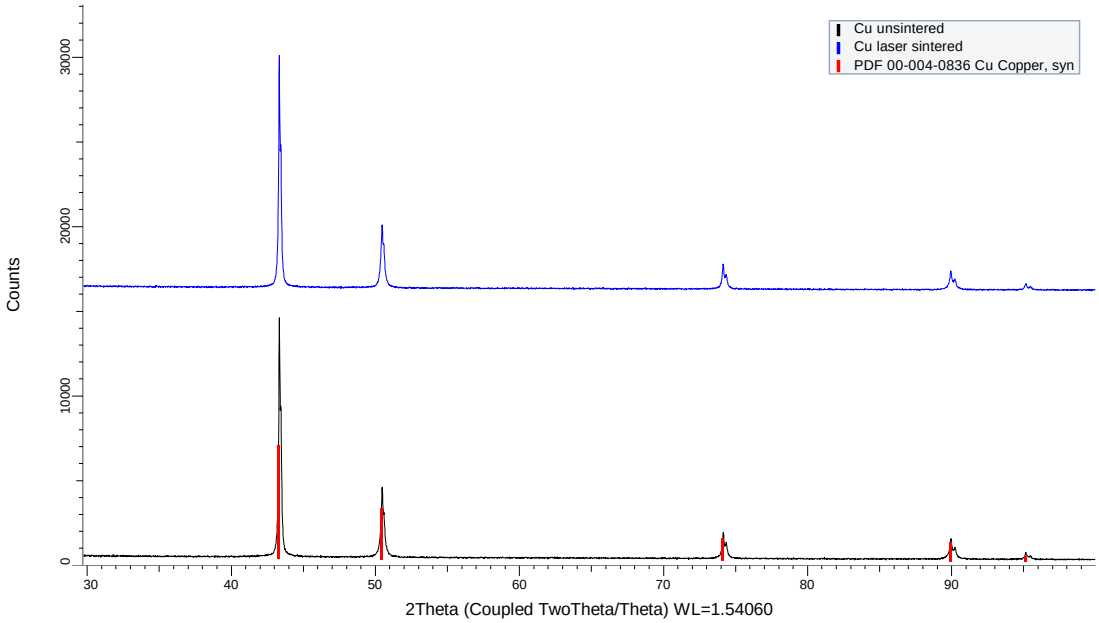


Figure 28. XRD spectrum of Cu NPs before (bottom graph) and after (top graph) laser sintering.

3.4 Sintering induced by Laser Irradiation of a Single Layer of Copper (Cu) Nanoparticle (NP) Ink

A study was conducted to investigate what kind of substrates would be most suited for multi-layered laser sintering of dry copper ink. The material heating induced by the laser is highly specially localised. So much so that laser sintering of the Cu NPs on heat sensitive substrates, *i.e.* poly(ethylene terephthalate) (PET), acrylonitrile butadiene styrene (ABS), cardboard and paper. PET and glass are most common substrate materials used in literature for single-layer metal NP deposition and sintering. They were therefore chosen as the two substrate materials to be investigated under single-layer Cu NP deposition and laser sintering to make an informed decision on which one of the two materials will be used for multi-layer builds. An example of sintering Cu NPs on PET and glass can be see in Figure 29 in a) and b), respectively.

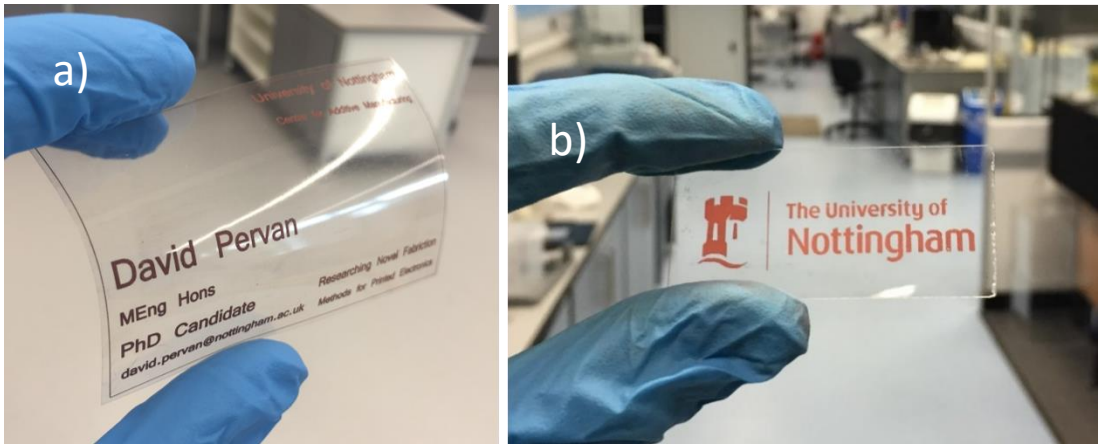


Figure 29. Example images of laser sintered Cu NP ink in **a) on PET** and in **b) on glass**.

Single laser line scans were carried out. The two independent variables investigated were laser power and laser speed. Both were incrementally varied within their operating range from minimum to maximum. The optical microscopy images in Figure 30 are exemplary optical microscope images of each of the four identified outcomes which were clearly differentiable by eye. In each case the laser was scanned vertically across the area captured in the image.

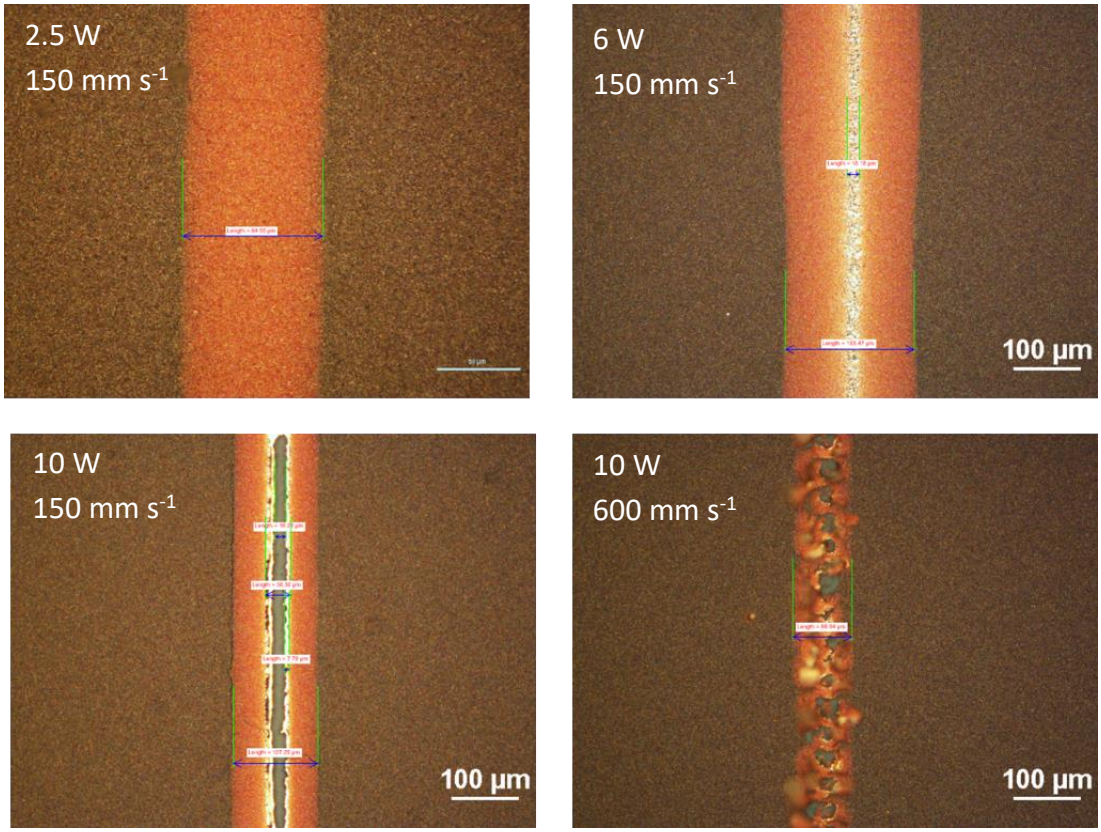


Figure 30. Optical microscope image of the result of a single vertical laser line pass. Cu which was not exposed to laser irradiation is unsintered and appears brown. The laser speed and power is indicted. **Top left:** The vertical line affected by the laser exposure in the centre of the image (orange coloured) appears to be evenly sintered. **Top right:** Most of the vertical line affected by the laser exposure in the centre of the image (orange and yellow coloured) appears to be evenly sintered (orange coloured). The very central line (bright-yellow coloured) appears to be strongly sintered or melted. Among this area small holes (dark dots) are present which likely indicate the absence of copper in these areas. **Bottom left:** The very centre of the line (appears dark) has been entirely ablated due to the laser exposure. Next to the ablated area is an accumulation of copper which appears to be melted (bright yellow coloured). Beyond the melted copper there is sintered copper (orange coloured) which is surrounded by unsintered copper (brown coloured). **Bottom right:** The vertical line affected by the laser exposure in the centre of the image (lighter in colour than the surrounded brown coloured copper) is partially ablated.

Process window mapping of those four laser processing outcomes was carried out on two different substrates, PET (polyethylene terephthalate) and glass. The film thickness of the bar coated copper ink was varied by using different bar coaters. It was measured through WLI.

With increasing laser irradiance and decreasing laser speed, energy exposure increases. Therefore, the energy exposure is the highest in the bottom right corner and lowest in the top left corner of all the contour maps (Figure 31 and Figure 32). With increasing film thickness the energy delivered by the laser affects a greater volume of copper. So at constant energy delivered from the laser and increasing film thickness a greater volume of copper particles is exposed to the same amount of energy – or in other words the energy per volume of copper ratio decreases. This explains why with increasing film thickness the process window of an evenly sintered result becomes larger towards the bottom right corner of the process window map.

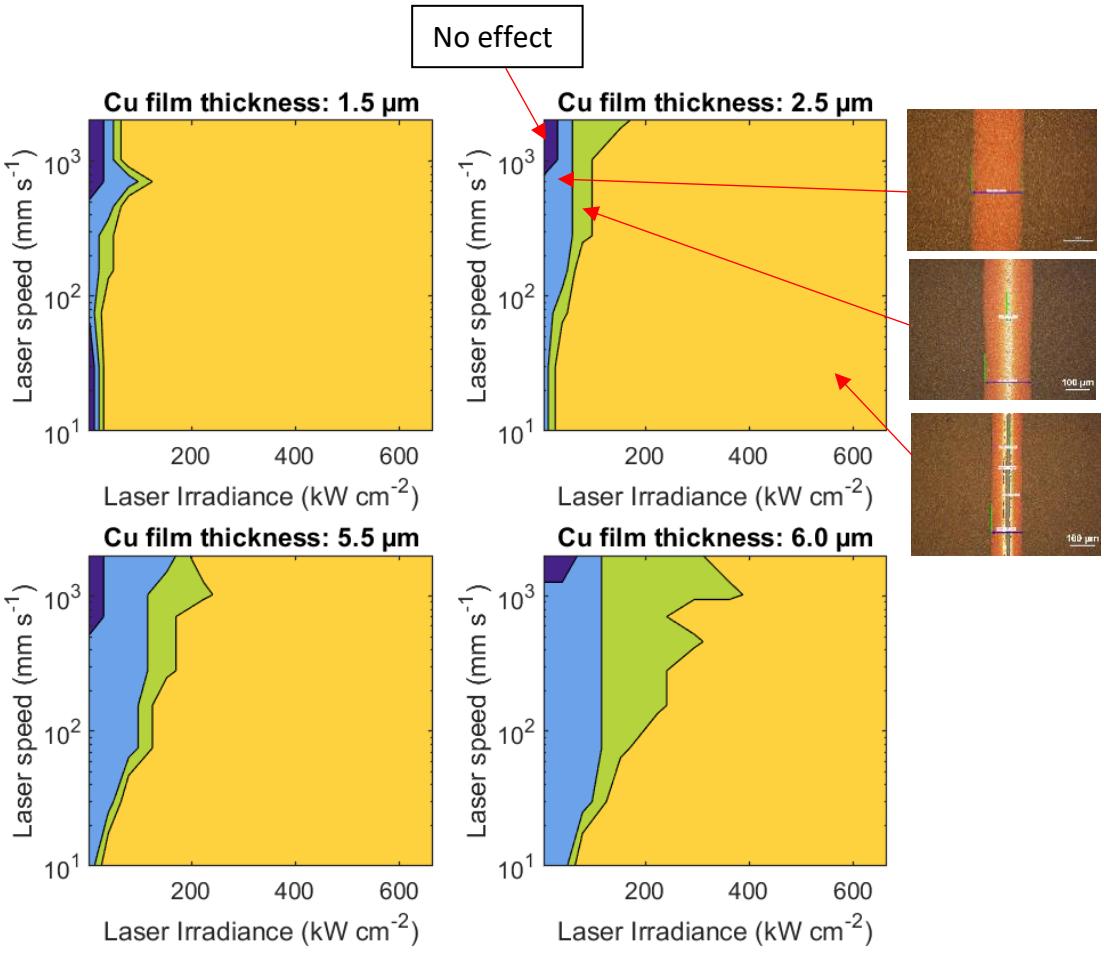


Figure 31. Process window contour maps of different identified sintering phenomena at varying laser irradiance and laser speed on four different Cu film thicknesses on a **PET substrate**. The images (see Figure 30) and labels indicate dark blue: no effect, light blue: evenly sintered, green: strongly sintered, yellow: continuously ablated and melted.

On glass substrates (Figure 32) the same effect as on PET can be seen; with increasing film thickness the process window of an evenly sintered result increases. For all of the four different film thicknesses, the process window for an evenly sintered result is larger on glass than the equivalent process window on PET. Contrary to PET substrates, however, on glass substrates ablation occurred at all film thicknesses at high laser irradiance and speed (top right corners of process window maps).

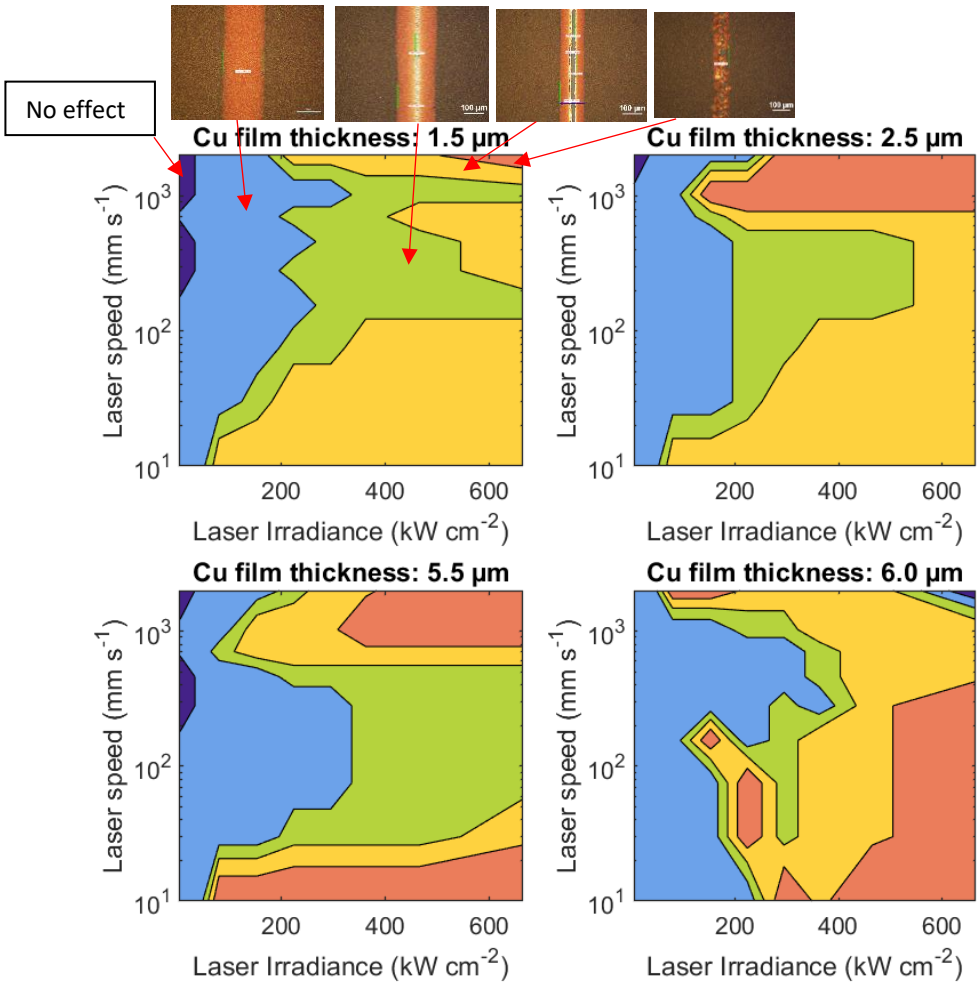


Figure 32. Process window contour maps of different identified sintering phenomena at varying laser irradiance and laser speed on four different Cu film thicknesses on a **glass substrate.** The images (see Figure 30) and labels indicate dark blue: no effect, light blue: evenly sintered, green: strongly sintered, yellow: continuously ablated and melted, red: ablated.

The relationship between the laser energy input and the width of the area sintered as a consequence of a single line laser was investigated. For all the laser sintering

carried out for the process window maps in Figure 31 and Figure 32, the energy input was plotted against the sintered line width. The laser fluence was calculated by

$$F = \frac{\mathrm{P}}{\mathrm{U}\,\mathrm{D}} \qquad \text{Equation 12}$$

where F is the laser fluence (J cm^{-2}), P is the laser power (W), U is the laser velocity (mm s^{-1}), and D is the laser spot diameter (on average 32 µm as measured in Figure 19). To measure the sintered line width, an optical microscope (Nikon Eclipse LV100ND) was used to take images of each sintered line. The width of the sintered lines was then averaged on a pixel basis using image analysis using MATLAB. The thinnest sintered (and conductive) line measured was approximately 15 µm wide; an optical microscope image of it can be seen in the *Appendix* (Figure 97).

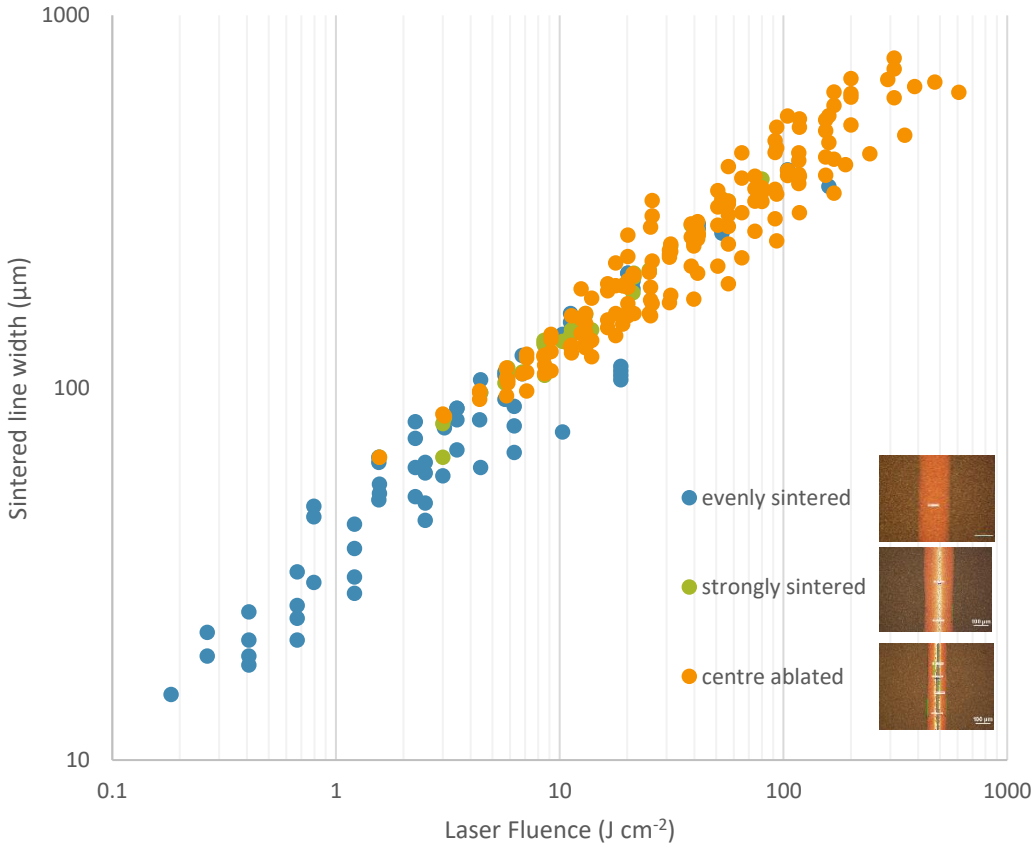


Figure 33. Sintered line width against laser fluence on a single layer of Cu NPs on **PET substrates**. The descriptions of the sintering state relate to Figure 31 as indicated.

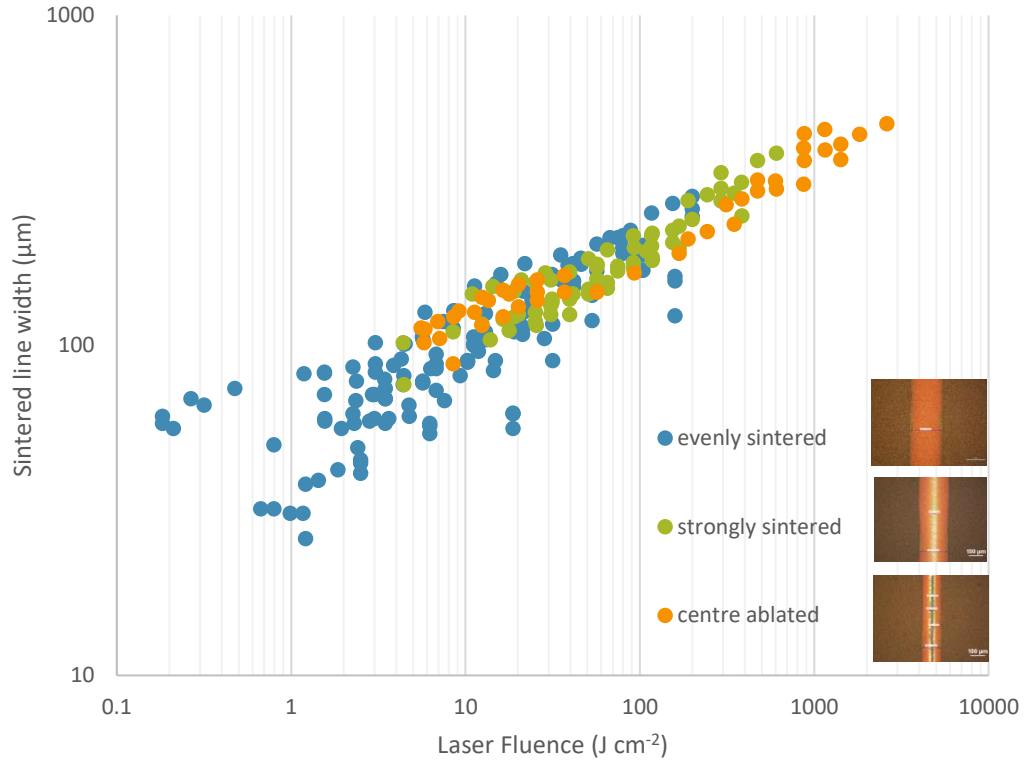


Figure 34. Sintered line width against laser fluence on a single layer of Cu NPs on a **glass substrate**. The descriptions of the sintering state relate to Figure 32 as indicated.

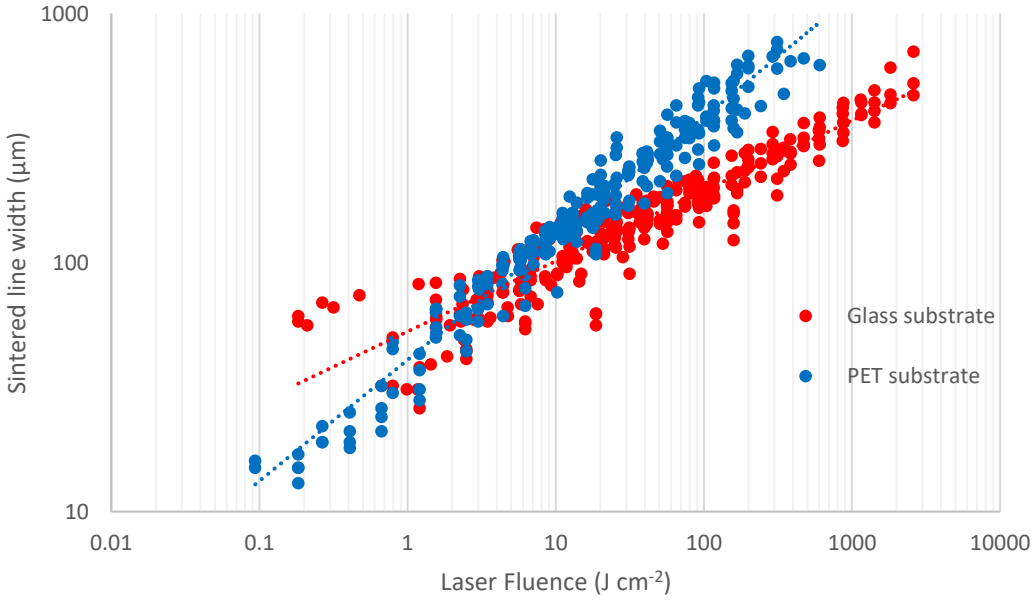


Figure 35. Plot of energy input against sintered line width on a **glass substrate** (green data points) **and** on a **PET substrate** (blue data points). To highlight the overall trend of each of the substrates, trendlines are shown, which are in the form of power function

From Figure 35, it can be seen that there is a clear positive correlation between laser fluence and sintered line width for both, a PET as well as a glass substrate. However, the increase is greater on the PET substrate than on the glass substrate. The great majority of the sintered line widths measured are larger than the laser spot size (32 x 32 µm as measured in Figure 19). The sintering beyond the width of the area, which was directly exposed to laser radiation is therefore induced by the heat flow. The fact that the correlation between laser fluence and sintered line with follows a different trend for the two substrates strongly suggests that the kind of substrate influences this heat flow away from the area directly exposed by the laser scan.

Fourier's Law of heat conduction states

$$\dot{Q} = -kA\frac{\mathrm{dT}}{\mathrm{dx}} \qquad \text{Equation 13}$$

where $\dot{Q}$ is the heat flow rate by conduction (W), k is the thermal conductivity of the material (W m^{-1} K^{-1}), A is the cross-sectional area normal to the direction of heat flow (m^2), dT is the temperature difference (K), and dx is the spatial distance in the direction of heat flow (m) (Arpaci, 1966). Considering one-dimensional heat flow as a consequence of laser exposure through the substrate away from the Cu NP bed we can assume the cross-sectional area normal to the direction of heat flow (A) and the temperature difference (dT) to be equal for the two different substrates. However, the thermal conductivity (k) and the spatial distance in the direction of heat flow (dx) are not the same. In the case of PET, $k = 0.13\ W\ m^{-1}\ K^{-1}$ (Speight, 2005) and $dx = 100 \times 10^{-6}\ m$ (the thickness of the PET used was 100 µm) therefore the term $\frac{k}{dx}$ becomes $1300\ W\ K^{-1}$. In the case of glass, $k = 1.4\ W\ m^{-1}\ K^{-1}$ (Powell et al., 1966) and $dx = 1 \times 10^{-3}\ m$ (the thickness of the glass used was 1 mm) therefore the term $\frac{k}{dx}$ becomes $1400\ W\ K^{-1}$. Assuming A and dT are the same in both cases, it follows that $\dot{Q}_{PET} < \dot{Q}_{glass}$, meaning the PET substrate used has less heat flow associated with it and hence insulates more than the glass substrate. As all other processing variables (i.e. ink deposition) were the same this likely explains the fact that with

increasing laser fluence the sintered line width increases at a higher rate on the PET substrate than on the glass substrate.

For the PET substrate in Figure 33 at a laser fluence of around 7 J cm^{-2}, one can say that below this laser fluence the great majority of data points indicate an evenly sintered result and above this laser fluence the great majority of data points indicate a result where the centre of the laser scan was ablated. For the glass substrate in Figure 34, however, a similarly segregating laser fluence value cannot be identified as there is more of an overlap in terms of laser fluence of data points indicating an evenly sintered result and a result where the centre of the laser scan was ablated. A laser fluence of 7 J cm^{-2} is also indicated by a vertical red line in Figure 34. In Figure 34 compared with Figure 33, there were significantly more evenly sintered data points above a laser fluence of 7 J cm^{-2}. Moreover, the ratio of strongly sintered to centre ablated lines is higher in Figure 34 than in Figure 33. The reason for this disparity is hypothesised to be the differences in associated heat flow of the two substrates which was shown previously. The glass substrate has a higher heat flow associated with it and hence acts of more of a thermal sink compared to the PET substrates. A laser scan which results in the centre of the scan line being ablated is likely due to a localised temperature build-up, which results in overly high temperature gradients causing damage to the material.

It seems reasonable to conclude that the glass substrate, considering it is a more efficient heat-sink than the PET substrate, would be able to prevent this harmful thermal damage at higher laser fluences. To prevent harmful thermal heat build-up as a consequence of this finding, glass substrate was chosen as the substrate of choice for multi-layered builds.

3.5 *Additive Manufacture (AM) of Multi-layered Copper (Cu) Microparts from Nanoparticle (NP) feedstock – A Comparison Between Bar Coating and Inkjet Printing*

Sequential ink deposition and laser sintering was used to manufacture multi-layered Cu microparts of approximately 300 µm height (unless stated otherwise). For the ink deposition, bar coating and inkjet printing were used. This section reports the results of the characterisations of the multi-layered Cu microparts in terms of their internal porosity, surface roughness, mechanical properties, density, and sheet resistance. The following results are reported as comparisons between bar coated and inkjet printed samples.

3.5.1 *Scanning Electron Microscopy (SEM) Imaging of Cross-sections of Multi-layered Copper (Cu) Microparts*

SEM images were carried out to visually inspect Cu micropart cross-sections as well as to quantify porosity through image analysis.

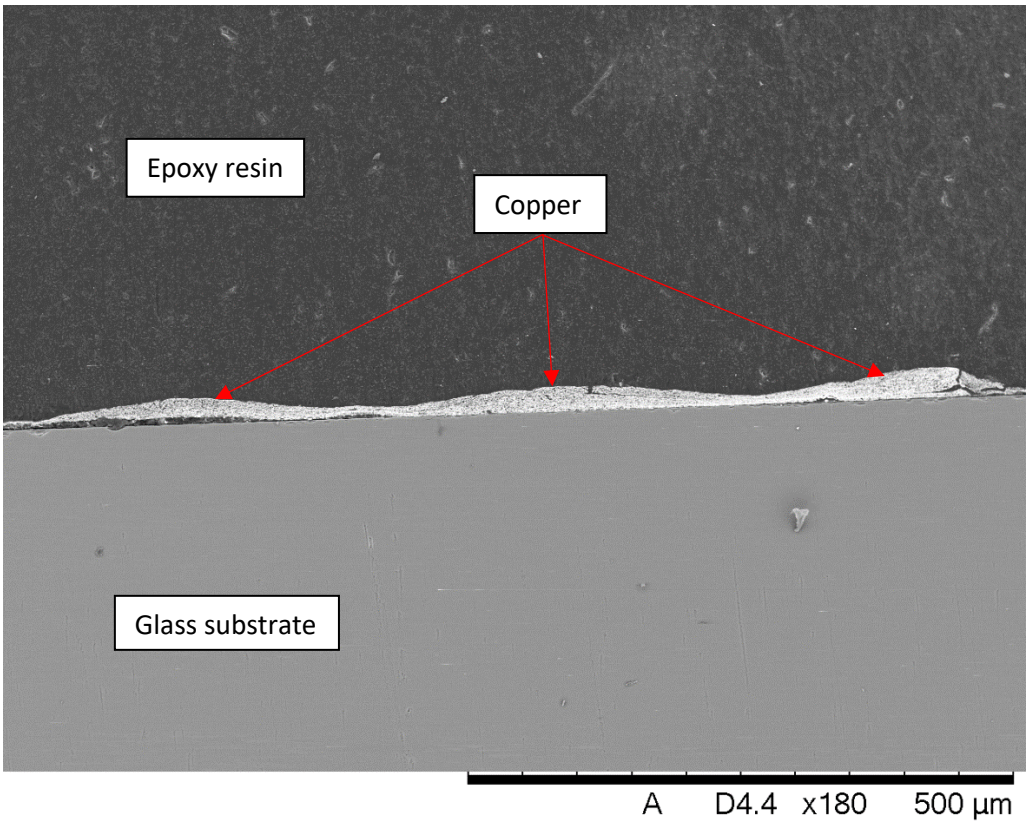


Figure 36. SEM image of the cross section of 100 layers of **inkjet printed** copper. Labels indicate the location of the epoxy resin, the copper and the substrate.

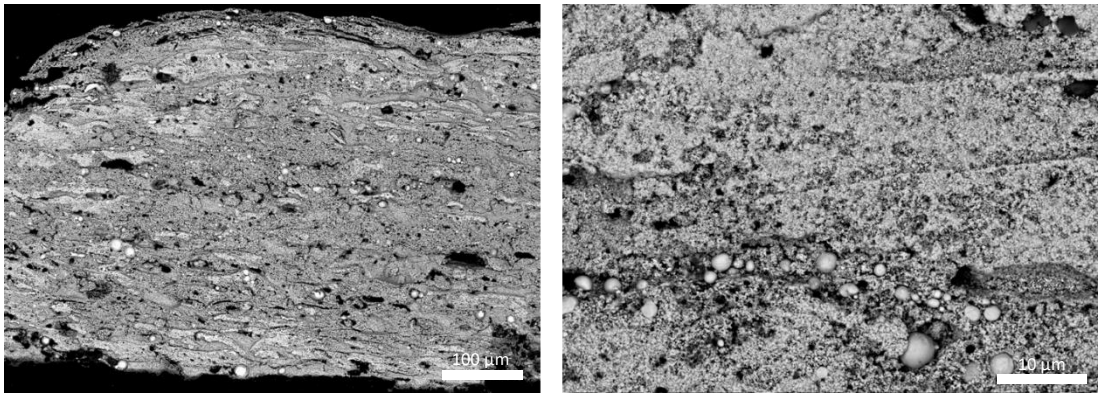


Figure 37. Backscatter electron SEM images of a vertical cross-section of the sequentially inkjet printed and laser processed Cu sample.

The backscatter electron SEM images of the inkjet printed Cu sample (Figure 37) reveal an inhomogeneous internal microstructure. Particle sizes appear to be predominantly in the nano-range with some particles being orders of magnitude larger (up to approximately 15 µm) randomly scattered across the cross-section. In a similar fashion some pores of up to approximately 50 µm mostly horizontal in orientation are located randomly across the cross-section.

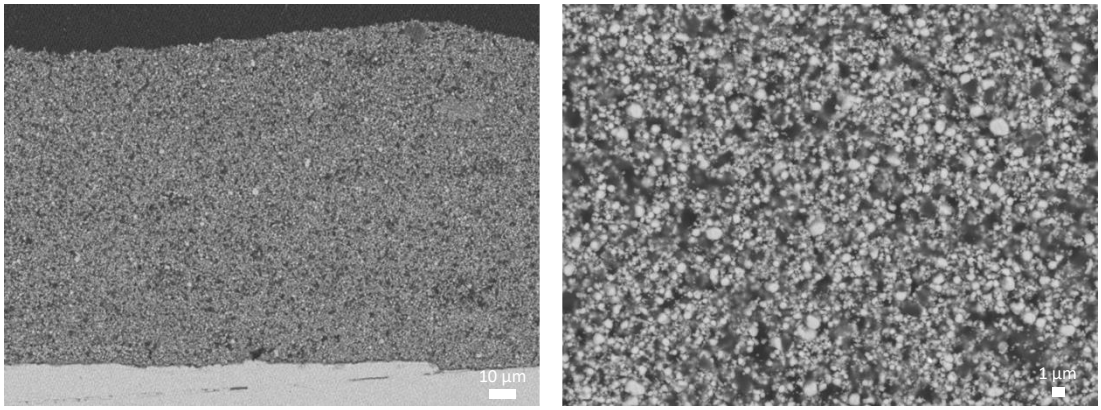


Figure 38. Backscatter electron SEM images of a vertical cross-section of the sequentially **bar coated** and laser processed Cu sample.

The backscatter electron SEM images of the bar coated Cu sample (Figure 38) reveal a porous yet relatively homogeneous internal microstructure characterised by particles and pores on a scale ranging from the nanometres to a few micrometres.

The internal microstructure of the inkjet printed samples was significantly less homogeneous than the bar coated samples. Despite the heating of the inkjet printing

platform to facilitate the drying, it is believed that the inkjet printed film just prior to laser sintering was not as dry as the bar coated film. As a consequence, the flashing of organic residue caused irregular sintering characterised by irregular particle and pore sizes (see Figure 38).

3.5.2 Quantification of the Internal Porosity through Image Analysis of Scanning Electron Microscopy (SEM) images of Cross-sections of Multi-layered Printed Copper (Cu) Microparts

The Internal porosity was quantified from image analysis of SEM images of cross-sections of multi-layered Cu samples.

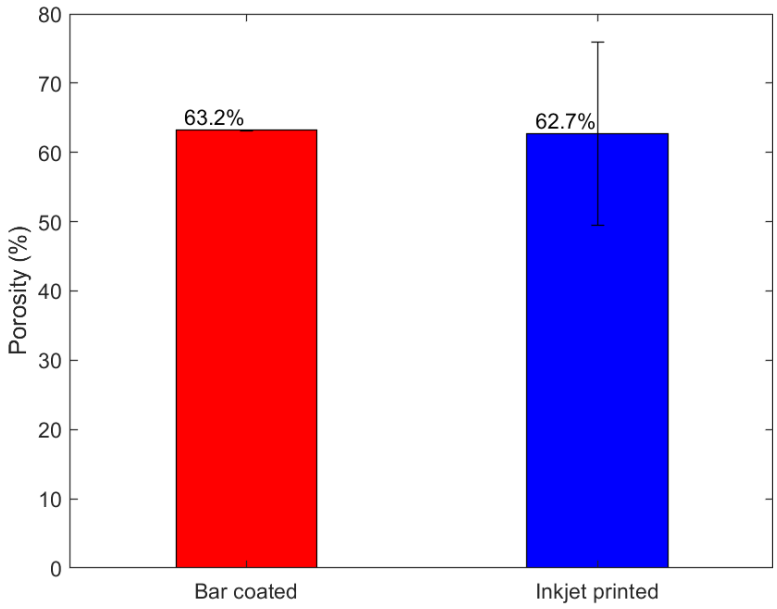


Figure 39. Porosity of bar coated and inkjet printed samples obtained through image analysis of backscatter SEM images of cross sections (Figure 38). Error bars indicate standard deviation.

The comparison in porosity obtained though image analysis in Figure 39 shows a very similar average porosity of the bar coated and the inkjet printed samples, however, the standard deviation associated with the porosity measurements of the inkjet printed samples is significantly greater than for the bar coated samples.

3.5.3 An Investigation into Surface Roughness of the Multi-layered Printed Copper (Cu) Microparts through White Light Interferometry (WLI)

The samples analysed in Figure 40 were all approximately 100 µm high. The bar coated and inkjet printed samples took on average 15 and 300 layers, respectively, to reach the desired height of 100 µm. The arithmetical mean roughness (commonly referred to as S_a) is a common surface roughness indicator which quantifies as an absolute value the average difference in height at each recorded point to the arithmetical mean height of a surface. Figure 40 shows the top surface of 100 µm high inkjet printed samples were on average 53.5 % rougher than the bar coated samples in terms of their arithmetical mean height.

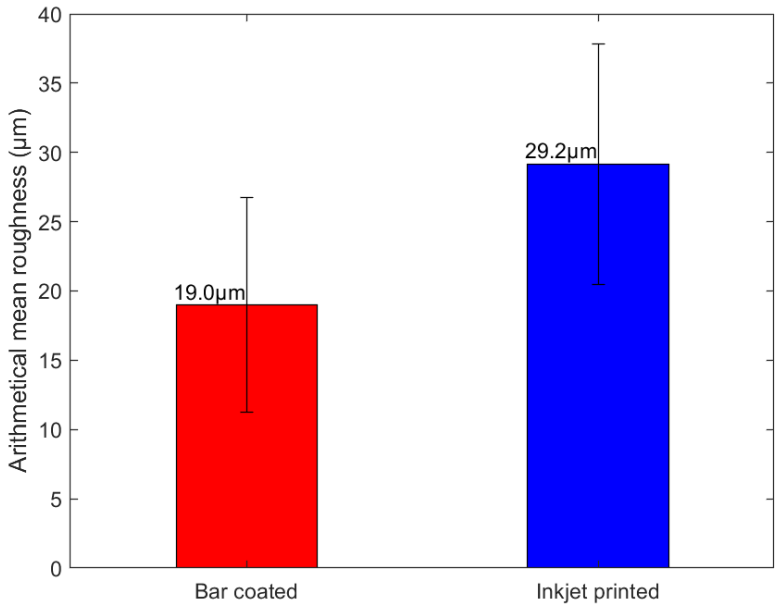


Figure 40. Arithmetical mean height (surface roughness) of the top surface of 100 µm high bar coated and the inkjet printed samples. Error bars indicate standard deviations.

Vaithilingam et al. measured surface roughness of Ag structures which consisted of 50 and 100 inkjet printed and IR sintered layers (Vaithilingam et al., 2017). They report an approximately twofold increase in surface roughness with the twofold increase in layer height. They reasoned this to be due to surface roughness being an accumulation of the roughness of printed layers, suggesting an approximately linear relationship between surface roughness and layers printed. The inkjet printed sample in this work (see Figure 40) was made of three times the amount of inkjet

printed layers and was found to have approximately three times the arithmetic mean height. Therefore, it can be said that the inkjet printed sample from this work concurs with Vaithilingam et al.'s finding and follows the same linear relationship between surface roughness and number of layers printed, as follows

$$S_{A\ stack} = n_{layers}\, S_{A\ layer} \qquad \text{Equation 14}$$

where $S_{A\ stack}$ is the top surface roughness of the stack of layers, n_{layers} is the number of layers, and $S_{A\ layer}$ is the average surface roughness per layer.

It was previously discussed in section 3.3.5 "*The Impact of the Deposited Layer Thickness on the Additive Manufacturing (AM) Process of Multi-layered Copper (Cu) Microparts from Nanoparticle (NP) Feedstock"* that bar coated layers (1 to 9 µm) are significantly thicker than inkjet printed layers (0.1 to 0.5 µm). As for the bar coated and inkjet printed samples compared in Figure 40, with bar coating the amount of layers required to reach a part height of 100 µm was 15 whereas inkjet printing required 300 layers, hence inkjet printing required 20 times the amount of layers to reach the same height. It follows that with bar coating and inkjet printing, the average layer height was 6.7 and 0.3 µm. Assuming the linear relationship between surface roughness and number of layers printed proposed in Equation 14 applies not just exclusively to inkjet printing but also to bar coating, substituting the respective top surface roughness and the number of layers of the bar coated and inkjet printed samples from Figure 40 into Equation 14, it follows that the bar coated and inkjet printed samples have an average surface roughness per layer of 1.3 and 0.1 µm respectively. Therefore, each bar coated layer is on average 12.7 times more rough than the average inkjet printed layer. The average layer thickness of bar coated layers is 20 times greater than the average inkjet printed layer thickness. It can thus be concluded that bar coated structures will have less top surface roughness compared with inkjet printed structures of the same height. This is independent of the absolute height, as long as the printed structures have the same height.

3.5.4 An Investigation into Mechanical Properties of the Multi-layered Printed Copper (Cu) Microparts using Nanoindentation

Indentation hardness and creep were investigated. The predominant deformation mechanisms of the bar coated samples as well as the inkjet printed samples appeared to be viscous, elastic, and plastic deformation. As shown in Figure 41, the indentation hardness of the bar coated samples was on average 55.8 % higher than the indentation hardness of the inkjet printed samples.

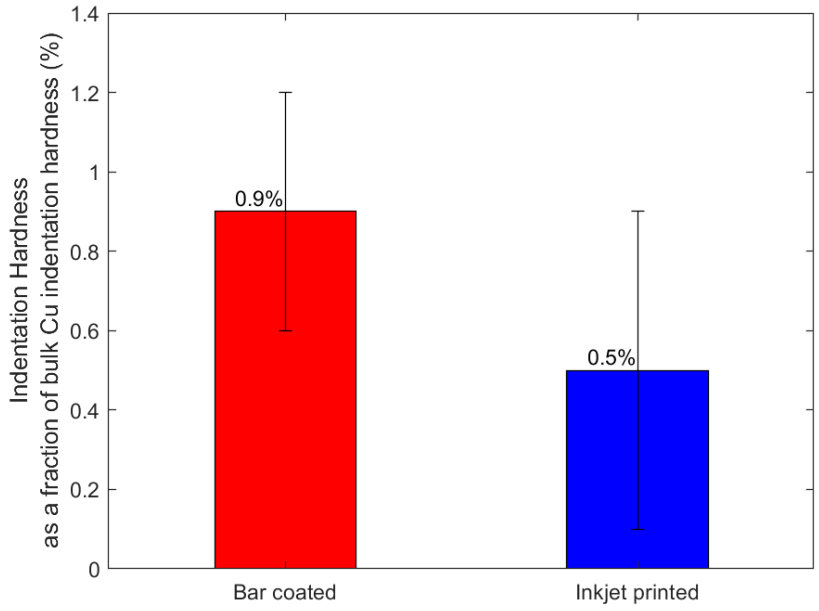


Figure 41. Indentation hardness as a fraction of bulk Cu indentation hardness. Error bars indicate standard deviations.

The creep distance over 5 seconds divided by the maximum plastic deformation of the inkjet printed samples was approximately the same as bulk Cu. The measurement of the inkjet printed samples was on average 88.3 % higher the bar coated samples. The standard deviation of the inkjet printed sample was 404.0 % higher than the standard deviation of the bar coated sample.

The creep measurements are the result of viscous flow of the material under constant load. Viscous flow commonly continues beyond the hold time into the unloading. Elastic deformation as well as viscous flow therefore both impact the indentation modulus of the unloading. As Young's modulus only describes the

stiffness (relationship between stress and strain) as a result of solely its elastic properties, indentation modulus cannot accurately describe Young's modulus in this case and was not presented in this work.

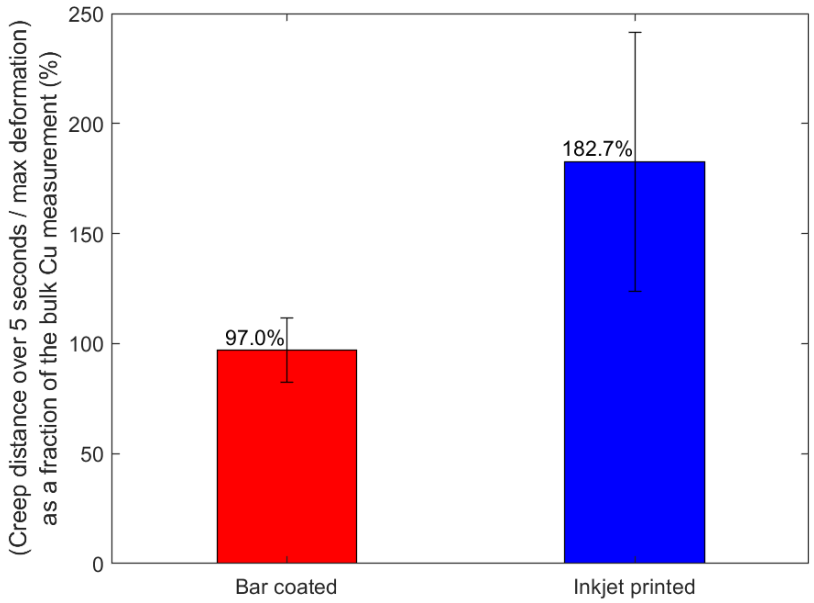


Figure 42. Creep distance over 5 seconds as a fraction of maximum deformation. The result is shown here as a fraction of the bulk Cu measurement. Error bars indicate standard deviations.

Jiang et al. studied the impact of surface roughness on indentation hardness of Cu (Jiang et al., 2008). They showed through simulations and experimental data that increasing surface roughness significantly reduces indentation hardness. This relationship is particularly clear if the indentation depth is not significantly greater than the characteristic size of the surface roughness. In this study, the maximum indentation depth for the bar coated and inkjet printed samples were on average 16.4 and 13.6 µm respectively, and the arithmetical mean height (common surface roughness quantification) for the bar coated and inkjet printed samples were 19.0 and 29.2 µm respectively (Figure 40). Hence the average surface roughness measurements were even greater than the average maximum indentation depths. It can therefore be concluded that the proximity of the surface roughness and the indentation depths contributed to the low indentation hardness measurements.

The indentation hardness of the bar coated samples were found be on average 55.8 % higher than the inkjet printed samples (see Figure 41). Both were on average below 1 % of the measured indentation hardness of bulk Cu sample. Based on similar findings of highly nanoporous materials in the literature (Meyers and Chawla, 1964; Tabor, 1951), the main reason for this low hardness is likely to be the high porosity of the samples which was found to be greater than 60 % for both printing methods (see Figure 39).

Srivatsan et al. used two different Cu powders with an average particle size of 100 nm and 13 µm and consolidated the mixture through Plasma Pressure Compaction (P^2C) (Srivatsan et al., 2001). The powder was poured into a graphite die and compressed with 40 MPa pressure using graphite plungers. During the compression a DC voltage was applied for 3 min to accelerate densification of the material by inducing resistance heating which raises local temperature and thus facilitates mass diffusion. Srivatsan et al. report their process is capable of causing heating rates of up to 500 °C min^{-1}. The 100 nm and 13 µm particle size samples were found to have a density of 99 % and 95 %, respectively and an indentation hardness of 2.42 and 1.26 GPa, respectively. These indentation hardness results are in the same range as the measured indenation hardness of the bulk Cu sample in this study (1.45 GPa). Srivatsan et al.'s study shows that even when using nano-sized Cu particles as a starting point, a final material hardness similar to bulk Cu can be achieved. However, compared to the methodology employed in this study, Srivatsan's methodology has several drawbacks. Firstly, the equipment cost and the energy requirement are both assumed to much greater. Cu heated above 100 °C for more than a few seconds undergoes rapid oxidation. The smaller the particle size and hence the bigger the surface area-to-volume ratio, the faster this chemical reaction takes place. With nano-sized particles the oxidation occurs almost instantaneously. Srivatsan et al.'s process involves elevated temperatures above 100 °C for time durations in excess of seconds. In order to achieve non-oxidised electrically conductive final Cu microparts, despite not being explicitly mentioning it, Srivatsan et al. must have conducted the pressure and electrical treatment of in a low-oxygen environment. For this the process must be carried out in to air-tight sealed container under a constant gas flow

(commonly argon or nitrogen are used). This requirement adds cost as well as process design complexity. Secondly, Srivatsan et al.'s particle sintering process is not selective in nature. The pressure and electric current cannot be applied selectively as it is the case with laser irradiation in this study. This makes Srivatsan et al.'s process impossible to be applied to an additive manufacturing process.

Vaithilingam et al. inkjet printed and sintered using an infrared (IR) source up to 1,000 layers of Ag NP ink (Vaithilingam et al., 2018). Unlike in this study in which nanoindentation was used, Vaithilingam et al. used Vickers hardness (HV) to quantify hardness. Their reported hardness was higher than cast commercially pure Ag and lower than sterling Ag and cold-worked Ag. Vaithilingam et al. hypothesised that the existence of carbon, oxygen and possibly a fraction of other metals in the sample matrix and exposure of the printed layers to IR power source for prolonged time may have altered the microstructure and thus increased the hardness of the printed sample compared to the conventional as-cast samples. This hypothesis is neither backed up with evidence nor explained. The comparable hardness to the bulk metal hardness of Vaithilingam et al. is a stark contrast to the hardness below 1 % of the bulk metal hardness in this report. There are three significant differences between Vaithilingam et al.'s process and the process in this study. Firstly, the conductive metal printed was Ag in Vaithilingam et al.'s case and Cu in the case of this study. Secondly, the particle size distributions differ. Vaithilingam et al. state that the size of the Ag NPs used in the study was less than 100 nm. In this study the average particle size of the Cu NPs used was found to be 330 nm (see Figure 25). It has been widely reported and well understood in literature that the temperature required to induce particle sintering is proportional to the bulk material melting temperature as well as inversely proportional to the particle size (Fang and Wang, 2010). Considering Ag has a lower bulk material melting point than Cu (962 and 1,085 °C respectively) it follows that just by the nature of the material Vaithilingam et al. required a lower temperature. Thirdly, the sintering process differed. Even though both sintering sources are photonic IR sources, significant differences exist. Vaithilingam et al.'s IR source is non-selective, additionally even though it is not stated the exposure time can be assumed to be in excess of 1 s. In the case of this study, the IR source is a laser

which due to the optics in the scan head is selective as a spot size of 32 x 32 µm. At a scan rate of 250 mm s^{-1} the average exposure time is therefore approximately 4 orders of magnitude lower. It was previously mentioned in section 3.3.1 "*The Size of the Metal Particles Used and The Sintering Process",* sintering describes mass transport phenomena which are inherently time dependent. It is therefore logical that Vaithilingam et al., who employed sintering times approximately 4 orders of magnitude higher than in this study, achieved a higher degree of densification and consequentially a greater hardness. As explained in section 3.3.1.2 "*Sintering Time"* in order to achieve the stated aim of additively manufacturing electrically conductive multi-layered Cu structures in an ambient environment, comparable sintering times would have cause detrimental oxidation of the Cu.

Vaithilingam et al. state that drop spacing negatively correlates with micropart porosity and hence positively correlates with micropart hardness. They reported a decrease of the drop spacing from 50.8 to 42.3 µm resulted in an increase of 29 % in hardness. The impact of drop spacing of the inkjet printing on micropart properties was not investigated in this study, however, Vaithilingam et al.'s findings indicate that regarding the inkjet printed samples, adjusting drop spacing will likely have an impact on materials properties such as hardness and should therefore be investigated.

3.5.5 An Investigation into the Density and a Heat Treatment to Increase Density of the Multi-layered Printed Copper (Cu) Microparts

In order to quantify density, the mass of the samples was measured using a scientific scale and divided by the volume of the samples which was measured using white light interferometry. For this, the samples were placed on an even surface, a scan of the sample including the surrounding surface was carried out. From this scan, the volume of the sample was calculated.

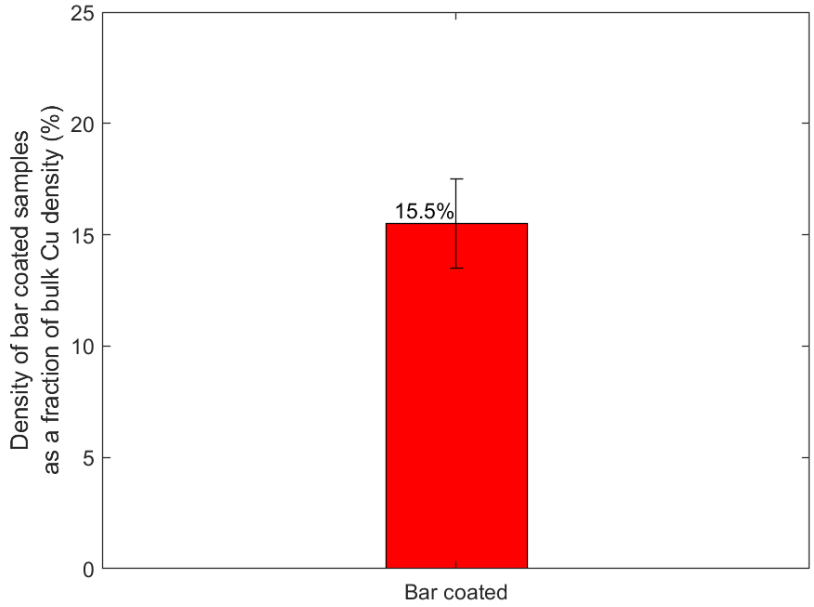


Figure 43. Density as a fraction of bulk Cu density. The error bars indicate standard deviation.

The average density of the bar coated samples was found to be 15.5 % of bulk Cu density (8,960 kg m^{-3}). It was not possible to obtain the density of the inkjet printed samples as they were too fragile to be removed from the glass substrate they were printed on without significant damage.

Inspired by Bai and Williams' post-printing heat treatment to reduce porosity and increase density (Bai and Williams, 2018), heat treatment at the same temperatures was carried out but under argon flow whereas Bai and Williams used hydrogen flow (for complete methodology see section 3.2.13 *"Heat Treatment of Printed and Sintered Multi-layered Copper (Cu) Microparts to Enhance Densification"*). The heat-treated samples came out grey in colour (see Figure 44). Resistance was found to be above the measureable range of the multimeter used; it was therefore not considered to be electrically conductive. It was hypothesised that the Cu samples oxidised. In order to validate this hypothesis, an XRD spectrum was taken which confirmed complete oxidation of the Cu (XRD spectrum in *Appendix* section 8.3.1 Figure 90).

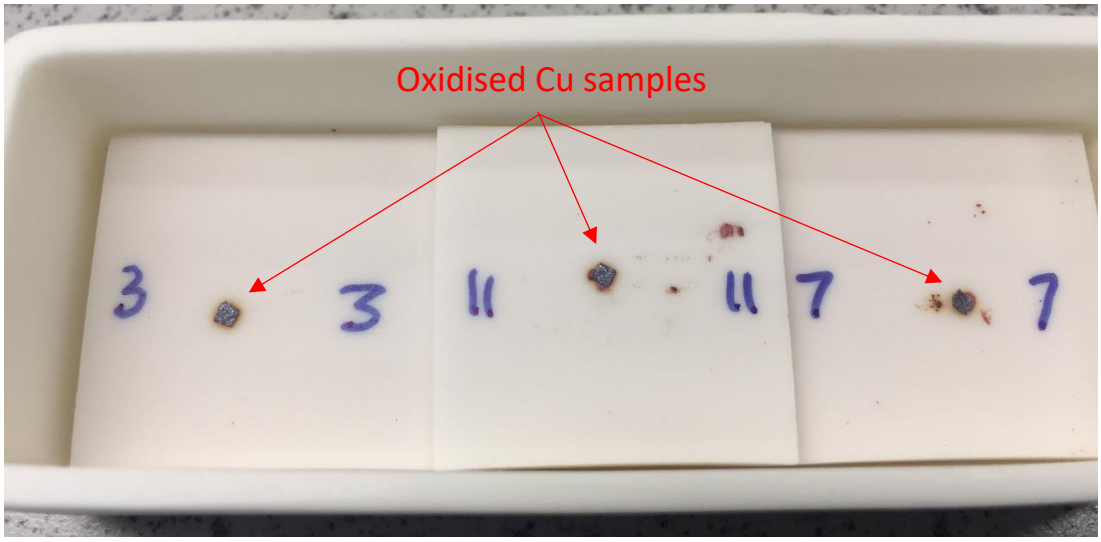


Figure 44. Photo of oxidised Cu samples after heat treatment indicated by red arrows.

The low density of the bar coated and laser sintered microparts of on average 15.5 % as a faction of bulk Cu density (see Figure 43) is significantly lower than multi-layered Cu microparts manufactured through different AM processes. SLM, for instance, has been able to produce multi-layered Cu parts with densities of up to 96.5 % (Zhang et al., 2013). Bai and Williams used binders to consolidate Cu powder (Bai and Williams, 2018). Their binder jetted green part densities were between 42.3 and 50.5 %. Though not quite as low as in this study their densities were also insufficiently low. In order to increase part density, Bai and Williams employed post-printing heat treatment to densify their green parts. The heat treatment was carried out at temperatures of 1,025 to 1,075 °C in a pure hydrogen atmosphere to prevent oxidation and to reduce any existing Cu oxide back to elemental Cu. The heat treatment led to a volumetric shrinkage of between 23.7 and 35.5 % and significantly increased the Cu part densities to a final part density of between 70.3 and 80.8 %. This remarkable increase in part density was taken as an inspiration to attempt to increase part density of the multi-layered Cu microparts additively manufactured in this study. A tube furnace and the same temperatures and temperature profiles as Bai and Williams were used. It was not possible to use hydrogen gas for this experiment so argon gas was used instead. As demonstrated by the XRD scan in Figure 90, the Cu microparts came out completely oxidised. No practical reason for this such as a gas leak or loose furnace sealings could be found. It has thus been

hypothesised that the oxygen concentration in the tube furnace was not sufficiently low to prevent oxidation of the Cu micropart. The Cu NPs which were used in this study with an average particle size of 330 nm (see Figure 25) have a significantly higher surface-area-to-volume ratio than the Cu powder with particle sizes in the micron-range used by Bai & Williams. The NPs were therefore more reactive towards any oxygen that may be present despite being in a sealed environment under gas flow. Additionally, the gases that were used act as suppressants for Cu oxidation in a different way. Argon is an inert gas towards Cu and prevents oxidation solely by passively shielding the Cu from oxygen. Hydrogen, on the other hand, reacts with Cu oxide as follows:

$$Cu_2O + H_2 \xrightarrow{yields} 2\,Cu + H_2O \qquad \text{Equation 15}$$

$$CuO + H_2 \xrightarrow{yields} Cu + H_2O \qquad \text{Equation 16}$$

Hence as well as also passively shielding the Cu from oxygen, hydrogen additionally actively reverses Cu oxidation. It is believed that a combination those two factors explains the oxidation of the multi-layered Cu microparts during the heat treatment in this study, namely the small particle size making the material more reactive towards oxygen as well as the use of which is less effective at preventing Cu oxidation argon rather than hydrogen.

3.5.6 An Investigation of Electrical Properties of the Multi-layered Printed Copper (Cu) Microparts through Sheet Resistance Measurements

The four-point probe was used to carry out sheet resistance measurements of the multi-layered Cu microparts throughout the build height. Taking into account the spatial dimensions of the microparts, the sheet resistance measurements were also converted to resistivity.

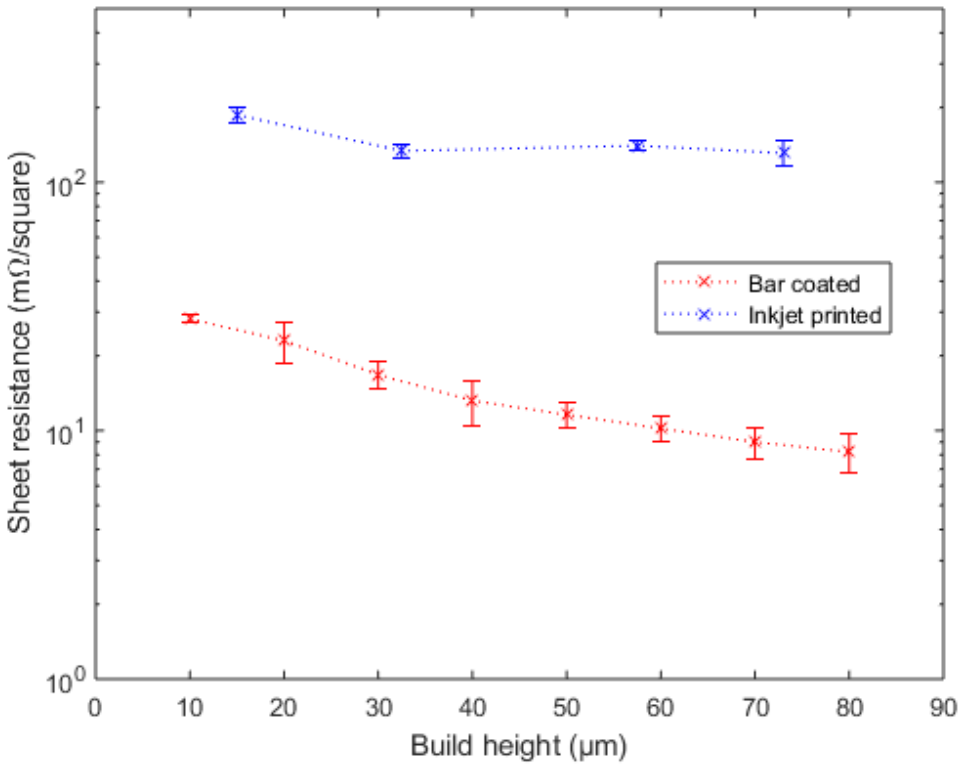


Figure 45. Sheet resistance against build height for the two different ink deposition methods. Error bars indicate standard deviations. Note, the y-axis is logarithmic to better visualise the two data sets.

The sheet resistance decreases with increasing build height for both, the bar coated and the inkjet printed samples (see Figure 45). The sheet resistance of the bar coated sample is approximately one order of magnitude lower across the entire build height than the inkjet printed sample. Sheet resistance describes the resistance of a thin film to the flow of electric current (Topsøe, 1968). The volume of the electrically conductive material increases with increasing build height. Sheet resistance is a measurement of the absolute resistance of a thin film to the flow of electricity which is dependent on the volume of the object. The greater the volume (at constant resistivity) the lower the sheet resistance, therefore it is logical that sheet resistance decreases with increasing build height.

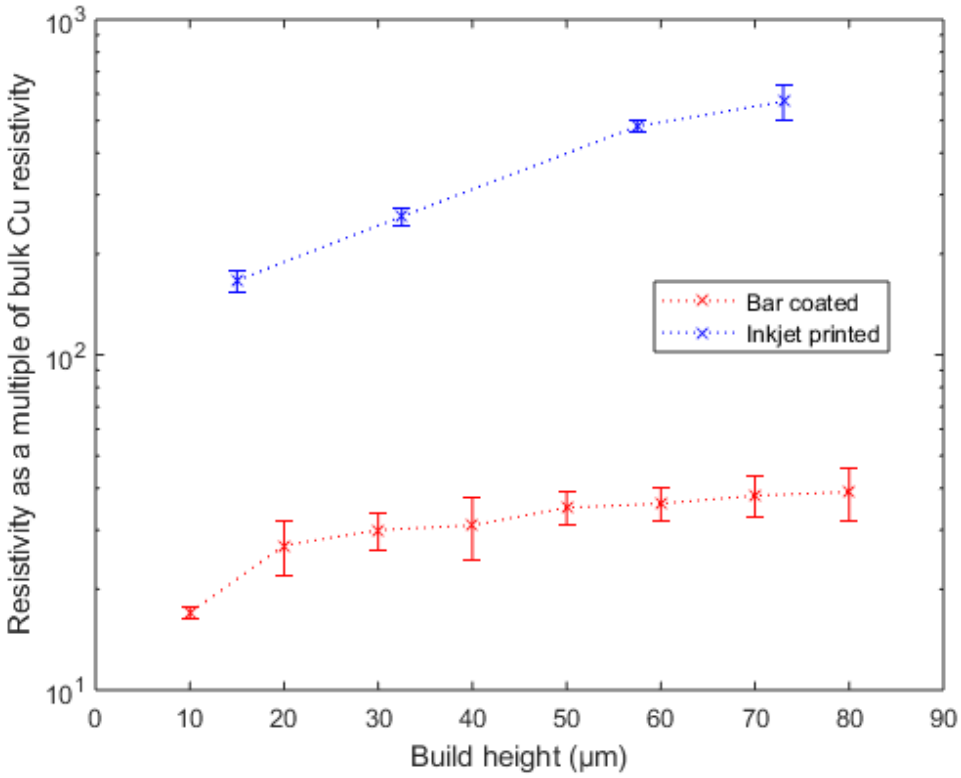


Figure 46. The resistivity as a multiple of bulk Cu resistivity against build height for the two different ink deposition methods. Error bars indicate standard deviations. Note, the y-axis is logarithmic to better visualise the two data sets.

Equation 9 was used to obtain resistivity. The resistivity was plotted as a multiple of bulk Cu resistivity (1.68 x 10-8 Ω m). In general, resistivity describes a material property which (whilst being dependant on the nature of the material and its temperature) is independent of its special expansion, *i.e.* shape or size. It describes the resistance of a material of a unit length and unit cross-sectional area. A mere increase in volume (at constant resistivity) which comes with the increase in build height does therefore not impact resistivity. It can be seen from Figure 46 that the resistivity (here expressed as a multiple of bulk Cu resistivity) increases with increasing build height for both the bar coated as well as the ink jet printed sample. The range of the resistivities across the entire build height of the inkjet printed sample are on average 11.7 times higher than the bar coated sample. The relative increase in resistivity across the build height of the inkjet printed samples is greater than the equivalent of the bar coated samples.

For both bar coated as well as the inkjet printed samples, with increasing build height, sheet resistance decreases and resistivity increased (see Figure 46).

Comparing one printed and sintered layer with two printed and sintered layers it is clear that the prior does not contain an interlayer whereas the latter does indeed contain an interlayer – between the first and the second layer. It is believed that interlayer sintering occurs, otherwise the entire structure would be made of loose layers without any structural integrity. However, this interlayer sintering is likely not as strong as the sintering that occurs within each layer. In some of the cross-sectional SEM images the interlayer was clearly visible (an example can be seen in Figure 47). It is hypothesised that the interlayer does not conduct electricity as well as the layer itself; this would explain why the material resistivity increases with increasing build height, because with increasing build more layers and hence more interlayers are added to the material.

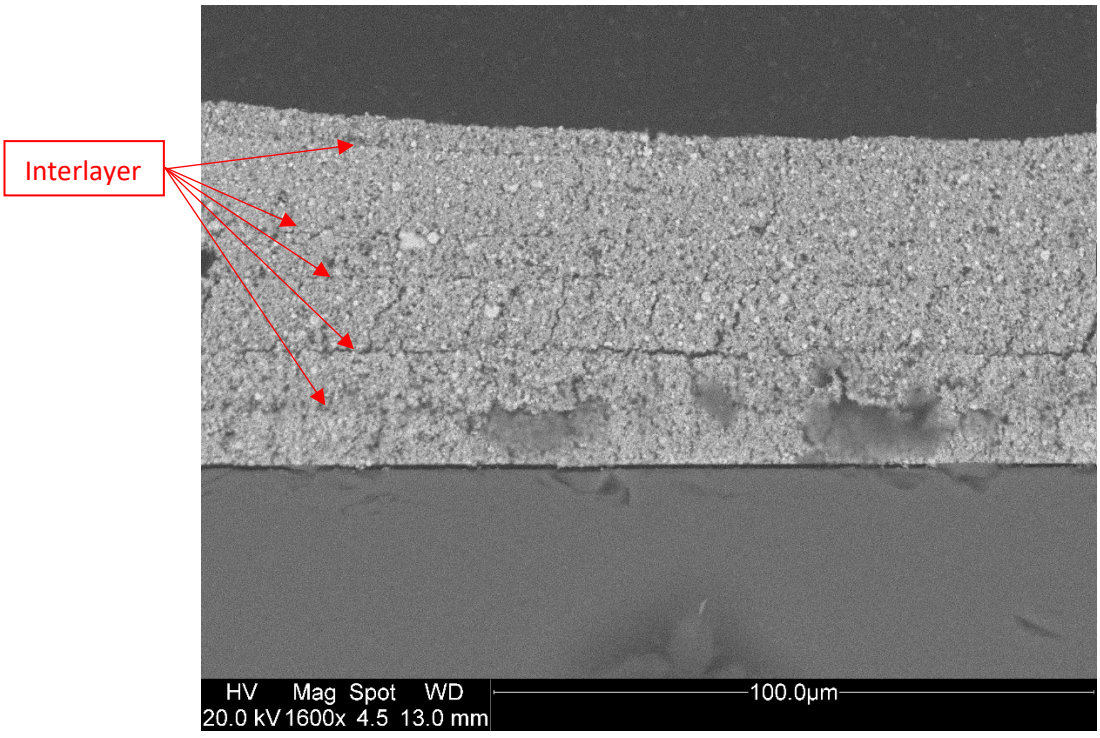


Figure 47. Backscatter electron SEM image of a vertical cross-section of a multi-layered Cu sample. The five interlayers of the six layers present are indicated by red arrows.

Neither Vaithilingam et al. nor Saleh et al. measured resistivity throughout the build (Saleh et al., 2017; Vaithilingam et al., 2018, 2017); both were therefore not able to provide data on the resistivity with increasing build height comparable to Figure 45 or Figure 46. The only comparable data set in the literature is by Xu et al., however, it is for Ag NP ink rather than Cu NP ink (Xu et al., 2017). The authors do not state how their stated resistivity values were obtained. Xu et al. report no conductivity below 6 printed and sintered layers and a decreasing resistivity between 6 and 15 layers approaching a resistivity of 3 times bulk Ag. This finding is somewhat contrary to this study in which an increase in resistivity with increase micropart height was reported in Figure 46. The reason for this disparity appears to be that Xu et al.'s layers were highly inconsistent and unconnected which was not the case in this study. It therefore took Xu et al. 6 layers to achieve a particle network which is connected at all to enable any conductivity at all. Xu et al. does not provide any quantification of the thickness per layer or the thickness of the accumulated structure, only the number of layers is reported. Inkjet printing parameters are also not stated and there is no mention of 3-dimensionality. Assuming a common inkjet printed layer height it can be concluded that Xu et al. maximum thickness is well below 10 µm, which profoundly changes the nature of the analysed changes in resistivity compared to the significantly taller structures analysed in this study. Moreover, the description of a de facto resistivity value as conductivity raises doubts regarding the quality of Xu et al.'s study.

In this study the resistivity of the bar coated samples was between 17 and 39 times bulk Cu resistivity and the inkjet printed samples was between 167 and 569 times bulk Cu resistivity (see Figure 45). Comparing this to the only comparable studies in the literature, Vaithilingam et al. inkjet printed and IR sintered up to 1,000 layers of Ag NP ink and reported a final micropart resistivity of between 8 and 14 times of bulk Ag resistivity (Vaithilingam et al., 2017). Saleh et al., who also inkjet printed up 1,000 layers of Ag NP ink but used UV sintering rather than IR sintering, recorded resistivity with increasing sintering time and the resistivity reaches a minimum after approximately 10 seconds at approximately 30 times bulk Ag resistivity (Saleh et al., 2017). As it was previously discussed in section 3.3.1.2 "*Sintering Time"*, both

Vaithilingam et al. as well as Saleh et al. employed significantly longer sintering times than in this study, as both authors used Ag rather than Cu NPs and so rapid and detrimental oxidation is not an issue. Despite sintering times being approximately 4 orders of magnitude lower in this study, the bar coating and laser sintering process was able to produce multi-layered electrically conductive metal structures with resistivities in the same range as the ones reported by Vaithilingam et al. and Saleh et al. (all resistivities with respect to their bulk metal resistivity).

3.6 Discussion of the Comparison between Inkjet Printing and Bar Coating as a Deposition Methods for Additive Manufacture of Multi-layered Printed Copper (Cu) Parts from Nanoparticle (NP) Feedstock

For the purpose of additively manufacturing a multi-layered Cu micropart with properties close to a bulk Cu micropart, it is clear from the Results chapter 3.5 *Additive Manufacture (AM) of Multi-layered Copper (Cu) Microparts from Nanoparticle (NP) feedstock – A Comparison Between Bar Coating and Inkjet Printing* that in terms of the material aspects tested the inkjet printed samples did not come out as closely to bulk Cu as the bar coated samples.

It is believed that the following aspects led to this discrepancy. The Cu inks used was for the inkjet printing and bar coating were not exactly the same. While in both cases the metal NPs were made of Cu, the ink formulations differed. For an ink to be inkjet printable, it needs to be capable of repeated droplet formation through piezo electrically operated nozzles. The ink's rheological properties such as viscosity, surface tension and volatility therefore are required to fall within specific narrow ranges to enable droplet formation of the inkjet printer-and-cartridge-combination used. In the case of the inkjet printer and cartridges used according to the manufacturer of both they are defined as viscosity: 0.010 – 0.012 Pa s, surface tension: 0.028 – 0.033 N m^{-1}, particle size: ideally no more than 210 nm, fluid evaporation: the ink must not dry at the nozzle-air-interface so a low evaporation rate high boiling point is required (FUJIFILM Dimatix, 2016). Additionally, high particle

suspension stability as well as the inhibition of particle agglomeration is required to prevent inkjet nozzle clogging and to provide an acceptable shelf life for the ink.

However, during bar coating the ink does not flow through the confined space of a nozzle and no droplet formation is required. The only requirement is that the ink is spreadable with a hand coater or a doctor blade. From the experimental work conducted it was concluded the only requirement is a metal weight loading of between 15 and 50 wt%, hence almost no ink formulation was required. Significantly, unlike inkjet printing which requires a high boiling point, it was found that with bar coating it was possible to use a significantly more volatile solvent such as propan-2-ol, which has a boiling point of 83 °C. In contrast, the boiling point of the main solvent in the inkjet ink (2-(2-ethoxyethoxy)ethanol)) is 210 °C.

3.7 Summary of Additive Manufacturing (AM) of Multi-layered Printed Copper (Cu) Microparts from Nanoparticle (NP) Feedstock

Electrically conductive multi-layered Cu microparts were successfully additively manufactured from Cu nanoparticle feedstock using low power laser sintering in an ambient environment. The Cu microparts were found to be of low-density and highly porous. This had a significant negative effect on their mechanical properties which were far off from bulk Cu properties. However, the electrical properties were not as significantly affected since resistivities close to bulk Cu were still achieved, similar to comparable literature which produced much higher micropart densities. This suggests that even with a highly porous sintered particle network, resistivities close to bulk metal are achievable. Similar material characteristics of laser sintered metal NP structures are reported in literature (Niittynen et al., 2014).

The sintering phenomenon and its associated degree of densification is the predominant parameter affecting final micropart characteristics such as mechanical and electrical properties. The stated aim of the study to sinter Cu NPs in an ambient environment necessitates very short sintering times to avoid oxidation. This limits the degree of maximal possible densification possible. In order to increase micropart

density an additional heat treatment was attempted. However, the Cu microparts oxidised, it is believed, due to in part a lack in availability of the right gas during the heat treatment. Based on the literature this post-printing heat treatment should be able to significantly densify the microparts and it hoped this will be proven in the future.

The comparison of two different deposition methods has shown that compared to inkjet printing, bar coating is more time-efficient as with bar coating more volatile solvents can be used and its deposited layers are significantly thicker. Moreover, the structures manufactured through bar coating were found to have significantly better electrical properties and more robust mechanical properties.

The ability to additively manufacture electrically conductive multi-layered Cu structures from a nanoparticle feedstock in an ambient environment means multi-layered Cu microparts can be additively manufactured with significantly lower equipment and running cost than all comparable processes. This is largely because a sealed low-oxygen environment is not necessary as well as the laser being a low power fibre laser compared to the high-power lasers which are commonly used in SLM for instance. The significantly reduced cost of the process has the potential to make AM of multi-layered Cu microparts more affordable and hence more widely commercialisable.

4 2D PRINTING AND SINTERING OF COPPER (Cu) AND SILVER (Ag) NANOPARTICLES

4.1 Introduction

This chapter investigates the sintering process of Cu and Ag NPs. Printing and sintering of Cu NPs is generally considered to be more challenging than Ag NPs. As explained in the Literature Review subchapter 2.3.3 *"Post-deposition Annealing of Nanoparticles"* this is because Cu sintering requires higher temperatures than Ag and also because at elevated temperatures (> 80 °C) in an air environment, Cu has the tendency to rapidly oxidise which is detrimental to its electrical conductivity (Li et al., 1991). However, Cu is a much cheaper material than Ag. The aim of this chapter is to investigate the impact of the addition of small amounts (≤ 25 wt%) of Ag to Cu NPs on the sintering process. Firstly, the sintering process of solely Cu NPs and solely Ag NPs are investigated separately using FEG-SEM imaging of *in-situ* thermal sintering inside the microscope. Secondly, Cu NPs inks with additions of up to 25 wt% Ag are deposited and sintered through laser irradiation, Intense Pulsed Light (IPL) exposure, and through thermal heat. The impact of the Ag additions on oxidation stability and electrical resistance is investigated. A discussion follows which based on the results discusses the sintering behaviour of Cu and Ag NPs and whether additions of Ag to Cu NPs can harness synergistic effects beneficial for the sintering process.

4.2 Materials and Methodology

This section describes the equipment, methods and materials used. This involves NP ink synthesis and formulation, NP ink deposition and laser, IPL, and thermal sintering, as well as the characterisation of the sintered tracks, i.e. SEM and EDX, LDA, DSC, XRD, and electrical sheet resistance measurements.

4.2.1 Copper Nanoparticle and Silver Nanoparticle Synthesis and Ink Formulation and Ink Deposition

The NP inks used in this chapter were synthesised by Bernard Christaud, an intern of Prof. Ed Lester, who was co-supervised by the author. The same synthesis process as

described in 3.2.1 *"Copper Nanoparticle Synthesis and Formulation"* was used to produce NP dispersions – the only difference being that the up-flow into the reactor (FS stream in Figure 15) consisted of other than copper nitrate ($Cu(NO_3)_2$) also of silver nitrate ($AgNO_3$) solutions at the following Ag/Cu weight (wt) ratios in deionised water.: 0/100, 1/99, 3/97, 8/92, and 25/75. The silver ions react in the reactor as described in Equation 17 and Equation 18.

Equation 17. Half reactions of Ag NP synthesis.

$$Ag^+ + e^- \rightarrow Ag^0$$
$$H_2PO_2^- + H_2O \rightarrow H_2PO_3^- + 2H^+ + 2e^-$$

Equation 18. Full reaction of Ag NP synthesis.

$$2Ag^+ + H_2PO_2^- + H_2O \rightarrow 2Ag^0 + H_2PO_3^- + 2H^+$$

Energy-dispersive X-ray (EDX) spectroscopy analysis of the final inks showed that the final Ag weight loadings with respect to the total metal content (Ag content + Cu content) in the inks were on average: 0, 1, 3, 8 and 25 wt% (note, from here onwards they will be referred to as 0, 1, 3, 8, and 25 wt% Ag). The EDX scans can be found in the *Appendix* section 8.6.

Bar coating was used to deposit Cu and Ag inks. The same methodology was used as explained in the previous subchapter 3.2.2 *"Deposition of Copper (Cu) Nanoparticle (NP) Ink through Bar Coating"*.

4.2.2 Particle Sintering of Copper (Cu) – Silver (Ag) Hybrid Inks

Three different sintering techniques were used to anneal deposited inks to investigate the impact of the addition of Ag to Cu NPs on electrical resistance: laser sintering, intense pulsed light (IPL) sintering, and thermal sintering.

The laser sintering methodology described in section 3.2.5 *"Laser Irradiation of Copper (Cu) Nanoparticle (NP) Ink to Induce Particle Sintering"* was used.

A Heraeus Noblelight flash lamp system was used for IPL sintering. The sample was placed under the flashlight at a distance of 15 mm between the bottom of the lamp and the surface of the sample. The sample was exposed to a single flash with a flash duration of 6 ms at a voltage of 400 V.

Thermal sintering in air of Cu and Cu-Ag NP was carried out to investigate oxidation and its impact on electrical sheet resistance. A generic chemistry lab hotplate was used for thermal sintering in air. A thermocouple was placed onto the sample surface and glued down using heat-resistant Kapton® tape (consists of polyimide with silicone adhesive) to ensure physical contact between the probe and material. The temperature was increased in 10° steps from room temperature to 265 °C. At each temperature step the temperature was held for 2 minutes. At the end of the 2 minutes hold-time a sheet resistance reading was taken with the four-point probe as explained in section 3.2.11 *"Electrical Sheet Resistance and Resistivity Measurements of Multi-layered Copper (Cu) Microparts"*. The same experiment was repeated three times; averages and standard deviations were determined.

4.2.3 Thermally Induced Nanoparticle (NP) Sintering in-situ the Electron Microscope

In order to obtain FEG-SEM images of particle sintering in real time, NPs were thermally sintered *in-situ* the microscope. This provided unique visual information on mass transport phenomena occurring at a sub-micrometer scale.

A Field Emission Gun Scanning Electron Microscopy (FEG-SEM) (JEOL 7100F FE-SEM) which uses an in-lens Schottky field emission source was used which is fitted with an integrated Oxford Instruments X-Max silicon drift detector for EDX analysis. It was fitted with a Gatan Murano 525 *in situ* heating stage (see Figure 48). The transferable carriage assembly is coupled with mating electrical contact pins for a heater and a temperature sensor. The sample is mounted on a consumable semiconductor

hotplate made of silicon, located on a ceramic block support. A power booster provides power up to 20 W, while the temperature of the hotplate is controlled by a USB temperature controller, which displays the temperature of a thermocouple that is in contact with the underside of the hotplate. The cooling of the system is enabled by a water recirculating system. Once installed into the carriage assembly, the hot plate is covered by a metallic shield with a 2 mm sized circular aperture: this is done in order to protect the components inside the SEM from the light emission and radiative heating effects, while enabling the imaging of the specimen surface through the aperture, located above the centre of the hotplate.

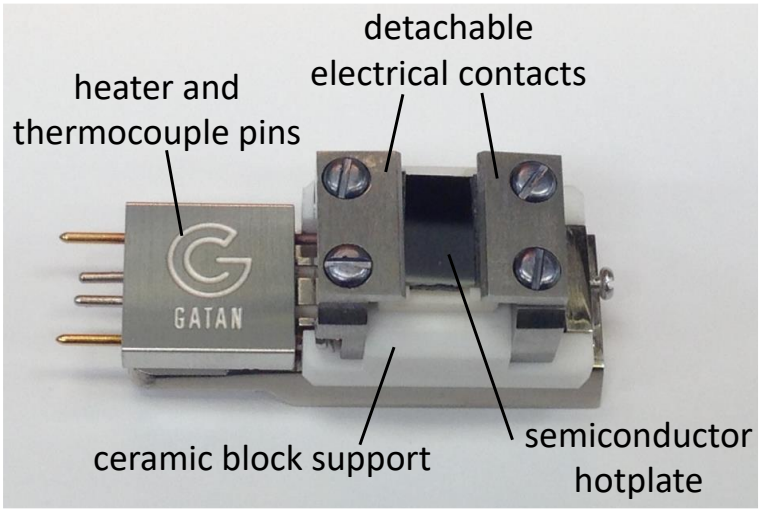


Figure 48. Murano 525 Gatan *in situ* heating stage with labels. ("Murano 525 Gathan heating stage, User Manual," n.d.)

The heating stage was programmed through its software to incrementally increase its temperature by 30 degrees at a time. At each 30-degree temperature increment the temperature was kept constant for 10 minutes. Right afterwards, for the following 5 minutes, images were captured using the secondary electron detector. The FEG-SEM was operated at 15 keV and the sample was kept at a working distance of 12.5 mm.

4.2.4 Image Analysis of FEG-SEM Images of Nanoparticles (NPs)

In order to quantify attributes of the images obtained during the thermal sintering *in-situ* the microscope, image analysis was carried out. As the particle morphology

and the particle size distribution were significantly different for the Cu and Ag NPs, different image analysis techniques were employed to extract information as described below.

Image analysis SEM images of Cu NPs was carried out as follows. For the aim of detecting particles, automated edge detection through image analysis gave inaccurate results. The following manual particle highlighting methodology was chosen because it enabled capture of overlapping particles.

SEM images were printed out on paper. An acetate was placed on top of the printout. A thin marker pen was used to highlight edges of particle as well as the scaling bar of the SEM image. The acetates with the highlighted particle edges were then scanned (example in the centre of Figure 49) and analysed using MATLAB as follows. The scanned images were converted to a black-and-white binary image using a global threshold. Continuous objects of fewer than 100 pixels were considered image noise and were removed (example on the right of Figure 49). Particle sizes were obtained using the MATLAB command "regionprops" which measures properties of connected objects in a binary image. The diameter is thereby calculated of a sphere with the same area of the connected objects in the image analysed. The obtained particles diameters were scaled from number of pixels to the equivalent size in nanometres. An example MATLAB script that was written and used can be seen in *Appendix* section 8.2.

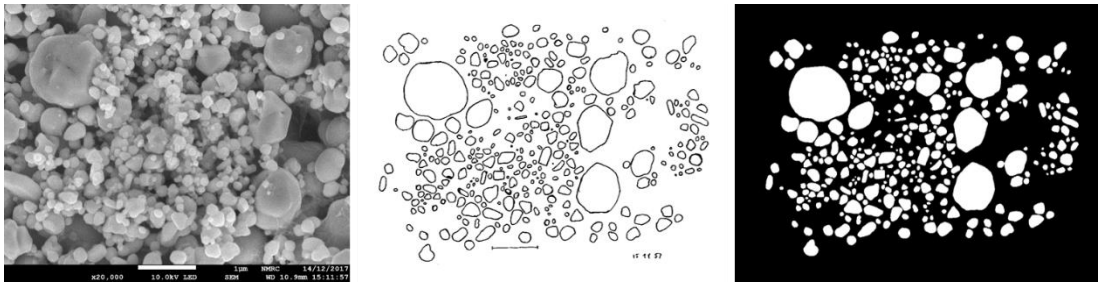


Figure 49. Example of steps involved in particle size distribution quantification from left to right; left: Secondary electron SEM image of Cu particles; centre: scan of the acetate with manually highlighted particles; right: converted to binary for image analysis.

For the image analysis of the Cu particles involved in particle fusion, SEM images of consecutive temperature steps were visually compared to identify the fusing and the fused particle. The edges of those particles were then manually highlighted using the software Image J version 1.52a. Statistical analysis was sub-sequentially performed of the particle dimensions.

Image analysis SEM images of Ag NPs was carried out as follows. Ag NP FEG-SEM images were analysed using MATLAB. All images that were used during the analysis were taken at the same magnification of 35,000x. Images were binarised using a global threshold. Continuous objects of fewer than 75 pixels were considered image noise and were removed. To obtain the number of particles in a frame the MATLAB command “regionprops” which counts the number of continuous objects. The number of particles in the frame prior to any heating (at room temperature) was averaged. Subsequent numbers of particles at increased temperatures were averaged and taken as a fraction of the average number of particles at room temperature.

4.2.5 Laser Diffraction Analysis (LDA) of Copper (Cu) – Silver (Ag) Hybrid Inks

LDA was carried out to quantify the particle size distribution of the NP inks. The ISO 13320:2009 (Particle size analysis – Laser diffraction methods) standard was followed using a Malvern Mastersizer 3000 and its wet cell to carry out laser diffraction particle size analysis (British Standards Institute, 2009).

Pigment concentrate was diluted in propan-2-ol (purchased from Sigma Aldrich) to an obscuration level of approximately 15 %. It was then passed through a beam which alternates between a monochromatic red laser and blue light. The light scattered by particles was measured by multi-element detectors at various angles for a total of 3.5 min for each sample. Using optical models and mathematical procedures, the Mastersizer software then transformed the numerical scattering data to yield the volumetric particle size distribution.

Volumetric particle size distribution determination is based on the Fraunhofer diffraction theory which states that particles scatter light in all directions with an intensity pattern which is dependent on particle size, particle shape and optical properties of the particle (Born and Wolf, 2002).

4.2.6 Differential Scanning Calorimetry (DSC) of Copper (Cu) – Silver (Ag) Hybrid Inks

DSC analysis was carried out to identify the melting point temperature of the Cu and Cu-Ag materials. DSC measurements were carried out on TA Instruments unit (TA Q600). The sample ink was placed into an alumina pan and heated up at a temperature ramp of 10 degree min^{-1} under constant 100 ml min^{-1} nitrogen flow to prevent oxidation.

4.2.7 X-ray Diffraction (XRD) Analysis of Copper (Cu) – Silver (Ag) Hybrid Inks

XRD analysis was carried out to inspect whether oxidation occurred during the various sintering techniques as well as to quantify the increases in mean crystallite size as a consequence of sintering. Samples analysed were $35 \times 35\ mm$ (nominal values) squares. The same methodology as explained in section 3.2.8 *"Investigations into Potential Oxidation of the Copper (Cu) Nanoparticle (NP) Ink due to Laser Irradiation"* was used.

4.2.8 Sheet Resistance Measurements of Sintered Copper (Cu) – Silver (Ag) Hybrid Inks

Sheet resistance measurements were carried out to quantify electrical resistance to analyse the impact of additions of Ag to Cu NPs for the various sintering techniques employed. The same methodology described in section 3.2.11 *"Electrical Sheet Resistance and Resistivity Measurements of Multi-layered Copper (Cu) Microparts"* was used.

4.3 Characterisation of Copper (Cu) – Silver (Ag) Hybrid Inks

The Cu and Cu-Ag NP inks were characterised using XRD to confirm the elemental composition of the materials and using laser diffraction analysis to understand the impact of Ag addition on the particle size distribution. With increasing Ag content, the characteristic Ag peak increases at the expense of the characteristic Cu peak (see Figure 50).

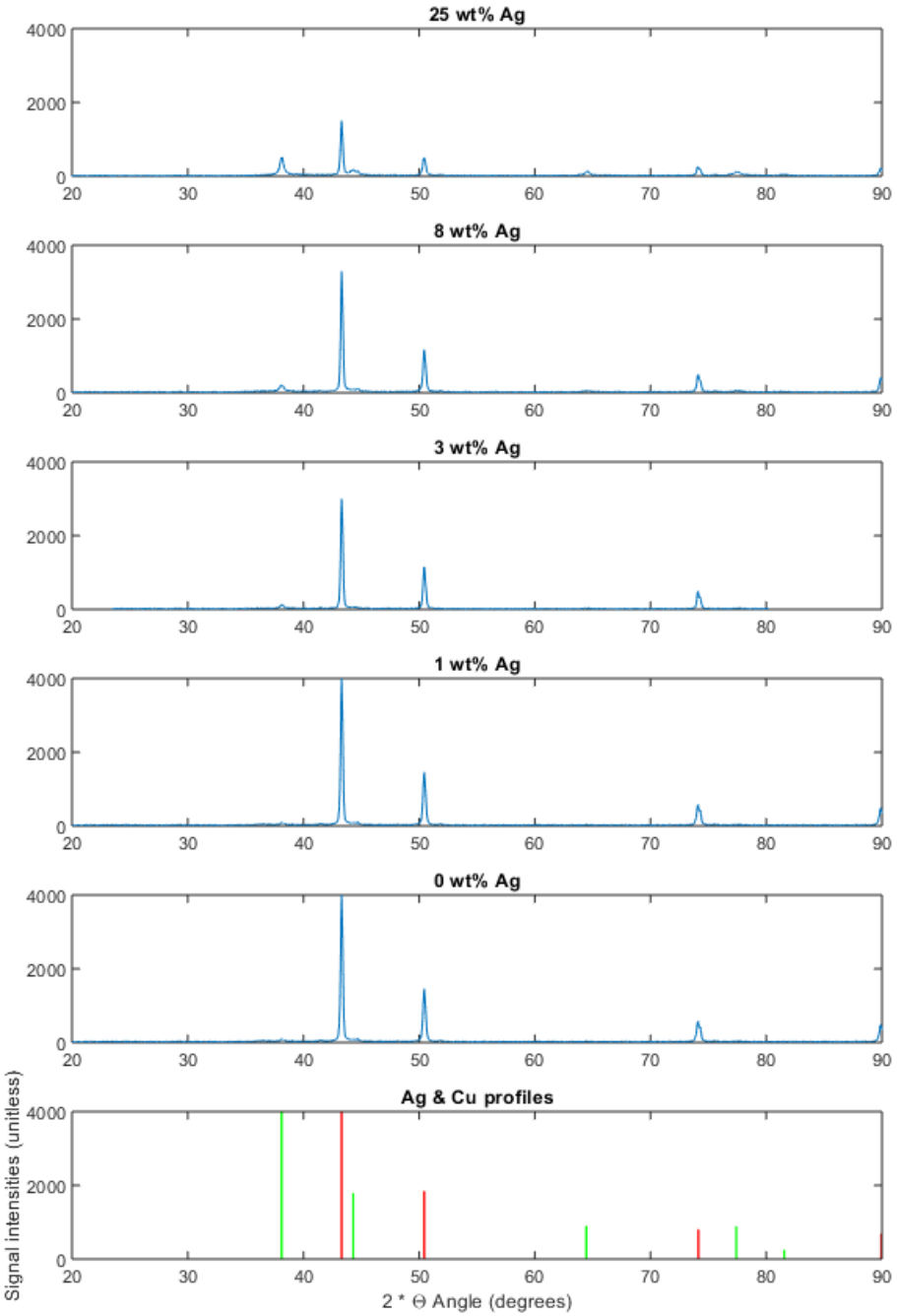


Figure 50. XRD spectra of NP of varying Ag/Cu mass ratios. In the bottom plot characteristic Ag and Cu peaks are indicated in green and red respectively.

The four different pigment concentrates were analysed using LDA. For each graph in Figure 51, the section with the largest absolute gradient which also appears linear, represents the majority of the volumetric particle distribution. With increasing Ag content, the above described section of the graph moves horizontally to the left. Therefore, with increasing Ag content particle diameter decreases.

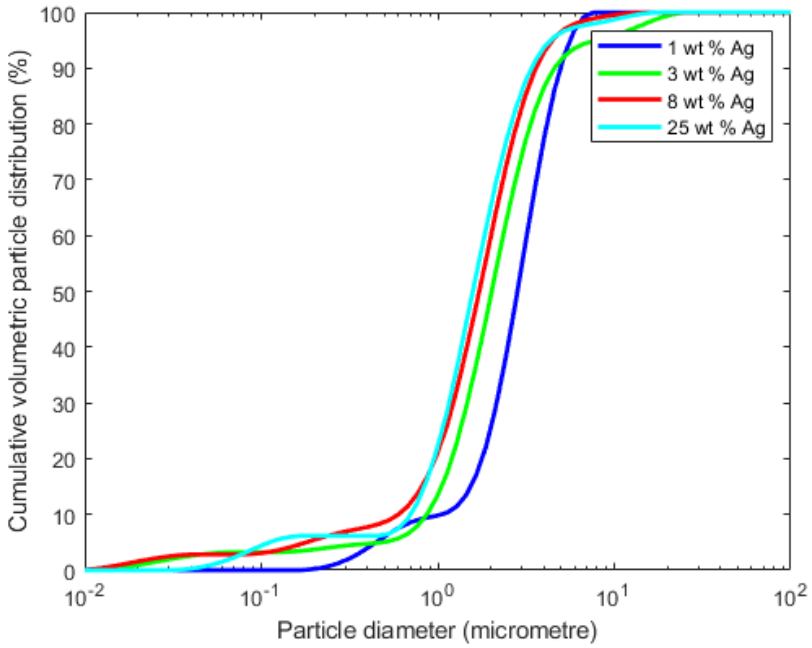


Figure 51. LDA analysis of Cu inks with varying Ag content.

4.4 Laser Sintering of Copper (Cu) – Silver (Ag) Hybrid Inks

Laser sintering of the Cu and Cu-Ag NPs was carried out. It was previously established in section 3.2.8 *"Investigations into Potential Oxidation of the Copper (Cu) Nanoparticle (NP) Ink due to Laser Irradiation using X-ray Diffraction (XRD)"* that no Cu oxidation occurred during laser sintering. The laser sintered samples were electrically characterised to understand the impact of Ag addition on sheet resistance.

Increasing Ag wt% loading between 0 and 8 % does not significantly impact sheet resistance. At 25 wt% Ag concentration the sheet resistance slightly increases.

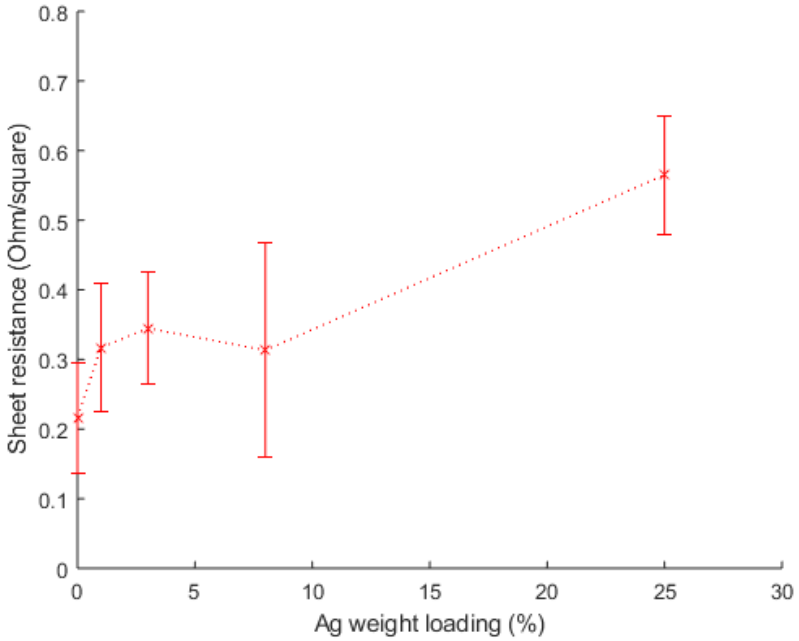


Figure 52. Sheet resistance of laser sintered Cu NPs containing varying Ag concentrations. Error bars indicate standard deviation.

4.5 Intense Pulsed Light (IPL) Sintering of Copper (Cu) – Silver (Ag) Hybrid Inks

IPL sintering of the Cu and Cu-Ag NPs was carried out. XRD analysis before and after IPL sintering was carried out to identify whether Cu oxidation occurred. The IPL sintered samples were electrically characterised to understand the impact of Ag addition on sheet resistance.

As previously with laser sintering (see Figure 28), with IPL sintering no copper oxide peak is evident in the laser sintered XRD spectrum (Figure 91 in *Appendix* section 8.3.1). It was therefore concluded that no copper oxidation occurred during IPL sintering. With IPL sintering there was no clear trend between Ag weight loading and sheet resistance, similar to laser sintering (Figure 52). Compared to laser sintering, the IPL sintered materials all achieved lower sheet resistance values.

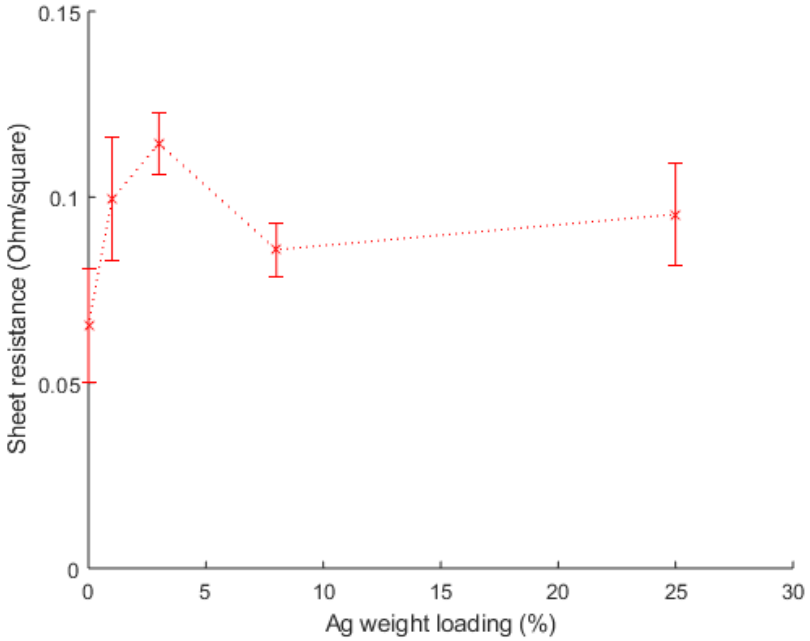


Figure 53. Sheet resistance of IPL sintered Cu NPs containing varying Ag concentrations. Error bars indicate standard deviations

4.6 Thermal Sintering of Copper (Cu) – Silver (Ag) hybrid inks

Thermal sintering of the Cu and Cu-Ag NPs in an oxygen-containing environment and in an oxygen-free environment were carried out.

4.6.1 Air (Oxygen-containing) Environment

In order to investigate thermal sintering in an air environment, XRD scans were taken before and after the sintering of the materials. Electrical characterisation was obtained at regular temperature intervals during the thermal sintering through sheet resistance measurements. XRD scans (in *Appendix* section 8.3.3) showed that the initial Cu content of the materials with Ag content of 0, 1, 3, and 8 wt% were completely oxidised after the thermal treatment in an air environment. Solely the material with 25 wt% Ag shows a significant characteristic Cu peak after the thermal treatment (see Figure 96 in *Appendix*). Through the Scherrer equation (see Equation 3) it was calculated that thermal sintering of the 25 wt% Ag in Cu material resulted in on average a 117 % increase in mean Ag crystallite size (see Figure 54).

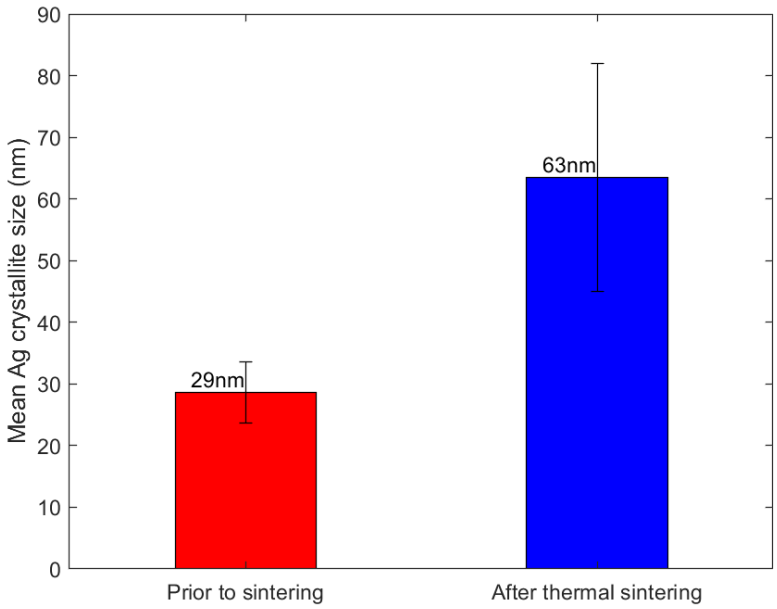


Figure 54. Mean Ag crystallite size before and after thermal sintering. The data can be found in *Appendix* section 8.3 Table 10.

Across all of the materials thermally sintered in air, the mean Cu_2O crystallite size after thermal sintering was found to be on average 15 nm which is around 4.7 % of the mean Cu crystallite size before thermal sintering (see Figure 55). The mean CuO crystallite size after thermal sintering was found to be 19 nm which is around 6.0 % of the mean Cu crystallite size before thermal sintering.

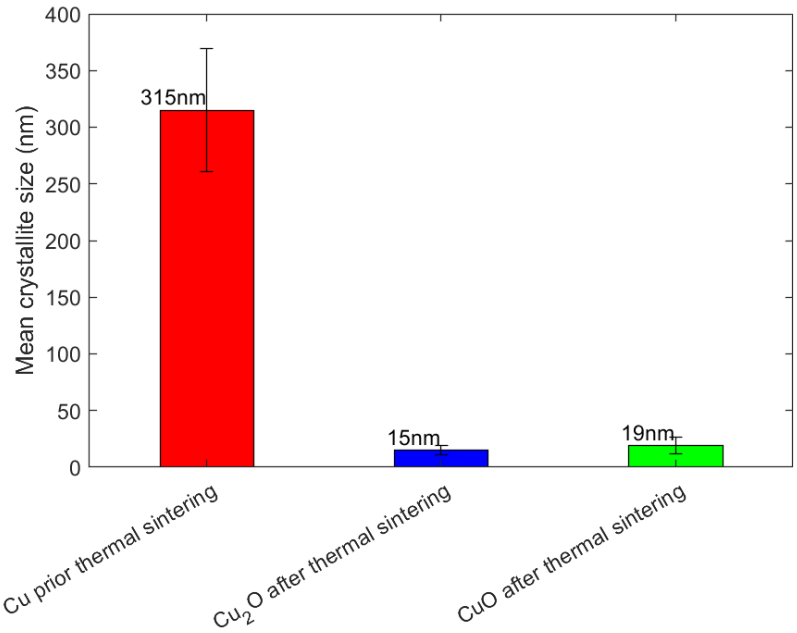


Figure 55. Mean crystallite size before thermal sintering of Cu NP and mean crystallite sizes after thermal sintering of Cu2O and CuO. The data can be found in *Appendix* section 8.3 Table 11.

During the temperature increase, there are three events that can theoretically occur.

In the previous DSC measurement of the Cu particles (see Figure 24 in section 3.3.1.1 *"Particle Size and Sintering Temperature")* it was found that Cu particle sintering starts at 155 °C. Visual observation of the material containing 0 wt% Ag and 100 % (of the metal content) Cu showed that a distinctive colour change from dark red (usual Cu colour) to dark blue-gray (common colour of copper oxide) occurred during the thermal treatment (in an air environment) at around approximately 90 °C – at a significantly lower temperature than 155 °C. Thermal sintering in air of Cu NPs containing 0 and 1 wt% Ag did not show any measurable electrical conductivity, therefore those materials are not represented by graphs in Figure 56. This appears to be logical because Cu NPs oxidisation occurs at a lower temperature than the Cu NP sintering as explained previously.

However, the Cu NPs containing 3, 8, and 25 wt% Ag showed measurable electrical conductivity (see Figure 56). Two hypothesis or a combination of both are conceivable an explanation for what caused the measured electrical conductivity.

Firstly, the Cu content entirely oxidised and the Ag migrated to form a connected grid to conduct electricity. Secondly, in some areas the Ag content acted as a protective barrier between the Cu and the air and thereby prevented Cu oxidation in some areas, enabling the sintering of Cu particles which in turn enabled electrical conductivity.

The crucial aspect here is at which temperature does the Ag become mobile. In the results the later section 4.6.2.2 *"Electron Microscopy Analysis of Copper (Cu) and Silver (Ag) Nanoparticle Sintering in-situ the Microscope"* it is shown that Ag NPs showed the highest change in NPs neck formation between 170 and 200 °C. This neck formation is the consequence of enabled mass transport of the Ag. In the *Literature Review* section 2.3.4 *"Cu-Ag synergies"* it was stated that in the literature on Cu-Ag core-shell particles the Ag shell is able to protect the Cu core from oxidation up to a temperature depending on the publication between 100 °C (Chen et al., 2013) and 400 °C (Njagi et al., 2017; Tsai et al., 2013) with the great majority between 150 and 250 °C (Chee and Lee, 2014, 2017; Kim et al., 2014; J. Li et al., 2017; W. Li et al., 2017; Pajor-Świerzy et al., 2017a, 2017b; Park et al., 2015; Y. S. Park et al., 2016; Tian et al., 2016; Yim et al., 2016; Zhang et al., 2010); at this point the Ag shell starts to dewet the Cu core and the Ag accumulates on the surface, thereby leaving the Cu surface exposed to potential oxidation. The results from the later section 4.6.2.2 therefore fall within the same temperature range of the great majority of the of the literature findings. The electrical resistance of the Cu NP materials with 3, 8 and 25 wt% Ag content below 185 °C was too high to be measured. At 185 °C and at higher temperatures the materials showed measurable electrical conductivity. The fact that the temperature at which the materials became electrically conductive falls within the temperature range at which the Ag was found to be most mobile (170 to 200 °C) is an indication that the Ag mobility was responsible for enabling electrical conductivity and that thus the first hypothesis is true.

For the second hypothesis to be true, Ag must have protected Cu from oxidising from the onset of Cu oxidation at 80 °C up to the sintering temperature of the Cu NPs. As mentioned, the great majority of the literature on thermal sintering of Cu-Ag core-

shell particles agrees that the Ag shell is able to protect the Cu from oxidation only up to a temperature at which the Ag becomes mobile and dewets the Cu surface – leaving it exposed for Cu oxidation to occur. The results from the later section 4.6.2.2 show a maximum mobility of the Ag between 170 and 200 °C. It is unlikely that from Ag protected Cu NPs sintered prior to the Ag becoming highly mobile (170 to 200 °C) because no electrical conductivity was measurable below 185 °C.

All in all it can be said that the first hypothesis is more likely to have cause electrical conductivity than the second hypothesis. Based on these findings it can be concluded that from a threshold level of as low as 3 wt% Ag there is sufficient Ag present to form a connected network of Ag which conducts electricity.

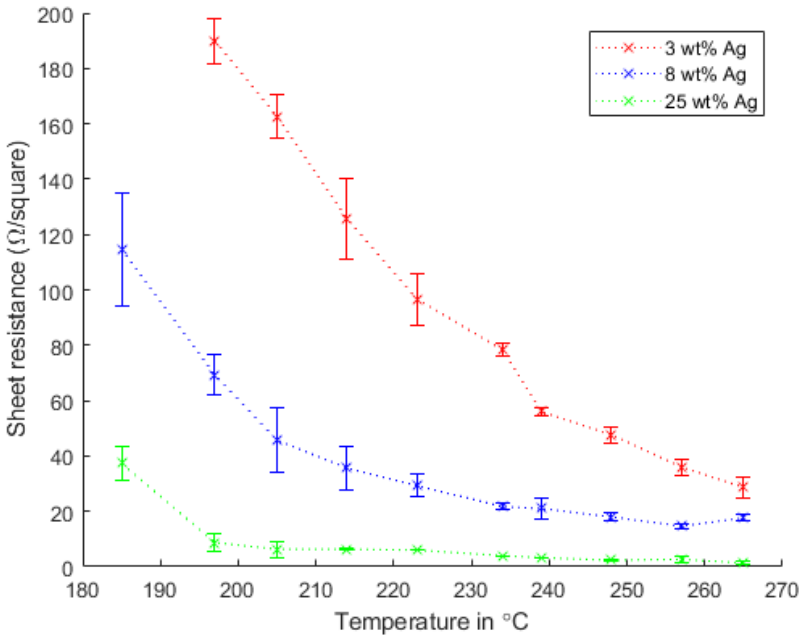


Figure 56. Sheet resistance against temperature during thermal sintering of Cu NPs containing varying Ag concentrations. Error bars indicate standard deviations.

4.6.2 Oxygen-free Environment

Cu and/or Ag oxidation impacts the mass transport phenomena involved in particle sintering as it chemically change the composition of the material. The absence of oxygen allows analysis of the elemental metal NP sintering process without Cu or Ag oxidation occurring. Thermal sintering of the Cu and Cu-Ag materials in an oxygen-

free environment was analysed using DSC scans to detect bulk melting points, the thermal sintering was monitored *in-situ* an SEM and the acquired images were quantified using image analysis. SEM and EDX of thermally sintered 25 wt% Ag in Cu in an oxygen-free environment were carried out and theoretical simulations of the implications of the results were carried out.

4.6.2.1 Bulk Melting Point Analysis of Copper (Cu) – Silver (Ag) Hybrid Inks in an Oxygen-free Environment

DSC measurements were carried out on each of the Ag-Cu NP inks. All DSC curves can be found in the *Appendix* section 8.6. For each curve, the bulk melting point temperature was obtained from the peak of the endothermic peak associated with melting. From Figure 57 it can be seen that with increasing Ag wt% the melting point decreases.

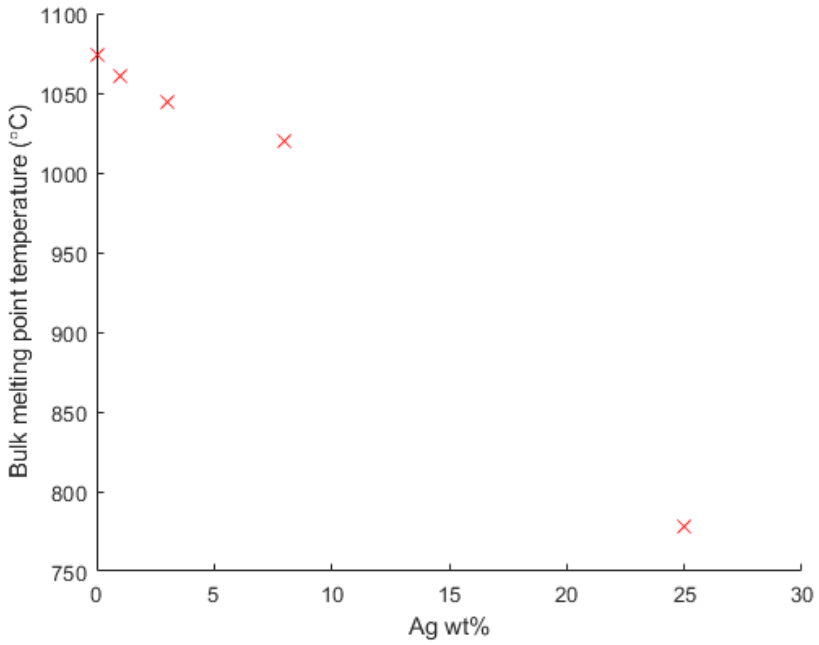


Figure 57. Bulk melting point temperature of Cu NPs containing varying Ag concentrations.

4.6.2.2 Electron Microscopy Analysis of Copper (Cu) and Silver (Ag) Nanoparticle Sintering in-situ the Microscope

Cu NPs were heated up under vacuum *in-situ* a FEG-SEM using a host stage (as explained in *Materials and Methodology* section 4.2.3). Secondary electron images were taken of the same sample location at regular temperature intervals to monitor NP sintering. Examples of a Cu NP cluster as well as a NP bed can be seen in Figure 58 and Figure 59, respectively.

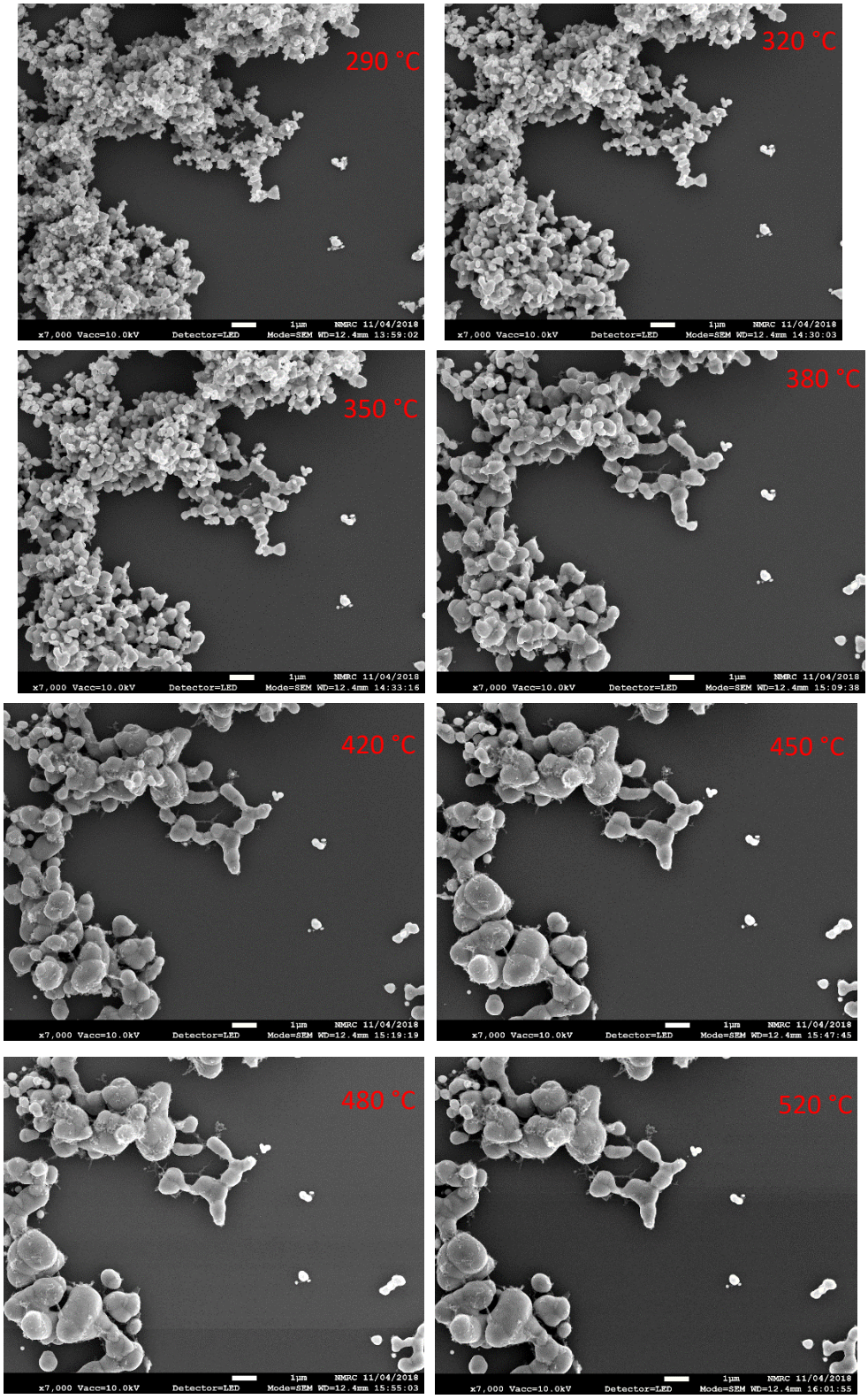


Figure 58. Secondary electron SEM images of Cu NPs acquired at the same location at various temperatures indicated by the red labels.

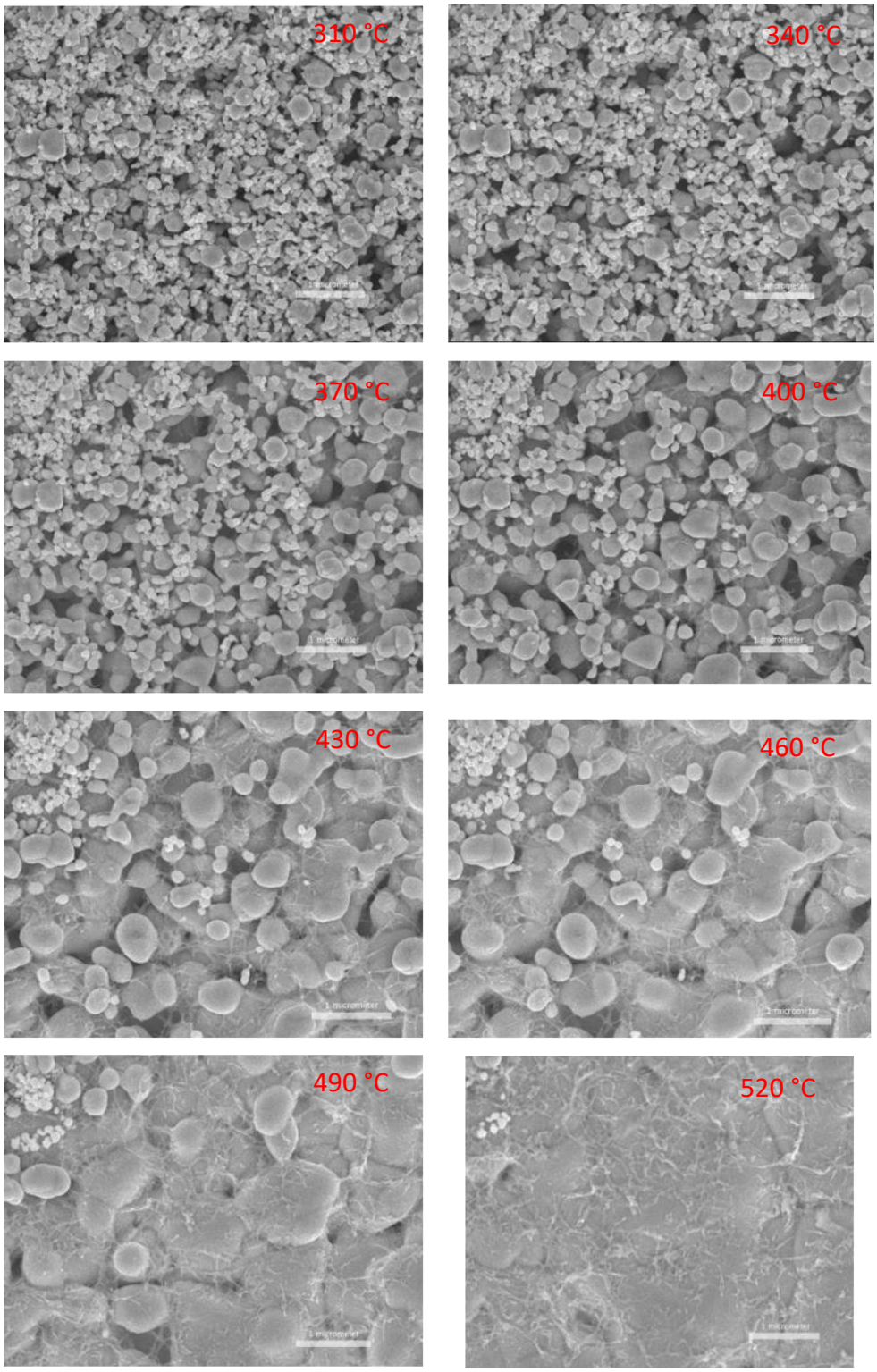


Figure 59. Secondary electron SEM images of a Cu NP bedacquired at the same location at various temperatures indicated by the red labels.

The average particle diameters were obtained at regular temperature intervals through image analysis (see *Materials and Methodology*section 4.2.4 "*Image*

Analysis of FEG-SEM Images of Nanoparticles (NPs)"). Figure 60 shows with increasing temperature between 400 and 490 °C two parameters increase due to particle sintering, firstly the average particle diameter and secondly the standard deviation of the particle size distribution.

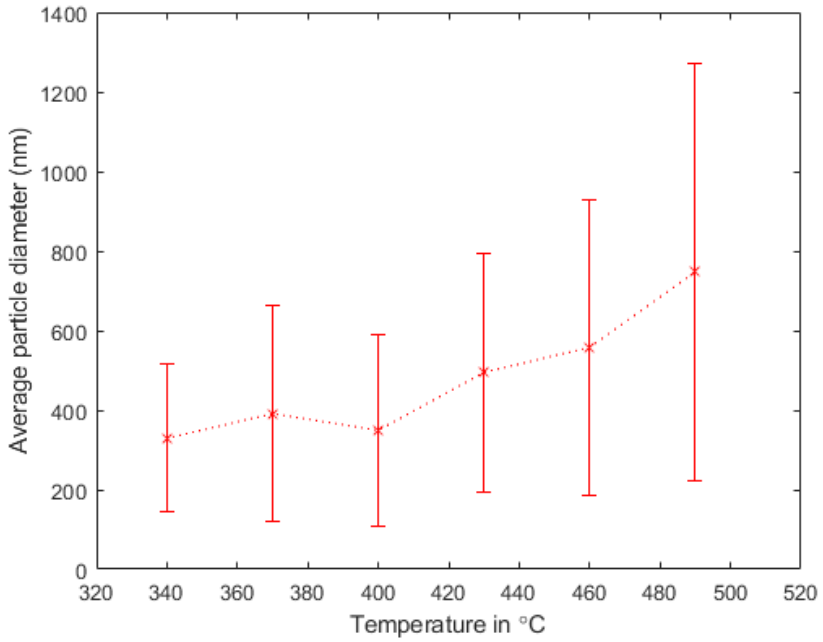


Figure 60. Average Cu particle diameter with increasing temperature. Error bars indicate standard deviation of the particle size distribution.

Inter-particle diffusion leads to coarsening of particles when NPs are in contact during sintering (Fang and Wang, 2010). Large particles will grow at the expense of small particles. The particles involved in this particle fusion were distinguished; a smaller particle fusing into a larger particle is described as a *fusing* particle and the larger particle counterpart which receives the smaller particle is described as a *fused* particle. Above 350 °C particle sizes of *fused* particles were unobtainable because from the 2D SEM images it was impossible to reliably determine whether a *fused* particle was a distinct and separate particle or whether it had sintered with its neighbouring matter.

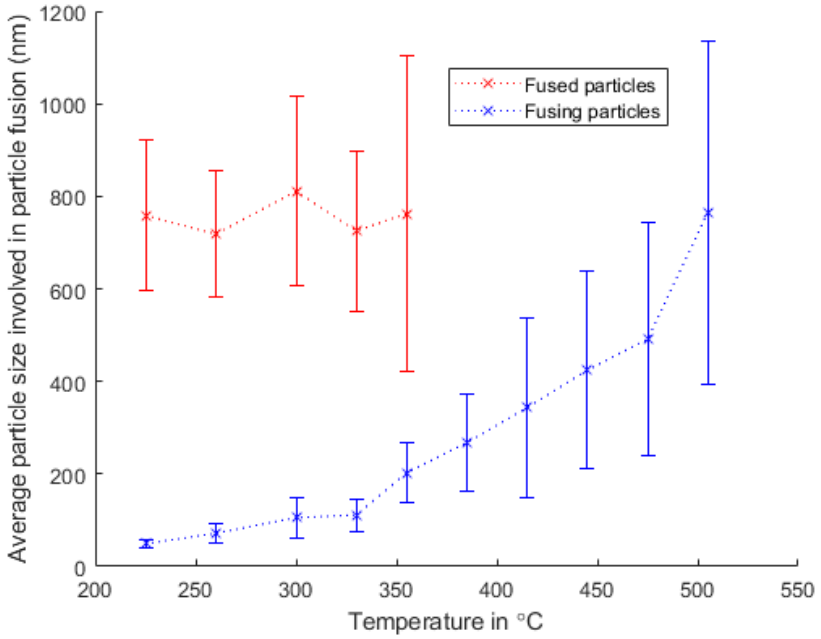


Figure 61. Average Cu particle size involved in the particle fusion with increasing temperature. Error bars indicate standard deviation of the particle size distributions.

With increasing temperature, the average particle size of *fusing* particles does not change significantly. The average *fusing* particle size as well as the standard deviation of the size distribution of *fusing* particles both increase with increasing temperature. The latter finding is coherent with the thermodynamics of particle sintering. The driving force for mass transport during sintering increases with decreasing particle size (Fang and Wang, 2010). This is because the driving force of sintering is affected by specific surface energy which increases with decreasing particle size (Campbell et al., 2002; Nanda et al., 2003). Consequentially, to induce particle fusion of larger particles a higher temperature is required to supply sufficient driving force for mass transport which is reflected in the "*Fusing* particle" graph in Figure 61.

In 1950 Herring first introduced the scaling law, which relates the sintering phenomenon to the size of the particles involved in it (Herring, 1950). The scaling law was denoted by Herring as:

$$\Delta t_2 = \lambda^n \Delta t_1 \qquad \text{Equation 19}$$

where $\lambda = \frac{R_2}{R_1}$, R_1 and R_2 are particle radii and n depends on the specific mass transport mechanism of the sintering phenomenon as follows: $n = 1$ for viscous flow, $n = 2$ for evaporation and condensation, $n = 3$ for volume diffusion, and $n = 4$ for grain boundary diffusion or surface diffusion. The scaling law can be rearranged as follows:

$$n = \frac{\log\frac{\Delta t_2}{\Delta t_1}}{\log\frac{R_2}{R_1}} \qquad \text{Equation 20}$$

In Figure 62 the exponent n from Equation 19 was calculated using Equation 20 for each temperature interval and its corresponding SEM image from Figure 59.

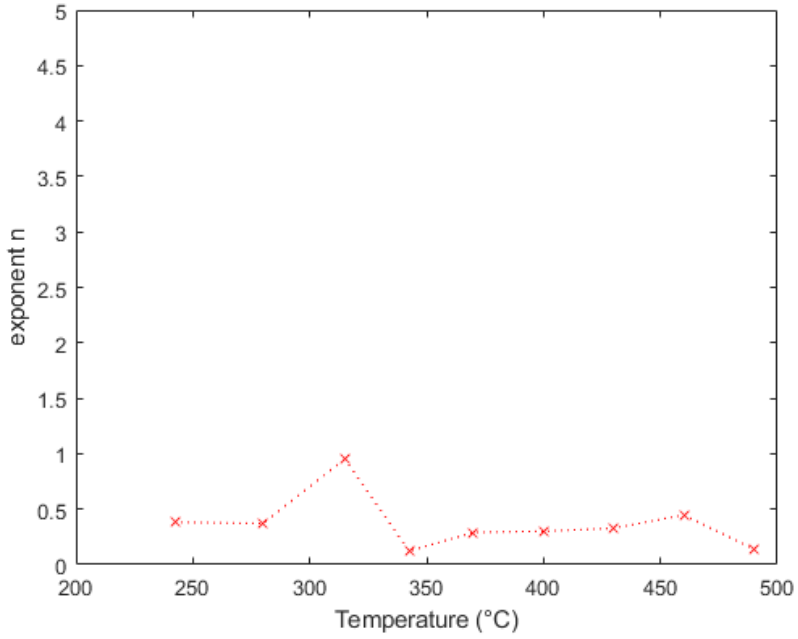


Figure 62. The sintering phenomenon characterising exponent n with increasing temperature.

The calculated exponents n from Equation 19 across the temperature range in Figure 62 are on average 0.5 and do not rise above 1 so it can be concluded that the mass transport mechanism of the sintering of the Cu particles is viscous flow according to Herring.

Just as for Cu NPs, secondary electron images were also taken of Ag NPs of the same sample location at regular temperature intervals during *in-situ* heat treatment under vacuum inside a FEG-SEM. Compared to the Cu NPs (Figure 59) the particle sintering of the Ag NP (see Figure 63) is noticeably different – it takes places at lower temperatures and the dominant sintering mass transport phenomenon appears to be different. Rather particle fusion during which entire smaller particles fuse into adjacent larger particles (Cu NPs), Ag NPs appear to predominantly form necks.

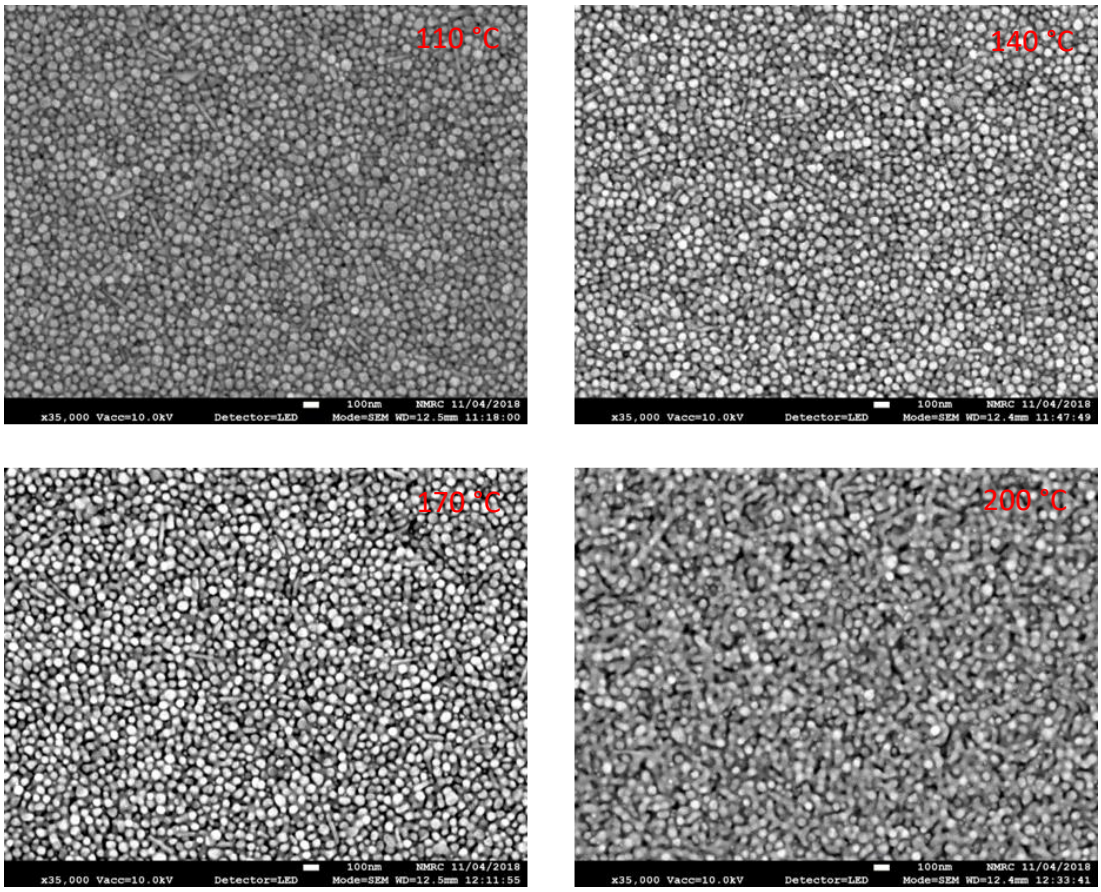


Figure 63. Secondary electron SEM image of Ag NPs taken at various temperatures indicated by the red labels.

Images such as the ones in Figure 63 were analysed using image analysis (see *Materials and Methodology*section 4.2.4 *"Image Analysis of FEG-SEM Images of Nanoparticles (NPs)"*). The fraction of sintered Ag NPs of the total number of initially unsintered Ag NPs was quantified and plotted in Figure 64. There is a rapid increase in the amount of particles sintered between 100 and 200 °C with the highest rate of change between 170 and 200 °C (see Figure 65).

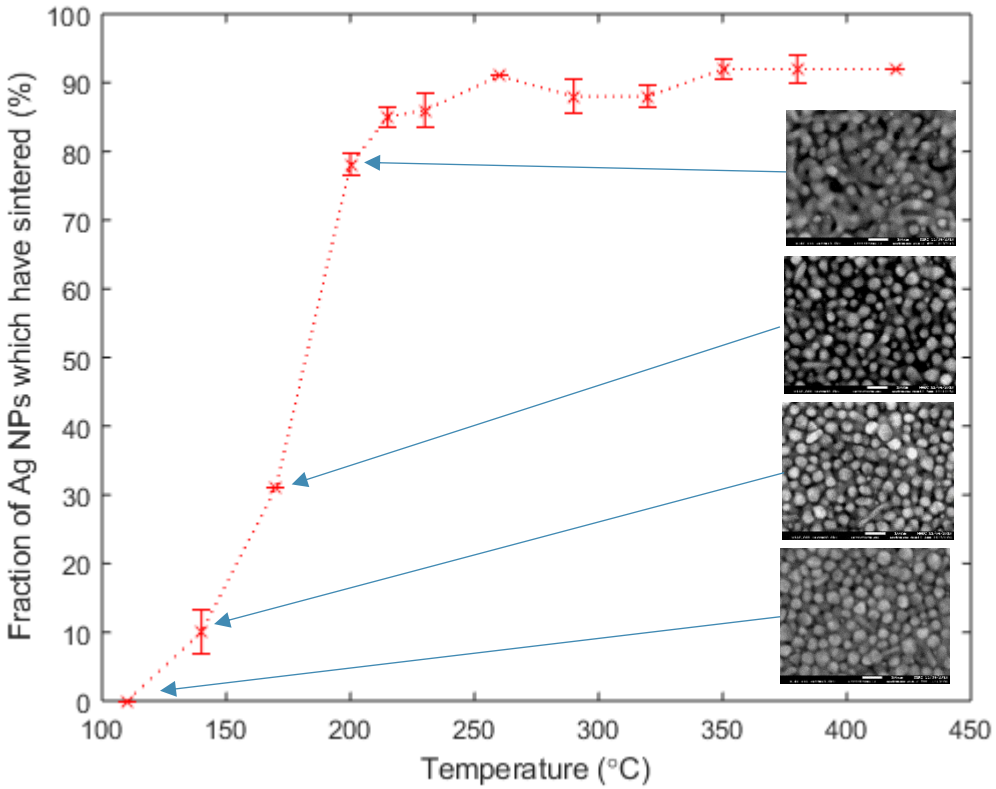


Figure 64. Plot of the fraction of Ag NPs on the sample surface which have sintered against temperature. Exemplary images are included with arrow indications to the correspond data points. Error bars indicate standard deviation.

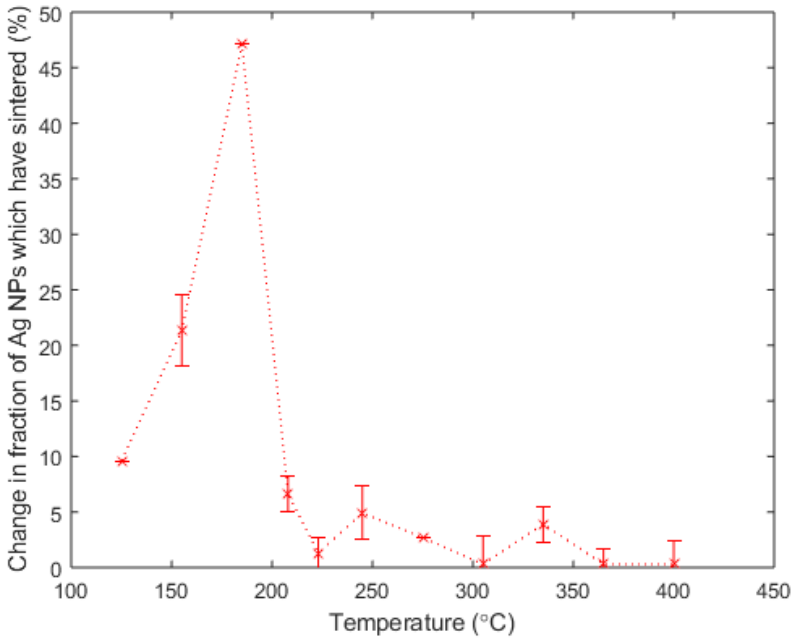


Figure 65. Change in fraction of Ag NPs which have sintered with increasing temperature. Error bars indicate standard deviation.

4.6.2.3 Electron Microscopy (EM) and Energy-dispersive X-ray (EDX) Spectroscopy Analysis of Thermally Sintered Cu-Ag NPs

Backscatter electron images of the NPs with the highest Ag content (25 wt%) after they were thermally sintered *in-situ* the EM were obtained using a FEG-SEM. Additionally EDX spectra were acquired and overlaid with the backscatter electron images.

SEM images obtained using the backscatter detector are informed by high-energy electrons which are reflected or back-scattered out of the specimen interaction volume by elastic scattering interactions with specimen atom. Heavy elements backscatter electrons stronger than light elements. Therefore, heavy elements appear lighter and light elements darker in backscatter electron images. Ag is a heavier element than Cu (atomic numbers of 47 and 29, respectively). In the following examples (see Figure 66 and Figure 67) regions of the particles are lighter and darker in brightness. Hence it can be assumed lighter and darker regions are predominantly Ag and Cu, respectively. To investigate this hypothesis EDX map spectra were obtained and overlaid with the backscatter electron images (see Figure 66 and Figure 67). EDX point spectra were also obtained (location of the point spectra are highlighted in Figure 66 and Figure 67) and the Cu/Ag wt ratio of those point spectra was quantified (see Table 1 and Table 2). The EDX scans confirm that the lighter regions of the particles are indeed regions of high Ag concentration and the darker regions are regions of high Cu concentration. From the backscatter electron images and the corresponding EDX scans, particularly in Figure 67, it is possible to see that a great fraction of Ag is located in the necking regions of Cu particles. This observation was the basis for the calculations in the following sub-chapter *Theoretical Simulation of the Neck Formation of Silver (Ag) and Copper (Cu) Nanoparticle (NP) Sintering*.

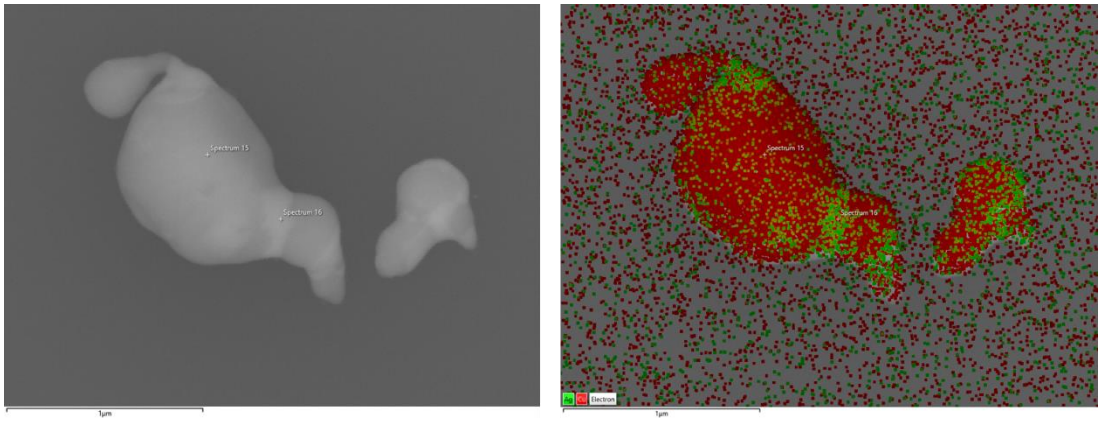


Figure 66. Backscatter electron SEM images: on the left containing Cu and Ag with indications of where EDX point spectra were taken and on the right the SEM image is overlaid with an EDX scan where red represents Cu and green represents Ag.

	Spectrum 15	Spectrum 16
Cu/Ag wt ratio	10.5	0.8

Table 1. Cu/Ag wt ratio of point spectra indicated in Figure 66.

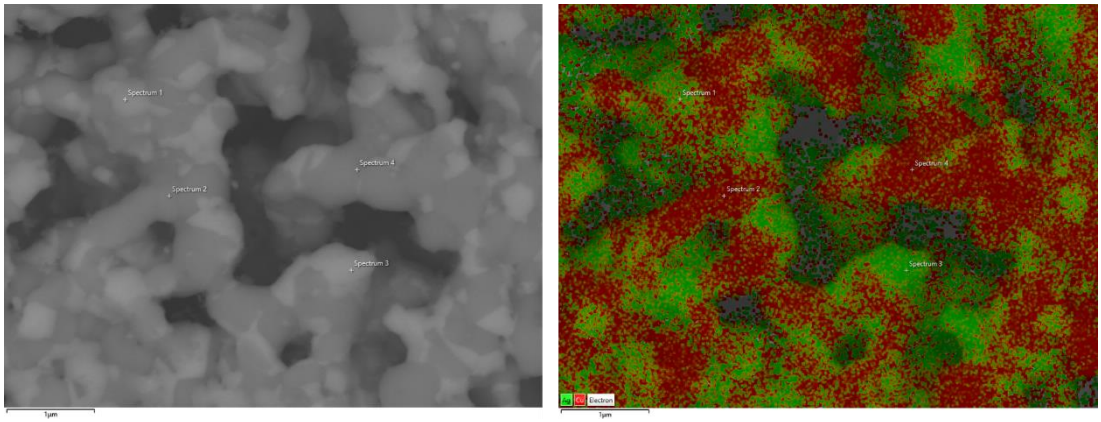


Figure 67. Backscatter electron SEM images: on the left containing Cu and Ag with indications of where EDX point spectra were taken and on the right the SEM image is overlaid with an EDX scan where red represents Cu and green represents Ag.

	Spectrum 1	Spectrum 2	Spectrum 3	Spectrum 4
Cu/Ag wt ratio	0.3	6.6	0.1	6.4

Table 2. Cu/Ag wt ratio of point spectra indicated in Figure 67.

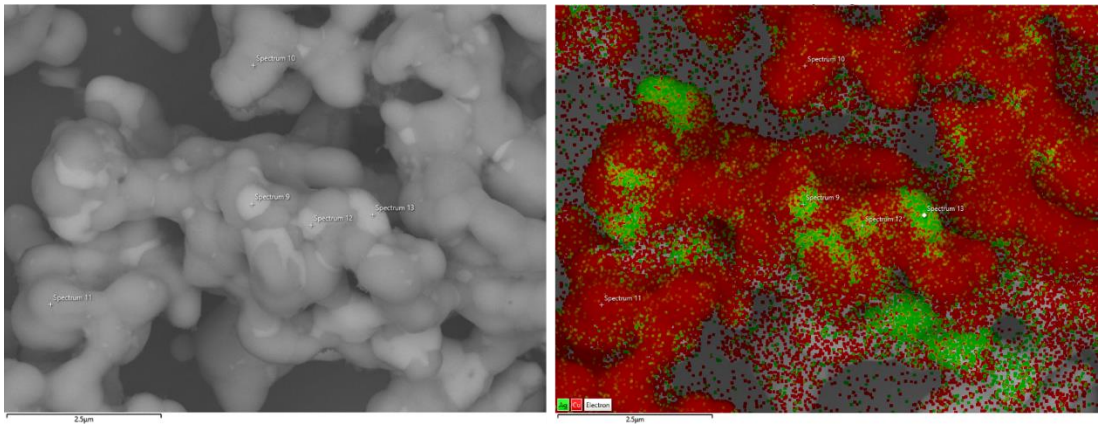


Figure 68. Backscatter electron SEM images: on the left containing Cu and Ag with indications of where EDX point spectra were taken and on the right the SEM image is overlaid with an EDX scan where red represents Cu and green represents Ag.

	Spectrum 9	Spectrum 10	Spectrum 11	Spectrum 12	Spectrum 13
Cu/Ag wt ratio	0.3	49.4	33.6	0.3	0.1

Table 3. Cu/Ag wt ratio of point spectra indicated in Figure 68Figure 73.

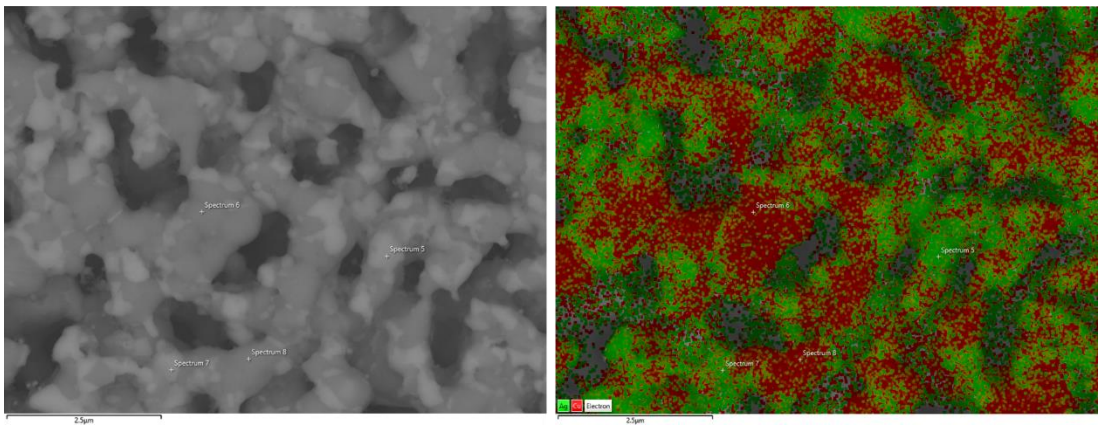


Figure 69. Backscatter electron SEM images: on the left containing Cu and Ag with indications of where EDX point spectra were taken and on the right the SEM image is overlaid with an EDX scan where red represents Cu and green represents Ag.

	Spectrum 5	Spectrum 6	Spectrum 7	Spectrum 8
Cu/Ag wt ratio	0.1	14.6	0.2	12.5

Table 4. Cu/Ag wt ratio of point spectra indicated in Figure 69.

4.6.3 Theoretical Simulation of the Neck Formation of Silver (Ag) and Copper (Cu) Nanoparticle (NP) Sintering

When the adjacent particle contact area increases in size, this contact region is described as a neck, which is illustrated in Figure 70 (German, 2010).

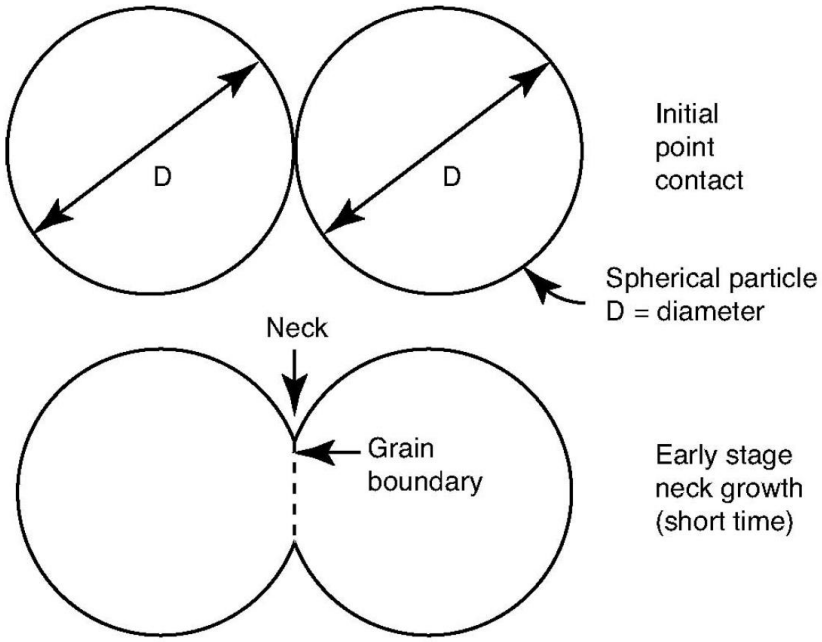


Figure 70. Labelled diagram illustrating a particle neck (adapted from German, 2010).

In the previous section 4.6.2.3 "*Electron Microscopy (EM) and Energy-dispersive X-ray (EDX) Spectroscopy Analysis of Thermally Sintered Cu-Ag NPs"* for the Cu-Ag NPs with 25 wt% Ag content it was found that as a result of heat treatment of the Ag predominantly accumulates in the necking regions of Cu particles. In the previous section 4.6.2.2 *"Electron Microscopy Analysis of Copper (Cu) and Silver (Ag) Nanoparticle Sintering in-situ the Microscope"* it was shown that Ag generally becomes mobile and sinters at a lower temperature than Cu. Those two findings combined led to a theoretical investigation into the impact of Ag accumulation in the necking region of Cu particles on the inter-particle electrical resistance (see Figure 71 for a sketch).

This simulation does not accurately reflect the Cu-Ag particle matrix from the previous section 4.6.2.3. The main reason for this is that while a significantly proportion of the Ag content but not all of it appears to have accumulated in the

necking region of Cu particle. The aim of this simulation is to computationally model the impact of the observed phenomenon. It is hoped the results will facilitate the design operating conditions such as the Ag/Cu ratio if this phenomenon is to be exploited to reduce electrical resistance of a Cu particle network through Ag accumulation in the Cu neck. Thereby theoretically small amounts (< 1 %) of Ag can significantly reduce the electrical resistance of a particle network which is mainly made up Cu – a much cheaper material than Ag.

The calculations are based on the following assumptions:

- Cu particles are perfectly spherical
- The outside shape of the silver neck is cylindrical
- Cu and Ag electrical resistivities are $1.68 \times 10^{-8}\ \Omega\ m$ and $1.59 \times 10^{-8}\ \Omega\ m$, respectively (Matula, 1979)

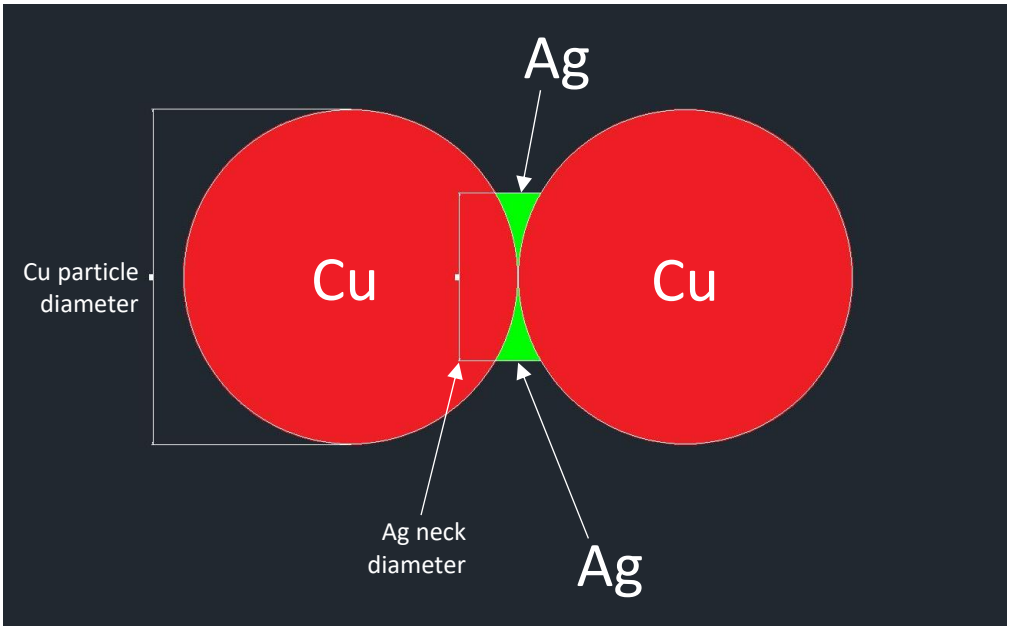


Figure 71. Sketch of Ag accumulation in the necking region of two adjacent Cu particles of equal diameter.

Various sintering states of two neighbouring Cu particles were considered – from the two Cu particles just about touching each other to a Cu neck formation of up to one tenth of the Cu particle diameter. As the Cu particle distribution was found to be wide (see Figure 25), the case of neighbouring Cu particle with varying diameter ratios was

also considered. The following theoretical calculations were carried out for a minimum of no maximum accumulation of Ag in the neck and up to 1/2 of the Cu particle diameter.

Electrical resistance is defined as

$$R = \rho \frac{l}{A} \qquad \text{Equation 21}$$

where R is electrical resistance (Ω), ρ is electrical resistivity (Ω m), l is the length of the object (m), and A is the cross-sectional area of the object (m^2). In this case (see Figure 72) the object of interest does not have a constant cross-sectional area (A) across the length of the object (l), *i.e.* the cross-sectional area is a function of the position along the object (x).

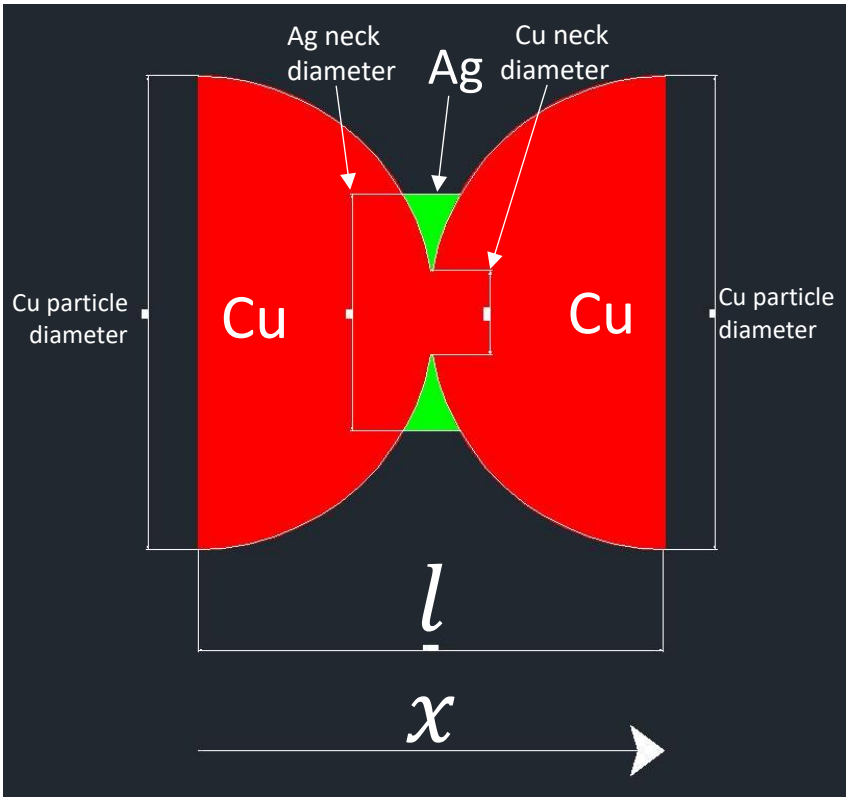


Figure 72. Sketch of Ag accumulation in the necking region of two adjacent sintered Cu particles of equal diameter. "x" indicates the one-dimensional spatial position along the sintered object.

In order to obtain an accurate representation of the dimensional term $\frac{l}{A}$ from Equation 21, an integral is taken of the function describing the cross-sectional area ($A(x)$) over the length (l) of the object. The following equation was used to calculate the inter-particle resistance

$$R = \rho \int_0^l \frac{1}{A(x)} dx \qquad \text{Equation 22}$$

(Meaden, 2013; Rodríguez-Valverde and Tirado-Miranda, 2009), where $A(x)$ describes the cross-sectional area as a function of the one-dimensional position along the object (see Figure 72).

The following three different independent variables were investigated: Ag/Cu mass ratio, Cu-Cu neck size prior to Ag addition, Cu/Cu adjacent particle size ratio. The MATLAB scripts that were developed and used can be found in the *Appendix* section 8.8.

4.6.3.1 Adjacent Copper (Cu) Particles of Equal Size

The particle and necking arrangement simulated in this section is shown in Figure 73. Two adjacent Cu particles of equal diameter have formed a neck of between one tenth to one third of the Cu particle diameter. Ag fills up the neck up to half the diameter of the Cu particle. The inter-particle resistance reduction between the two adjacent Cu particles due to the Ag accumulation in the necking region is shown in Figure 74.

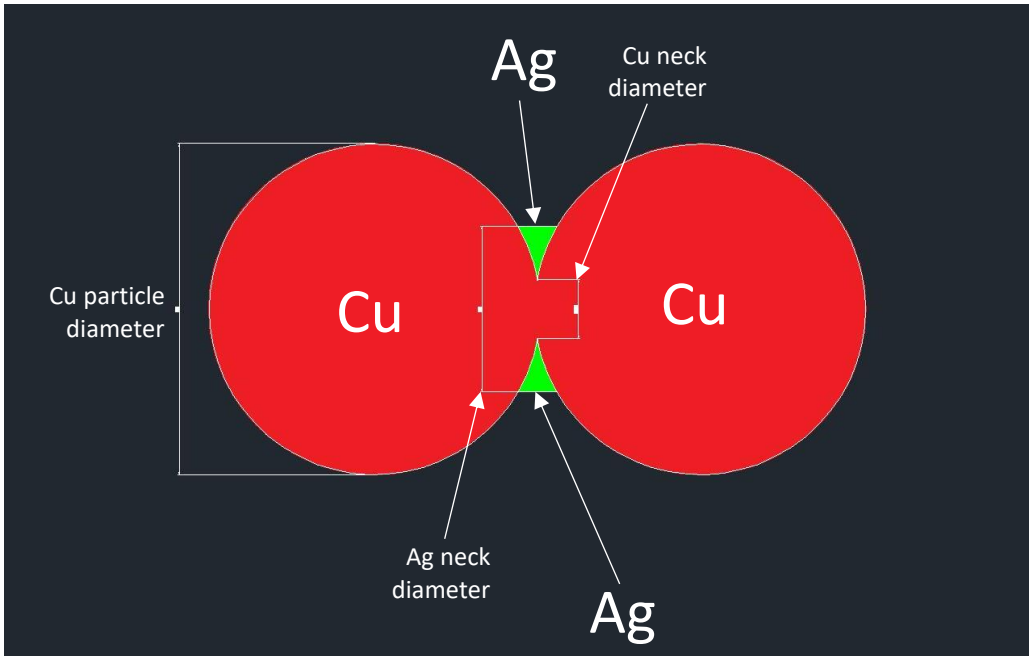


Figure 73. Sketch of Ag accumulation in the necking region of two adjacent Cu particles of equal diameter.

Generally speaking, adding Ag to the neck of two adjacent Cu particles reduces inter-particle resistance. From Figure 74 it can be seen that with increasing neck formation between the two adjacent Cu particles, the addition of Ag (up to the same Ag/Cu mass ratio of 0.4×10^{-3} for instance) causes less of a reduction of the inter-particle resistance. The trends shown in Figure 74 are independent of varying particle size as long as the particle sizes of the two adjacent Cu particles are equal.

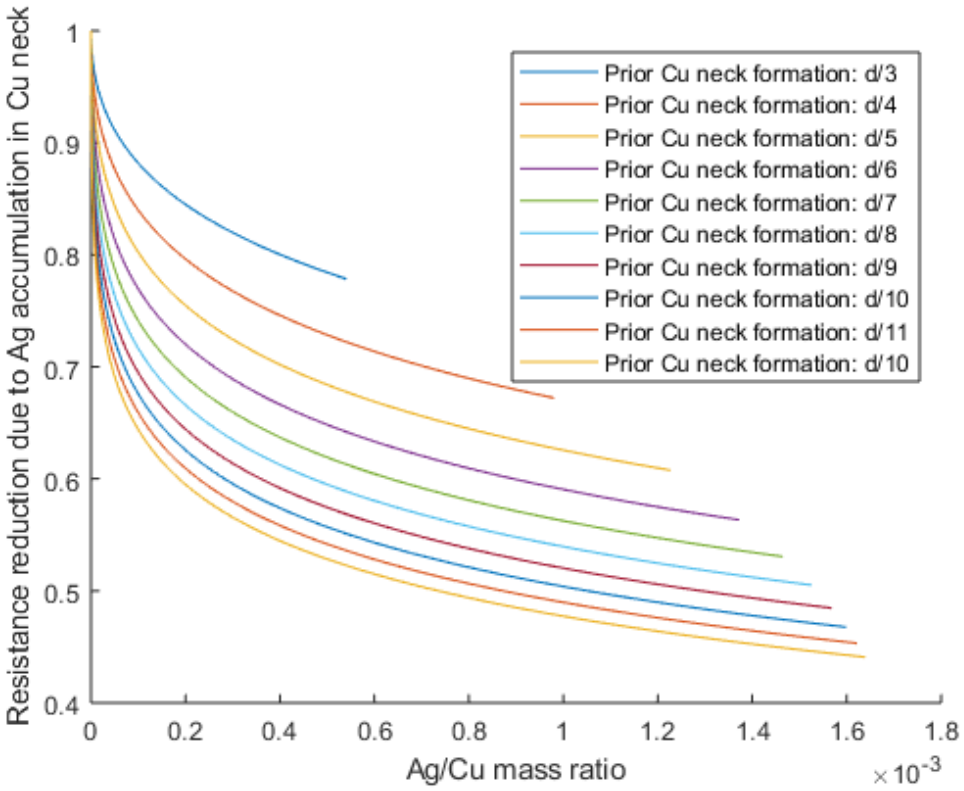


Figure 74. Theoretical resistance reduction between two Cu particles due to Ag accumulation in the Cu necking area with increasing Ag/Cu mass ratio up to a maximum of d/2 of the neck is filled with Ag. Each graphs ends when a Ag neck filling of d/2 is reached. "d" in the label stands for Cu particle diameter.

4.6.3.2 Adjacent Copper (Cu) Particles of Varying Size

The particle and necking arrangement simulated in this section is shown in Figure 75. Two adjacent Cu particles with differing diameter have formed a neck of between one eighth to one quarter of the larger Cu particle diameter. Ag fills up the neck up to one third of the diameter of the larger Cu particle. The inter-particle resistance reduction between the two adjacent Cu particles due to the Ag accumulation in the necking region for various Cu-Cu neck sizes are shown in Figure 76 to Figure 78.

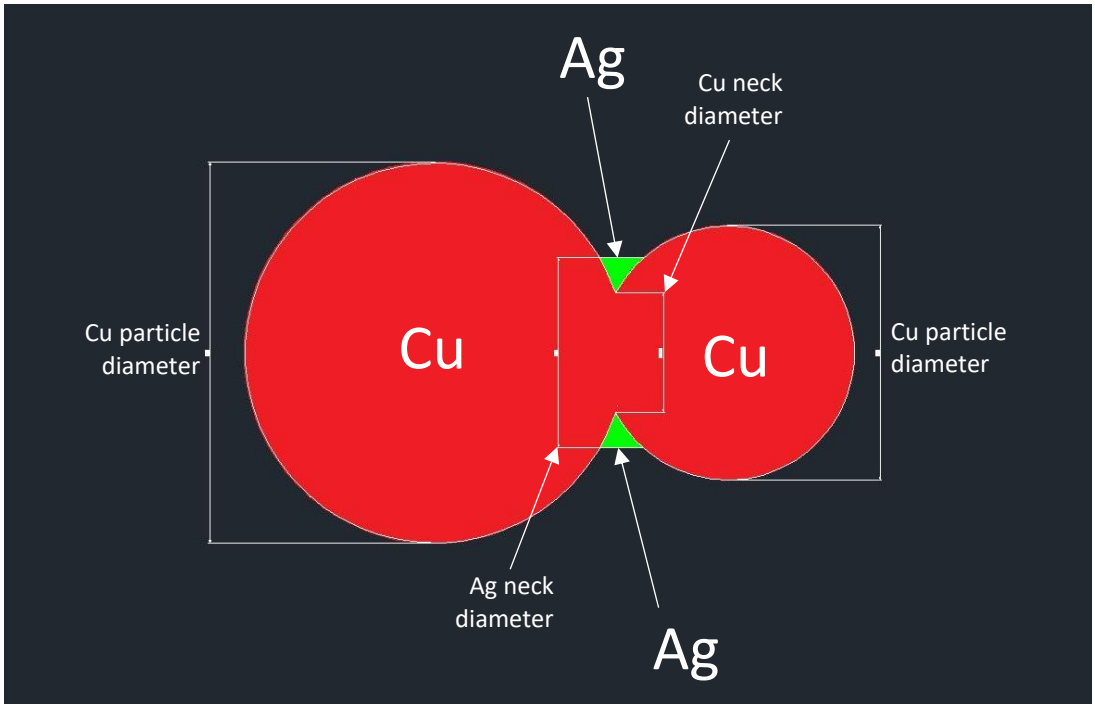


Figure 75. Sketch of Ag accumulation in the necking region of two adjacent Cu particles which are not equal in diameter.

From Figure 76, Figure 77, and Figure 78 two observations can be made. Firstly, it can be seen that, at a constant prior Cu-Cu neck formation, the bigger the size difference between the two adjacent Cu particles, the less of a reduction of the inter-particle resistance is caused by the addition of Ag (up to the same Ag/Cu mass ratio of 0.5 x 10^{-4} for instance). Secondly, at a constant Cu/Cu adjacent particle size ratio, the smaller prior neck between the adjacent Cu particles, the bigger the reduction in inter-particle resistance due to the addition of Ag (up to the same Ag/Cu mass ratio of 0.5 x 10^{-4} for instance).

Assuming that Ag accumulates in Cu adjacent particle necks this means that according to these results, in order to cause the biggest possible reduction in inter-particle electrical resistance with the least relative amount of Ag added, two aspects are desirable: a low degree neck formation among the Cu particles as well as a narrow Cu particle size distribution.

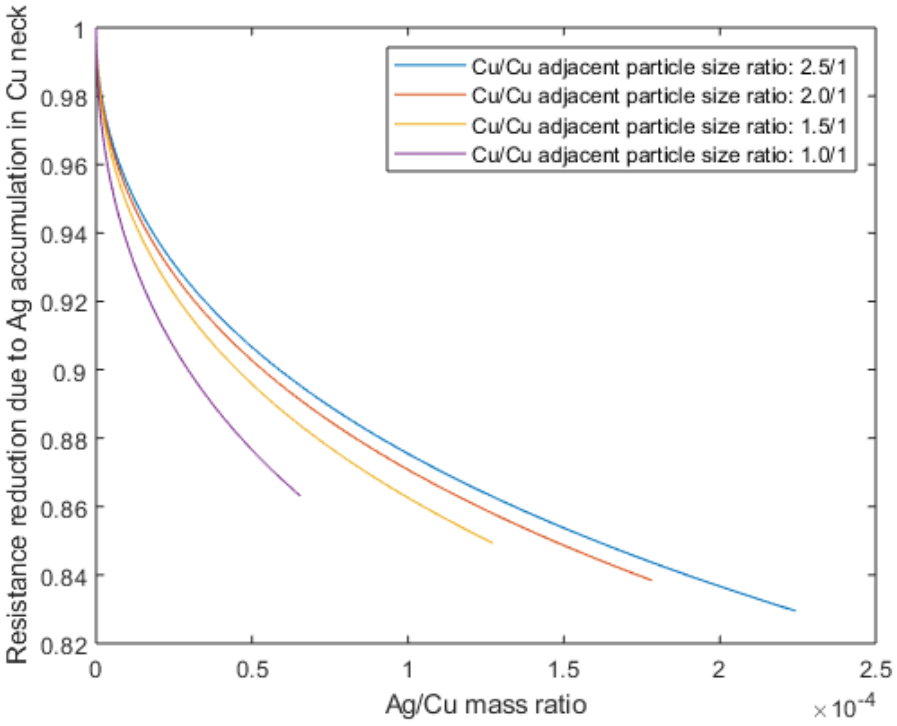


Figure 76. Cu-Cu neck size: d/4. "d" refers to the diameter of the larger Cu particle diameter. Each graphs ends when a maximum Ag neck filling of d/3 is reached.

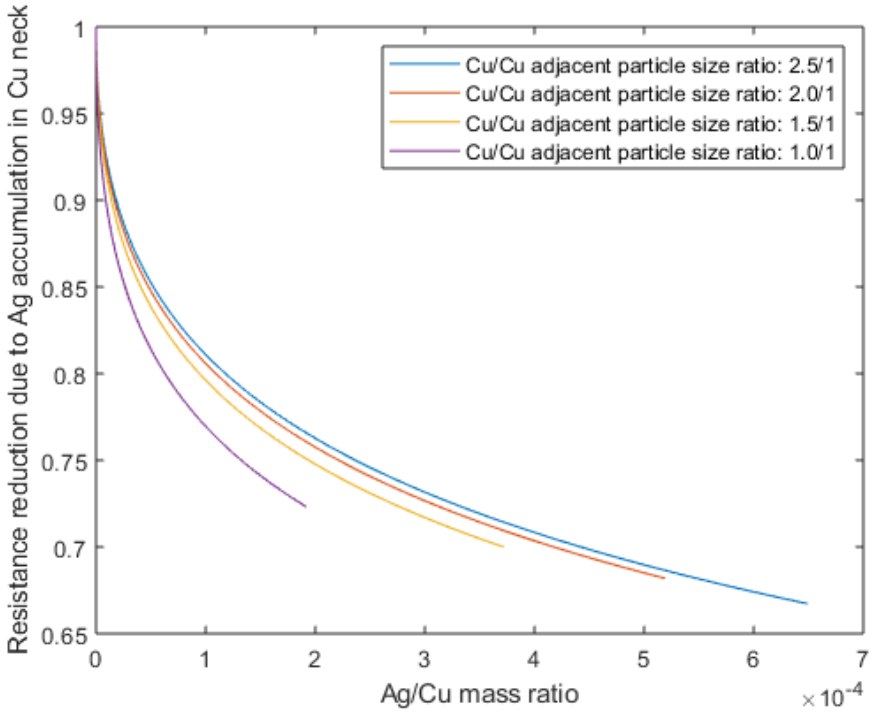


Figure 77. Cu-Cu neck size: d/6. "d" refers to the diameter of the larger Cu particle diameter. Each graphs ends when a maximum Ag neck filling of d/3 is reached.

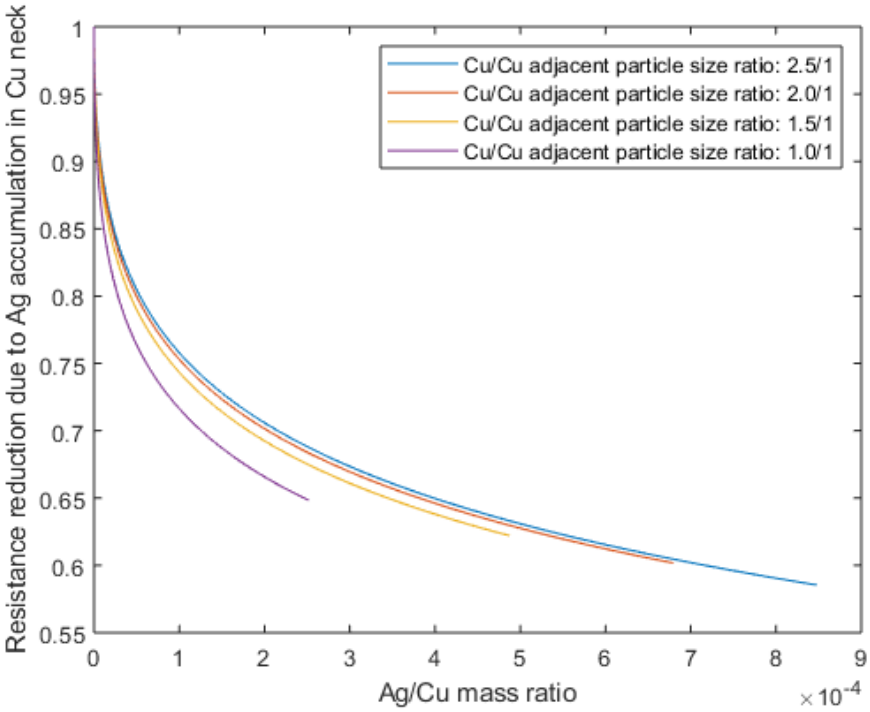


Figure 78. Cu-Cu neck size: d/8. "d" refers to the diameter of the larger Cu particle diameter. Each graphs ends when a maximum Ag neck filling of d/3 is reached.

4.7 Discussion

The aim of this discussion is to investigate if synergistic effects of an addition of Ag to Cu NPs can be utilised for the application of printed electronics.

4.7.1 Ultra-fast Nanoparticle (NP) Sintering

Plenty of literature exists on laser and IPL sintering of either Cu or Ag NP ink. However, no prior literature exists on laser or IPL sintering of a hybrid Cu-Ag NP ink – making these results the first of this kind. For both laser sintering as well as IPL sintering it was found that the addition of Ag does not significantly reduce sheet resistance (see Figure 52 and Figure 53).

It was shown in Figure 28 and Figure 91 that neither laser irradiation nor IPL exposure caused Cu oxidation. In terms of bulk metal properties, Cu only has a 5.6 % higher resistivity than Ag. Consequentially, considering that no Cu oxidisation occurred, the

addition of Ag to Cu did not significantly impact the sheet resistance of the sintered material.

LDA analysis in Figure 51 showed that an increase in Ag content decreases the particle size distribution. Ample literature has shown that the smaller a particle size distribution, the lower its sintering temperature (see Figure 23; section 3.3.1.1 *"Particle Size and Sintering Temperature"* elaborates on this phenomenon). At a constant heat treatment, one would expect a material with a lower sintering temperature to sinter to a higher degree of densification which would be reflected in a lower electrical resistance. However, the impact of the Ag content lowering the particle size distribution leading to a higher degree of densification and a lower electrical resistance was insignificant (see Figure 52 and Figure 53).

It is possible that the addition of Ag to Cu NPs impacts the absorbance of light of the material. This effect was not measured in this work. There is no literature on the light absorbance of Cu-Ag hybrid NPs. Literature on pure Cu and Ag NPs exists, however, results vary significantly depending on *e.g.* particle size and ink formulation (Dang et al., 2011; Lu et al., 2005) so it remains unknown what the effect of the Ag addition was on the light absorbance in this work. Further work should measure the light absorbances of Cu-Ag hybrid materials at the wavelength of the light source used (1,064 nm in the case of the laser used in this work for laser sintering). An increased light absorbance could be advantageous for lowering the light power required for sintering.

It can be concluded that for sintering during which there is no risk of Cu oxidation, the addition of Ag does not improve electrical performance while at the same time increasing the cost due to the higher cost of Ag compared to Cu.

4.7.2 Slow Nanoparticle (NP) Sintering

4.7.2.1 Oxygen-containing Environment

It was shown in Figure 54 that thermal sintering increases the mean Ag crystallite size by 117 %. This concurs with literature by Moon et al. and Grouchko et al. who report an increase in mean Ag crystallite size due to thermal sintering of 80 % and 133 % respectively (Grouchko et al., 2009; Moon et al., 2005). The observed Ag grain growth is a strong indicator that Ag sintering occurred.

Interestingly, it was shown in Figure 56 that the sheet resistance significantly reduced for the materials with 3, 8 and 25 wt% Ag content. As previously stated, the XRD scans of the materials containing 3 and 8 wt% Ag after thermal treatment in air showed no significant characteristic Cu peak but they showed characteristic CuO and Cu_2O peaks which are both dielectric. It follows that the reduction in sheet resistance likely was a result of the Ag content which formed a connected grid enabling the continuous flow of electrons. As one can see from Figure 56, the higher the Ag content, the lower the sheet resistance at any temperature. No such finding in the literature has been reported, that it is possible to significantly reduce electrical resistance of a Cu-Ag material through thermal sintering in air with as little as 3 wt% Ag content.

It is well known that Cu rapidly oxidises at elevated temperatures (Li et al., 1991). With decreasing particle size, the surface area-to-volume ratio increases and thus the rate of oxidation increases. As expected, this was also found to be the case in this study. The XRD scans after the thermal treatments in the oxygen-containing environment detected no significant amounts of unoxidised Cu for the materials containing 0, 1, 3 and 8 wt% Ag (see Figure 92 to Figure 95). Solely the material containing 25 wt% Ag showed a significant unoxidised Cu peak after the thermal treatment (see Figure 96). One hypothesis for this finding is that in the case of the material containing 25 wt% Ag, the high Ag content is forming a protective barrier for some of the Cu to stop it from oxidising. The prevailing theory in literature on the predominant mass transport of Ag in Cu-Ag NP systems during thermal treatment is that Ag can act as a protective physical barrier to prevent Cu oxidation. At a temperature which varies depending on the publication from approximately 100 to

500 °C, however, the protective Ag shell delaminates from the Cu and accumulates (Chen et al., 2013; Choi and Lee, 2016; Jung et al., 2011; Kim et al., 2014; Lee et al., 2015; J. Li et al., 2017; Njagi et al., 2017; Pajor-Świerzy et al., 2017a, 2017b; Y. S. Park et al., 2016; Tsai et al., 2013; Yan et al., 2012; Yim et al., 2016; Zhang et al., 2010). It is believed that this difference in Ag delamination temperature depends predominantly on the thickness of Ag shell which in turn depends on the material synthesis methodology. This delamination and accumulation of Ag appears to be independent of whether the thermal treatment was carried out in an air or in an inert (i.e. nitrogen, argon) atmosphere. The following section investigates this phenomenon of delamination, mass transport and accumulation of Ag in Cu-Ag NP systems.

4.7.2.2 Low-oxygen Environment

Below 375 °C, Cu and Ag are nearly completely immiscible (Sheng et al., 2002). However, at higher temperatures Cu and Ag can form a eutectic system together (Subramanian and Perepezko, 1993). This is because Cu and Ag exhibit a positive enthalpy of mixing (Wolverton et al., 1998), Cu and Ag have a large lattice mismatch of 12 % (Pearson, 1967), and the two elements only have a small difference in electronegativity of 0.03 (Pauling, 1960). Subramanian and Perepezko derived a phase diagram from selected published data (see Figure 79). In Figure 57 the melting points of the Cu-Ag particle systems analysed (containing 0, 1, 3, 8, and 25 wt% Ag) were shown. Considering the bulk melting points of Cu and Ag being 1,085 and 962 °C respectively, it is clear that the reported melting point of the material with 25 wt% Ag content was well below the theoretical bulk melting points of both Cu and Ag. Moreover, all of the melting points reported in Figure 57 broadly follow Subramanian and Perepezko's phase diagram in Figure 79.

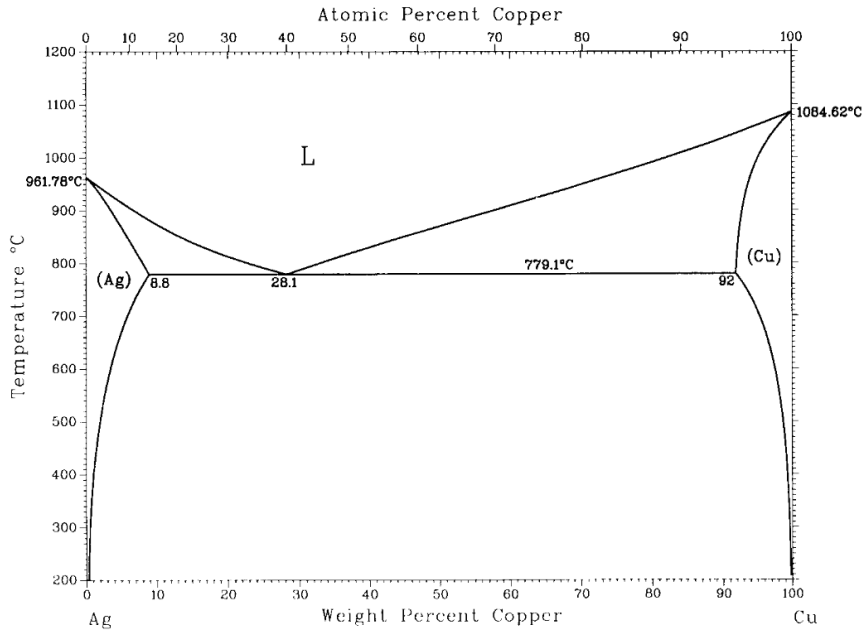


Figure 79. Ag-Cu phase diagram derived from experimental data (Subramanian and Perepezko, 1993).

Cu and Ag forming a eutectic system with a melting point reduction beyond the melting point of Ag is a potentially a way to harness synergistic effects of combining Ag with Cu. However, according to Subramanian and Perepezko only at an Ag wt loading of above approximately 30 % is the melting point of the system below the melting point of pure Ag. In fact, the minimum melting point temperature obtainable occurs at a 71.9 wt% Cu and 28.1 wt% Ag. For the aim of harnessing synergistic processing effects of adding small amounts of significantly more expensive Ag to cheaper Cu (Ag is approximately 75 times as expensive in terms of their raw material price (Money Metals Exchange, 2019)), the benefits of forming a eutectic system with small amounts of silver (≤ 25 wt%) are insignificant.

In section 4.6.2.2 "*Electron Microscopy Analysis of Copper (Cu) and Silver (Ag) Nanoparticle Sintering in-situ the Microscope"*, Cu and Ag NPs were thermally sintered *in-situ* in an SEM and images were taken at regular temperature intervals. There is some literature in which SEM images are used to characterise already sintered Cu and Ag NPs in various sintering states (Ida et al., 2010; Kim and Nishikawa, 2015; Yeadon et al., 1997). Solely Mittal and Lin have reported *in-situ* Cu NP sintering and monitoring inside a TEM (Mittal and Lin, 2015). However, their only analysis is

entirely descriptive rather than quantitative, and it is rather difficult to follow due to the TEM image quality being very poor. No quantitative analysis at regular temperature intervals throughout the sintering process of Cu and Ag *in-situ* NP sintering exists in the public domain. The advantage of this method is that the very same particles or particle clusters can be monitored and specific changes be identified and tracked throughout the entire temperature ramp. The general limitation of taking top-down SEM images from one perspective is that information about multi-layered morphology has to be inferred from a 2D image. The error can be minimised by increasing the particle count as the thereby the probability of capturing a representative sample of the particle distribution increases.

It was found that the Ag NPs sinter at significantly lower temperatures than the Cu NPs (see Figure 60 and Figure 64). According to Yan et al. and Messing et al., Herring's scaling law (see Equation 20) applied to NPs can be rearranged to:

$$n\ ln\left(\frac{d_1}{d_2}\right) = \frac{Q}{R}\left(\frac{1}{T_2} - \frac{1}{T_1}\right) \qquad \text{Equation 23}$$

where, n signifies the specific diffusion mechanism of densification (see Equation 20), d_1 and d_2 are adjacent particle sizes, Q is the activation energy, R is the gas constant, and T_1 and T_2 are the corresponding sintering temperatures of d_1 and d_2 (Messing and Kumagai, 1994; Yan and Rhodes, 1983). It follows from Equation 23 that with increasing ratio of adjacent particle sizes, the activation energy required to induce particle sintering increases. The Ag particles were found to have a much narrower particle size distribution than Cu (see Figure 63 compared to Figure 59). Moreover, Ag NPs have inherently lower sintering temperatures than Cu particles due Ag having a lower bulk melting point (Ag: 962 °C; Cu: 1,085 °C). It thus follows from Equation 23 that the activation energy for the Ag NPs was lower than for the Cu NPs which explains why the Ag sintered at significantly lower temperatures than the Cu (see Figure 60 and Figure 64).

In the case of Cu NPs sintering (see Figure 59) it was found that the predominant mass transport phenomenon is viscous flow (see Figure 62). Smaller particles thereby fuse into adjacent larger particles and hence larger particles grow at the expense of smaller particles. The average particle size distribution consequentially increases with increasing temperature (see Figure 60).

Ag NP sintering was found to be remarkably different. Smaller particles fusing into adjacent larger particles, as it was the case with the Cu NPs, did not occur as obviously in the case of Ag therefore the equivalent data of “fusing” and “fused” particles could not be captured. Rather than entirely fusing into one another, the Ag NPs predominantly formed necks between adjacent particles (see Figure 63). Quantitative data was obtained through image analysis distinguishing whether Ag particles remained discrete or had undergone some kind of sintering such as necking (see Figure 64). Based on the literature (Bonevich and Marks, 1992; Shi et al., 2005) it is believed that surface diffusion is the main sintering mechanism responsible for the neck formation of the Ag NPs. As diffusion is a time-dependant process, temperature intervals were maintained for the same time duration after which the images were taken. During surface diffusion the sintered particles retain their initial adhesion structure with no reorientation. The driving force for sintering can be considered a chemical potential difference between facet surfaces and the neck region (Fang and Wang, 2010), leading to neck formation.

It was previously established that Ag sinters at lower temperatures than Cu (see Figure 60 and Figure 64) which is consistent with the literature (Grouchko et al., 2009; Kim et al., 2010; Tsai et al., 2013) and thermodynamic theory. The melting temperature of a material is proportional to its cohesive energy which is described by the Lindemann Law (Ross, 1969). Ag and Cu have cohesive energies of 2.95 eV per atom (Grouchko et al., 2014) and 3.50 eV per atom (Delley et al., 1983) respectively. Due to the lower cohesive energy of Ag compared to Cu, a more prominent melting point reduction of Ag than Cu is anticipated (Ino, 1969). Ag therefore also becomes mobile at lower temperatures. The mobility of the interfacial Ag is further enhanced by the Cu-Ag interface being less energetically stable than for instance a pure Ag

particle (Wang and Shin, 2017). With increasing mobility its migration is increasingly influenced by surface tension. The surface tension forces Ag into a shape which energetically most favourable. In the case of a two-material system consisting solely of Ag and air, for instance, (considering just surface tension as an acting force) the most energetically favourable shape for the Ag to take with the lowest surface area-to-volume-ratio would be a single sphere. In the case of a Cu and Ag particle system, Ag can have an Ag-air interface but also an Ag-Cu interface. Ag and Cu have surface tensions of 0.89 N m^{-2} (Bernard and Lupis, 1971) and 1.31 N m^{-2} (Harrison et al., 1977), respectively. In a liquid state the liquid with the lower surface tension will wet the one with the higher surface tension (Pereira and Da Silva, 2011). As Ag has a lower surface tension than Cu, it follows that Ag wets the Cu surface. The necking regions between two adjacent particles are energetically favourable locations for Ag to migrate to because the Ag-Cu interface is energetically more favourable than Ag-gas interface. Accumulation of Ag in Cu particle necks during thermal sintering is indeed what occurred as it is clear from section 4.6.2.3 "*Electron Microscopy (EM) and Energy-dispersive X-ray (EDX) Spectroscopy Analysis of Thermally Sintered Cu-Ag NPs"*.

The accumulation of Ag in the necks of Cu particles increases contact area between adjacent Cu particles and thereby enhances electrical conductivity. In order to give an informed recommendation on how to utilise this phenomenon for obtaining maximum electrical conductivity by adding a minimum amount Ag (more expensive than Cu) the theoretical calculations were carried out. No similar simulations were found in the literature. The reduction in Inter-particle resistance between two Cu particles of equal size due to accumulation of Ag in the neck was quantified in Figure 74. In every case, increasing the Ag/Cu weight ratio decreases particle electrical resistance. The greater the neck formation between the two Cu particles, the lower is the reduction in inter-particle electrical resistance due to the Ag accumulation in the neck, in other words, the addition of Ag becomes less effective in terms of reducing electrical inter-particle resistance. The temperature at which Cu particles start to form necks and the temperature at which Ag becomes mobile can indirectly be inferred from Figure 60 and Figure 64, respectively. In both cases, the temperature

depends on the melting point of the material as well as the particle size distribution. This has been shown in theoretical models relating particle size and materials properties to initial sintering temperature, most notably by Jiang and Shi (Jiang and Shi, 1998). To utilise the effect of Ag accumulation in Cu particle necks reducing electrical resistance, the chosen temperature for the heat treatment should be above the minimum temperature for the Ag to become mobile. Ideally this temperature should be below a temperature at which the Cu sinters to a high degree of densification to minimise Cu particle necks and hence maximise the impact of Ag accumulation in Cu particle necks.

Moreover, in Figure 76 to Figure 78 it was shown that an increasing Cu/Cu adjacent particle size ratio also decreases the reduction in inter-particle electrical resistance due to the Ag accumulation in the neck. In a Cu particle system with a wider particle size distribution, on average there will be an increased Cu/Cu adjacent particle size as opposed to if it's a narrow particle size distribution. It follows that the addition of Ag in order to reduce electrical resistance will be more effective with a narrow particle size distribution.

The simulation in section 4.6.3 "*Theoretical Simulation of the Neck Formation of Silver (Ag) and Copper (Cu) Nanoparticle (NP) Sintering"* combined with information on the temperature at which Ag becomes mobile and the temperature at which Cu starts to sinter has the potential to guide experimental design decisions in order to utilise the effect of relatively small amounts of Ag causing significant reductions in electrical resistance by accumulating in Cu particle necks.

4.8 Summary

This section investigated the use of Cu and Ag NPs in AM processes as well as the way small additions of Ag to Cu NPs can harness synergistic effects which can reduce AM process cost or complexity.

Cu and Ag NP inks were synthesised using a continuous hydrothermal process and subsequently formulated into a stable ink. The inks were characterised in terms of their particle size distribution and Ag/Cu wt ratio.

The materials were sintered and analysed using laser sintering, IPL sintering, as well as thermal sintering in an oxygen-containing environment and an inert environment. With laser sintering and IPL sintering, the addition of Ag brought about no significant improvement in terms of electrical resistance as no detrimental Cu oxidation occurred due to the fast heating and cooling. Despite Cu completely oxidising during thermal sintering in an oxygen-containing environment, the addition of Ag at solely ≥ 3 wt% reduced the electrical resistance significantly. During thermal sintering in an inert atmosphere to temperatures beyond the melting point of both materials, Cu and Ag formed a eutectic mixture, caused a reduction in melting point temperature. *In-situ* monitoring of thermal sintering Cu and Ag particles in an inert atmosphere showed that sintering of the Cu NPs occurred at significantly higher temperatures than sintering of the Ag NPs. Moreover, the mass transport phenomena of the sintering of the two materials differed: with Cu, smaller particles fused into adjacent larger particles through viscous flow whereas Ag particles formed necks through surface diffusion. During thermal sintering in an inert atmosphere of the NPs containing 25 wt% Ag and 75 wt% Cu, it was found that the Ag predominantly accumulates in the necks of adjacent Cu particles. This was reasoned to be the results of surface tension acting on the mobile Ag and the Ag-Cu interface being energetically favourable over the Ag-gas interface. To further investigate this phenomenon, a theoretical simulation was reported, calculating the reduction in Cu-Cu inter-particle resistance due to Ag accumulation in the necking region.

In conclusion it was found that the addition of small wt% of Ag to Cu NPs does not significantly harness improvements with fast sintering processes such as laser and IPL sintering. With slow sintering processes such as thermal sintering during which Cu oxidises, the addition of Ag can create a connected grid enabling electrical conductivity. During slow sintering it is also possible that the Ag accumulates in the necking region of Cu particles which can significantly reduce electrical resistance.

5 A CYCLIC BENDING STUDY OF INKJET PRINTED AND LASER SINTERED COPPER (Cu) AND SILVER (Ag) TRACKS ON FLEXIBLE PET SUBSTRATES

5.1 Introduction

The most widely reported application of AM with metal NPs is printed electronics. One of the advantages of printed electronics over traditional subtractive manufacturing of electronics is that electrically conductive tracks can be printed onto heat-sensitive flexible materials. This enables the manufacture of flexible electronics, such as wearable sensors. For this, an understanding of the impact of bending on the electrical resistance and microstructure is key. Copper (Cu) nanoparticle (NP) ink is considered a cost-effective alternative to silver (Ag) NP ink. This chapter assesses whether Cu NPs can replace Ag NPs for the manufacture of flexible electronics. Cu and Ag tracks were inkjet printed and laser sintered at various layers and widths. The tracks were subjected to automated bending cycles during which the change in electrical resistance was measured.

5.2 Materials and Methodology

This section lays out the equipment, methods and materials used. This involves NP ink synthesis and formulation, NP inkjet printing and laser sintering, the cyclic bending experimental setup and operation, as well as the characterisation of the tracks, i.e. SEM and EDX, optical light microscopy, XRD analysis, and electrical resistance measurements.

5.2.1 Copper (Cu) and Silver (Ag) Nanoparticle (NP) Inks Used, Ink Deposition and Laser Processing

The Cu NP inkjet ink was the same ink used in chapter 3 (see sub-chapter 3.2.1 for description and *Appendix* 8.1 for the technical data sheet). The metal weight loading is stated as 35 to 37 % by the manufacturer. The main solvent is diethylene glycol monoethyl ether (DGME).

The Ag NP ink was purchased from Sigma-Aldrich. The metal weight loading is stated as 39 % by the manufacturer. The main solvent is triethylene glycol monoethyl ether (TGME).

For ink deposition the same inkjet printing methodology was used as explained in section 3.2.3 *"Deposition of Copper (Cu) Nanoparticle (NP) Ink through Inkjet Printing"*. The substrate was polyethylene terephthalate (PET) of 100 µm thickness.

The inkjet printed tracks were laser sintered using the same laser system as described in section 3.2.5 *"Laser Irradiation of Copper (Cu) Nanoparticle (NP) Ink to Induce Particle Sintering"*.

5.2.2 Imaging Copper (Cu) and Silver (Ag) Tracks: Light Microscopy, Scanning Electron Microscopy (SEM), and Energy-dispersive X-ray (EDX) Spectroscopy Analysis

Once manufactured, each sample was inspected using a Nikon Eclipse LV100ND and Nikon NIS-Elements microscope imaging software. This was to quantify the width and height of each track. The width was measured to a precision of $1\ \mu m$ directly within the software. The thickness was measured using depth of focus. Initially, the microscope was focused on the surface of the print. Then it was focused on the substrate by altering the clamp height. The clamp height scale gave a height measurement to a precision of 1 µm. Each dimension was measured at three evenly spaced points across each sample.

For the SEM and EDX analysis, the same methodology as explained in the previous *Materials and Methodology* section 3.2.12 was used. SEM and EDX analysis was conducted on the surface of the thickest samples of 1,500 µm (nominal) width for each NP ink after completing bending to 1,000 cycles.

5.2.3 *Investigations into Potential Oxidation of Copper (Cu) and Silver (Ag) Tracks due to Laser Irradiation using X-ray Diffraction (XRD)*

Glancing angle XRD was carried out using a Bruker D8 Advanced (the same equipment as previously in section 3.2.8). A glancing angle of 1.2° was used with a step size of 0.0375° and a counting time of 20 seconds. The scans were carried out for 2θ values between 10° and 79°. Samples analysed were 20 x 20 mm (nominal values) squares.

5.2.4 *Cyclic Bending of Inkjet Printed and Laser Sintered Copper (Cu) and Silver (Ag) Tracks*

A custom test rig, shown in Figure 80, was designed and manufactured to carry out cycling bending. The rig was built and bending cycles were carried out by Greg Mungall, a master student from the Department of Mechanical, Materials and Manufacturing Engineering who was co-supervised by the author. The test rig (see a Figure 80) used solenoid with a 10 mm throw (3) to induce bending in the sample. Sample clamps (4) were fastened to the solenoid plunger and the height and length adjustable carriers (5 and 6 respectively). Both the solenoid and the carriers were fastened to a base rail. The solenoid was controlled using an Arduino Uno R3 USB Microcontroller (2) via a Velleman KA03 Motor and Power Shield (1) to allow high voltage operation of the solenoid. The Arduino was programmed using Arduino IDE and fed back cycle data to be viewed on the serial monitor.

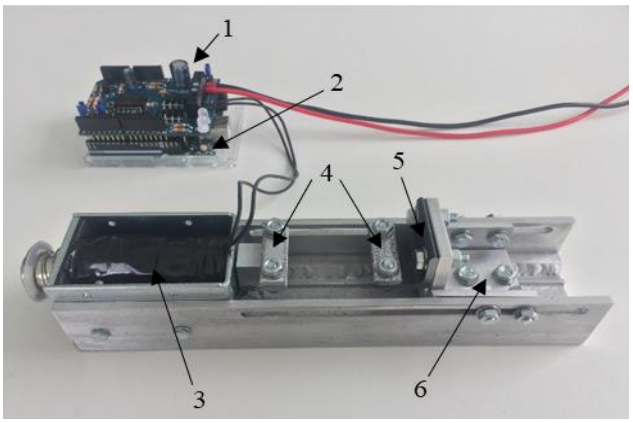


Figure 80. Cyclic bending test rig

The experimental setup is shown in Figure 81. The setup used a Rapid NP-9625-209G Regulated PSU Triple Out 0-30V 5V 12V 10A (1) to supply power to the solenoid. A USB cable connected the Arduino to the computer (2). A C-clamp (5) was used to prevent movement of the cyclic bending test rig (3) during operation. Figure 81 also shows how the sample (4) was clamped in the test rig. Each sample substrate was cut down to 15 mm width and they were secured so that the end of the track was flush with the clamp.

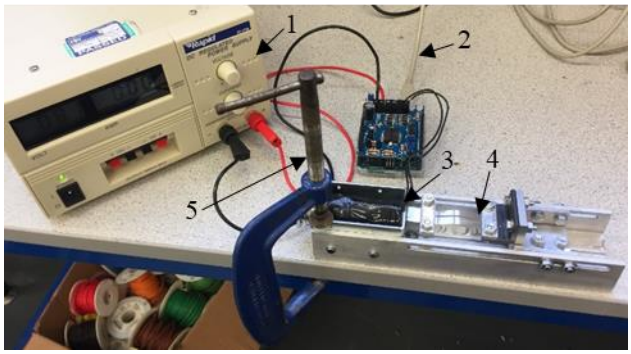


Figure 81. Cyclic bending experiment setup

Figure 82 shows the induced bend on the sample during the test rig's operation. The Arduino was programmed so that the solenoid completed cycles at 1 Hz. The power supply maintained 8.1 V for all samples to ensure an equal strain rate. Samples were initially fastened so that the samples had no bend. The carrier was then translated 1 mm towards the solenoid to induce a bend radius of approximately 20 mm (Figure 82 (A)). This initial positioning ensured the substrate bend was always in the same direction. During operation the solenoid throw then induces a bend radius of approximately 5 mm (Figure 82 (B)). Thereafter it retracts back to the initial position ending a cycle.

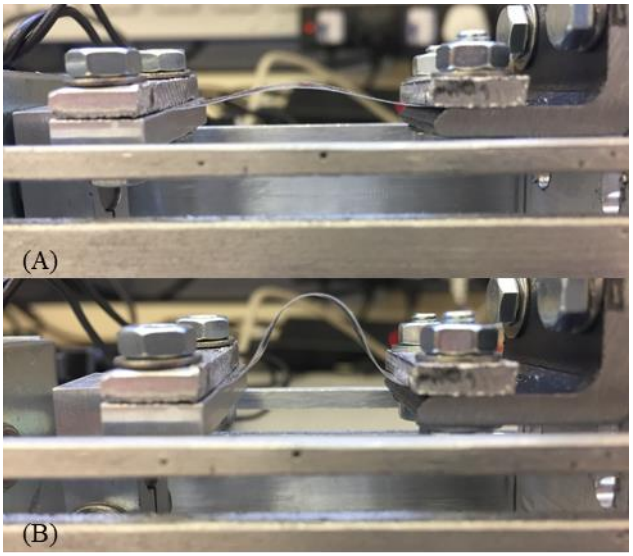


Figure 82. (A) shows the initial position with a sample bend radius of approximately 20 mm and (B) shows the full bend position with a sample bend radius of approximately 5mm

5.2.5 Electrical Characterisation of Inkjet Printed Tracks

Resistance measurements were obtained using a Uni-T Bench Type Digital Multimeter UT801, using two probes, at 0, 50, 100, 250, 500, and 1000 cycles. It was ensured that the probes were placed on the samples at exactly the same point (the outer most point). During operation an RS Pro Digital Thermometer was used to monitor substantial changes in air temperature which may have an effect on the resistance of the samples.

5.2.6 Experimental Matrix

The experiment matrix is shown in Table 5.

Sample number	NP Matrial	Printed Layers	Nominal track width
			µm
1	Ag	1	1500
2		2	100
3		2	800
4		2	1500
5		3	1500
6	Cu	3	1500
7		6	100
8		6	800
9		6	1500
10		9	1500

Table 5. Cyclic bending experiment matrix.

As shown in Table 5, 5 samples were manufactured for each material with thicknesses ranging from the least number of layers to produce a visibly consistent sample (3 layers for Cu, 1 layer for Ag) to three times this thickness. Three widths (100, 800, and 1500 µm) were produced for each thickness. The length of each sample was 30 mm. The experiment matrix was repeated three times to calculate mean values and reduce the statistical uncertainty.

5.2.7 Sample Manufacture

For each of the layer-and-ink-combinations in Table 6, 5 samples were manufactured and tested to allow for statistical analysis of the printing method to be conducted. It was found that Cu NP ink required at least three printed layers to produce a visibly consistent track. In comparison, Ag NP ink produced a consistent track with just one layer. Table 6 and Table 7 show the measured height and width data from the optical microscope inspection of each printed sample.

NP Material	Printed Layers	t
		µm
Ag	1	5.1 ± 0.5
	2	8.0 ± 0.5
	3	11.3 ± 0.3
Cu	3	7.0 ± 0.6
	6	9.8 ± 0.7
	9	14.3 ± 0.6

Table 6. Summarised height data for the printed samples. $\bar{t}$ is the measured track thickness including its standard deviation.

Table 6 shows that Ag produced printed tracks 27 % thinner than Cu. For the Ag track the first layer of ink deposited gave at 5.1 µm the tallest height per layer. Subsequent layers increased the track height nearly linearly 2.9 µm and 3.3 µm for the 2nd and 3rd layer, respectively. For the Cu track the first three layers of deposited ink gave a track height of 7.0 µm; the subsequent 2nd and 3rd set of three layers increased the track height by 2.8 µm and 4.5 µm respectively. Both samples showed a thickness STD, ranging from 0.3 µm to 0.7 µm, all of which are below 10 % of their respective sample means.

NP Material	E
	µm
Ag	289 ± 80.9
Cu	248 ± 34.1

Table 7. Summarised width data from the printed samples. Eis the measured systematic error and its standard deviation between the digitally programmed and the measured printed track width.

Table 7 shows that E for Ag is 16.5 % larger than Cu. The STD for Ag is also 137 % larger compared to Cu.

5.3 X-ray Diffraction (XRD) Elemental Analysis of Inkjet Printed and Laser Sintered Copper (Cu) and Silver (Ag) Tracks

Figure 83 shows the spectra produced by the XRD analysis of the films as deposited onto PET substrates. For the Cu sample, Bragg diffraction peaks were found for PET and Cu. The associated PDF cards have been identified in Figure 83. For the Ag

sample, Bragg diffraction peaks were found for PET and cubic Ag. Note that in both cases, PET is responsible for the broad peak at approximately 25° (100 plane) and its shoulder (110 plane). This was confirmed by completing XRD analysis on a blank PET substrate.

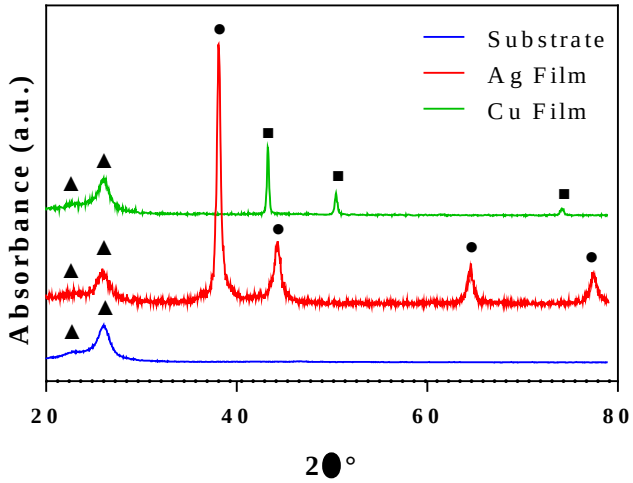


Figure 83. XRD diffraction patterns for Ag and Cu films printed onto PET substrates. The following PDF cards were used to identify the peaks ▲ PDF 00-050-2275 PET, ●PDF 00-004-0783 Ag Silver-3C, syn, ■ PDF 00-004-0836 Cu Copper, syn.

5.4 Particle Size Distribution Analysis of the Copper (Cu) and Silver (Ag) Nanoparticle (NP) inks

From the SEM image in Figure 84 the Ag NPs were found to be mostly spherical with a few rod-shaped particles. The mean particle diameter was found to be approximately 44 nm with a standard deviation of ± 13 nm determined through image analysis (see *Methodology* section 4.2.4 "*Image Analysis of FEG-SEM Images of Nanoparticles (NPs)"*).

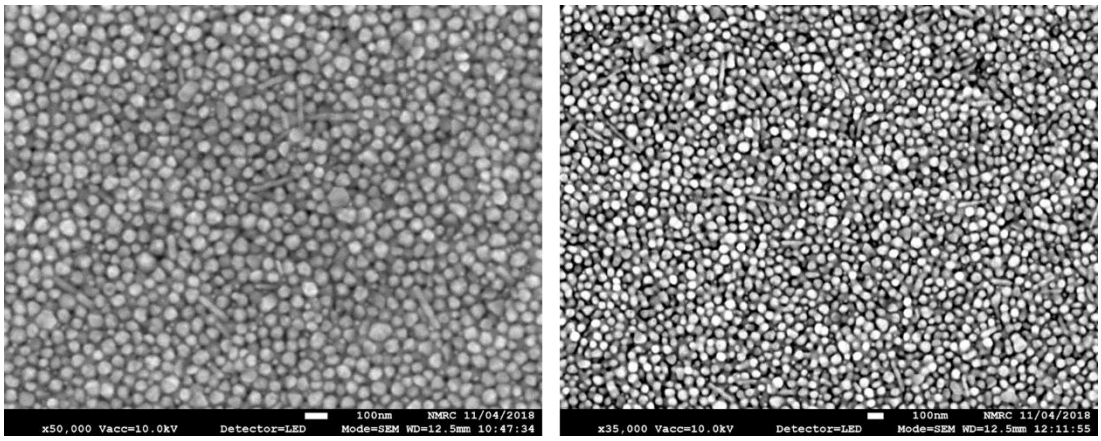


Figure 84. Secondary electron SEM images: on the left of an **unsintered** inkjet printed Ag NP film and on the right of a **laser sintered** inkjet printed Ag NP film. Both images are prior to cyclic bending.

From the SEM image in Figure 85 the Cu NPs were found to be less spherical than the Ag NPs. The mean particle diameter was found to be approximately 330 nm with a standard deviation of ± 186 nm determined through image analysis (see *Methodology* section 4.2.4 "*Image Analysis of FEG-SEM Images of Nanoparticles (NPs)"*).

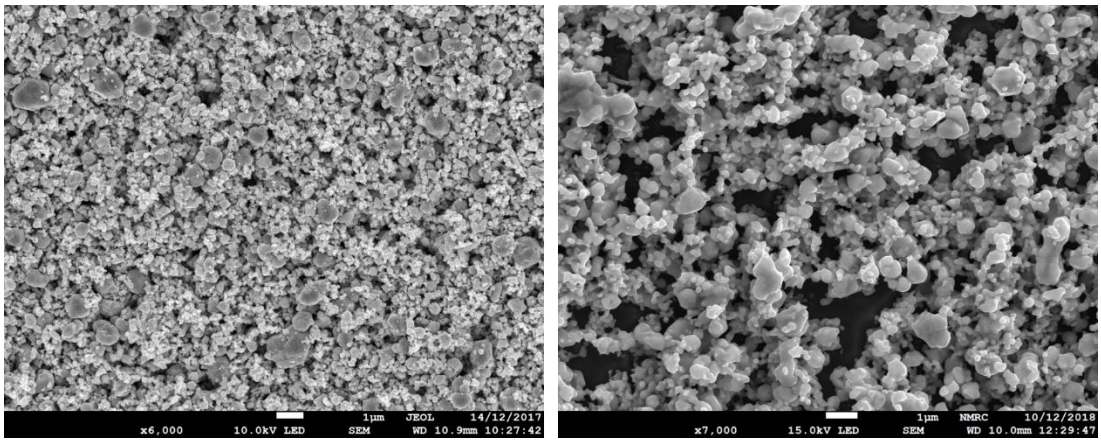


Figure 85. Secondary electron SEM images: on the left of an **unsintered** inkjet printed Cu particcle film and on the right of a **laser sintered** inkjet printed Cu particle film. Both images are prior to cyclic bending.

5.5 The Impact of Cyclic Bending on Electrical Resistance

Sample number	NP Material	Printed Layers	Nominal track width	xbulk metal resistivity prior to bending	Resistance prior to bending	xbulk metal resistivity after bending	Change in resistance after bending
			µm	Unitless	Ω	Unitless	Unitless
1	Ag	1	1500	135.8 ± 5.7	7.1 ± 0.3	149.4 ± 21.0	1.1 ± 0.0
2		2	100	217.2 ± 6.5	33.3 ± 1.0	239.0 ± 7.2	1.1 ± 0.0
3		2	800	153.4 ± 12.8	8.4 ± 0.7	168.8 ± 20.1	1.1 ± 0.1
4		2	1500	150.0 ± 12.0	5 ± 0.4	165.0 ± 33.0	1.1 ± 0.0
5		3	1500	152.6 ± 8.5	3.6 ± 0.2	167.8 ± 46.6	1.1 ± 0.1
6	Cu	3	1500	661.6 ± 49.8	27.9 ± 2.1	1058.6 ± 37.9	1.6 ± 0.2
7		6	100	202.9 ± 13.2	30.7 ± 2.0	527.6 ± 17.2	2.6 ± 0.3
8		6	800	533.4 ± 27.9	26.8 ± 1.4	1226.9 ± 45.8	2.3 ± 0.2
9		6	1500	737.0 ± 86.3	22.2 ± 2.6	1842.5 ± 83.0	2.5 ± 0.2
10		9	1500	600.7 ± 96.9	12.4 ± 2.0	2643.0 ± 213.1	4.4 ± 0.8

Table 8. Resistivity (as a multiple of bulk metal resistivity) prior and after bending as well as the sample resistance prior to bending and the change in resistance due to bending.

The data in Table 8 shows that Ag generally produced lower resistance values prior to bending compared to Cu with four out of five being below 10 Ω compared with all of Cu resistance values prior to bending being above 10 Ω. Both inks produced their lowest $\overline{R_{in}}$ when printed with the largest height and width, where Ag has a 71 % lower resistance than Cu. In both cases the highest resistance values prior to bending was seen at the lowest width, where Ag has a 9 % lower resistance than Cu.

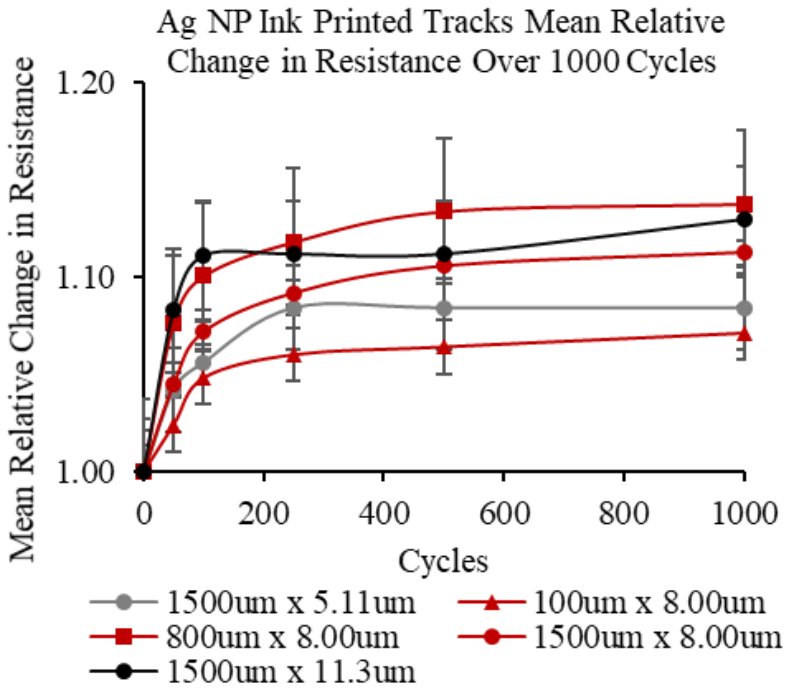


Figure 86. Graphical representation of the mean relative resistance over 1000 bending cycles for Ag NP ink printed tracks and the associated standard error.

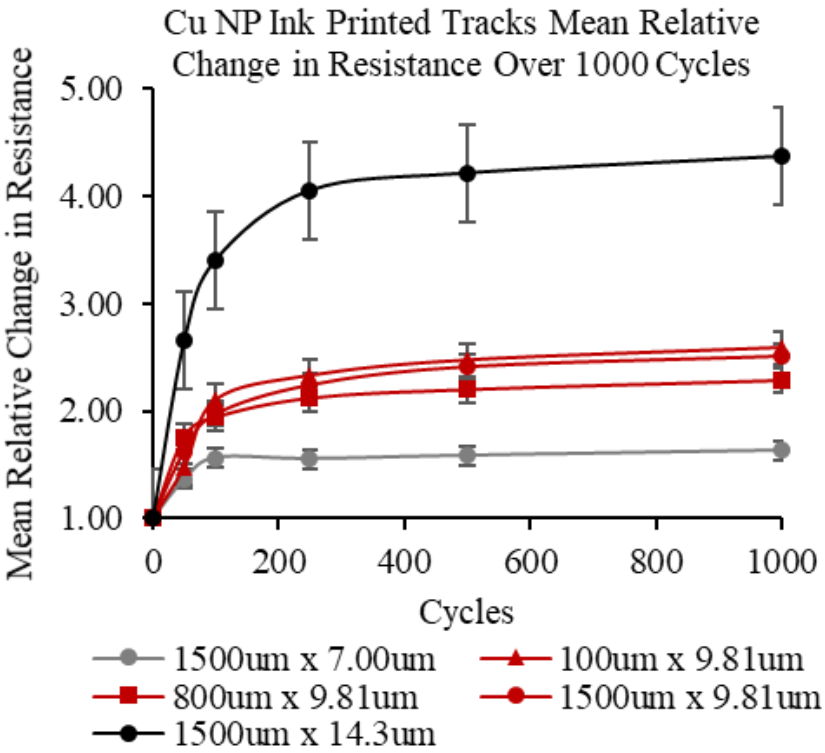


Figure 87. Graphical representation of the mean relative resistance over 1000 bending cycles for Cu NP ink printed tracks and the associated standard deviation.

Figure 86 and Figure 87 show that the range of the change in resistance due to bending was insignificant for Ag while it was on average 2.7 for Cu. The lowest change in resistance due to bending of Ag was 34 % less than the lowest for Cu. Sample height had an insignificant effect on change in resistance due to bending for Ag. However, for Cu the change in resistance due to bending increased on average by 0.4 per µm height increase. For both inks, width has no significant effect on the relative change in resistance. Figure 86 and Figure 87 show that for both Ag and Cu that change in resistance due to bending increases considerably in the first 100 to 200 cycles before levelling out.

5.6 Scanning Electron Microscopy (SEM) and Energy-dispersive X-ray (EDX) Spectroscopy Analysis of Copper (Cu) and Silver (Ag) Tracks Before and After Cyclic Bending

Figure 88 and Figure 89 show Ag and Cu SEM and EDX imagery of printed track surfaces after bending the samples for 1,000 cycles. Figure 88 (a) shows Ag had a smooth surface without visible cracks. In comparison, Figure 89 (a) shows Cu had large defects, resembling cracks in the track perpendicular to the direction of bending. EDX of Ag tracks (Figure 88 (b) showed an even spread of Ag with trace amounts of oxygen (O) and carbon (C). EDX of Cu (Figure 89 (b)) shows Cu an even spread out around the surface also with trace amounts of oxygen and carbon. No variations in the abundance of elements were visible around cracks or print defects.

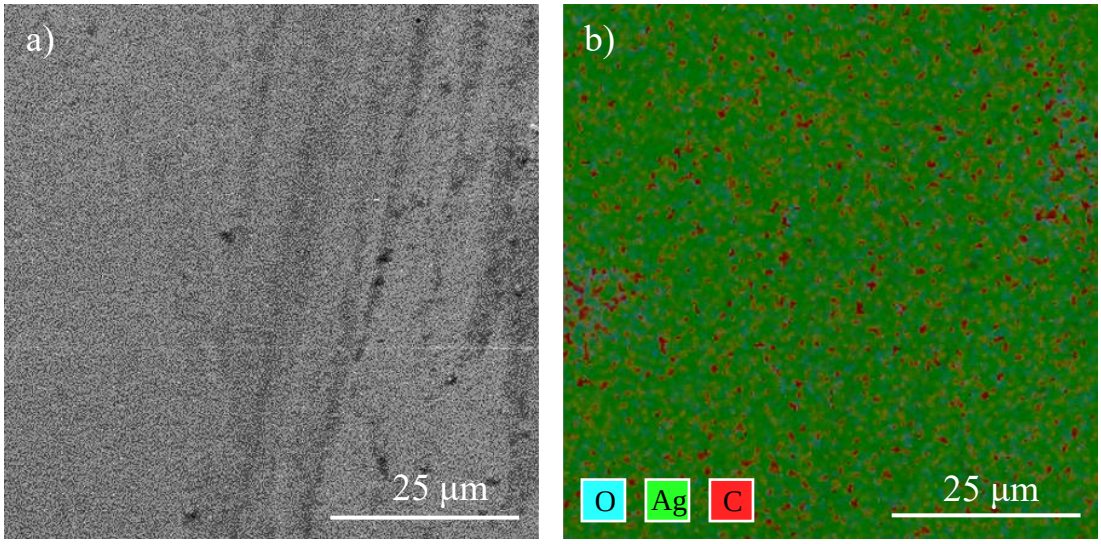


Figure 88. Secondary electron SEM image (a) and an EDX scan (b) taken from the surface of 9.8 µm thick Ag track printed onto (PET) after 1,000 bends.

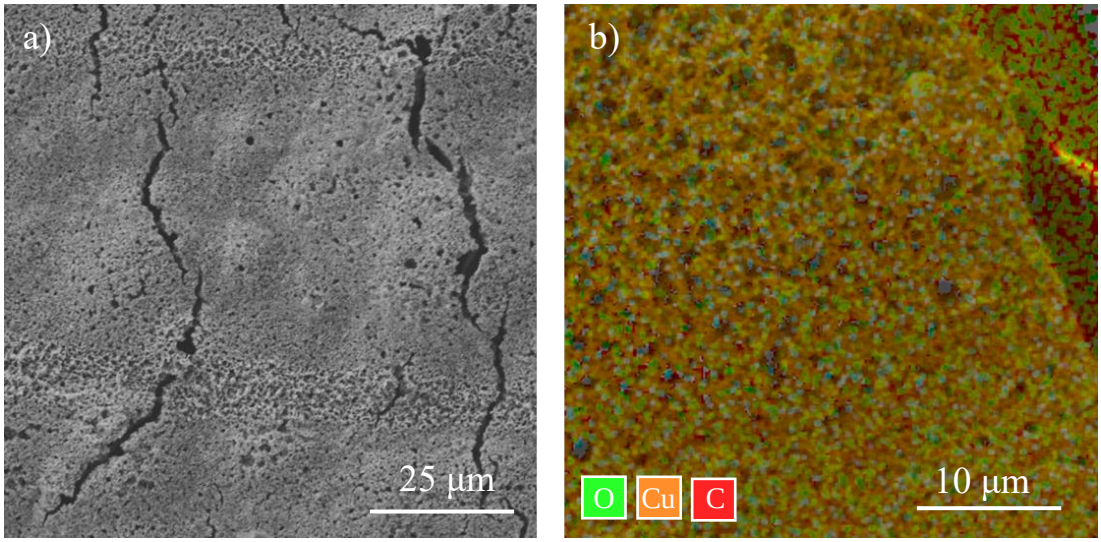


Figure 89. Secondary electron SEM image (a) and an EDX scan (b) taken from the surface of 9.8 µm thick Cu track printed onto (PET) after 1,000 bends. Large vertical micro cracks are visible in (a).

5.7 Discussion

5.7.1 Printing and Sintering Characteristics

Analysis of the thickness of the printed tracks revealed Ag NP ink could produce lower thickness tracks than Cu NP ink (see Table 6). This could be due to the smaller particle size of the Ag (44 nm) compared to Cu (330 nm). The track thicknesses produced in this study (between 5.1 and 14.3 µm) were comparatively greater than studies in the

literature investigating the impact of cyclic bending on resistance for both Cu and Ag NP inks (between 0.2 and 3.2 µm). The different printing methods used is likely to be a reason for this difference, i.e. bar coating (Kwon et al., 2016), spin coating (Jaehwan Lee et al., 2014; Min et al., 2016), or gravure printing (Yang et al., 2014). Literature studies with methodologies using inkjet printing of Ag NP ink (Glushko et al., 2016) and Cu NP ink (Niittynen et al., 2015) reported average track thicknesses of 700 nm and 270 nm respectively per printed layer. Their inks had metal loadings of 20 wt% and 12 wt%, respectively, whereas in this study the metal loading of both inks were 35 wt%. The increased metal loading in this study likely contributed to an increase in layer thickness.

Inspection and statistical analysis of the width of the printed tracks revealed a systematic error between digital and printed width (see Table 7). This systematic error has also been reported in literature for Cu NP tracks as 280 µm (Niittynen et al., 2015). This value is larger than the one reported in this work, although the study did not complete adequate statistical analysis of the error. For both inks, ink spreading due to the high wettability (tendency for a fluid to spread on a solid) of the inks on PET film has been reported as the reason for this increase in width (Niittynen et al., 2015) and was likely reason for the systematic error in this study. Reporting this allows for future calibration of the inkjet printer to produce more accurate results. The required design tolerance and the uncertainty of these results should be considered before implementing the calibration, especially for narrow prints.

The XRD analysis (see Figure 83) demonstrates that the sintering method of laser sintering used in this study successfully inhibits the formation of Cu oxides. This concurs with the literature that uses selective laser sintering (Kwon et al., 2016) which confirms the sintering process to be effective. It demonstrates that identical printing and sintering methodologies can be used for both inks.

5.7.2 The Impact of Cyclic Bending on Electrical Resistance

The cyclic bending experimentation showed that the relative change in resistance over 1,000 bending cycles for Cu NP printed tracks was on average 170 % higher than for Ag NP printed tracks (see Figure 86, Figure 87, Table 8). From this experiment it is possible to conclude that Ag NP printed tracks are more suited to high cycle bending applications. In literature, no studies were found which directly compare change in resistance due to cyclic bending of Cu and Ag NP which were manufactured using the same printing and sintering methodology and which used the same cyclic bending parameters. However, separate studies on each individual material exist which report similar increases of resistance of Cu and Ag NP printed tracks. Results of Ag NP printed tracks vary between reporting no significant increase in resistance (Jaehwan Lee et al., 2014) and reporting a small increase in resistance of 5 % (Yang et al., 2014) both over 1,000 bending cycles. Results of Cu NP printed tracks report relative increases in resistance of less than 5 % (Kwon et al., 2016) and 30 % (Min et al., 2016) also both over 1,000 bending cycles. So the increase in resistance due to cyclic bending of the Ag NP printed tracks correlates with findings from literature but the Cu NP printed tracks showed a significantly higher increase than reported in literature.

Visual and microscopy inspection of the samples after the cyclic bending experiment showed significant cracks perpendicular to the bending direction on the Cu sample (Figure 89 (a)). No such cracks we visible on the Ag sample (Figure 88 (a)). This finding suggests crack formation and propagation was the main cause for increases in resistance due to the cyclic bending. This has been well established in similar studies in literature (Alzoubi et al., 2011; Glushko et al., 2016; Graz et al., 2009; Jaehwan Lee et al., 2014; Min et al., 2016; Yang et al., 2014).

To investigate this discrepancy, it is worth considering the known similarities and differences between the Ag and Cu NP inks which were used. The metal weight loading is the same for the two inks. They differ in their ink formulations. Their main solvents (TGME for Ag and DGME for Cu) are chemically very similar and are therefore unlikely to have made an impact. Based on the ink information provided

by the ink manufacturers it remains unknown whether the exact remaining components of the ink formulation are the same or differ for the two inks. Again, this aspect was not considered to be the main factor influencing change in resistance as a result of cyclic bending and was therefore not further investigated. Two significant differences between the two inks were identified, namely the metal itself and the particle size distribution. Both significantly impact sintering behaviour which in turn effects mechanical properties of the sintered material.

Both Ag and Cu considered to be highly ductile. This is because they both form close-packed face-centred cubic lattice structures with relatively little corrugation between sheets of metal atoms. Planes can therefore slip past each other relatively easily. The ductility of Ag is reported to be higher than Cu (AZoM, n.d., n.d.). The microstructure of the laser sintered metal nanoparticles in this work is highly porous and the degree of densification is relatively low (see Figure 84 and Figure 85). It is therefore believed that the microstructure, specifically the degree of densification in the inter-particle area governs the impact of the strain on the material as a consequence of bending, as opposed to the ductility of the bulk metal.

The bulk metal itself is relevant as Ag has a lower bulk melting point (962 °C) than Cu (1,085 °C). Moreover, the Ag average particle size (44 nm) was significantly lower than Cu (330 nm). It has been widely reported and well understood in literature that the temperature required to induce particle sintering is proportional to the bulk material melting temperature as well as inversely proportional to the particle size (Fang and Wang, 2010). For laser sintering of the Ag and Cu track the same laser scan settings were used hence the same energy density was delivered. Consequentially, laser sintering induced a higher increase densification of the Ag track than the Cu track. A more densified particle bed has higher shear strength and is less prone to cracking under tensile load.

As for the width of the particle size distribution Figure 84 and Figure 85 and their image analysis found a mean particle size of 44 nm and a standard deviation of ± 13 nm for the unsintered Ag NPs and a mean particle size of 330 nm and a standard

deviation of ± 186 nm for the unsintered Cu NPs. It follows that their dimensionless standard deviation to mean-size ratio are 29.5 % and 56.4 % for Ag and Cu respectively. Hence the Ag ink has a smaller average particle size and also a smaller relative and absolute particle size spread. Ample literature has shown through theoretical simulations as well as experimentally that an increase in dimensionless standard deviation results in an increased particle bed packing density (Brouwers, 2006; Clusel et al., 2009; Furnas, 1931; Sohn and Moreland, 1968). Therefore, one would expect the Cu NPs to have a higher packing density than the Ag NPs. Lui et al. studied the impact of different packing densities on the shear strength of Ag NP and found a clear correlation between initial packing density of the NPs and shear strength of the sintered objects systems (Liu et al., 2019). This raises the question why the Ag track formed less cracks and was found to be more resilient to cyclic bending, than the Cu track. The reason for this is believed to be the sintering phenomenon and their mass transport mechanisms occurring during laser sintering. During the initial grain growth of nanoparticles, describing the process of densification up to $90\ \%$ relative density, necks will form and grow between adjacent particles (Coble, 1958; Johnson and Cutler, 1963; Kingery and Berg, 1955; Kuczynski, 1949). The width of the particle distribution has an impact on the predominant mass transport phenomenon characterising the neck formation between particles. If the particle size ratio between two adjacent particles is below a certain critical particle size ratio R_C, neck formation will occur. If, however, the particle size ratio between two adjacent particles is above R_C, in addition to neck formation inter-particle diffusion will occur (Fang and Wang, 2010). R_C is defined as

$$\mathrm{R}_C = -\frac{1}{\cos\varphi_e} \qquad \text{Equation 24}$$

, where $\cos\varphi_e$ is the dihedral angle relating surface energy and grain boundary energy (Lange, 1984). Consequentially, the wider the particle size distribution the higher the inter-particle diffusion. Since the dimensionless standard deviation to mean-size ratio of the Ag NPs was 91.2 % higher the Cu NP one, there is reason to believe that during laser sintering there was more inter-particle diffusion took place.

Increased inter-particle diffusion causes a greater redistribution of particle matter, specifically of smaller particles towards larger particles, resulting in a less uniform mass distribution within the track. This is evident in the SEM images of the laser sintered NP tracks (see Figure 85). A track with a less uniform mass distribution is more prone to crack formation and propagation if stress/strain is applied (Liu et al., 2019). Crack formation and propagation is likely the predominant mechanism causing the relative change in resistance during cyclic bending for the Cu NP tracks as it can be seen in Figure 89 (a) and as it has also been reported in literature (Jaehwan Lee et al., 2014; Min et al., 2016; Yang et al., 2014). The formation of these cracks relieves the stress/strain experienced on the surface of the tracks. The taller the tracks the greater is the stress/strain experienced on the surface and hence lead to increasing crack formation. This was evident in this study, as the printed track thickness did not have a significant impact on relative change in resistance over 1,000 bending cycles for the Ag tracks, however, for Cu NP tracks, increasing printed track thickness increased relative change in resistance (see Table 5 and Table 8).

This finding highlights the significance of the particle size distribution width on the resilience to crack formation of printed tracks under cyclic bending. No literature was found which investigates this relationship. In order to confirm the hypothesis, that an increased particle size distribution width reduces resilience towards crack formation under cyclic bending, it would be necessary to repeat the experiment using the same particle material but two different particle size distributions, one narrow and one wide distribution.

5.8 Summary

The major conclusions from this study comparing Cu and Ag NP inks for inkjet printed and laser sintered electronics are as follows:

The Fujifilm Dimatix inkjet printer demonstrated a systematic error between digital and actual print widths with both inks. Ink spreading caused an increase in printed

track widths between digital and actual track width of 289 µm and 248 µm for Ag and Cu NP inks, respectively.

XRD analysis demonstrated that laser sintering is effective for sintering both Ag and Cu NP inks. In particular, no oxides were present in Cu NP ink sintered tracks.

Ag NP ink printed tracks were demonstrated to be more resilient to cyclic bending than Cu NP ink printed tracks with regards to relative change in resistance over 1,000 cycles. Cu NP ink tracks increased in resistance between 60 and 340 % whereas all Ag NP tracks consistently increased in resistance by 10 %.

SEM analysis demonstrated that crack growth was the major driver for the observed increase in resistance of the Cu NP ink tracks. With increasing track height, surface stress/strain increases, crack growth increases, and finally relative change in resistance increases. Ag NP ink tracks showed no detectable cracks.

The findings of this study suggest that an increase in particle size distribution width can have a negative impact on track resilience to crack formation under cyclic bending. The reason for this was hypothesised to be that a wider particle size distribution causes mass distribution uniformity during sintering in turn reducing resilience to cracking. A narrower particle size distribution is better suited for printed and flexible electronics circuitry applications.

6 CONCLUSION & RECOMMENDATIONS FOR FUTURE WORK

A novel low-power process to successfully additively manufacture electrically conductive multi-layered Cu microparts from NP feedstock in an air environment was developed with significantly lower equipment and running cost than all comparable processes. This is largely because a sealed low-oxygen environment was not necessary as well as the laser being a low power fibre laser. Two different Cu ink deposition methods were used and compared, namely bar coating and inkjet printing. The microparts were found to be unoxidised but of low density and highly porous. This had a significant negative effect on the mechanical micropart properties which were far off from bulk Cu properties. The stated aim of the study to sinter Cu NPs in an ambient environment necessitates very short sintering times to avoid oxidation. This limits the degree of densification possible. A heat treatment to densify the manufactured microparts was attempted in order to improve these mechanical properties. Despite the heat treatment being carried out under inert argon flow, the microparts oxidised turning them electrically dielectric. However, the electrical properties were not as significantly affected; electrical resistivities close to bulk Cu were still achieved, similar to comparable literature which produced much higher micropart densities. Future work should focus on two aspects. Firstly, achieving increased densification through heat treatments of final microparts. Oxygen concentrations have to be sufficiently low in the heat treatment chamber. It is anticipated that this is possible as it been demonstrated in the literature. Secondly, as opposed to being carried out manually, automated system should be built capable of automated NP ink deposition and its spreading using the bar coater. It is hoped that this future work together with the knowledge created through this thesis will enable AM of multi-layered Cu microparts from NP feedstock in an air environment at significantly lower cost than comparable AM processes.

The impact of additions of Ag to Cu NPs was investigated for ultra-fast and slow sintering techniques. With both ultra-fast sintering techniques, namely IPL and laser sintering, it was found that the addition of Ag to Cu NPs does not significantly impact electrical conductivity. The reason for this was that during ultra-fast sintering the Cu NPs do not oxidise. Since the bulk electrical resistivity of Ag is only marginally lower

(5.7 %) than the Cu bulk electrical resistivity, the possible impact of the Ag on the electrical conductivity of the sintered particle system is limited. Considering Ag is more expensive than Cu, the addition of Ag can be concluded to be undesirable. However, for slow thermal particle sintering the addition of Ag was found to be beneficial. In an air environment the Cu oxidised and hence became dielectric but at Ag content 3, 8 and 25 wt% the Ag there was a significant reduction in electrical resistance. It was hypothesised this was due to the Ag content migrating forming a connected grid capable of conducting electricity. During thermal sintering in an inert environment it was found that the Ag content accumulates primarily around the necks of adjacent Cu particles. This was reasoned to be the results of surface tension acting on the mobile Ag and the Ag-Cu interface being energetically favourable over the Ag-gas interface. This phenomenon was further investigated in a theoretical simulation, calculating the theoretical reduction in Cu-Cu inter-particle resistance due to Ag accumulation in the necking region to inform process design if this phenomenon is to be exploited to reduce electrical resistance in a Cu particle network with a low amount of Ag. Future work would be useful to experimentally validate the predicted theoretical trends of the simulation of the impact of Ag accumulation in Cu adjacent particle necks. This would entail measuring the electrical resistivity of Cu NPs with additions of various Ag concentrations after thermal sintering at various temperatures in an inert environment.

The impact of cyclic bending on electrical resistance of inkjet printed and laser sintered Cu NP and Ag NP tracks was investigated. Ag NP tracks were found to be more resilient to cyclic bending than Cu NP tracks. SEM analysis showed that crack growth was the major driver for the observed increase in resistance of the Cu NP tracks which was not found to be the case with the Ag NP tracks. It was hypothesised that the greater width of the Cu particle size distribution compared to Ag likely contributed to the Cu tracks being less resilient to cyclic bending. Future work should investigate this hypothesis by measuring the impact of cyclic bending on electrical resistance of various particle size distribution widths of the same material (e.g. Cu or Ag NPs).

7 REFERENCES

3T RPD®, 2014. 3T produces Pure Copper Heat Exchanger using metal 3D Printing [WWW Document]. URL https://www.3trpd.co.uk/3t-success-with-pure-copper-am-production/ (accessed 11.30.17).

Aksomaityte, G., Poliakoff, M., Lester, E., 2013. The production and formulation of silver nanoparticles using continuous hydrothermal synthesis. Chem. Eng. Sci. 85, 2–10. https://doi.org/10.1016/j.ces.2012.05.035

Alam, M., Mavroidis, C., Langrana, N., Bidaud, P., 1999. Mechanism design using rapid prototyping, in: Proceedings of the 10th World Congress on the Theory of Machines and Mechanisms; June 20 - 24. University of Oulu, Finland, pp. 930–938.

Alting, L., Kimura, F., Hansen, H.N., Bissacco, G., 2003. Micro Engineering. CIRP Ann. 52, 635–657.

Alzoubi, K., Lu, S., Sammakia, B., Poliks, M., 2011. Factor Effect Study for the High Cyclic Bending Fatigue of Thin Films on PET Substrate for Flexible Displays Applications. J. Disp. Technol. 7, 348–355. https://doi.org/10.1109/JDT.2010.2076772

Amato, K.N., Gaytan, S.M., Murr, L.E., Martinez, E., Shindo, P.W., Hernandez, J., Collins, S., Medina, F., 2012. Microstructures and mechanical behavior of Inconel 718 fabricated by selective laser melting. Acta Mater. 60, 2229–2239. https://doi.org/10.1016/j.actamat.2011.12.032

Amendola, V., Meneghetti, M., Granozzi, G., Agnoli, S., Polizzi, S., Riello, P., Boscaini, A., Anselmi, C., Fracasso, G., Colombatti, M., Innocenti, C., Gatteschi, D., Sangregorio, C., 2011. Top-down synthesis of multifunctional iron oxide nanoparticles for macrophage labelling and manipulation. J. Mater. Chem. 21, 3803–3813. https://doi.org/10.1039/c0jm03863f

Anderson, C., 2012. Makers: The New Industrial Revolution. Crown Business, New York.

Argun, A.A., Aubert, P.-H., Thompson, B.C., Schwendeman, I., Gaupp, C.L., Hwang, J., Pinto, N.J., Tanner, D.B., Macdiarmid, A.G., Reynolds, J.R., 2004. Multicolored Electrochromism in Polymers: Structures and Devices. Chem. Mater. 16, 4401–4412. https://doi.org/10.1021/cm049669l

Arpaci, V.S., 1966. Conduction heat transfer, Vol. 237. ed. Addison-Wesley, Reading, MA. https://doi.org/10.1036/1097-8542.155700

AZoM, n.d. Properties: Silver - Applications and Properties of Silver [WWW Document]. URL https://www.azom.com/properties.aspx?ArticleID=600 (accessed 6.10.20a).

AZoM, n.d. Properties: An Introduction to Copper [WWW Document]. URL https://www.azom.com/properties.aspx?ArticleID=597 (accessed 6.10.20b).

Bächer, M., Bickel, B., James, D., Pfister, H., 2012. Fabricating articulated characters from skinned meshes. ACM Trans. Graph. 31, 47–51.

Bai, Y., Williams, C.B., 2018. Binder jetting additive manufacturing with a particle-free metal ink as a binder precursor. Mater. Des. 147, 146–156. https://doi.org/10.1016/j.matdes.2018.03.027

Bai, Y., Williams, C.B., 2015. An exploration of binder jetting of copper. Rapid Prototyp. J. 21, 793–814. https://doi.org/10.1108/RPJ-12-2014-0180

Ballman, A.A., Laudise, R.A., 1963. Hydrothermal growth, in: The Art and Science of Growing Crystals. pp. 231–251.

Beaman, J., Barlow, J., Bourell, D., Crawford, R., Marcus, H., McAlea, K., 1997. Solid freeform fabrication: a new direction in manufacturing. Kluwer Acad. Publ. Norwell, MA 2061, 25–49.

Bernard, G., Lupis, C.H.P., 1971. The surface tension of liquid silver alloys: Part I. Silver-gold alloys. Metall. Trans. 2, 555–559. https://doi.org/10.1007/BF02663348

Bonevich, J.E., Marks, L.D., 1992. Sintering behavior of ultrafine ceramic particles.

MRS Online Proc. Libr. Arch. 286, 3–8.

Born, M., Wolf, E., 2002. Elements of the theory of diffraction, in: Principles of Optics. Electromagnetic Theory of Propagation, Interference and Diffraction of Light. Cambridge University Press, Cambridge, U.K., pp. 436–471.

British Standards Institute, 2009. ISO 13320:2009 Particle size analysis — Laser diffraction methods.

Brouwers, H.J.H., 2006. Particle-size distribution and packing fraction of geometric random packings. Phys. Rev. E - Stat. Nonlinear, Soft Matter Phys. 74, 031309. https://doi.org/10.1103/PhysRevE.74.031309

Buffat, P., Borel, J.P., 1976. Size effect on the melting temperature of gold particles. Phys. Rev. A 13, 2287–2298. https://doi.org/10.1103/PhysRevA.13.2287

Caglioti, G., Paoletti, A., Ricci, F.P., 1958. Choice of collimators for a crystal spectrometer for neutron diffraction. Nucl. Instruments 3, 223–228. https://doi.org/10.1016/0369-643X(58)90029-X

Cali, J., Calian, D.A., Amati, C., Kleinberger, R., Steed, A., Kautz, J., Weyrich, T., 2012. 3D-Printing of Non-Assembly, Articulated Models. Acm Trans. Graph. 31, 130–138. https://doi.org/Artn 130 10.1145/2366145.2366149

Calvert, P., 2001. Inkjet printing for materials and devices. Chem. Mater. 13, 3299–3305. https://doi.org/10.1021/cm0101632

Campbell, C.T., Parker, S.C., Starr, D.E., 2002. The effect of size-dependent nanoparticle energetics on catalyst sintering. Science (80-.). 298, 811–814. https://doi.org/10.1126/science.1075094

Campbell, T., Kalia, R.K., Nakano, A., Vashishta, P., Ogata, S., Rodgers, S., 1999. Dynamics of Oxidation of Aluminum Nanoclusters using Variable Charge Molecular-Dynamics Simulations on Parallel Computers. Phys. Rev. Lett. 82, 4866–4869.

Canfield, S., Frecker, M.I., 1999. Design of Compliant Mechanisms for Amplification

of Induced Strain Actuators., in: ASME Design Automation Conference. Las Vegas, NV.

Chang, J., Ge, T., Sanchez-Sinencio, E., 2012. Challenges of printed electronics on flexible substrates. Midwest Symp. Circuits Syst. 582–585. https://doi.org/10.1109/MWSCAS.2012.6292087

Chang, J.B., Liu, V., Subramanian, V., Sivula, K., Luscombe, C., Murphy, A., Liu, J., Fréchet, J.M.J., 2006. Printable polythiophene gas sensor array for low-cost electronic noses. J. Appl. Phys. 100, 14506. https://doi.org/10.1063/1.2208743

Chang, K., Kim, Y.H., Kim, Y.J., Yoon, Y.J., 2007. Functional antenna integrated with relative humidity sensor using synthesised polyimide for passive RFID sensing. Japanese J. Appl. Physics, Part 1 Regul. Pap. Short Notes Rev. Pap. 43, 7–8. https://doi.org/10.1049/el

Chang, S.-C., Liu, J., Bharathan, J., Yang, Y., Onohara, J., Kido, J., 1999. Multicolor Organic Light-Emitting Diodes Processed by Hybrid Inkjet Printing. Adv. Mater. 11, 734–737. https://doi.org/10.1002/(SICI)1521-4095(199906)11:9<734::AID-ADMA734>3.0.CO;2-D

Chee, S.-S., Lee, J.-H., 2014. Preparation and oxidation behavior of Ag-coated Cu nanoparticles less than 20 nm in size. J. Mater. Chem. C 2, 5372–5381. https://doi.org/10.1039/C4TC00509K

Chee, S.S., Lee, J.H., 2017. Preparation and characterization of sub-20 nm CuX@Ag1core-shell nanoparticles by changing concentration of silver precursor. Mater. Chem. Phys. 185, 176–182. https://doi.org/10.1016/j.matchemphys.2016.10.020

Chen, Z., Cao, Y., Qian, J., Ai, X., Yang, H., 2010. Facile synthesis and stable lithium storage performances of Sn-sandwiched nanoparticles as a high capacity anode material for rechargeable Li batteries. J. Mater. Chem. 20, 7266–7271. https://doi.org/10.1039/c0jm00829j

Chen, Z., Meng, H., Xing, G., Chen, C., Zhao, Y., Jia, G., Wang, T., Yuan, H., Ye, C.,

Zhao, F., Chai, Z., Zhu, C., Fang, X., Ma, B., Wan, L., 2006. Acute toxicological effects of copper nanoparticles in vivo. Toxicol. Lett. 163, 109–120. https://doi.org/10.1016/j.toxlet.2005.10.003

Chen, Z., Mochizuki, D., Maitani, M.M., Wada, Y., 2013. Facile synthesis of bimetallic Cu-Ag nanoparticles under microwave irradiation and their oxidation resistance. Nanotechnology 24, 1–9. https://doi.org/10.1088/0957-4484/24/26/265602

Choi, E.B., Lee, J.H., 2016. Submicron Ag-coated Cu particles and characterization methods to evaluate their quality. J. Alloys Compd. 689, 952–958. https://doi.org/10.1016/j.jallcom.2016.08.009

Choi, H., Veriansyah, B., Kim, J., Kim, J.D., Kang, J.W., 2010. Continuous synthesis of metal nanoparticles in supercritical methanol. J. Supercrit. Fluids 52, 285–291. https://doi.org/10.1016/j.supflu.2010.01.015

Clare, A.T., Chalker, P.R., Davies, S., Sutcliffe, C.J., Tsopanos, S., 2008. Selective laser melting of high aspect ratio 3D nickel-titanium structures two way trained for MEMS applications. Int. J. Mech. Mater. Des. 4, 181–187. https://doi.org/10.1007/s10999-007-9032-4

Clusel, M., Corwin, E.I., Siemens, A.O.N., Bruji, J., 2009. A granocentric model for random packing of jammed emulsions. Nature 460, 611–615. https://doi.org/10.1038/nature08158

Coble, R.L., 1958. Initial Sintering of Alumina and Hematite. J. Am. Ceram. Soc. 41, 55–62.

Compton, B.G., Lewis, J.A., 2014. 3D-printing of lightweight cellular composites. Adv. Mater. 26, 5930–5935. https://doi.org/10.1002/adma.201401804

Conner, B.P., Manogharan, G.P., Martof, A.N., Rodomsky, L.M., Rodomsky, C.M., Jordan, D.C., Limperos, J.W., 2014. Making sense of 3-D printing: Creating a map of additive manufacturing products and services. Addit. Manuf. 1, 64–76. https://doi.org/10.1016/j.addma.2014.08.005

Crump, S.S., 1992. Apparatus and method for creating three-dimensional objects. 5121329.

Cullity, B.D., Stock, S.R., 2014. Elements of X-Ray Diffraction, 3rd ed. Pearson Education Limited. https://doi.org/10.1016/0014-5793(79)80596-7

Cummins, G., Desmulliez, M.P.Y., 2012. Inkjet printing of conductive materials : a review. Circuit World 38, 193–213. https://doi.org/10.1108/03056121211280413

Dang, T.M.D., Le, T.T.T., Fribourg-Blanc, E., Dang, M.C., 2011. Synthesis and optical properties of copper nanoparticles prepared by a chemical reduction method. Adv. Nat. Sci. Nanosci. Nanotechnol. 2. https://doi.org/10.1088/2043-6262/2/1/015009

De Gans, B.J., Duineveld, P.C., Schubert, U.S., 2004. Inkjet printing of polymers: State of the art and future developments. Adv. Mater. 16, 203–213. https://doi.org/10.1002/adma.200300385

Deckard, C.R., Beaman, J.J., Darrah, J.F., 1992. Method for selective laser sintering with layerwise cross-scanning. 5155324.

Deegan, R.D., Bakajin, O., Dupont, T.F., Huber, G., Nagel, S.R., Witten, T.A., 1997. Capillary flow as the cause of ring stains from dried liquid drops. Nature 389, 827–829.

Delley, B., Ellis, D.E., Freeman, A.J., Baerends, E.J., Post, D., 1983. Binding energy and electronic structure of small copper particles. Phys. Rev. B 27, 2132–2144. https://doi.org/10.1103/PhysRevB.27.2132

Demazeau, G., 2011. Solvothermal and hydrothermal processes: The main physico-chemical factors involved and new trends. Res. Chem. Intermed. 37, 107–123. https://doi.org/10.1007/s11164-011-0240-z

Dyos, G.T., 2012. The handbook of Electrical Resistivity : new materials and pressure effects. Institution of Engineering and Technology, London, UK.

Fang, Z Z, Wang, H., 2010. Sintering of ultrafine and nanosized particles, in: Fang, Zhigang Zak (Ed.), Sintering of Advanced Materials - Fundamentals and Processes. Woodhead Publishing, pp. 434–473. https://doi.org/http://dx.doi.org/10.1533/9781845699949.3.434

Felton, S.M., Tolley, M.T., Onal, C.D., Rus, D., Wood, R.J., 2013. Robot self-assembly by folding: A printed inchworm robot, in: IEEE International Conference on Robotics and Automation (ICRA); May 6-10. Karlsruhe, Germany, pp. 277–282. https://doi.org/10.1109/ICRA.2013.6630588

Feygin, M., Hsieh, B., 1991. Laminated object manufacturing: A simpler process. Solid Free. Fabr. Symp. Austin, TX, Aug, 12–14.

Foley, T.J., Johnson, C.E., Higa, K.T., 2005. Inhibition of Oxide Formation on Aluminum Nanoparticles by Transition Metal Coating. Chem. Mater. 17, 4086–4091. https://doi.org/10.1021/cm047931k

Fraunhofer ILT, 2017. Grünes Licht für neues 3D-Verfahren [WWW Document]. URL https://www.ilt.fraunhofer.de/de/presse/pressemitteilungen/pm2017/pressemitteilung-30-08-2017.html (accessed 11.30.17).

Fraunhofer Institute for Laser Technology (ILT), 2011. Generative Fertigung von Kupferbauteilen mit Selective Laser Melting [WWW Document]. URL https://www.ilt.fraunhofer.de/content/dam/ilt/de/documents/Leistungsangebote/lasermaterialbearbeitung/HZ_Generative_Fertigung_von_Kupferbauteilen_mit_SLM_2011.pdf (accessed 11.30.17).

Frigola, P., Harrysson, O.A., Horn, T.J., West, H.A., Aman, R.L., Rigsbee, J.M., Ramirez, D.A., Murr, L.E., Medina, F., Wicker, R.B., Rodriguez, E., 2014. Fabricating copper components with electron beam melting. Adv. Mater. Process. 172, 20–24.

FUJIFILM Dimatix, 2016. FUJIFILM Dimatix Materials Printer Jettable Fluid Formulation Guidelines [WWW Document]. URL https://www.fujifilmusa.com/shared/bin/Dimatix_Materials_Printer_Jettable_

Fluid_Formulation_Guidelines_05-13.pdf (accessed 5.4.19).

Furnas, C.C., 1931. Grading Aggregates: I—Mathematical Relations for Beds of Broken Solids of Maximum Density. Ind. Eng. Chem. 23, 1052–1058. https://doi.org/10.1021/ie50261a017

Gamerith, S., Klug, A., Scheiber, H., Scherf, U., Moderegger, E., List, E.J.W., 2007. Direct Ink-Jet Printing of Ag–Cu Nanoparticle and Ag-Precursor Based Electrodes for OFET Applications. Adv. Funct. Mater. 17, 3111–3118. https://doi.org/10.1002/adfm.200600762

Gao, W., Zhang, Y., Ramanujan, D., Ramani, K., Chen, Y., Williams, C.B., Wang, C.C.L., Shin, Y.C., Zhang, S., Zavattieri, P.D., 2015. The status, challenges, and future of additive manufacturing in engineering. Comput. Des. 69, 65–89. https://doi.org/10.1016/j.cad.2015.04.001

German, R.M., 2010. Thermodynamics of sintering, in: Fang, Z.Z. (Ed.), Sintering of Advanced Materials - Fundamentals and Processes. Woodhead Publishing, pp. 3–32. https://doi.org/10.1533/9781845699949.1.3

Giannatsis, J., Dedoussis, V., 2009. Additive fabrication technologies applied to medicine and health care: a review. Int. J. Adv. Manuf. Technol. 40, 116–127.

Gibson, I., Rosen, D., Stucker, B., 2015. Additive Manufacturing Technologies: Rapid Prototyping to Direct Digital Manufacturing, in: Additive Manufacturing Technologies: 3D Printing, Rapid Prototyping, and Direct Digital Manufacturing, Second Edition. Springer, New York, NY, pp. 128–145. https://doi.org/10.1007/978-1-4939-2113-3

Glushko, O., Cordill, M.J., Klug, A., List-Kratochvil, E.J.W., 2016. The effect of bending loading conditions on the reliability of inkjet printed and evaporated silver metallization on polymer substrates. Microelectron. Reliab. 56, 109–113. https://doi.org/10.1016/j.microrel.2015.10.007

Goldfarb, M., Speich, J.E., 1999. A Well-Behaved Revolute Flexure Joint for Compliant Mechanism Design. J. Mech. Des. 121, 424.

https://doi.org/10.1115/1.2829478

Graz, I.M., Cotton, D.P.J., Lacour, S.P., 2009. Extended cyclic uniaxial loading of stretchable gold thin-films on elastomeric substrates. Appl. Phys. Lett. 94. https://doi.org/10.1063/1.3076103

Griffith, A.A., 1921. VI. The phenomena of rupture and flow in solids. Philos. Trans. R. Soc. london. Ser. A, Contain. Pap. a Math. or Phys. character 221, 163–198.

Grouchko, M., Kamyshny, A., Magdassi, S., 2009. Formation of air-stable copper–silver core–shell nanoparticles for inkjet printing. J. Mater. Chem. 19, 3057. https://doi.org/10.1039/b821327e

Grouchko, M., Kamyshny, A., Mihailescu, C.F., Anghel, D.F., Magdassi, S., 2011. Conductive Inks with a "Built-In" Mechanism That Enables Sintering at Room Temperature. ACS Nano 5, 3354–3359. https://doi.org/10.1021/nn2005848

Grouchko, M., Roitman, P., Zhu, X., Popov, I., Kamyshny, A., Su, H., Magdassi, S., 2014. Merging of metal nanoparticles driven by selective wettability of silver nanostructures. Nat. Commun. 5, 1–5. https://doi.org/10.1038/ncomms3994

Guo, N., Leu, M.C., 2013. Additive manufacturing: Technology, applications and research needs. Front. Mech. Eng. 8, 215–243. https://doi.org/10.1007/s11465-013-0248-8

Hague, R., Mansour, S., Saleh, N., 2004. Material and design considerations for Rapid Manufacturing. Int. J. Prod. Res. 42, 4691–4708. https://doi.org/10.1080/00207840410001733940

Halonen, E., Heinonen, E., Mäntysalo, M., 2013. The Effect of Laser Sintering Process Parameters on Cu Nanoparticle Ink in Room Conditions. Opt. Photonics J. 03, 40–44. https://doi.org/10.4236/opj.2013.34A007

Harrison, D.A., Yan, D., Blairs, S., 1977. The surface tension of liquid copper. J. Chem. Thermodyn. 9, 1111–1119.

He, J., Li, D., Lu, B., Wang, Z., Tao, Z., 2006. Custom fabrication of composite tibial

hemi-knee joint combining CAD/CAE/CAM techniques. Proc. Inst. Mech. Eng. H. 220, 823–30. https://doi.org/10.1243/09544119jeim207

Herring, C., 1950. Effect of change of scale on sintering phenomena. J. Appl. Phys. 21, 301–303. https://doi.org/10.1063/1.1699658

Higashitani, K., Yoshida, K., Tanise, N., Murata, H., 1993. Dispersion of coagulated colloids by ultrasonication. Colloids Surfaces A Physicochem. Eng. Asp. 81, 167–175. https://doi.org/10.1016/0927-7757(93)80243-8

Hilder, M., Winther-Jensen, B., Clark, N.B., 2009. Paper-based, printed zinc–air battery. J. Power Sources 194, 1135–1141.

Ho, C.C., Murata, K., Steingart, D.A., Evans, J.W., Wright, P.K., 2008. A SUPER INK JET PRINTED ZINC-SILVER 3D MICROBATTERY. J. Micromechanics Microengineering 19, 094013.

Huang, D., Liao, F., Molesa, S., Redinger, D., Subramanian, V., 2003. Plastic-Compatible Low Resistance Printable Gold Nanoparticle Conductors for Flexible Electronics. J. Electrochem. Soc. 150, G412–G417. https://doi.org/10.1149/1.1582466

Huang, Q., Zhu, Y., 2019. Printing Conductive Nanomaterials for Flexible and Stretchable Electronics: A Review of Materials, Processes, and Applications. Adv. Mater. Technol. 4, 1–41. https://doi.org/10.1002/admt.201800546

Hull, C.W., 1986. Apparatus for production of three-dimensional objects by stereolithography. 4575330.

Ida, K., Sugiyama, Y., Chujyo, Y., Tomonari, M., Tokunaga, T., Sasaki, K., Kuroda, K., 2010. In-situ TEM studies of the sintering behavior of copper nanoparticles covered by biopolymer nanoskin. J. Electron Microsc. (Tokyo). 59, 75–80. https://doi.org/10.1093/jmicro/dfq055

Ino, S., 1969. Stability of multiply-twinned particles. J. Phys. Soc. Japan 27, 941–953.

ISO/ASTM, 2015. ISO / ASTM52900-15, Standard Terminology for Additive

Manufacturing – General Principles – Terminology, International Organization for Standardization. https://doi.org/10.1520/ISOASTM52900-15

Jacobs, P., 1992. Rapid Prototyping & Manufacturing: Fundamentals of Stereolithography. Society of Manufacturing Engineers.

Jiang, Q., Shi, F.G., 1998. Size-dependent initial sintering temperature of ultrafine particles. J. Mater. Sci. Technol. 14, 171–172.

Jiang, W.G., Su, J.J., Feng, X.Q., 2008. Effect of surface roughness on nanoindentation test of thin films. Eng. Fract. Mech. 75, 4965–4972. https://doi.org/10.1016/j.engfracmech.2008.06.016

Johnson, D.L., Cutler, I.B., 1963. Diffusion Sintering: I, Initial Stage Sintering Models and Their Application to Shrinkage of Powder Compacts. J. Am. Ceram. Soc. 46, 541–545. https://doi.org/10.1111/j.1151-2916.1963.tb14606.x

Joo, M., Lee, B., Jeong, S., Lee, M., 2011. Laser sintering of Cu paste film printed on polyimide substrate. Appl. Surf. Sci. 258, 521–524. https://doi.org/10.1016/j.apsusc.2011.08.076

Jung, D.S., Lee, H.M., Kang, Y.C., Park, S.B., 2011. Air-stable silver-coated copper particles of sub-micrometer size. J. Colloid Interface Sci. 364, 574–581. https://doi.org/10.1016/j.jcis.2011.08.033

Kaden, L., Matthäus, G., Ullsperger, T., Engelhardt, H., Rettenmayr, M., Tünnermann, A., Nolte, S., 2017. Selective laser melting of copper using ultrashort laser pulses. Appl. Phys. A 123, 596. https://doi.org/10.1007/s00339-017-1189-6

Kamyshny, A., Magdassi, S., 2014. Conductive nanomaterials for printed electronics. Small 10, 3515–3535. https://doi.org/10.1002/smll.201303000

Kamyshny, A., Steinke, J., Magdassi, S., 2011. Metal-based Inkjet Inks for Printed Electronics. Open Appl. Phys. J. 4, 19–36. https://doi.org/10.2174/1874183501104010019

Kim, C.K., Lee, G.J., Lee, M.K., Rhee, C.K., 2014. A novel method to prepare Cu@Ag core-shell nanoparticles for printed flexible electronics. Powder Technol. 263, 1–6. https://doi.org/10.1016/j.powtec.2014.04.064

Kim, D., Jeong, S., Lee, S., Park, B.K., Moon, J., 2007. Organic thin film transistor using silver electrodes by the ink-jet printing technology. Thin Solid Films 515, 7692–7696. https://doi.org/10.1016/j.tsf.2006.11.141

Kim, H.S., Dhage, S.R., Shim, D.E., Hahn, H.T., 2009. Intense pulsed light sintering of copper nanoink for printed electronics. Appl. Phys. A Mater. Sci. Process. 97, 791–798. https://doi.org/10.1007/s00339-009-5360-6

Kim, K., Kim, K.L., Shin, K.S., 2011. Co-reduced Ag/Pd bimetallic nanoparticles: Surface enrichment of Pd revealed by Raman spectroscopy. J. Phys. Chem. C 115, 14844–14851. https://doi.org/10.1021/jp203160z

Kim, M., Nishikawa, H., 2015. Effects of bonding temperature on microstructure , fracture behavior and joint strength of Ag nanoporous bonding for high temperature die attach Ag nanoporous sheet ENIG finished Cu disk (upper) t = 2 mm , = 3 mm ENIG finished Cu disk C deposition layer. Mater. Sci. Eng. A 645, 264–272.

Kim, S.J., Stach, E.A., Handwerker, C.A., 2010. Fabrication of conductive interconnects by Ag migration in Cu-Ag core-shell nanoparticles. Appl. Phys. Lett. 96, 1–3. https://doi.org/10.1063/1.3364132

Kingery, W.D., Berg, M., 1955. Study of the Initial Stages of Sintering by Viscous Flow, Evaporation—Condensation, and Self-Diffusion. J. Appl. Phys. 26, 1205–1212. https://doi.org/10.1007/978-94-009-0741-6_22

Ko, Seung Hwan, Chung, J., Pan, H., Grigoropoulos, C.P., Poulikakos, D., 2007. Fabrication of multilayer passive and active electric components on polymer using inkjet printing and low temperature laser processing. Sensors Actuators A 134, 161–168. https://doi.org/10.1016/j.sna.2006.04.036

Ko, Seung H, Pan, H., Grigoropoulos, C.P., Luscombe, C.K., Fr, J.M.J., 2007. All-inkjet-

printed flexible electronics fabrication on a polymer substrate by low-temperature high-resolution selective laser sintering of metal nanoparticles. Nanotechnology 18, 345202. https://doi.org/10.1088/0957-4484/18/34/345202

Kruth, J.P., Froyen, L., Van Vaerenbergh, J., Mercelis, P., Rombouts, M., Lauwers, B., 2004. Selective laser melting of iron-based powder. J. Mater. Process. Technol. 149, 616–622. https://doi.org/10.1016/j.jmatprotec.2003.11.051

Kuczynski, G.C., 1949. Study of the sintering of glass. J. Appl. Phys. 20, 1160–1163. https://doi.org/10.1063/1.1698291

Kwon, J., Cho, H., Eom, H., Lee, H., Suh, Y.D., Moon, H., Shin, J., Hong, S., Ko, S.H., 2016. Low-Temperature Oxidation-Free Selective Laser Sintering of Cu Nanoparticle Paste on a Polymer Substrate for the Flexible Touch Panel Applications. ACS Appl. Mater. Interfaces 8, 11575–11582. https://doi.org/10.1021/acsami.5b12714

Laliberté, T., Gosselin, C.M., Côté, G., 1999. Rapid prototyping of mechanisms, in: Proceedings of the 10th World Congress on the Theory of Machines and Mechanisms; June 20 - 24. University of Oulu, Finland, pp. 959–964.

Lange, F.F., 1984. Sinterability of Agglomerated Powders. J. Am. Ceram. Soc. 67, 83–89. https://doi.org/10.1111/j.1151-2916.1984.tb09620.x

Lee, B., Kim, Y., Yang, S., Jeong, I., Moon, J., 2009. A low-cure-temperature copper nano ink for highly conductive printed electrodes. Curr. Appl. Phys. 9, e157–e160. https://doi.org/10.1016/j.cap.2009.03.008

Lee, C., Kim, N.R., Koo, J., Lee, Y.J., Lee, H.M., 2015. Cu-Ag core-shell nanoparticles with enhanced oxidation stability for printed electronics. Nanotechnology 26, 455601. https://doi.org/10.1088/0957-4484/26/45/455601

Lee, Jeonghyeon, Lee, B., Jeong, S., Kim, Y., Lee, M., 2014. Microstructure and electrical property of laser-sintered Cu complex ink. Appl. Surf. Sci. 307, 42–45. https://doi.org/10.1016/j.apsusc.2014.03.127

Lee, J.W., Lan, P.X., Kim, B., Lim, G., Cho, D., 2008. Fabrication and Characteristic Analysis of a Poly (propylene fumarate) Scaffold Using Micro-Stereolithography Technology. J. Biomed. Mater. Res. Part B Appl. Biomater. An Off. J. Soc. Biomater. Japanese Soc. Biomater. Aust. Soc. Biomater. Korean Soc. Biomater. 87, 1–9. https://doi.org/10.1002/jbm.b.31057

Lee, Jaehwan, Kim, S., Lee, Jinjae, Yang, D., Park, C., Ryu, S., Park, I., 2014. A stretchable strain sensor based on a metal nanoparticle thin fi lm for human motion detection. Nanoscale 11932–11939. https://doi.org/10.1039/c4nr03295k

Lee, K., Hee, R., Yang, D., Hu, S., 2008. Advances in 3D nano / microfabrication using two-photon initiated polymerization. Prog. Polym. Sci. 33, 631–681. https://doi.org/10.1016/j.progpolymsci.2008.01.001

Lee, M.-Y., Chang, C.-C., Ku, Y.C., 2008. New layer-based imaging and rapid prototyping techniques for computer-aided design and manufacture of custom dental restoration. J. Med. Eng. Technol. 32, 83–90. https://doi.org/10.1080/03091900600836642

Lester, E., Blood, P., Denyer, J., Giddings, D., Azzopardi, B., Poliakoff, M., 2006. Reaction engineering: The supercritical water hydrothermal synthesis of nano-particles. J. Supercrit. Fluids 37, 209–214. https://doi.org/10.1016/j.supflu.2005.08.011

Leuders, S., Thöne, M., Riemer, A., Niendorf, T., Tröster, T., Richard, H.A., Maier, H.J., 2013. On the mechanical behaviour of titanium alloy TiAl6V4 manufactured by selective laser melting: Fatigue resistance and crack growth performance. Int. J. Fatigue 48, 300–307. https://doi.org/10.1016/j.ijfatigue.2012.11.011

Li, D., Sutton, D., Burgess, A., Graham, D., Calvert, P.D., 2009. Conductive copper and nickel lines via reactive inkjet printing. J. Mater. Chem. 19, 3719–3724. https://doi.org/10.1039/b820459d

Li, J., Mayer, J.W., Colgan, E.G., 1991. Oxidation and protection in copper and copper alloy thin films. J. Appl. Phys. 70, 2820–2827. https://doi.org/10.1063/1.349344

Li, J., Yu, X., Shi, T., Cheng, C., Fan, J., Cheng, S., Li, T., Liao, G., Tang, Z., 2017. Depressing of Cu[sbnd]Cu bonding temperature by composting Cu nanoparticle paste with Ag nanoparticles. J. Alloys Compd. 709, 700–707. https://doi.org/10.1016/j.jallcom.2017.03.220

Li, W., Hu, D., Li, L., Li, C., Jiu, J., Chen, C., Ishina, T., Sugahara, T., Suganuma, K., 2017. Printable and flexible copper-silver alloy electrodes with high conductivity and ultrahigh oxidation resistance. ACS Appl. Mater. Interfaces acsami.7b05308. https://doi.org/10.1021/acsami.7b05308

Li, W.W., Wang, Y., Wang, M., Li, W.W., Tan, J., You, C., Chen, M., 2016. Synthesis of stable CucoreAgshell&Ag particles for direct writing flexible paper-based electronics. RSC Adv. 6, 62236–62243. https://doi.org/10.1039/c6ra11965d

Lipson, H., 2007. Printable 3D models for customized hands-on education., in: Mass Customization and Personalization (MCPC); October 7-10. MIT Cambridge, Massachusetts.

Lipson, H., Moon, F.C., Hai, J., Paventi, C., 2005. 3-D Printing the History of Mechanisms. J. Mech. Des. 127, 1029. https://doi.org/10.1115/1.1902999

Liu, W., Wang, Y., Zheng, Z., Wang, C., An, R., Tian, Y., Kong, L., Xu, R., 2019. Laser sintering mechanism and shear performance of Cu–Ag–Cu joints with mixed bimodal size Ag nanoparticles. J. Mater. Sci. Mater. Electron. 1–7. https://doi.org/10.1007/s10854-019-01094-6

Loffredo, F., Burrasca, G., Quercia, L., 2007. Gas sensor devices obtained by ink-jet printing of polyaniline suspensions. Macromol. Symp. 247, 357–363.

Lopez-Espiricueta, D., Fearon, E., Edwardson, S., Dearden, G., 2016. Direct write processing of multi-micron thickness copper nano-particle paste on flexible substrates with 532 nm laser wavelength. Phys. Procedia 83, 194–203.

https://doi.org/10.1016/j.phpro.2016.08.008

Lu, C.A., Lin, P., Lin, H.C., Wang, S.F., 2007. Characterization of the low-curing-temperature silver paste with silver 2-ethylhexanoate addition. Japanese J. Appl. Physics, Part 1 Regul. Pap. Short Notes Rev. Pap. 46, 251–255. https://doi.org/10.1143/JJAP.46.251

Lu, Y., Liu, G.L., Lee, L.P., 2005. High-density silver nanoparticle film with temperature-controllable interparticle spacing for a tunable surface enhanced Raman scattering substrate. Nano Lett. 5, 5–9. https://doi.org/10.1021/nl048965u

Lupo, D., Clemens, W., Breitung, S., 2013. Applications of Organic and Printed Electronics, Applications of Organic and Printed Electronics. Boston, MA, USA. https://doi.org/10.1007/978-1-4614-3160-2

Magdassi, S., Grouchko, M., Kamyshny, A., 2010. Copper nanoparticles for printed electronics: Routes towards achieving oxidation stability. Materials (Basel). 3, 4626–4638. https://doi.org/10.3390/ma3094626

Marcus, L., St, J.J., Barlow, W., David, L.B., Crawford, H., 1994. Solid Freeform Fabricatin Proceedings, in: SFF Symposium; August 8-10. Austin, Texas.

Marinov, V.R., Atanasov, Y.A., Khan, A., Vaselaar, D., Halvorsen, A., Schulz, D.L., Chrisey, D.B., 2007. Direct-write vapor sensors on FR4 plastic substrates. IEEE Sens. J. 7, 937–944. https://doi.org/10.1109/JSEN.2007.895964

Matilainen, V., Piili, H., Salminen, A., Syvänen, T., Nyrhilä, O., 2014. Characterization of process efficiency improvement in laser additive manufacturing. Phys. Procedia 56, 317–326. https://doi.org/10.1016/j.phpro.2014.08.177

Matula, R.A., 1979. Electrical resistivity of copper, gold, palladium, and silver. J. Phys. Chem. Ref. Data 8, 1147–1298. https://doi.org/10.1063/1.555614

Mavroidis, C., DeLaurentis, K.J., Won, J., Alam, M., 2000. Fabrication of Non-Assembly Mechanisms and Robotic Systems Using Rapid Prototyping. J. Mech.

Des. 123, 516–524. https://doi.org/10.1115/1.1415034

Mazumder, J., Schifferer, A., Choi, J., 1999. Direct materials deposition: designed macro and microstructure. Mater. Res. Innov. 3, 118–131. https://doi.org/10.1007/s100190050137

Meaden, G.T., 2013. Electrical resistance of metals. Springer.

Messing, G.L., Kumagai, M., 1994. Low-temperature sintering of α-alumina-seeded boehmite gels.

Meyers, M.A., Chawla, K.K., 1964. Mechanical Metallurgy. Principles and Applications. Prentice-Hall, Englewood Cliffs, NJ.

Min, H., Lee, B., Jeong, S., Lee, M., 2016. Laser-direct process of Cu nano-ink to coat highly conductive and adhesive metallization patterns on plastic substrate. Opt. Lasers Eng. 80, 12–16. https://doi.org/10.1016/j.optlaseng.2015.12.007

Mittal, J., Lin, K.-L., 2015. Exothermic low temperature sintering of Cu nanoparticles. Mater. Charact. 109, 19–24. https://doi.org/10.1016/j.matchar.2015.09.009

Möller, R., Schüler, T., Günther, S., Carlsohn, M.R., Munder, T., Fritzsche, W., 2008. Electrical DNA-chip-based identification of different species of the genus Kitasatospora. Appl. Microbiol. Biotechnol. 77, 1181–1188. https://doi.org/10.1007/s00253-007-1241-0

Money Metals Exchange, 2019. Money Metals Exchange [WWW Document]. URL https://www.moneymetals.com/ (accessed 5.26.19).

Moon, K.S., Dong, H., Maric, R., Pothukuchi, S., Hunt, A., Li, Y.I., Wong, C.P., 2005. Thermal behavior of silver nanoparticles for low-temperature interconnect applications. J. Electron. Mater. 34, 168–175. https://doi.org/10.1007/s11664-005-0229-8

Morisada, Y., Nagaoka, T., Fukusumi, M., Kashiwagi, Y., Yamamoto, M., Nakamoto, M., 2010. A low-temperature bonding process using mixed Cu-Ag

nanoparticles. J. Electron. Mater. 39, 1283–1288. https://doi.org/10.1007/s11664-010-1195-3

Munz, O.J., 1956. Photo-glyph recording. 2775758.

Murano 525 Gathan heating stage, User Manual, n.d.

Nanda, K.K., Maisels, A., Kruis, F.E., Fissan, H., Stappert, S., 2003. Higher Surface Energy of Free Nanoparticles. Phys. Rev. Lett. 91, 106102-1–4. https://doi.org/10.1103/PhysRevLett.91.106102

NASA, 2017. NASA Tests First 3-D Printed Bi-Metallic Rocket Engine Part [WWW Document]. URL https://www.nasa.gov/centers/marshall/news/news/releases/2017/nasa-tests-first-3-d-printed-rocket-engine-part-made-with-two-different-alloys.html (accessed 12.1.17).

NASA, 2015. NASA 3-D Prints First Full-Scale Copper Rocket Engine Part [WWW Document]. URL https://www.nasa.gov/marshall/news/nasa-3-D-prints-first-full-scale-copper-rocket-engine-part.html (accessed 12.1.17).

Niittynen, J., Abbel, R., Mäntysalo, M., Perelaer, J., Schubert, U.S., Lupo, D., 2014. Alternative sintering methods compared to conventional thermal sintering for inkjet printed silver nanoparticle ink. Thin Solid Films 556, 452–459. https://doi.org/10.1016/j.tsf.2014.02.001

Niittynen, J., Sowade, E., Kang, H., Baumann, R.R., Mäntysalo, M., 2015. Comparison of laser and intense pulsed light sintering (IPL) for inkjet-printed copper nanoparticle layers. Sci. Rep. 5, 1–10. https://doi.org/10.1038/srep08832

Njagi, J.I., Netzband, C.M., Goia, D. V., 2017. Deposition of hermetic silver shells onto copper flakes. J. Colloid Interface Sci. 488, 72–78. https://doi.org/10.1016/j.jcis.2016.10.087

Onal, C.D., Wood, R.J., Rus, D., 2011. Towards printable robotics: Origami-inspired planar fabrication of three-dimensional mechanisms, in: IEEE International

Conference on Robotics and Automation; May 9-13. IEEE, Shanghai, China, pp. 4608–4613. https://doi.org/10.1109/ICRA.2011.5980139

Onuh, S., Yusuf, Y., 1999. Rapid prototyping technology: applications and benefits for rapid product development. J. Intell. Manuf. 10, 301–311.

Pajor-Świerzy, A., Farraj, Y., Kamyshny, A., Magdassi, S., 2017a. Effect of carboxylic acids on conductivity of metallic films formed by inks based on copper@silver core-shell particles. Colloids Surfaces A Physicochem. Eng. Asp. 522, 320–327. https://doi.org/10.1016/j.colsurfa.2017.03.019

Pajor-Świerzy, A., Farraj, Y., Kamyshny, A., Magdassi, S., 2017b. Colloids and Surfaces A : Physicochemical and Engineering Aspects Air stable copper-silver core-shell submicron particles : Synthesis and conductive ink formulation. Colloids Surfaces A Physicochem. Eng. Asp. 521, 272–280. https://doi.org/10.1016/j.colsurfa.2016.08.026

Parekh, D.P., Cormier, D., Dickey, M.D., 2015. Multifunctional Printing: Incorporating Electronics into 3D Parts Made by Additive Manufacturing, in: Bandyopadhyay, A., Bose, S. (Eds.), Additive Manufacturing. CRC Press, Boca Raton, FL, pp. 215–258. https://doi.org/doi:10.1201/b18893-9

Park, B.K., Kim, D., Jeong, S., Moon, J., Kim, J.S., 2007. Direct writing of copper conductive patterns by ink-jet printing. Thin Solid Films 515, 7706–7711. https://doi.org/10.1016/j.tsf.2006.11.142

Park, J.H., Jeong, S., Lee, E.J., Lee, S.S., Seok, J.Y., Yang, M., Choi, Y., Kang, B., 2016. Transversally Extended Laser Plasmonic Welding for Oxidation-Free Copper Fabrication toward High-Fidelity Optoelectronics. Chem. Mater. 28, 4151–4159. https://doi.org/10.1021/acs.chemmater.6b00013

Park, S.-H., Kim, H.-S., 2014. Flash light sintering of nickel nanoparticles for printed electronics. Thin Solid Films 550, 575–581. https://doi.org/10.1016/j.tsf.2013.11.075

Park, S.W., Sugahara, T., Hatamura, M., Kagami, N., Sakamoto, S., Nagao, S.,

Suganuma, K., 2015. Surface modification of Cu flakes through Ag precipitation for low-temperature pressureless sintering bonding. Mater. Lett. 151, 68–71. https://doi.org/10.1016/j.matlet.2015.03.054

Park, Y.S., An, C.Y., Kannan, P.K., Seo, N., Zhuo, K., Yoo, T.K., Chung, C.H., 2016. Fabrication of dendritic silver-coated copper powders by galvanic displacement reaction and their thermal stability against oxidation. Appl. Surf. Sci. 389, 865–873. https://doi.org/10.1016/j.apsusc.2016.08.008

Pauling, L., 1960. The Nature of the Chemical Bond... Cornell University Press, Ithaca, NY.

Pawlow, P., 1909. Über die Abhängigkeit des Schmelzpunktes von der Oberflächenenergie eines festen Körpers. Zeitschrift für Phys. Chemie 65, 1–35. https://doi.org/10.1515/zpch-1909-6532

Pearson, W.B., 1967. A Handbook of Lattice Spacings and Structures of Metals and Alloys. Pergamon, Oxford, U.K.

Pereira, Z.S., Da Silva, E.Z., 2011. Cold welding of gold and silver nanowires: A molecular dynamics study. J. Phys. Chem. C 115, 22870–22876. https://doi.org/10.1021/jp207842v

Perelaer, J., De Gans, B.J., Schubert, U.S., 2006. Ink-jet printing and microwave sintering of conductive silver tracks. Adv. Mater. 18, 2101–2104. https://doi.org/10.1002/adma.200502422

Perelaer, J., de Laat, A.W.M., Hendriks, C.E., Schubert, U.S., 2008. Inkjet-printed silver tracks: low temperature curing and thermal stability investigation. J. Mater. Chem. 18, 3209. https://doi.org/10.1039/b720032c

Perelaer, J., Jani, R., Grouchko, M., Kamyshny, A., Magdassi, S., Schubert, U.S., 2012. Plasma and Microwave Flash Sintering of a Tailored Silver Nanoparticle Ink, Yielding 60% Bulk Conductivity on Cost-Effective Polymer Foils. Adv. Mater. 24, 3993–3998. https://doi.org/10.1002/adma.201200899

Perelaer, J., Smith, P.J., Mager, D., Soltman, D., Volkman, S.K., Subramanian, V., Korvink, J.G., Schubert, U.S., 2010. Printed electronics: the challenges involved in printing devices, interconnects, and contacts based on inorganic materials. J. Mater. Chem. 20, 8446. https://doi.org/10.1039/c0jm00264j

Pham, D., Dimov, S., 2003. Rapid prototyping and rapid tooling—the key enablers for rapid manufacturing. Proc. Inst. Mech. Eng. Part C J. Mech. Eng. Sci. 217, 1–23.

Pogson, S.R., Fox, P., Sutcliffe, C.J., O'Neill, W., 2003. The production of copper parts using DMLR. Rapid Prototyp. J. 9, 334–343. https://doi.org/10.1108/13552540310502239

Powell, R.W., Ho, C.Y., Liley, P.E., 1966. Thermal conductivity of selected materials, NSRDS-NBS 8 National Standard Reference Data Series. Washington D.C., USA.

Priest, J.W., Smith, C., DuBois, P., 1997. Liquid Metal Jetting for Printing Metal Parts. Proc. 8th Solid Free. Fabr. Symp. 1–9.

Qin, Y., 2010. Micromanufacturing engineering and technology. William Andrew.

Quadros, M.E., Marr, L.C., 2010. Environmental and human health risks of aerosolized silver nanoparticles. J. Air Waste Manag. Assoc. 60, 770–781. https://doi.org/10.3155/1047-3289.60.7.770

Rae, A., Hammer-Fritzinger, D., 2006. Creating metal and nonmetal nanosystems using conductive jettable inks. Solid State Technol. 49, 53–56.

Ramirez, D.A., Murr, L.E., Li, S.J., Tian, Y.X., Martinez, E., Martinez, J.L., Machado, B.I., Gaytan, S.M., Medina, F., Wicker, R.B., 2011. Open-cellular copper structures fabricated by additive manufacturing using electron beam melting. Mater. Sci. Eng. A 528, 5379–5386. https://doi.org/10.1016/j.msea.2011.03.053

Rengier, F., Mehndiratta, A., von Tengg-Kobligk, H., Zechmann, C.M., Unterhinninghofen, R., Kauczor, H.-U., Giesel, F.L., 2010. 3D printing based on

imaging data: review of medical applications. Int. J. Comput. Assist. Radiol. Surg. 5, 335–341. https://doi.org/10.1007/s11548-010-0476-x

RK Print, n.d. RK Print K Hand Coaters [WWW Document]. URL www.rkprint.com (accessed 5.6.18).

Rodríguez-Valverde, M.Á., Tirado-Miranda, M., 2009. A simpler derivation of the integral formula of electrical resistance. Eur. J. Phys. 30, L47. https://doi.org/10.1088/0143-0807/30/4/L01

Ross, M., 1969. Generalized Lindemann melting law. Phys. Rev. 184, 233–242. https://doi.org/10.1103/PhysRev.184.233

Rotello, V.M., 2004. Nanoparticles : building blocks for nanotechnology. Springer Science & Business Media.

Roy, N., Jou, W., Feng, H., Jeong, J., Wang, Y., Cullinan, M., 2017. LASER SINTERING OF COPPER NANOPARTICLES: A SIMPLIFIED MODEL FOR FLUENCE ESTIMATION AND VALIDATION, in: ASME 2017 12th International Manufacturing Science and Engineering Conference. Los Angeles, CA, USA, pp. 1–7. https://doi.org/10.1115/MSEC2017-2975

Sachlos, E., Czernuszka, J., 2003. Making tissue engineering scaffolds work. Review: the application of solid freeform fabrication technology to the production of tissue engineering scaffolds. Eur Cell Mater 5, 39–40.

Sachs, E.M., Haggerty, J.S., Cima, M.J., Williams, P.A., 1993. Three-dimensional printing techniques. 5204055 A.

Saleh, E., Zhang, F., He, Y., Vaithilingam, J., Fernandez, J.L., Wildman, R., Ashcroft, I., Hague, R., Dickens, P., Tuck, C., 2017. 3D Inkjet Printing of Electronics Using UV Conversion. Adv. Mater. Technol. 2, 2–9. https://doi.org/10.1002/admt.201700134

Schwartz, L.H., Cohen, J.B., 1987. Diffraction from Materials, 2nd ed. Springer-Verlag Berlin Heidelberg GmbH.

Sekitani, T., Nakajima, H., Maeda, H., Fukushima, T., Aida, T., Hata, K., Someya, T., 2009. Stretchable active-matrix organic light-emitting diode display using printable elastic conductors. Nat. Mater. 8, 494–499. https://doi.org/10.1038/NMAT2459

Sheng, H.W., Wilde, G., Ma, E., 2002. The competing crystalline and amorphous solid solutions in the Ag-Cu system. Acta Mater. 50, 475–488. https://doi.org/10.1016/S1359-6454(01)00374-3

Shi, J.L., Deguchi, Y., Sakabe, Y., 2005. Relation between grain growth, densification and surface diffusion in solid state sintering - A direct observation. J. Mater. Sci. 40, 5711–5719. https://doi.org/10.1007/s10853-005-1474-7

Shrotriya, V., 2009. Organic photovoltaics: Polymer power. Nat. Photonics 3, 447–449. https://doi.org/10.1038/nphoton.2009.130

Simonelli, M., Aboulkhair, N., Rasa, M., East, M., Tuck, C., Wildman, R., Salomons, O., Hague, R., 2019. Towards digital metal additive manufacturing via high-temperature drop-on-demand jetting. Addit. Manuf. 30, 100930. https://doi.org/10.1016/j.addma.2019.100930

Singare, S., Liu, Y., Li, D., Lu, B., Wang, J., He, S., 2007. Individually Prefabricated Prosthesis for Maxilla Reconstruction. https://doi.org/10.1111/j.1532-849X.2007.00266.x

Singer, F., Deisenroth, D.C., Hymas, D.M., 2017. Additively manufactured copper components and composite structures for thermal management applications, in: 16th IEEE ITHERM Conference. p. 174.

Singh, K.B., Tirumkudulu, M.S., 2007. Cracking in drying colloidal films. Phys. Rev. Lett. 98, 218302. https://doi.org/10.1103/PhysRevLett.98.218302

Singh, M., Haverinen, H.M., Dhagat, P., Jabbour, G.E., 2010. Inkjet Printing—Process and Its Applications. Adv. Mater. 22, 673–685. https://doi.org/10.1002/adma.200901141

Smith, P.J., Shin, D.Y., Stringer, J.E., Derby, B., Reis, N., 2006. Direct ink-jet printing and low temperature conversion of conductive silver patterns. J. Mater. Sci. 41, 4153–4158. https://doi.org/10.1007/s10853-006-6653-1

Sohn, H.Y., Moreland, C., 1968. The Effect of Particle Size Distribution on Packing Density. Can. J. Chem. Eng. 46, 162–167. https://doi.org/https://doi.org/10.1002/cjce.5450460305

Soltani, a, Khorramdel Vahed, B., Mardoukhi, a, Mäntysalo, M., 2015. Laser sintering of copper nanoparticles on top of silicon substrates. Nanotechnology 27, 035203. https://doi.org/10.1088/0957-4484/27/3/035203

Song, K., Kim, D., Li, X.-S., Jun, T., Jeong, Y., Moon, J., 2009. Solution processed invisible all-oxide thin film transistors. J. Mater. Chem. 19, 8881–8886. https://doi.org/10.1039/b912554j

Song, Y., Yan, Y., Zhang, R., Xu, D., Wang, F., 2002. Manufacture of the die of an automobile deck part based on rapid prototyping and rapid tooling technology. J. Mater. Process. Technol. 120, 237–242.

Speight, J.G., 2005. LANGE'S HANDBOOK OF CHEMISTRY, Sixteenth. ed. McGraw-Hill, Lramie, Wyoming, USA.

Sriraman, M.R., Babu, S.S., Short, M., 2010. Bonding characteristics during very high power ultrasonic additive manufacturing of copper. Scr. Mater. 62, 560–563. https://doi.org/10.1016/j.scriptamat.2009.12.040

Srivatsan, T.S., Ravi, B.G., Naruka, A.S., Riester, L., Yoo, S., Sudarshan, T.S., 2001. A study of microstructure and hardness of bulk copper sample obtained by consolidating nanocrystalline powders usng plasma pressure compaction. Mater. Sci. Eng. A 311, 22–27. https://doi.org/10.1016/S0921-5093(01)00931-5

Subramanian, P.R., Perepezko, J.H., 1993. Section II: Phase Diagram Evaluations The Ag-Cu (Silver-Copper) System. J. Phase Equilibria 14, 62–75.

Subramanian, V., Fréchet, J.M.J., Chang, P.C., Huang, D.C., Lee, J.B., Molesa, S.E., Murphy, A.R., Redinger, D.R., Volkman, S.K., 2005. Progress toward development of all-printed RFID tags: materials, processes, and devices. Proc. IEEE 93, 1330–1338. https://doi.org/10.1109/JPROC.2005.850305

Sukhotskiy, V., Karampelas, I.H., Garg, G., Verma, A., Tong, M., Vader, S., Vader, Z., Furlani, E.P., 2017. Magnetohydrodynamic Drop-on-Demand Liquid Metal 3D Printing. Solid Free. Fabr. Symp. 1806–1811.

Tabor, D., 1951. The hardness of metals. Clarendon Press.

Tang, S.V.Y., Lester, E., Khlobystov, A., 2014. Synthesis of nanomaterials for biomedical applications. University of Nottingham.

Tang, Y., Loh, H.T., Wong, Y.S., Fuh, J.Y.H., Lu, L., Wang, X., 2003. Direct laser sintering of a copper-based alloy for creating three-dimensional metal parts. J. Mater. Process. Technol. 140, 368–372. https://doi.org/10.1016/S0924-0136(03)00766-0

The University of Nottingham, n.d. Centre for Additive Manufacturing - The University of Nottingham [WWW Document]. URL https://www.nottingham.ac.uk/research/groups/cfam/ (accessed 10.12.17).

Thirumangalath, S.C., Vader, S., Vader, Z., 2017. Liquid Metal 3D Printing: A Magnetohydrodynamic Approach. A. Shvets, A. Drobotov, I. Gushin, A. Avdeev, Izv. VSTU 9, 1–11.

Thomas, C., Gaffney, T., Kaza, S., 1996. Rapid prototyping of large scale aerospace structures, in: Aerospace Applications Conference; February 10. IEEE, Manhattan Beach, California, pp. 219–230.

THOR LABS, 1999. 1/2" (12 mm or 13 mm) Travel Motorized Actuators [WWW Document]. URL https://www.thorlabs.de/newgrouppage9.cfm?objectgroup_id=1882 (accessed 5.4.19).

Tian, Y., Jiang, Z., Wang, Chenxi, Ding, S., Wen, J., Liu, Z., Wang, Chunqing, 2016. Sintering mechanism of the Cu-Ag core-shell nanoparticle paste at low temperature in ambient air. RSC Adv. 6, 91783–91790. https://doi.org/10.1039/c6ra16474a

Tolosa, I., Garciandía, F., Zubiri, F., Zapirain, F., Esnaola, A., 2010. Study of mechanical properties of AISI 316 stainless steel processed by "selective laser melting", following different manufacturing strategies. Int. J. Adv. Manuf. Technol. 51, 639–647. https://doi.org/10.1007/s00170-010-2631-5

Topsøe, H., 1968. Geometric factors in four point resistivity measurement. Bulletin 472, 63.

Tsai, C., Chen, S., Song, J., Chen, I., Lee, H., 2013. Thermal stability of Cu @ Ag core-shell nanoparticles. Corros. Sci. 74, 123–129. https://doi.org/10.1016/j.corsci.2013.04.032

Vaezi, M., Seitz, H., Yang, S., 2013. A review on 3D micro-additive manufacturing technologies. Int. J. Adv. Manuf. Technol. 67, 1721–1754. https://doi.org/10.1007/s00170-012-4605-2

Vaithilingam, J., Saleh, E., Körner, L., Wildman, R.D., Hague, R.J.M., Leach, R.K., Tuck, C.J., 2018. 3-Dimensional inkjet printing of macro structures from silver nanoparticles. Mater. Des. 139, 81–88. https://doi.org/10.1016/j.matdes.2017.10.070

Vaithilingam, J., Simonelli, M., Saleh, E., Senin, N., Wildman, R.D., Hague, R.J.M., Leach, R.K., Tuck, C.J., 2017. Combined Inkjet Printing and Infrared Sintering of Silver Nanoparticles using a Swathe-by-Swathe and Layer-by-Layer Approach for 3-Dimensional Structures. ACS Appl. Mater. Interfaces 9, 6560–6570. https://doi.org/10.1021/acsami.6b14787

Vitos, L., Ruban, A.V., Skriver, H.L., Kollar, J., 1998. The surface energy of metals. Surf. Sci. 411, 186–202. https://doi.org/https://doi.org/10.1016/S0039-6028(98)00363-X

Wang, J., Shin, S., 2017. Sintering of multiple Cu–Ag core–shell nanoparticles and properties of nanoparticle-sintered structures. RSC Adv. 7, 21607–21617. https://doi.org/10.1039/c7ra02611k

Wang, J., Shin, S., Hu, A., 2016. Geometrical Effects on Sintering Dynamics of Cu-Ag Core-Shell Nanoparticles. J. Phys. Chem. C 120, 17791–17800. https://doi.org/10.1021/acs.jpcc.6b05515

Wang, X., Liu, J., Wang, Y., Fu, Y., 2017. Fabrication of friction-reducing texture surface by selective laser melting of ink-printed (SLM-IP) copper (Cu) nanoparticles(NPs). Appl. Surf. Sci. 396, 659–664. https://doi.org/10.1016/j.apsusc.2016.11.003

Wang, Z., Teng, Y., Li, D., 2004. Fabrication of custom-made artificial semi-knee joint based on rapid prototyping technique: computer-assisted design and manufacturing. Chinese J. reparative Reconstr. Surg. 18, 347–351.

Wei, Y., Li, Y., Torah, R., Tudor, J., 2015. Laser curing of screen and inkjet printed conductors on flexible substrates, in: Symposium on Design, Test, Integration and Packaging of MEMS/MOEMS, DTIP 2015. pp. 4–7. https://doi.org/10.1109/DTIP.2015.7160991

White, L.R., 1982. Capillary rise in powders. J. Colloid Interface Sci. 90, 536–538. https://doi.org/10.1016/0021-9797(82)90319-8

Wolf, F.M., Perelaer, J., Stumpf, S., Bollen, D., Kriebel, F., Schubert, U.S., 2013. Rapid low-pressure plasma sintering of inkjet-printed silver nanoparticles for RFID antennas. J. Mater. Res. 28, 1254–1261. https://doi.org/10.1557/jmr.2013.73

Wolverton, C., Ozoliņš, V., Zunger, A., 1998. First-principles theory of short-range order in size-mismatched metal alloys: Cu-Au, Cu-Ag, and Ni-Au. Pysical Rev. B 57, 4332.

XJET [WWW Document], n.d. URL http://www.xjet3d.com/ (accessed 11.25.17).

Xu, H., Tang, X., Sun, H., Zhao, H., Li, M., 2017. Conductivity of silver and copper film printed by particle-free reactive inks, in: 18th International Conference on Electronic Packaging Technology, ICEPT 2017. pp. 1470–1473. https://doi.org/10.1109/ICEPT.2017.8046713

Yabuki, A., Arriffin, N., 2010. Electrical conductivity of copper nanoparticle thin films annealed at low temperature. Thin Solid Films 518, 7033–7037. https://doi.org/10.1016/j.tsf.2010.07.023

Yan, J., Zou, G., Wu, A., Ren, J., Hu, A., Zhou, Y.N., 2012. Polymer-protected Cu-Ag mixed NPs for low-temperature bonding application. J. Electron. Mater. 41, 1886–1892. https://doi.org/10.1007/s11664-012-2008-7

Yan, M.F., Rhodes, W.W., 1983. Low temperature sintering of TiO2. Mater. Sci. Eng. 61, 59–66. https://doi.org/10.1016/0025-5416(83)90126-X

Yang, M., Chon, M.W., Kim, J.H., Lee, S.H., Jo, J., Yeo, J., Ko, S.H., Choa, S.H., 2014. Mechanical and environmental durability of roll-to-roll printed silver nanoparticle film using a rapid laser annealing process for flexible electronics. Microelectron. Reliab. 54, 2871–2880. https://doi.org/10.1016/j.microrel.2014.07.004

Yap, C.Y., Chua, C.K., Dong, Z.L., Liu, Z.H., Zhang, D.Q., Loh, L.E., Sing, S.L., Yap, C.Y., Chua, C.K., Dong, Z.L., Liu, Z.H., Zhang, D.Q., Loh, L.E., 2016. Review of selective laser melting : Materials and applications. Appl. Phys. Rev. 2, 1–21. https://doi.org/10.1063/1.4935926

Yeadon, M., Yang, J.C., Averback, R.S., Bullard, J.W., Olynick, D.L., Gibson, J.M., 1997. In-situ observations of classical grain growth mechanisms during sintering of copper nanoparticles on (001) copper. Appl. Phys. Lett. 71, 1631–1633. https://doi.org/10.1063/1.120000

Yim, C., Sandwell, A., Park, S.S., 2016. Hybrid Copper-Silver Conductive Tracks for Enhanced Oxidation Resistance under Flash Light Sintering. ACS Appl. Mater. Interfaces 8, 22369–22373. https://doi.org/10.1021/acsami.6b07826

Yin, Z.P., Huang, Y.A., Bu, N.B., Wang, X.M., Xiong, Y.L., 2010. Inkjet printing for flexible electronics: Materials, processes and equipments. Chinese Sci. Bull. 55, 3383–3407. https://doi.org/10.1007/s11434-010-3251-y

Yoshioka, Y., Jabbour, G.E., 2006. Desktop inkjet printer as a tool to print conducting polymers. Synth. Met. 156, 779–783. https://doi.org/10.1016/j.synthmet.2006.03.013

Yu, X., Li, J., Shi, T., Cheng, C., Liao, G., Fan, J., Li, T., Tang, Z., 2017. A green approach of synthesizing of Cu-Ag core-shell nanoparticles and their sintering behavior for printed electronics. J. Alloys Compd. 724, 365–372. https://doi.org/10.1016/j.jallcom.2017.07.045

Zenou, M., Ermak, O., Saar, A., Kotler, Z., 2014. Laser sintering of copper nanoparticles. J. Phys. D. Appl. Phys. 47, 1–11. https://doi.org/10.1088/0022-3727/47/2/025501

Zhang, D.Q., Liu, Z.H., Chua, C.K., 2013. High value manufacturing : advanced research in virtual and rapid prototyping, in: High Value Manufacturing: Advanced Research in Virtual and Rapid Prototyping: Proceedings of the 6th International Conference on Advanced Research in Virtual and Rapid Prototyping. Leiria, Portugal, pp. 285–289.

Zhang, Q., Xie, J., Lee, J.Y., Zhang, J., Boothroyd, C., 2008. Synthesis of Ag@AgAu metal core/alloy shell bimetallic nanoparticles with tunable shell compositions by a galvanic replacement reaction. Small 4, 1067–1071. https://doi.org/10.1002/smll.200701196

Zhang, R., Lin, W., Lawrence, K., Wong, C.P., 2010. Highly reliable, low cost, isotropically conductive adhesives filled with Ag-coated Cu flakes for electronic packaging applications. Int. J. Adhes. Adhes. 30, 403–407. https://doi.org/10.1016/j.ijadhadh.2010.01.004

8 APPENDIX

8.1 Technical Data Sheet of the Copper (Cu) Inkjet Nanoparticle (NP) Ink

Technical Data Sheet

Product Name: Copper inkjet ink (Product ID: **PP-IJCU-8001**)

Product Description: Copper inkjet ink is designed for inkjet printing for versatile use in electronic applications. The copper ink is designed to be rapidly cured using Xenon flash or laser systems.

Preparation: Sedimentation may occur naturally over the lifetime of the product. Gently stir (not shake) the ink thoroughly before use to ensure the product is well mixed whilst care should be taken to avoid introducing air bubbles. Do not replace used ink in the container. This ink is designed for drop-on-demand print-heads. Once printed the ink should be sintered using a Xenon flash lamp or laser for ultimate results.

Properties of the uncured copper inkjet ink **Test**	**Properties**
Solids content	35 – 37 %
Density	1.39
Viscosity	22 cPs @ 25 °C
Temperature at 12cP	45 °C
Surface tension (mN/m)	35.2
Substrate compatibility	Polyimide, ITO-glass, Paper

Ink curing conditions **Test**	**Typical Properties**
Sintering Technique Compatibility	Xenon flash lamp (Heraeus Noblelight), Laser

Properties of the cured ink **Test**	**Properties**
Adhesion	5B
Optimum volume resistivity (Flash lamp)	0.003 Ω/□/mil

Storage and Shelf-life: Containers should be stored as specified with lids tightly sealed. We cannot assume responsibility for an ink that has not been stored in appropriate conditions or where the ink has been contaminated following use.
Inkjet heads can be cleaned using solvents such as iso-propanol.

Safety and Handling: For safe use of this product, please review relevant material and safety datasheet (MSDS).

For more information please contact:
Promethean Particles Ltd. 1 – 3 Genesis Park, Midland Way, Nottingham, NG7 3EF, UK
Email: info@proparticles.co.uk
Tel: +44(0)115 9678119
www.prometheanparticles.co.uk

8.2 MATLAB Script of Image Analysis of Copper (Cu) Nanoparticle (NP) Sintering In-situ a Field-emission Gun Scanning Electron Microscope (FEG-SEM)

8.2.1 Analysis of Sintering Copper (Cu) Nanoparticles

```
% Round objects analysis by David Pervan

%% Read image
filepath = ('400.1.tif');
image = imread(filepath);
figure(1); imshow(image);

%% Threshold image
bw = im2bw(image,0.55);
figure(3); imshow(bw);

%% Invert image
bw_inverted = ~bw;

%% Remove noise
% remove all object containing fewer than 100 pixels
bw_noiseremoved = bwareaopen(bw_inverted,100);

%% Determine particle size

stats = regionprops(bw_noiseremoved,'EquivDiameter');

folder = 'D:\SEM Images;
baseFileName = '400.1_stats.xlsx';
fullFileName = fullfile(folder, baseFileName);

writetable(struct2table(stats),fullFileName)

diameters = zeros(numel(stats),1); % CHANGE STUCTURE

for i = 1:(numel(stats))
    diameters(i) = stats(i).EquivDiameter; %ideal
end

diameters = sort(diameters);

scale_bar = (3438-3204)/1000; % apply scale bar from pixels to
nanometres
diameters = diameters/scale_bar;

baseFileName = '400.1_diameters.xlsx';
fullFileName = fullfile(folder, baseFileName);
xlswrite(fullFileName,diameters)
```

8.2.2 Analysis of Sintering Silver (Ag) Nanoparticles

```
datedir = dir('C:\SEM Images');
filenames = {datedir.name};
```

```
n = numel(filenames);

for i = 3:n
    filename = datedir(i).name;
    im=imread(filename);
    cropped_im=imcrop(im,[1 1 1280 959]);

    %% binarise - global threshold
    bw = imbinarize(im_ cropped);

    bw_noiseremoved = bwareaopen(imbinarize,75); % remove all object
containing fewer than 75 pixels

    %% Determine particle properties
    stats = regionprops(bw_noiseremoved,'EquivDiameter');

    %% number of discrete particles
    no_p = 0;

    for j = 1:(numel(stats))
        if stats(j).Solidity > 0.9
            no_p = no_p+1;
        end
    end

    % save number of discrete particles
    sheet = 'Sheet1';
    xlRange = strcat('B',num2str(i-2));
    xlswrite('no_of_discrete_particles.xlsx',no_p,sheet,xlRange)
end
```

8.3 XRD Spectra

8.3.1 XRD Spectrum of a Bar Coated Multi-layered Cu Sample After Heat Treatment

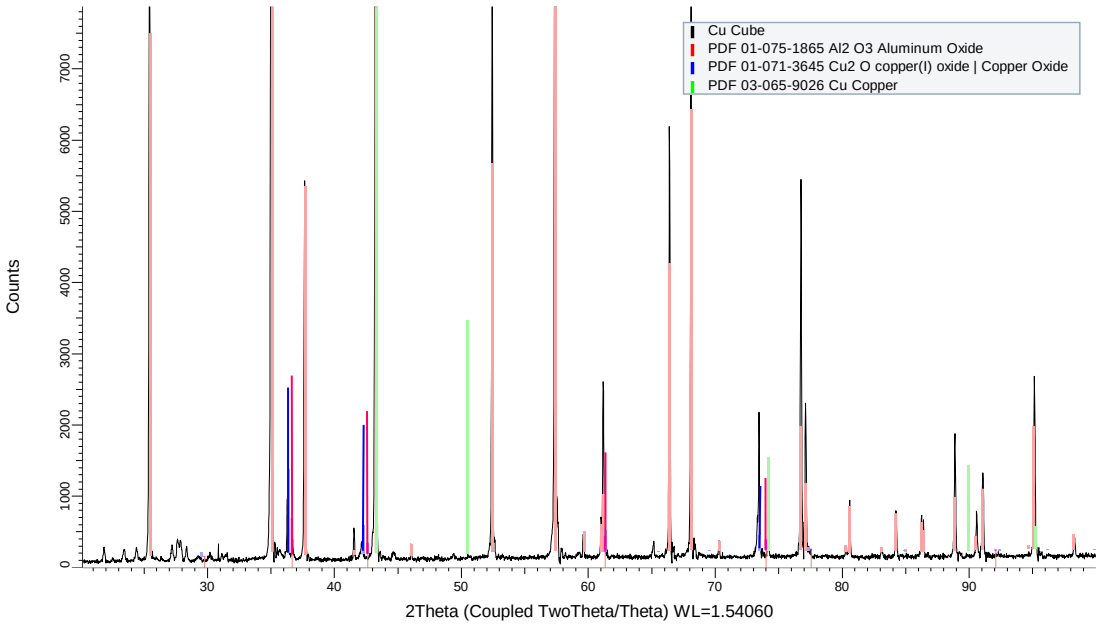


Figure 90. XRD spectrum of a bar coated Cu sample after heat treatment (Cu_2O and CuO peaks are highlighted in blue and pink, respectively). Note, the aluminium oxide peaks (highlighted in orange) stem from the substrate the sample was placed on during the XRD scan.

8.3.2 XRD Spectrum of Copper (Cu) Nanoparticles (NPs) prior and after Intense Pulsed Light (IPL) Sintering

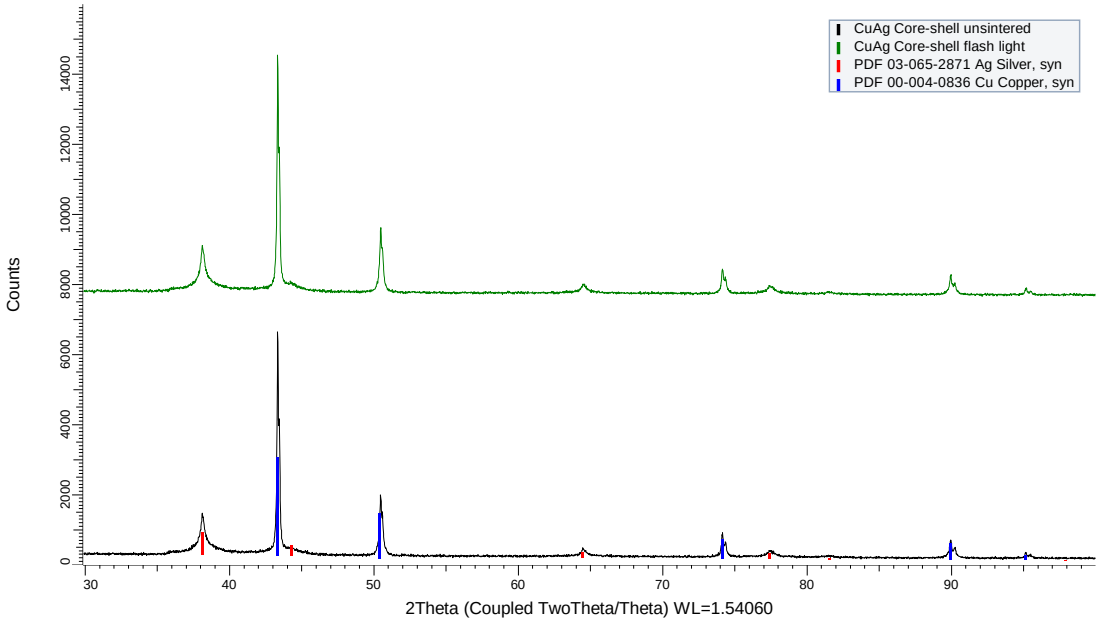


Figure 91. XRD Spectrum of Cu NPs before (bottom) and after (top) IPL sintering. Characteristic Cu and Ag peaks are indicated in blue and red, respectively.

8.3.3 XRD Spectra of Thermally Sintered Ag-Cu NPs in an Air Environment

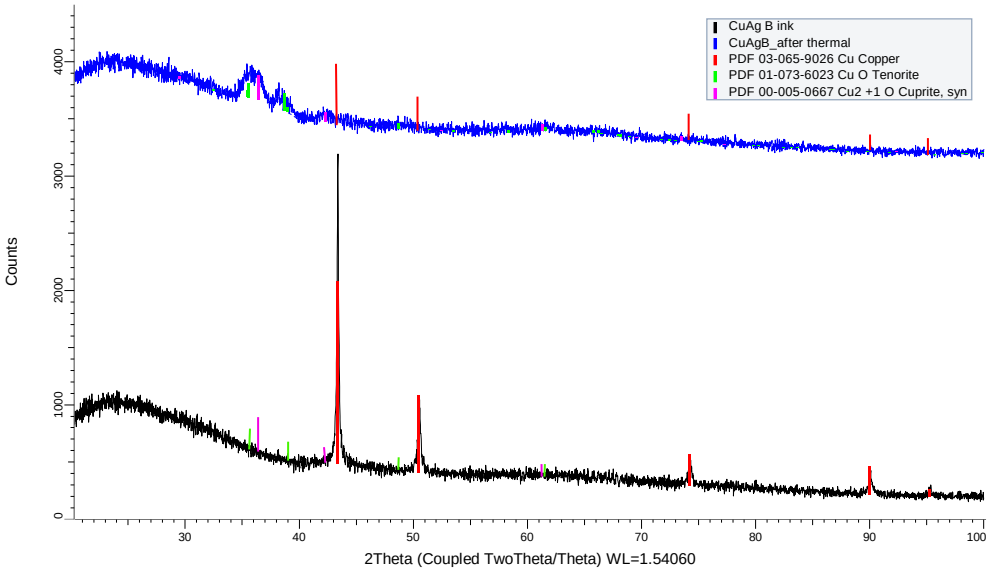


Figure 92. 0 wt% Ag in Cu NP before (bottom) and after (top) thermal sintering in air. Characteristic Cu, CuO, and Cu_2O peaks are indicated in red, green, and pink, respectively.

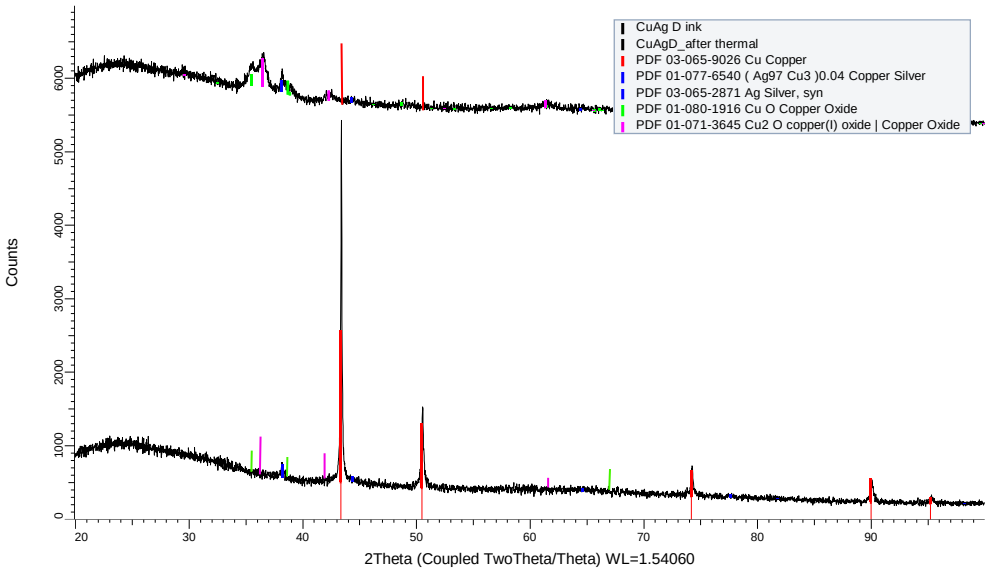


Figure 93. 1 wt% Ag in Cu NP before (bottom) and after (top) thermal sintering in air. Characteristic Cu, CuO, and Cu_2O peaks are indicated in red, green, and pink, respectively.

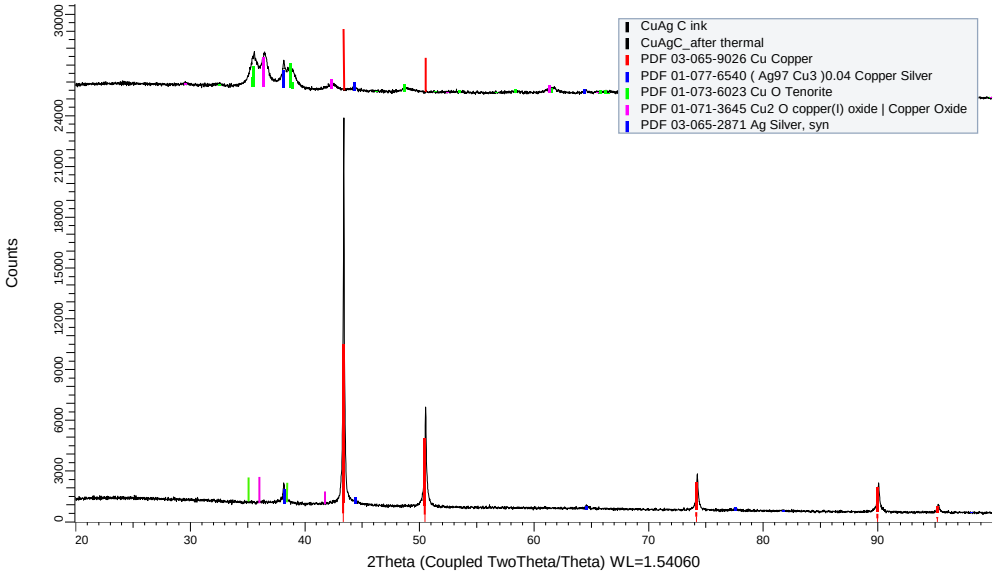


Figure 94. 3 wt% Ag in Cu NP before (bottom) and after (top) thermal sintering in air. Characteristic Ag, Cu, CuO, and Cu_2O peaks are indicated in blue, red, green, and pink, respectively.

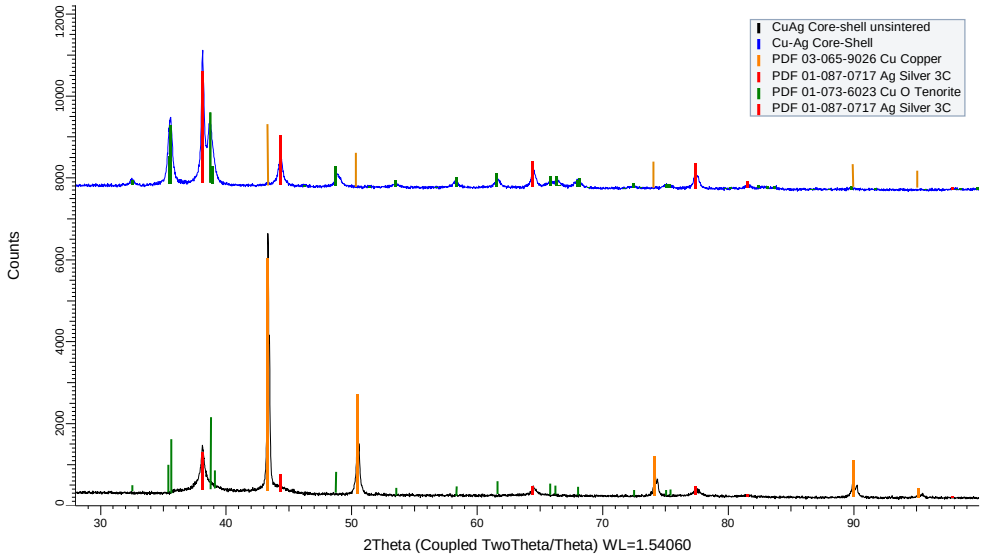


Figure 95. 8 wt% Ag in Cu NP before (bottom) and after (top) thermal sintering in air. Characteristic Ag, Cu, CuO peaks are indicated in blue, red, orange, and green, respectively.

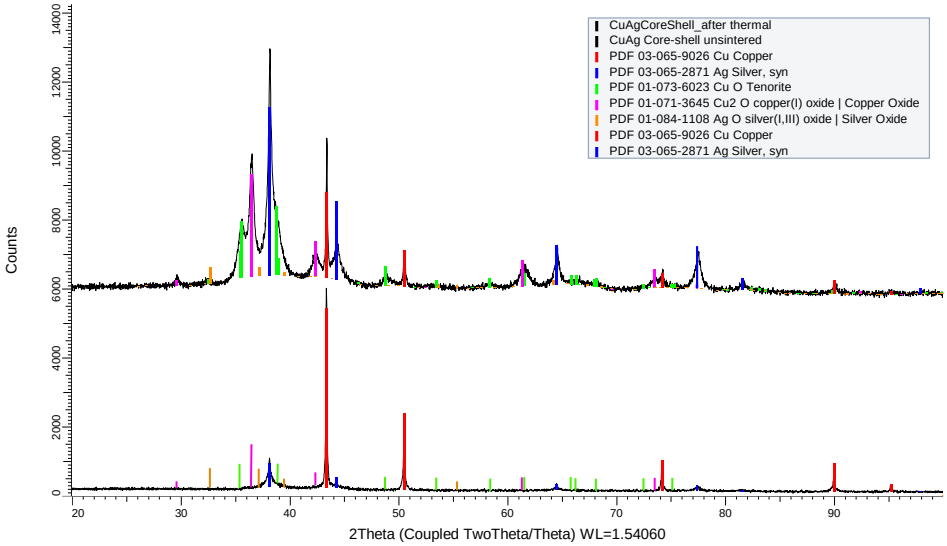


Figure 96. 25 wt% Ag in Cu NP before (bottom) and after (top) thermal sintering in air. Characteristic Ag, AgO, Cu, CuO, and Cu_2O peaks are indicated in blue, orange, red, green, and pink, respectively.

8.4 Data Tables of Mean Crystallite Sizes Before and After Sintering

Mean Cu crystallite size prior to laser sintering (nm)	Mean Cu crystallite size after laser sintering (nm)
315 ± 54	433 ± 73

Table 9. Mean Cu NP crystallite size before and after laser sintering obtained through the Scherrer Equation.

Mean Ag crystallite size prior to thermal sintering (nm)	Mean Ag crystallite size after thermal sintering (nm)
29 ± 5	63 ± 18

Table 10. Mean Ag crystallite size before and after thermal sintering.

Mean Cu crystallite size prior to thermal sintering (nm)	Mean Cu_2O crystallite size after thermal sintering (nm)	Mean CuO crystallite size after thermal sintering (nm)
166 ± 82	19 ± 7	15 ± 4

Table 11. Mean crystallite size before thermal sintering of Cu NP and mean crystallite sizes after thermal sintering of Cu_2O and CuO.

8.5 Optical Images of Laser Sintering Experiments

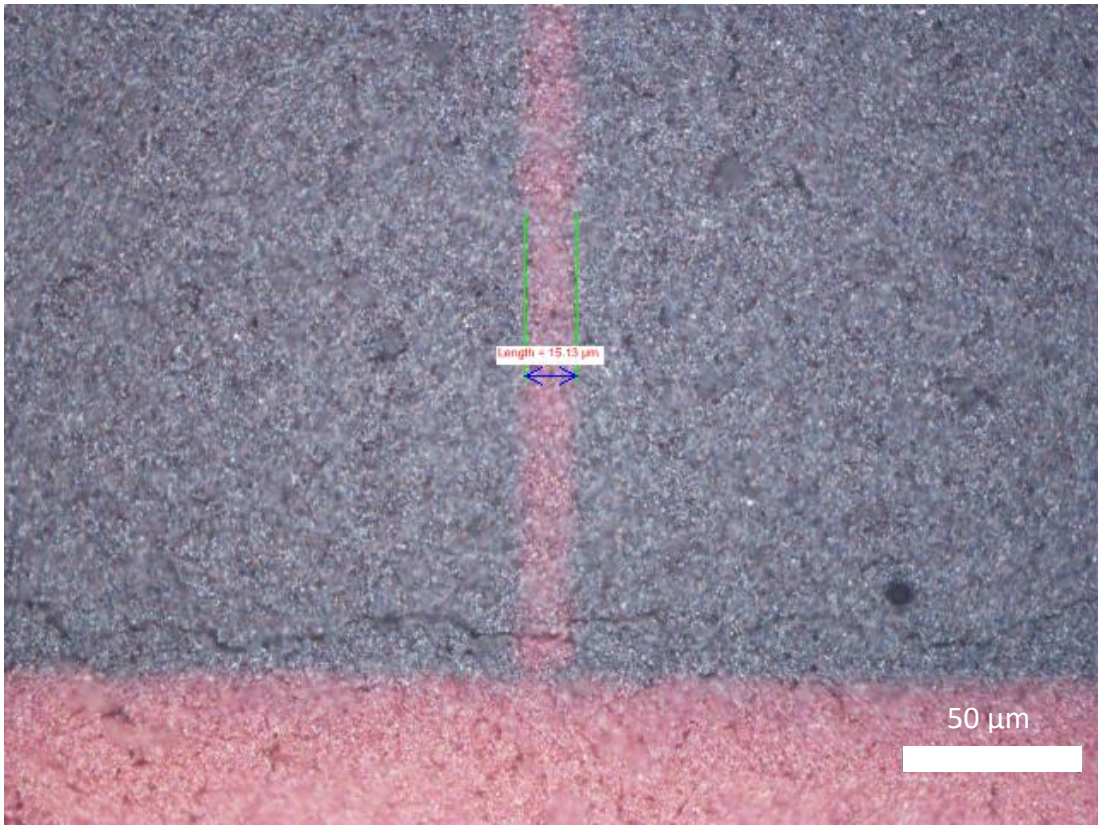


Figure 97. Optical microscope image of a sintered vertical line (appears pink in colour) with an approximate diameter of 15 µm, surrounded by unsintered copper (appears brown in colour). The line width is indicated by the label.

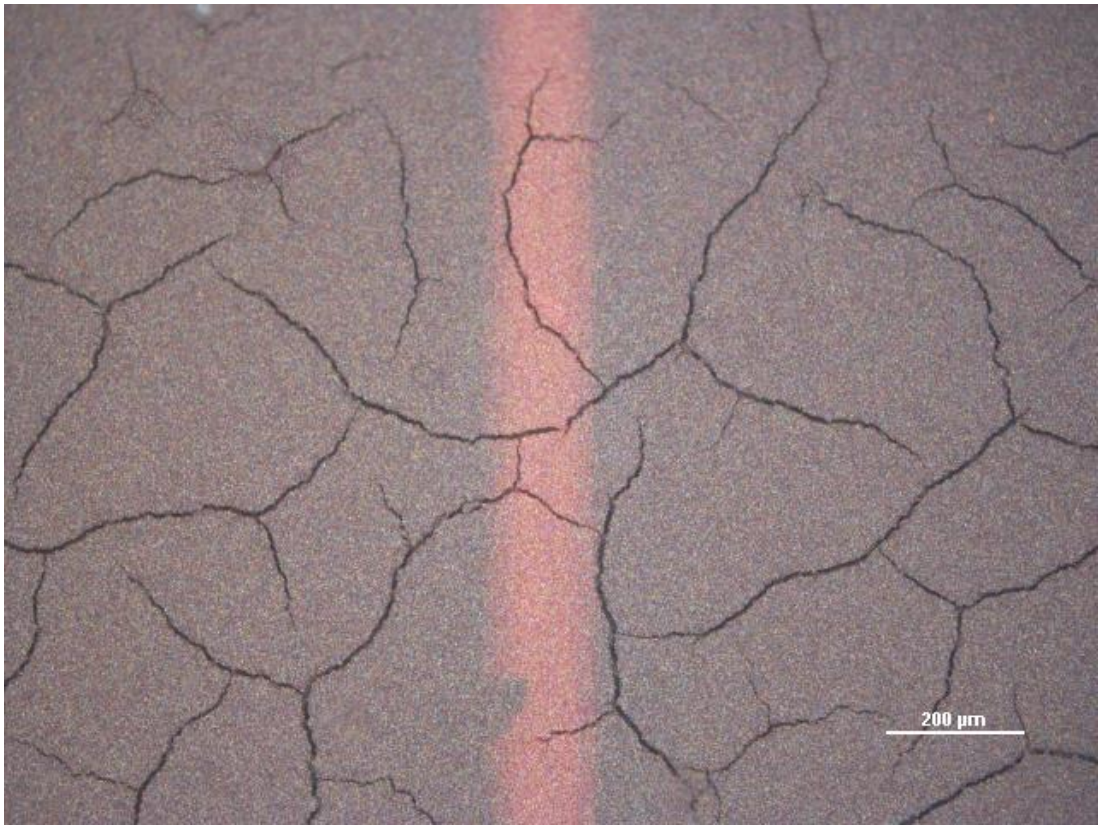


Figure 98. Optical microscope image of a bar coated layer with a thickness greater than its critical cracking thickness which was exposed to a single vertical laser scan.

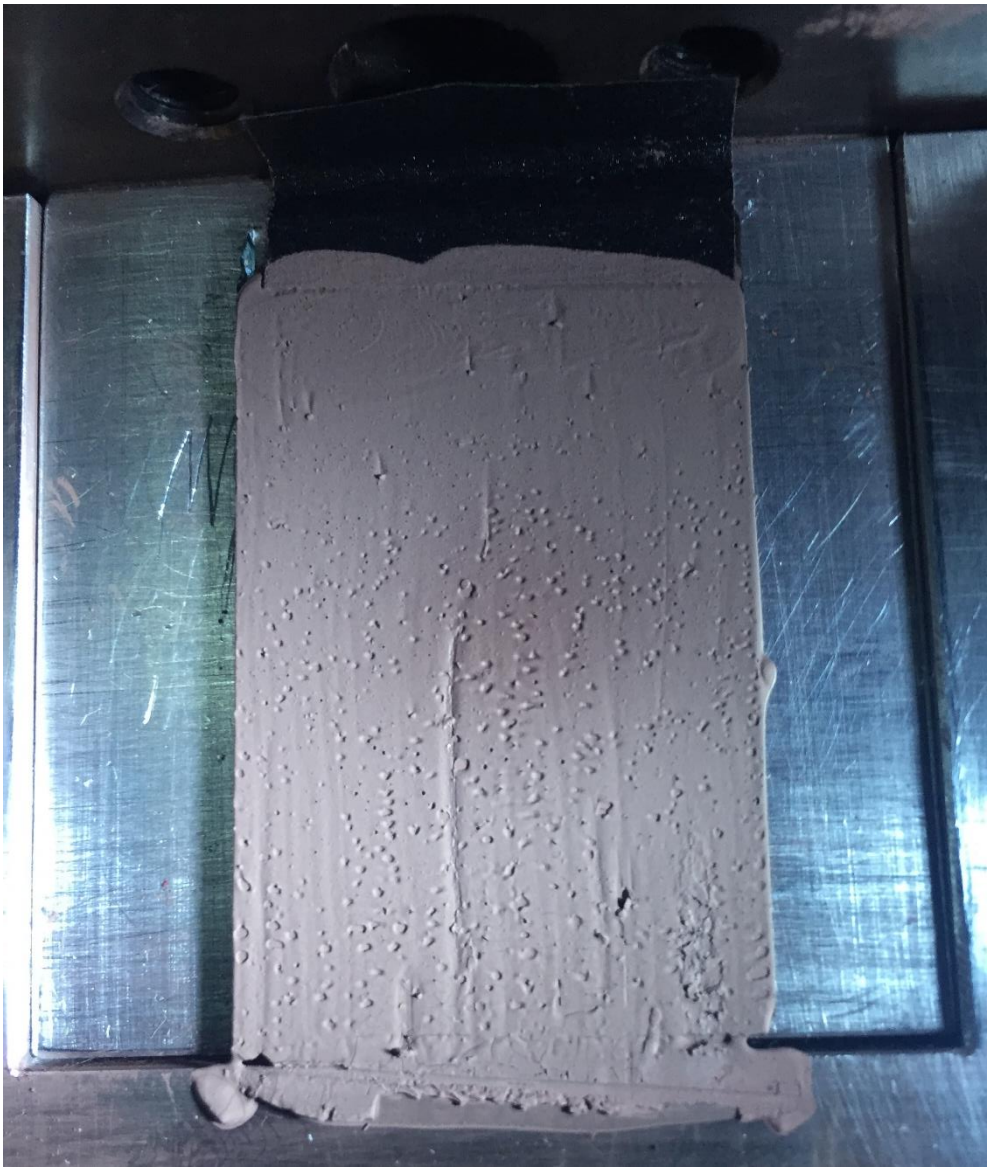


Figure 99. Optical image of an exemplary inhomogeneous bar coated layer.

8.6 Energy-dispersive X-ray (EDX) Spectroscopy Data from Copper (Cu) – Silver (Ag) Nanoparticle (NP) Ink

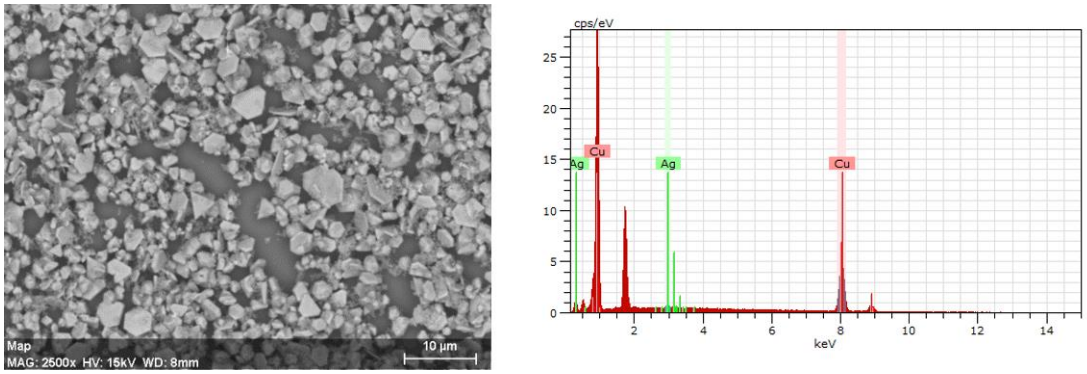


Figure 100. EDX data of 1/99 Ag/Cu NP ink. Left: Backscatter SEM image of the analysed area. Right: EDX spectrum of the same area.

Element	AN	series	Net	[wt.%]	[norm. wt.%]	[norm. at.%]	Error in %
Copper	29	K-series	22439	60.57829	63.89614	35.50052	1.926098
Silicon	14	K-series	34466	21.65635	22.84246	28.71502	0.922708
Carbon	6	K-series	2181	9.899673	10.44187	30.69358	1.438916
Oxygen	8	K-series	1479	2.102586	2.217744	4.893911	0.344613
Silver	47	L-series	704	0.570533	0.601781	0.196967	0.042784
			Sum:	94.80743	100	100	

Table 12. Quantified EDX data from Figure 100.

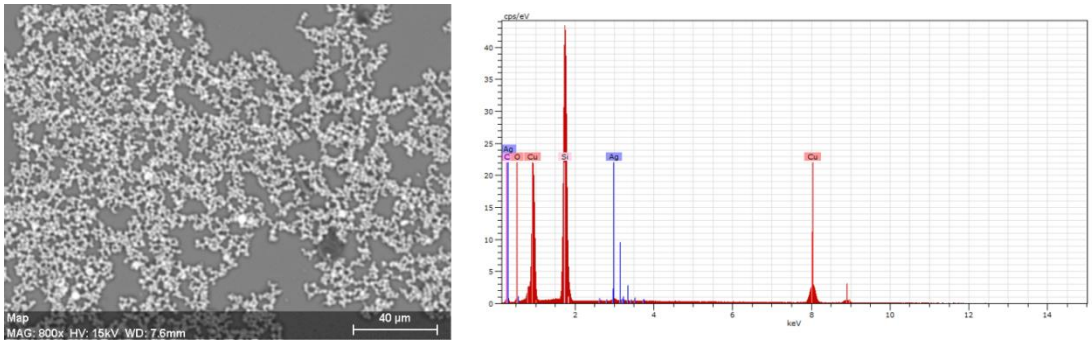


Figure 101. EDX data of 3/97 Ag/Cu NP ink. Left: Backscatter SEM image of the analysed area. Right: EDX spectrum of the same area.

Element	AN	series	Net	[wt.%]	[norm. wt.%]	[norm. at.%]	Error in %
Silicon	14	K-series	144402	50.07734	48.71053	50.36939	2.100827
Copper	29	K-series	18889	36.94697	35.93854	16.42473	1.184489
Carbon	6	K-series	2822	12.56764	12.22462	29.55849	1.754885
Oxygen	8	K-series	1423	1.865771	1.814846	3.294293	0.310497
Silver	47	L-series	2273	1.348265	1.311465	0.353094	0.067026
			Sum:	102.806	100	100	

Table 13. Quantified EDX data from Figure 101.

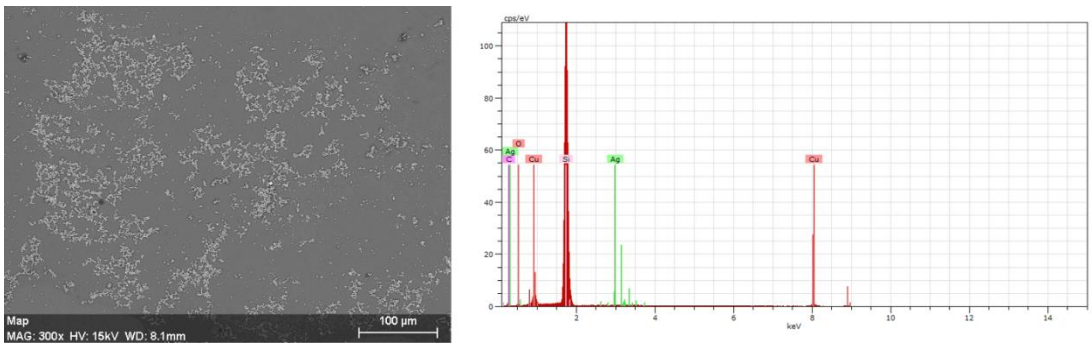


Figure 102. EDX data of 8/92 Ag/Cu NP ink. Left: Backscatter SEM image of the analysed area. Right: EDX spectrum of the same area.

Element	AN	series	Net	[wt.%]	[norm. wt.%]	[norm. at.%]	Error in %
Silicon	14	K-series	199731	83.9909	72.03844	60.87304	3.506626
Carbon	6	K-series	1763	19.21327	16.47909	32.56094	2.861435
Copper	29	K-series	2409	9.926754	8.514111	3.179757	0.336526
Oxygen	8	K-series	835	2.522455	2.163493	3.209184	0.451842
Silver	47	L-series	883	0.938412	0.804869	0.177083	0.054251
			Sum:	116.5918	100	100	

Table 14. Quantified EDX data from Figure 102.

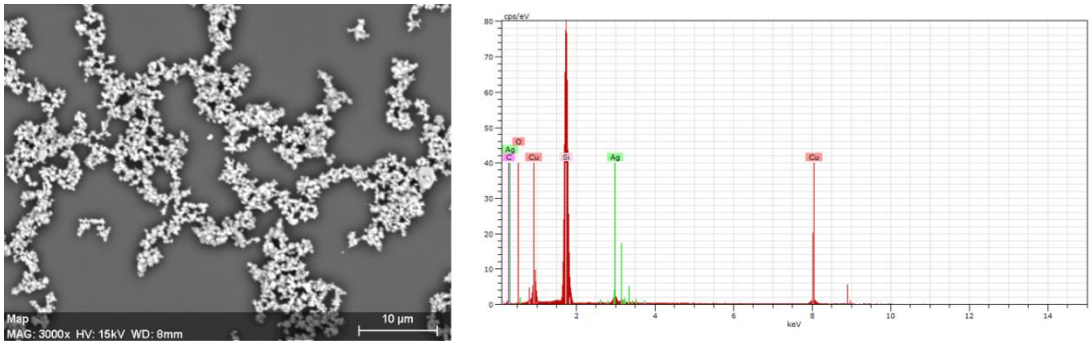


Figure 103. EDX data of 25/75 Ag/Cu NP ink. Left: Backscatter SEM image of the analysed area. Right: EDX spectrum of the same area.

Element	AN	series	Net	[wt.%]	[norm. wt.%]	[norm. at.%]	Error in %
Silicon	14	K-series	118171	68.61134	63.03411	59.90588	2.869106
Copper	29	K-series	3615	17.41542	15.99977	6.720499	0.57154
Carbon	6	K-series	1334	14.68074	13.48738	29.97261	2.296883
Silver	47	L-series	5813	6.952712	6.387546	1.580583	0.241721
Oxygen	8	K-series	330	1.187736	1.091188	1.820422	0.274571
			Sum:	108.8479	100	100	

Table 15. Quantified EDX data from Figure 103.

8.7 Differential Scanning Calorimetry (DSC) Curves of Copper (Cu) - Silver (Ag) NPs

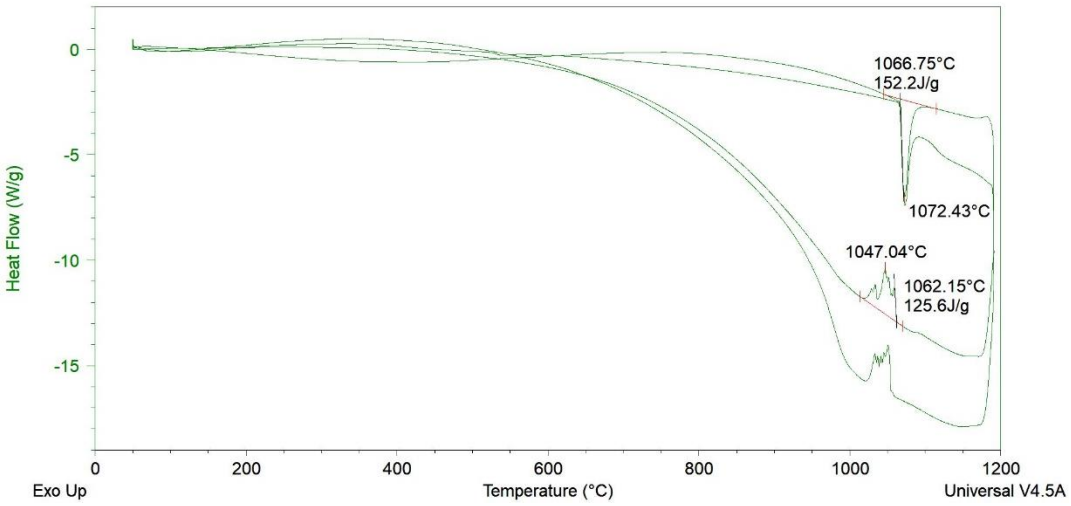


Figure 104. DSC curve of heat flow against temperature of the 100 wt% Cu NPs.

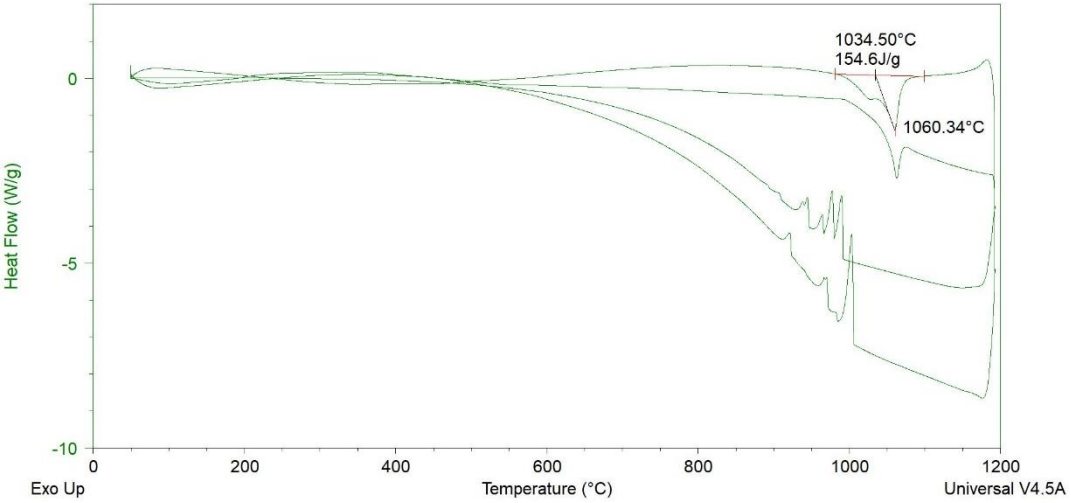


Figure 105. DSC curve of heat flow against temperature of the 1 wt% Ag and 99 wt% Cu NPs.

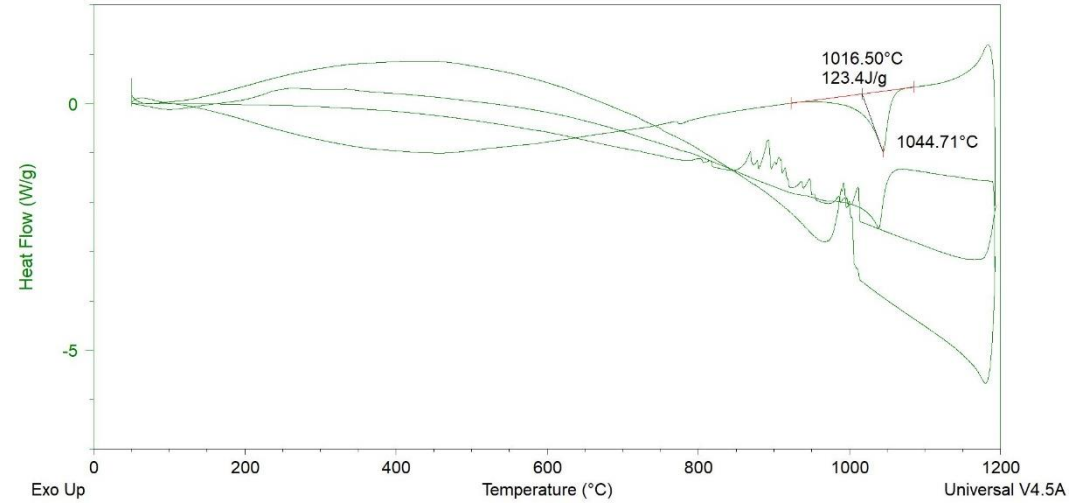


Figure 106. DSC curve of heat flow against temperature of the 3 wt% Ag and 97 wt% Cu NPs.

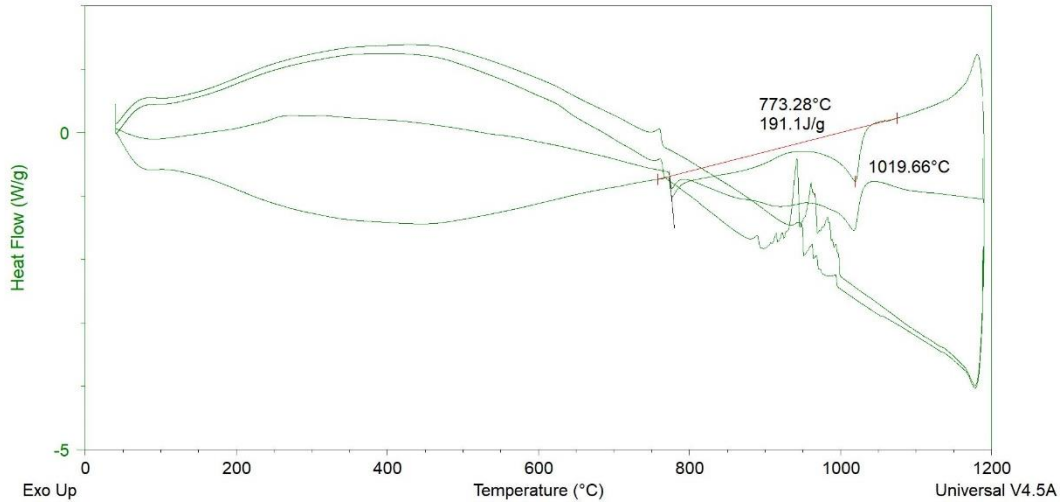


Figure 107. DSC curve of heat flow against temperature of the 8 wt% Ag and 92 wt% Cu NPs.

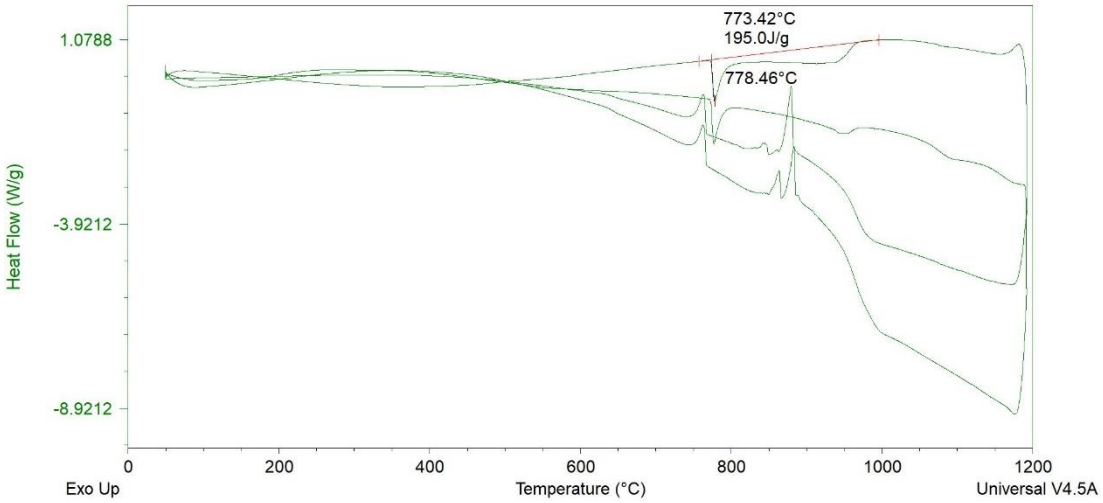


Figure 108. DSC curve of heat flow against temperature of the 25 wt% Ag and 25 wt% Cu NPs.

8.8 Computational Simulation of Ag Accumulation in Adjacent Copper (Cu) Particle Necks

8.8.1 Adjacent Copper (Cu) Particles of Equal Size: MATLAB Code

```
clear all

d = 330e-9;
r = d/2;

Cu_sint_deg = asind(1/(2*4));
Cu_volume = ((4/6)*pi*(r.^3)) - ( (pi/3)*((r-
(r*cosd(Cu_sint_deg)))^2)*(3*r-(r-(r*cosd(Cu_sint_deg)))) );
Cu_contact_area =  pi*(r*sind(Cu_sint_deg)).^2;

Cu_resistance = 1.68e-8;
```

```
Ag_resistance = 1.59e-8;

Ag_sint_deg = asind(1/(2*2));

no_of_points = 100;
no_of_steps = no_of_points-1;
interval = (Ag_sint_deg-Cu_sint_deg)/no_of_steps;

theta_for_plotting =  zeros(no_of_points,1,1);

Ag_contact_area = zeros(no_of_points,1,1);
final_segment_Ag_faction = zeros(no_of_points,1,1);
segment_final_Ag_volume = zeros(no_of_points,1,1);
segment_final_volume = zeros(no_of_points,1,1);
segment_final_carea = zeros(no_of_points,1,1);
segment_final_length = zeros(no_of_points,1,1);


Ag_Cu_mass_ratio = zeros(no_of_points,1,1);
contact_area_increase = zeros(no_of_points,1,1);

segment_Cu_resistance = zeros(no_of_points,1,1);
final_segment_resistance = zeros(no_of_points,1,1);
resistance_overall = zeros(no_of_points,1,1);
segment_Cu_average_carea = zeros(no_of_points,1,1);
segment_Cu_length = zeros(no_of_points,1,1);

res_av = zeros(no_of_points,1,1);
res_improvement = zeros(no_of_points,1,1);

final_segment_resistance_new = zeros(no_of_points,1,1);
final_segment_resistance2 = zeros(no_of_points,1,1);
resistance_overall2 = zeros(no_of_points,1,1);

noAg_segment_Cu_length = r*cosd(Cu_sint_deg);

fun = @(L) L/((r*sind(acosd(L/r))).^2);
    xmin = 0;
    xmax = (r*cosd(Cu_sint_deg));
    int_allCu_noAg = integral(fun,xmin,xmax,'ArrayValued',true);

    noAg_segment_Cu_resistance = Cu_resistance * 2*int_allCu_noAg /
pi;



int_Cu = zeros(no_of_points,1,1);
int_f_Cu = zeros(no_of_points,1,1);
int_f_Ag = zeros(no_of_points,1,1);

counter = 0;

for theta = Cu_sint_deg:interval:Ag_sint_deg % Cu_sint_deg
    counter = counter+1;
    theta_for_plotting(counter) = theta;

    segment_Cu_length(counter) = r*cosd(theta);
```

```
    segment_final_length(counter) = (r*cosd(Cu_sint_deg)) -
(r*cosd(theta));
    segment_final_carea(counter) = pi*(r*sind(theta)).^2;
    segment_final_Cu_volume = (pi/6) * segment_final_length(counter)
* ( 3*(r*sind(theta)).^2 + 3*(r*sind(Cu_sint_deg)).^2 +
segment_final_length(counter).^2 );
    segment_final_volume(counter) = segment_final_length(counter) *
segment_final_carea(counter);
    segment_final_Ag_volume(counter) = segment_final_volume(counter)
- segment_final_Cu_volume;

    Ag_contact_area(counter) = segment_final_carea(counter)-
Cu_contact_area;
    contact_area_increase(counter) =
(segment_final_carea(counter)/Cu_contact_area)-1;

    Ag_Cu_mass_ratio(counter) =
(10490*segment_final_Ag_volume(counter))/(8960*Cu_volume);

    if theta ~= Cu_sint_deg % ensure it won't be "NaN"
        final_segment_Ag_faction(counter) =
segment_final_Ag_volume(counter) / segment_final_volume(counter) ;
    else
        final_segment_Ag_faction(counter) = 0;
    end
    Cu_faction_in_final_segment = 1-
final_segment_Ag_faction(counter);

    fun = @(L) L/((r*sind(acosd(L/r))).^2);
    xmin = 0;
    xmax = segment_Cu_length(counter);
    int_Cu(counter) = integral(fun,xmin,xmax,'ArrayValued',true);

    segment_Cu_resistance(counter) = Cu_resistance *
2*int_Cu(counter) / pi;

    fun = @(L) L/((r*sind(acosd((r*cosd(Cu_sint_deg)-L)/r))).^2);
    xmin = segment_Cu_length(counter);
    xmax = (r*cosd(Cu_sint_deg));
    int_f_Cu(counter) = integral(fun,xmin,xmax,'ArrayValued',true);

    resistance_segment_final_Cu_part = Cu_resistance *
2*int_f_Cu(counter) / pi;

    fun = @(L) L/(((r*sind(acosd((r*cosd(Cu_sint_deg)-L)/r))).^2)-
((r*sind(Cu_sint_deg)).^2));
    xmin = segment_Cu_length(counter);
    xmax = (r*cosd(Cu_sint_deg));
    int_f_Ag(counter) = integral(fun,xmin,xmax,'ArrayValued',true);

    resistance_segment_final_Ag_part = Ag_resistance *
2*int_f_Ag(counter) / pi;

    final_segment_resistance(counter) = (
(1/resistance_segment_final_Cu_part) +
(1/resistance_segment_final_Ag_part) )^(-1);
    resistance_overall(counter) = segment_Cu_resistance(counter) +
final_segment_resistance(counter);
```

```
    res_improvement(counter) =
resistance_overall(counter)/noAg_segment_Cu_resistance;
end

figure(1)
hold on
plot(Ag_Cu_mass_ratio,res_improvement)
xlabel('Ag/Cu mass ratio')
ylabel('Resistance reduction due to Ag accumulation in Cu neck')
```

8.8.2 Adjacent Copper (Cu) Particles of Varying Size: MATLAB Code

```
clear all

l_d = 330e-9;
l_r = l_d/2;
particle_size_ratio = 1/1.0;
r_d = l_d*particle_size_ratio;
r_r = r_d/2;

l_Cu_sint_deg = asind(1/(2*8)); % must be smaller than r_r

if l_r*sind(l_Cu_sint_deg) >= r_r
    l_Cu_sint_deg = asind((r_r*.999)/l_r)
end

r_Cu_sint_deg = asind(l_r*sind(l_Cu_sint_deg)/r_r);

l_Cu_volume = ((4/6)*pi*(l_r.^3)) - ( (pi/3)*((l_r-
(l_r*cosd(l_Cu_sint_deg)))^2)*(3*l_r-(l_r-
(l_r*cosd(l_Cu_sint_deg)))) );
r_Cu_volume = ((4/6)*pi*(r_r.^3)) - ( (pi/3)*((r_r-
(r_r*cosd(r_Cu_sint_deg)))^2)*(3*r_r-(r_r-
(r_r*cosd(r_Cu_sint_deg)))) );
both_Cu_contact_area =  pi*(l_r*sind(l_Cu_sint_deg)).^2;

Cu_resistance = 1.68e-8;
Ag_resistance = 1.59e-8;

l_Ag_sint_deg = asind(1/(2*3)); % must be smaller than r_r hence
must be smaller or equal to particle size ratio % must be bigger
than l_Cu_sint_deg

if l_r*sind(l_Ag_sint_deg) > r_r
    l_Ag_sint_deg = asind(r_r/l_r)
end

r_Ag_sint_deg = asind(l_r*sind(l_Ag_sint_deg)/r_r);

no_of_points = 100;
no_of_steps = no_of_points-1;
interval = (l_Ag_sint_deg-l_Cu_sint_deg)/no_of_steps;

l_theta_for_plotting =  zeros(no_of_points,1,1);
r_theta_for_plotting =  zeros(no_of_points,1,1);
```

```
Ag_contact_area = zeros(no_of_points,1,1);
l_final_segment_Ag_faction = zeros(no_of_points,1,1);
r_final_segment_Ag_faction = zeros(no_of_points,1,1);

l_segment_final_Ag_volume = zeros(no_of_points,1,1);
l_segment_final_volume = zeros(no_of_points,1,1);
both_segment_final_carea = zeros(no_of_points,1,1);
l_segment_final_length = zeros(no_of_points,1,1);

r_segment_final_length = zeros(no_of_points,1,1);
r_segment_final_volume = zeros(no_of_points,1,1);
r_segment_final_Ag_volume = zeros(no_of_points,1,1);

Ag_Cu_mass_ratio = zeros(no_of_points,1,1);
contact_area_increase = zeros(no_of_points,1,1);

l_segment_Cu_resistance = zeros(no_of_points,1,1);
r_segment_Cu_resistance = zeros(no_of_points,1,1);
l_final_segment_resistance = zeros(no_of_points,1,1);
r_final_segment_resistance = zeros(no_of_points,1,1);

resistance_overall = zeros(no_of_points,1,1);
segment_Cu_average_carea = zeros(no_of_points,1,1);
l_segment_Cu_length = zeros(no_of_points,1,1);
r_segment_Cu_length = zeros(no_of_points,1,1);

res_av = zeros(no_of_points,1,1);
res_improvement = zeros(no_of_points,1,1);

final_segment_resistance_new = zeros(no_of_points,1,1);
final_segment_resistance2 = zeros(no_of_points,1,1);
resistance_overall2 = zeros(no_of_points,1,1);

fun = @(L) L/((l_r*sind(acosd(L/l_r))).^2);
    xmin = 0;
    xmax = (l_r*cosd(l_Cu_sint_deg));
    l_int_allCu_noAg = integral(fun,xmin,xmax,'ArrayValued',true);
    l_noAg_segment_Cu_resistance = Cu_resistance * l_int_allCu_noAg
/ pi;

fun = @(L) L/((r_r*sind(acosd(L/r_r))).^2);
    xmin = 0;
    xmax = (r_r*cosd(r_Cu_sint_deg));
    r_int_allCu_noAg = integral(fun,xmin,xmax,'ArrayValued',true);
    r_noAg_segment_Cu_resistance = Cu_resistance * r_int_allCu_noAg
/ pi;

overall_noAg_segment_Cu_resistance = l_noAg_segment_Cu_resistance +
r_noAg_segment_Cu_resistance;

l_int_Cu = zeros(no_of_points,1,1);
l_int_f_Cu = zeros(no_of_points,1,1);
l_int_f_Ag = zeros(no_of_points,1,1);

r_int_Cu = zeros(no_of_points,1,1);
r_int_f_Cu = zeros(no_of_points,1,1);
r_int_f_Ag = zeros(no_of_points,1,1);
```

```
counter = 0;

for l_theta = l_Cu_sint_deg:interval:l_Ag_sint_deg % Cu_sint_deg
    r_theta = asind(l_r*sind(l_theta)/r_r);
    counter = counter+1;
    l_theta_for_plotting(counter) = l_theta;
    r_theta_for_plotting(counter) = r_theta;

    l_segment_Cu_length(counter) = l_r*cosd(l_theta);
    r_segment_Cu_length(counter) = r_r*cosd(r_theta);

    l_segment_final_length(counter) = (l_r*cosd(l_Cu_sint_deg)) -
(l_r*cosd(l_theta));
    both_segment_final_carea(counter) = pi*(l_r*sind(l_theta)).^2;
    l_segment_final_Cu_volume = (pi/6) *
l_segment_final_length(counter) * ( 3*(l_r*sind(l_theta)).^2 +
3*(l_r*sind(l_Cu_sint_deg)).^2 + l_segment_final_length(counter).^2
);
    l_segment_final_volume(counter) =
l_segment_final_length(counter) * both_segment_final_carea(counter);
    l_segment_final_Ag_volume(counter) =
l_segment_final_volume(counter) - l_segment_final_Cu_volume;

    r_segment_final_length(counter) = (r_r*cosd(r_Cu_sint_deg)) -
(r_r*cosd(r_theta));
    r_segment_final_Cu_volume = (pi/6) *
r_segment_final_length(counter) * ( 3*(r_r*sind(r_theta)).^2 +
3*(r_r*sind(r_Cu_sint_deg)).^2 + r_segment_final_length(counter).^2
);
    r_segment_final_volume(counter) =
r_segment_final_length(counter) * both_segment_final_carea(counter);
    r_segment_final_Ag_volume(counter) =
r_segment_final_volume(counter) - r_segment_final_Cu_volume;

    Ag_contact_area(counter) = both_segment_final_carea(counter)-
both_Cu_contact_area;
    contact_area_increase(counter) =
(both_segment_final_carea(counter)/both_Cu_contact_area)-1;

    Ag_Cu_mass_ratio(counter) =
(10490*(l_segment_final_Ag_volume(counter)+r_segment_final_Ag_volume
(counter)))/(8960*(l_Cu_volume+r_Cu_volume));

    if l_theta ~= l_Cu_sint_deg % ensure it won't be "NaN"
        l_final_segment_Ag_faction(counter) =
l_segment_final_Ag_volume(counter) / l_segment_final_volume(counter)
;
    else
        l_final_segment_Ag_faction(counter) = 0;
    end
    l_Cu_faction_in_final_segment = 1-
l_final_segment_Ag_faction(counter);

    if r_theta ~= r_Cu_sint_deg % ensure it won't be "NaN"
        r_final_segment_Ag_faction(counter) =
r_segment_final_Ag_volume(counter) / r_segment_final_volume(counter)
;
    else
```

```
        r_final_segment_Ag_faction(counter) = 0;
    end
    r_Cu_faction_in_final_segment = 1-
r_final_segment_Ag_faction(counter);

    fun = @(L) L/((l_r*sind(acosd(L/l_r))).^2);
    xmin = 0;
    xmax = l_segment_Cu_length(counter);
    l_int_Cu(counter) = integral(fun,xmin,xmax,'ArrayValued',true);
    l_segment_Cu_resistance(counter) = Cu_resistance *
l_int_Cu(counter) / pi;

    fun = @(L) L/((r_r*sind(acosd(L/r_r))).^2);
    xmin = 0;
    xmax = r_segment_Cu_length(counter);
    r_int_Cu(counter) = integral(fun,xmin,xmax,'ArrayValued',true);
    r_segment_Cu_resistance(counter) = Cu_resistance *
r_int_Cu(counter) / pi;

    fun = @(L) L/((l_r*sind(acosd((l_r*cosd(l_Cu_sint_deg)-
L)/l_r))).^2);
    xmin = l_segment_Cu_length(counter);
    xmax = (l_r*cosd(l_Cu_sint_deg));
    l_int_f_Cu(counter) =
integral(fun,xmin,xmax,'ArrayValued',true);
    l_resistance_segment_final_Cu_part = Cu_resistance *
l_int_f_Cu(counter) / pi;

    fun = @(L) L/((r_r*sind(acosd((r_r*cosd(r_Cu_sint_deg)-
L)/r_r))).^2);
    xmin = r_segment_Cu_length(counter);
    xmax = (r_r*cosd(r_Cu_sint_deg));
    r_int_f_Cu(counter) =
integral(fun,xmin,xmax,'ArrayValued',true);
    r_resistance_segment_final_Cu_part = Cu_resistance *
r_int_f_Cu(counter) / pi;

    fun = @(L) L/(((l_r*sind(acosd((l_r*cosd(l_Cu_sint_deg)-
L)/l_r))).^2)-((l_r*sind(l_Cu_sint_deg)).^2));
    xmin = l_segment_Cu_length(counter);
    xmax = (l_r*cosd(l_Cu_sint_deg));
    l_int_f_Ag(counter) =
integral(fun,xmin,xmax,'ArrayValued',true);
    l_resistance_segment_final_Ag_part = Ag_resistance *
l_int_f_Ag(counter) / pi;

    fun = @(L) L/(((r_r*sind(acosd((r_r*cosd(r_Cu_sint_deg)-
L)/r_r))).^2)-((r_r*sind(r_Cu_sint_deg)).^2));
    xmin = r_segment_Cu_length(counter);
    xmax = (r_r*cosd(r_Cu_sint_deg));
    r_int_f_Ag(counter) =
integral(fun,xmin,xmax,'ArrayValued',true);
    r_resistance_segment_final_Ag_part = Ag_resistance *
r_int_f_Ag(counter) / pi;

    l_final_segment_resistance(counter) = (
(1/l_resistance_segment_final_Cu_part) +
(1/l_resistance_segment_final_Ag_part) )^(-1);
```

```
    r_final_segment_resistance(counter) = (
(1/r_resistance_segment_final_Cu_part) +
(1/r_resistance_segment_final_Ag_part) )^(-1);

    resistance_overall(counter) = l_segment_Cu_resistance(counter) +
l_final_segment_resistance(counter) +
r_segment_Cu_resistance(counter) +
r_final_segment_resistance(counter);

    res_improvement(counter) =
resistance_overall(counter)/overall_noAg_segment_Cu_resistance;
end

figure(1)
plot(Ag_Cu_mass_ratio,res_improvement)
xlabel('Ag/Cu mass ratio')
ylabel('Resistance reduction due to Ag accumulation in Cu neck')
hold on
```